Experimental investigation of flow structures in a shallow embayment using 3D-PTV

Yulia AKUTINA

Doctor of Philosophy

Department of Civil Engineering and Applied Mechanics

McGill University

Montréal, Québec

October 2015

A thesis submitted to McGill University in partial fulfillment of the requirements of the degree of Doctor of Philosophy.

To my mother, my father, and my Peter.
To all my big and beloved family.

Being a scientist means spending ten years pursuing an idea, realizing it is false, finding the strength to admit it, and then turn around and pursue the opposite idea with equal passion. Prof. Greg Lawrence, UBC.

ABSTRACT

Understanding the structure of the flow in shallow embayments is crucial for quantifying mass transfer (nutrients, sediments or pollution) between the main flow and groyne fields in rivers. Most previous research has focused on two-dimensional flow structures in embayments. Also, the rigid-lid assumption was often employed neglecting the effects of surface gravity waves that can occur in the embayment as a result of resonant coupling between the natural frequency of the embayment and the flow. In the present work a fully three-dimensional flow field and gravity waves are investigated in a laboratory setting using three-dimensional particle tracking velocimetry (3D-PTV). Three cameras were mounted above an open channel (40 cm wide) with a square embayment on its side (24x24 cm). Trajectories of neutrally-buoyant particles (0.23 mm in diameter) used as flow tracers were simultaneously recorded with the cameras at a rate of 600 frames per second. Fully three-dimensional instantaneous and time-averaged velocity and vorticity fields were calculated from the particle tracks and surface oscillations caused by gravity waves were approximated from the highest particle positions. 3D-PTV was performed for the first time through the water's free surface. Two methods were developed to assess different components of the velocity error showing that accurate measurements through a free water surface are possible when the average displacement of particles per frame is much smaller than the wavelength of surface oscillations. The results of the 3D-PTV measurements show a regular quasi-two-dimensional recirculating gyre in the embayment. However, the exchange process between the embayment and the channel flow is fully three-dimensional. It exhibits a -5/3 slope of the frequency spectrum of velocity fluctuations and the exchange shows significant variation with elevation above the bed. The flow enters the embayment along the bed closer to the downstream end and leaves through the top 20% of the water depth all along

the interface. A secondary circulation within the embayment gyre appears in the time-averaged flow. It consists of a radial inflow along the bed towards the gyre core, upwelling at the embayment centre and spiralling outwards closer to the surface. The radial inflow is associated with the deceleration of the gyre by bottom friction and thus has a vertical extension corresponding to the bottom boundary-layer thickness. Görtler-like streamwise vortices were found in the boundary layer that curves along the three side walls of the embayment. Depending on the free-stream velocity, either one spiral structure or a pair of counter-rotating vortices on top of each other were present. All of these three-dimensional structures can have a significant effect on the exchange process, which therefore cannot be described by two-dimensional models. However, parameterizations based on stability arguments may be used in future to account for their feedback on the two-dimensional flow. Comparing cases with different intensities of gravity waves confirmed they increase the exchange between the embayment and the main channel, possibly due to the induced shear-layer undulation. However, they do not affect the overall pattern of three-dimensional structure described above. It is shown that gravity waves are resonantly amplified at certain free-stream velocities due to resonant coupling with the most energetic frequency of the main gyre within the embayment, contrary to previous studies. It is hoped that understanding the resonant state of the gravity waves may facilitate prediction of the increase in the exchange rate.

RÉSUMÉ

Comprendre la structure du flux dans une baie peu profonde est primordial pour quantifier le transfert de masse (nutriments, sédiments ou polluants) entre le courant principal et les épis de rivières. La plupart des études précédentes supposent un flux quasi-bidimensionnel dans les baies. Comme les ondulations de surface étaient négligées, les ondes de gravité de surface, qui peuvent être générée par un couplage résonant entre la baie et le courant principal, n'étaient pas prises en compte. Dans le cadre de ce travail, nous avons étudié un champ d'écoulement tridimensionnel en laboratoire, grâce à une méthode de vélocimétrie par suivi de particules tridimensionnelle (3D-PTV). Trois caméras ont été installées au-dessus d'un canal à surface libre (40 cm de largeur) avec une baie carrée sur l'un de ses côtés (24 cm par 24 cm). Les trajectoires de particules à flottabilité neutre (0.23 mm en diamètre), utilisées comme traceurs de l'écoulement, ont été enregistrées simultanément par les caméras à une fréquence de 600 images par seconde. Les champs tridimensionnels de vitesse et de vorticité, instantanés et moyennés dans le temps, ont été calculés à partir des trajectoires des particules. Les oscillations de surface dues aux ondes de gravité ont été approximées à partir des positions des particules les plus hautes. De plus, la méthode 3D-PTV est utilisée pour la première fois à travers la surface libre de l'eau. Deux méthodes ont été développées pour évaluer les composantes différentes de l'erreur de vélocité qui montrent que des mesures précises sont possibles à travers la surface libre de l'eau quand le déplacement moyen des particules par image est beaucoup plus petit que la longueur d'onde des oscillations de surface. Les résultats des mesures 3D-PTV montrent un tourbillon quasi-bidimensionnel stationnaire dans la baie. Néanmoins, les mesures montrent aussi que le processus d'échange entre la baie et l'écoulement dans le canal est totalement tridimensionnel. Il présente un spectre de fréquences avec une pente de

-5/3 et varie significativement avec la profondeur du canal. L'écoulement entre dans la baie le long du lit du canal, du côté aval, et ressort dans les 20% supérieurs de la hauteur d'eau sur toute l'interface. Un courant secondaire apparaît au sein du tourbillon dans la baie lorsque le flux est moyenné temporellement. Il consiste en un flux radial qui entre le long du lit vers le centre du tourbillon, monte au centre de la baie et ressort en spirale en surface. Le flux radial entrant s'associe à la décélération du tourbillon par friction de fond et connaît donc une extension verticale correspondant à l'épaisseur de la couche-limite inférieure. Des vortex de Görtler parallèles au courant se trouvent dans la couche-limite qui longe les trois côtés de la baie. Selon la vitesse du courant principal, se développe soit une structure en spirale soit une paire de vortex superposés tournant dans des sens opposés. Toutes ces structures tridimensionnelles influencent significativement le processus d'échange, qui ne peut donc pas être décrit par des modles bidimensionnels. Cependant, des paramétrages basés sur des arguments de stabilité pourront être utilisés pour modéliser leurs effets sur le courant bidimensionnel. La comparaison de cas avec des ondes gravité d'intensités différentes a confirmé que les structures tridimensionnelles accroissent notablement le taux d'échange entre la baie et l'écoulement principal, probablement en raison de l'ondulation induite de la couche de cisaillement. Cependant elles ne modifient pas la structure générale tridimensionnelle décrite précédemment. Nous montrons que les ondes de gravité sont amplifiées par résonance pour certaines vitesses du courant principal en raison d'un couplage résonant avec la fréquence de plus haute énergie du tourbillon principal dans la baie, contrairement à ce qui a été montré dans les études précédentes. Comprendre l'état résonant des ondes de gravité permettra de prévoir l'augmentation du taux d'échange.

ACKNOWLEDGEMENTS

The completion of this research would not have been possible without the help and support of many people. I would like to express gratitude to my thesis advisers, Professor Laurent Mydlarski and Professor Susan Gaskin, for their guidance and confidence in me. I am immensely grateful to Professor Laurent Mydlarski from whom I learnt a lot about experimental work and fluid mechanics. Not only did he provide me with scientific advice, but he could always find a kind word of encouragement when I needed it most. I am thankful to Professor Susan Gaskin who provided me with great freedom both in my research path and the execution. Professor Gaskin has also encouraged me to engage in scientific conferences, from which I benefited a great deal. I am also grateful to my advisers for giving me the opportunity to work with state-of-the-art equipment without which my work would not have been possible. In addition, I would like to acknowledge the support of the Faculty of Engineering from which I received the McGill Engineering Doctoral Award.

I would like to extend my deepest gratitude to the members of the technical staff who are both rare professionals and a pleasure to deal with. I would have been lost without the invaluable help of John Bartczak, who knows a way to solve any problem in the lab while telling a good joke. Jorge Sayat kindly helped me with all my computer-related problems, and also always gave me a boost with his good mood. My colleague Phil Roche, from the Photonic Systems Group who has lended me both a hand and equipment. We spent hours on very interesting technical discussions from which I learnt a lot.

A special thank you I owe to all the scientists supporting the open-source PTV code on their free time. Without Professor Alex Liberzon from Tel Aviv University who spent hours helping me with the code, I would not have been able to accomplish the data analysis.

I would like to thank my dear friend and a fellow graduate student Alejandro Perez Alvarado. We started our Ph.D. studies together and over the years he has been a trustworthy friend, a helpful colleague, and a person willing to spend hundreds of hours on nerdy scientific discussions with me. So did my wonderful friend Hossein Amini Kafiabad, from the Atmospheric and Oceanic Sciences department: not only he has been a pillar of support but also he came up with the idea of holding a turbulence journal club which we all attended and enjoyed tremendously for a long, long time. My friends Sisi Chen, from Atmospheric and Oceanic Sciences with her contagious enthusiasm and Lenin Del Rio Amador, from the Physics department with his humour and persistent will for solutions made the scientific debates even more pleasurable and fruitful. I will never forget those wonderful days of engagement, friendship and scientific stimulation. Thank you all, my friends.

I would also like to thank my mentor and beloved thesis adviser Victor Jouk from my batchelor's degree in Moscow. He never stopped supporting me and recently gave me an incredibly hard time about my Ph.D. thesis! I will never stop learning from his constructive criticism. Thank you for your love and care.

I received invaluable advice and support from my wonderful friends and colleagues Stoyan Rangelov, Dan Robb and Hauke Blanken, who have always been by my side. My colleague Cécile Defforge helped me to translate my abstract to French. Katerina Bondar and Sebastien Lavoie have been a part of my Canadian family (sorry, Québécois!). Thank you for adopting me.

I feel blessed to have such a wonderful network of friends and family, and I thank them for their support and love. Literally nothing would have happened without my amazing parents. They patiently listened to all of my ups and downs and always found exactly the right words to encourage me. No matter how bad things appear my mother and father always made me laugh. They went through everything with me and I believe they should also get a couple of PhDs for it. I look up to them and I wish one day I am half as good. My grandmother has always been by my side with her endless wisdom, humour and energy. I always felt the support of my wonderful three brothers standing behind me. I would also like to thank especially my grandfather Vsevolod Miller for holding my hand at all times along with my grandmother and my great uncle.

Lastly, and the mostly, I am forever indebted to my Peter, who has been everything to me, a faithful companion, a mentor and a dearest friend. It is impossible to appraise how much I learnt from you and how much you supported me. Thank you, my dear.

TABLE OF CONTENTS

LIST OF TABLES

Table — page

LIST OF FIGURES

CHAPTER 1
Introduction

1.1 Motivation

The transport of pollution and sediment by channel flows is one of the primary problems of river engineering. Irregularity of the banks, bays, harbours, groynes (man-made structures built to protect banks from erosion and improve navigation, Figure 1.1a) can change considerably the spreading rates and the spatial distribution of solutes and sediments in river flows (Valentine & Wood, 1977; Booij, 1989; Uijttewaal *et al.*, 2001). These slow-moving regions or "dead zones" at the banks of a channel are often generalized as embayments or cavities regardless of their origin (Figure 1.1b). Contaminated matter can settle and accumulate there, but can also be flushed out at a high stage (an event where the water level is high). Changes in the main-channel flow velocities can reverse the process from sedimentation to scouring inside the cavity. To predict this highly sensitive and variable behaviour, it is necessary to understand the exact mechanism by which the main current is interacting with the cavity and how the flow structures inside the embayment depend on changes in the main channel.

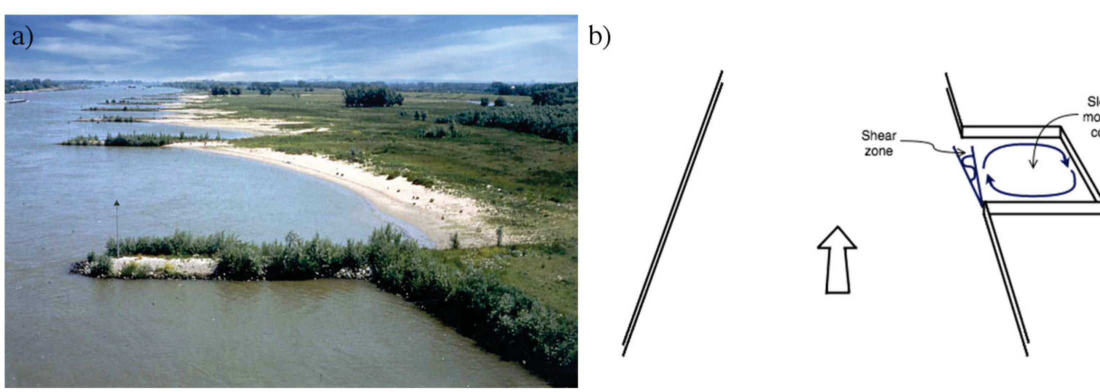

Figure 1.1: a) Groynes in the Waal river, Rhine basin, Netherlands (Courtesy: Mohamed F.M. Yossef). b) Schematic of a generalized embayment.

Traditionally, embayment flows have been treated as two-dimensional problems, where all the characteristics are averaged over the flow depth (Babarutsi & Ganoulis, 1989; Altai & Chu, 1997; Kimura & Hosoda, 1997). This approximation is not without basis, as river flows are usually shallow; that is, the flow depth is much smaller than the width of the river and the mixing process therefore occurs much faster in the vertical direction than in the horizontal plane. Thus, the time taken for vertical mixing in many cases can be neglected, and the flow can be treated as two-dimensional. At the same time, because the flow is shallow, one expects large velocity gradients in the vertical direction, and therefore potential for three-dimensionality.

The first evidence of the failure of the 2D approximation in a shallow embayment was presented by Uijttewaal *et al.* (2001). Two experimental techniques, one using surface velocities and the other depth-averaged characteristics, produced significantly different results. Also, considerable differences were found between the results of 2D Large Eddy Simulations (LES) and 3D LES of the shallow embayment (Hinterberger *et al.*, 2007). However, the exact reasons for these discrepancies are still not completely understood. In this work it is hypothesised that there may be two reasons for the poor performance of 2D models. One is the underestimation of the effect of 3D flow structures on the 2D velocity field. Indeed, some evidence of three-dimensionality was presented by Mizumura *et al.* (2003) and Constantinescu *et al.* (2009), who observed the flow to penetrate embayments along the bottom and to be ejected through the upper part of the interface. Gaskin *et al.* (2002) also presented evidence of a 3D secondary circulation within the embayment flow. The second possible reason for inaccuracy of these models is the common use of the rigid-lid approximation (Constantinescu *et al.*, 2009; Hinterberger *et al.*, 2007) which implies a flat water surface, neglecting the effects of surface gravity waves on mixing and exchange. Indeed, it was previously shown qualitatively by Tuna *et al.* (2013) that the exchange can be intensified by gravity waves in a shallow embayment. Also, the two reasons for poor performance of the commonly-used 2D models, three-dimensionalization and gravity waves, may be directly related to each other.

It is thus clear that a thorough and systematic study of the full flow structure and surface gravity waves in an embayment is required to further confirm or refute the validity of using 2D models to simulate the effect of "dead zones" on dispersion of pollutants and sediment transport in river flow. Also, it is possible that parametrization of the feedback of 3D structures and gravity waves on the 2D flow field can be implemented in the future. In order to do so, again, an understanding of their underlying mechanisms is necessary.

1.2 Objectives

This work is an experimental investigation into the flow structure of a shallow embayment. The main objective is to find the reasons for the failure of current 2D models to simulate the exchange process between an embayment and the channel flow. First, it is intended to verify the existence of three-dimensional flow structures, determine their form, intensity, and ultimately, conditions for their appearance. Second, the effect of the surface gravity waves on the exchange process will be investigated along with the conditions where their amplitudes become large.

The flow of a river past a shallow embayment will be physically modelled in a laboratory channel. Fully three-dimensional measurements are desired to capture the flow structures. This will be achieved by the use of three-dimensional particle tracking velocimetry (3D-PTV). Small neutrally buoyant particles are used as flow tracers. Their positions are simultaneously tracked in space and time using three cameras. Based on the 3D Lagrangian trajectories of the particles, the 3D velocity and vorticity fields are calculated and analysed. This technique allows capturing both time-averaged flow statistics and instantaneous turbulent characteristics of the flow.

Due to technical limitations 3D-PTV measurements are taken through the free surface of the flow. It therefore became a second goal of this research to investigate the refraction errors associated with the changing angle and position of the unsteady interface. Analysis of the steady and unsteady components of the errors, their differences in vertical and horizontal directions, and their spatial distribution will be performed.

Three flow conditions were chosen to get a qualitative assessment of the dependence of the turbulent structures on the free-stream velocity and on the gravity waves. The flow discharge is varied while keeping the flow depth and channel geometry constant. The lowest free-stream velocity has negligible gravity-wave amplitudes. The highest one exhibits significant surface oscillations in the transverse direction. This will allow us to study both the 3D flow structures, including their dependence on the free-stream velocity, and the gravity waves.

1.3 Organization of the thesis

The rest of this thesis is structured as follows. Chapter 2 reviews the literature on the following topics: free surface embayment flows, flow instabilities characteristic of shallow embayments, and the 3D particle tracking velocimetry technique. Chapter 3 explains the experimental method, including a description of the apparatus, the flow conditions, and the 3D-PTV method. The relations between turbulent scales and the temporal and spatial resolution of the measurements is also discussed. Chapter 4 is devoted to the assessment of the data quality, including free-stream conditions of the flow in the flume, convergence of time-averaged statistics, and finally, the error analysis, including an investigation of the velocity and velocity-derivative errors associated with unsteady surface oscillations.

The results of the 3D-PTV measurements and their analysis are presented in Chapter 5. The first section of this chapter introduces the general flow pattern with the use of some basic flow statistics. Section 2 is devoted to the 3D flow structures that were found. This includes the geometry of the exchange flow through the embayment opening, a 3D secondary circulation within the recirculation gyre, and Görtler-like streamwise vortices along the side walls of the embayment. Also, the analysis of the logarithmic slopes of the frequency spectra of velocity fluctuations at different locations is presented with regards to the dimensionality of the flow. The third and last section of this chapter describes the gravity waves that are present in the current experiments. The analysis of their spectra, conditions for resonant response in their amplitude, and their effect on the exchange process are discussed.

Chapter 6, the final chapter of this thesis, presents the conclusions. The first section provides the summary of the error analysis and its meaning with respect to the possibility of the optical measurements through an unsteady interface and its limitations. Next, a summary of the results of the flow structure analysis in a shallow embayment is presented. A short outline of the novel contributions of this work is given in Section 3. Finally, recommendations for future work are proposed in the last section.

CHAPTER 2
Literature review and background

In this chapter, literature on shallow embayment flows, as well as some background on flow instabilities that can appear in a shallow embayment, such as shear instability, Görtler Instability, centrifugal instability, and gravitational instability are presented. Also, a review of the 3D particle tracking velocimetry technique that is used in the current study is provided.

2.1 Free surface embayment flow

Over the years, much research has been done on embayment flows, some of which chose to consider realistic geometry. Groyne fields in rivers often have width-to-depth aspect ratios different from unity, the embayment region tends to be shallower than the main channel, and the bed in the embayment is often inclined towards the main channel. For example, Weitbrecht *et al.* (2008) studied the effects of the embayment's aspect ratio, groyne angles, and depth difference between the main channel and the embayment on the exchange process. Engelhardt *et al.* (2004) and Sukhodolov (2014) studied embayment flows in the field in the Elbe and Spree rivers. Constantinescu *et al.* (2009) investigated the effect of a series of groynes on the exchange process. However, in this work we chose to focus our attention on the simplest geometry possible (square cavity, flat bed). It is argued that this simpler flow is not completely understood, and therefore, it may be useful to reduce the problem to identify the cause and effect relation better. Thus, in this section the focus is on the fundamental simplified flow case.

A single recirculation region that forms in a square embayment adjacent to a channel is investigated. The recirculating flow in an embayment is defined by three distinct regions (Figure 2.1): i) a core region, or a "dead zone", at the centre of

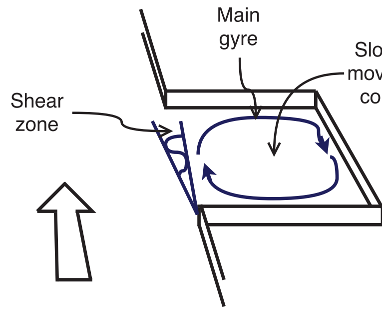

Figure 2.1: The three flow regions in an embayment (top view)

the embayment exhibiting relatively slow-moving flow, ii) an outer region, which is characterized by large-scale circulation or a gyre, and iii) a mixing layer, which develops along the embayment opening, where the slower moving fluid of the gyre meets the faster flowing fluid in the main channel; it is usually dominated by Kelvin-Helmholtz vortical structures with a vertical axis of rotation, which are considered to be responsible for the bulk of the exchange between the embayment and the main stream (Babarutsi & Ganoulis, 1989; Kimura & Hosoda, 1997; Uijttewaal *et al.*, 2001).

Due to environmental relevance (transport of pollutants and nutrients) the major focus of previous research was on the exchange process between the embayment and the main channel. Valentine & Wood (1977) first suggested, for the case of a cavity in a channel bed that the dimensionless exchange coefficient, k, is a constant independent of the free-stream velocity in accordance with the "dead zone" prediction stating that the exchange process is a first-order system. For the case of uniform depth in the embayment, which is implied herein, k can be calculated as

$$k = \frac{w}{U_\infty T}, \tag{2.1}$$

where U_∞ is the free-stream velocity (flow velocity in the channel), w is the cavity width, and T is the characteristic exchange time, which is usually obtained experimentally by measuring the decay of an initial concentration difference between the river and an embayment. However, the calculations of k in different studies yielded quite a spread of values. Altai & Chu (1997) found $k = 0.01 - 0.02$ for square cavities. Valentine & Wood (1977) obtained values between 0.01 and 0.03. Uijttewaal *et al.* (2001) found $k = 0.024$, irrespective of the river flow velocity and the cavity shape. However, Uijttewaal *et al.* (2001) also note that when the exchange coefficient was measured by floating particles, it yielded a value of k that was twice as large. Tuna *et al.* (2013) obtained $k = 0.03$ for the case of negligible gravity waves and 0.04 for the case with gravity waves. Two major reasons for these disagreements are proposed in this thesis: an underestimation of three-dimensional effects in addition to the effect of gravity waves.

Early research on the recirculating region in embayments and groyne fields employed the quasi-two-dimensional approximation (Babarutsi & Ganoulis, 1989; Altai & Chu, 1997; Kimura & Hosoda, 1997). These studies measured and calculated either the depth-averaged or surface characteristics of the flow and determined the retention time of dye in the recirculating region. Similarly, numerical studies used the shallow-water equations that consist of the depth-averaged continuity and momentum equations (Abbot, 1979). As was mentioned before, this approximation is valid since river flows are usually classified as "shallow" having a large width-to-depth ratio. This implies that the time taken for vertical mixing can be neglected, and the flow can be treated as quasi-two-dimensional. At the same time, the shallowness of the flow suggests large vertical velocity gradients that have a large potential for generation of three-dimensional flow structures. In particular, three-dimensionality can be expected when large vertical velocity gradients are superimposed on strong horizontal velocity gradients. This type of problem is generally called a shallow shear flow, which is a combination of a shear flow and a wall-bounded flow (Figure 2.2). It was extensively studied by Chu & Babarutsi (1988*a*); Chen & Jirka (1997); van Prooijen & Uijttewaal (2002). Shear flow is characterized by Kelvin-Helmholtz instability, which generates vortical structures with

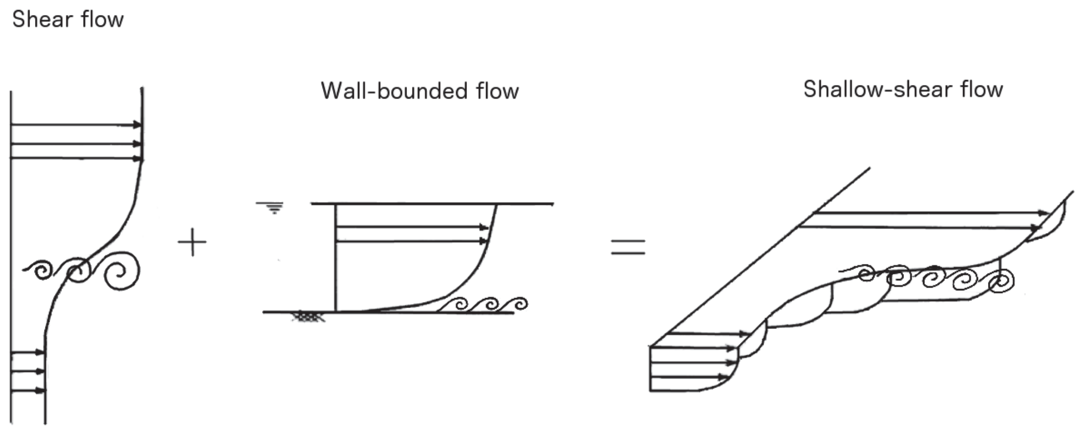

Figure 2.2: Mean flow profiles in a shallow shear layer (diagram adopted from van Prooijen & Uijttewaal (2002)).

a vertical axis of rotation. Wall-bounded flow exhibits Tolmien-Schlichting instability which results in so-called hairpin structures with horizontal vorticity. Thus, shallow shear flow has both, and one can expect non-linear interaction between these structures with consequent three-dimensional instability.

In the embayment there are two distinct regions that can be classified as shallow shear flow: the mixing layer and the gyre (Figure 2.3). It is thus fair to expect that a 2D model may be insufficient at providing a complete description of the flow in both the recirculating zone and the mixing layer. Indeed, recent studies have suggested that a two-dimensional model predicting flow patterns in an embayment is not adequate. The first evidence of this was given by Uijttewaal *et al.* (2001). The exchange rate between the main flow and the embayment was calculated using two different laboratory techniques: measurement of depth-averaged dye concentrations and tracking surface particles. The exchange rate obtained from the surface data was twice as high as that obtained from the depth-integrated dye concentrations. Discrepancies have been found in numerical simulations as well. Hinterberger *et al.* (2007) showed that two-dimensional Large Eddy Simulation (2D LES) of an

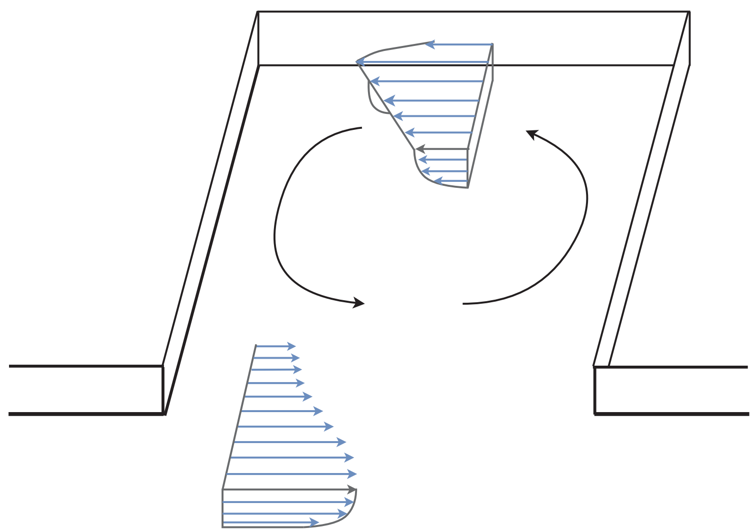

Figure 2.3: Shallow shear layers in the embayment flow.

embayment flow resulted in a mass exchange coefficient that was twice as high as the mass exchange coefficient calculated from a 3D LES. Other evidence of three-dimensionality of this flow was presented in Mizumura *et al.* (2003), Jamieson & Gaskin (2007*b*), and Constantinescu *et al.* (2009). The authors showed that the shear layer between the embayment and the main channel varies significantly with depth. Particles were observed to leave the embayment along the surface, and to enter it along the bottom. Also, Gaskin *et al.* (2002) presented evidence of a secondary circulation within the embayment gyre. Particles were observed to flow directly into the centre of the embayment along the bottom and get picked up by an upwelling motion within the gyre core.

The second factor mentioned as a possible reason for the disagreement in the calculations of the dimensionless exchange coefficient was the gravity waves. It was proposed that the exchange between an embayment and the channel does not depend on the free-stream velocity. However, gravity waves directly depend on it. Their amplitude grows discretely with the free-stream velocity in that, as one increases it, the different gravity-wave modes resonate with some flow structures and their amplitude increases. It was shown by Tuna *et al.* (2013) that the exchange coefficient is higher when gravity waves are strong in a shallow embayment. It is thus evident that a study of the gravity waves, their resonance mechanism and their effect on the flow structures and exchange, is needed. Also, a complete study of a fully three-dimensional flow field is necessary to recognize the three-dimensional flow structures, their origin, and the conditions for their appearance. If these goals can be achieved it may be possible to parametrize the feedback of these 3D structures and the gravity waves on the depth-averaged 2D fields and implement this into current river models.

We shall therefore start with an investigation of the kind of 3D structures that can be expected to appear in a shallow embayment. Every turbulent structure is a result of flow instability, and a few types of instabilities can occur in a shallow embayment: i) shear instability in the mixing-layer region, governed by the bed friction number (the ratio of bed friction force to the turbulent shear force, Chu *et al.* (1983)), ii) boundary-layer instability at the side walls of the embayment governed by the ratio between the centrifugal force and the viscous force, iii) the breakdown of cyclostrophic balance at the bottom boundary, also governed by the ratio of centrifugal and viscous forces, and lastly, iv) gravitational instability, governed by the Froude number, Fr, (the ratio of inertial to gravitational forces) (Ghidaoui & Kolyshkin, 1999). An overview of each of these types of instabilities will now be presented.

2.2 Instability of a shallow mixing layer

The mixing layer between the embayment and the main stream is dominated by coherent structures generated by the horizontal shear (Brown and Roshko 1974, Uijttewaal and Tukker 1998). They appear as a result of Kelvin-Helmholtz instability whose physical mechanism has been described by Batchelor (1967). The system of two flows of different velocities flowing parallel to each other is highly unstable. Batchelor describes how small sinusoidal displacements of a vortex sheet between the two flows leads to the generation of rotational motion in the shear layer. As a result, the sinusoidal displacement of a vortex sheet is amplified. This leads to exponential growth of the disturbance without any change in its form, as long as it is small enough not to affect the basic state (Drazin & Reid, 1981). In deep flows this process leads to relatively fast lateral mixing. However, in a shallow environment the growth of Kelvin-Helmholtz instability is suppressed. The initial growth rate of a shallow mixing layer is the same as that of a deep one. However, as the size of the Kelvin-Helmholtz structures becomes of the same scale as the water depth, bottom friction becomes important and the growth rate of the mixing layer is diminished. Thus, in shallow flows bottom friction exerts a stabilizing effect on Kelvin-Helmholtz instability which can be estimated by the stability parameter proposed by Chu & Babarutsi (1988*b*), $S = \frac{c_f \delta \bar{U}}{2 h_w \Delta U}$, where c_f is a friction coefficient, δ is the width of the mixing layer, $\bar{U}$ is the average velocity of the main flow, h_w is the flow depth, and ΔU is the velocity difference across the mixing layer.

Another instability that occurs in a shallow shear layer is the Tollmien-Schlichting instability. Klebanoff *et al.* (1962) described the evolution of Tollmien-Schlichting waves. Initially, they appear at the rigid boundary. They have a two-dimensional structure, and their axis of rotation is horizontal and normal to the flow. Tollmien-Schlichting waves progressively grow in amplitude downstream, and when they reach a critical value they become perturbed three-dimensionally, creating turbulent spots. Klebanoff and his colleagues interpreted the growth of three-dimensionality as a secondary instability of the Tollmien-Schlichting wave. This three-dimensional secondary instability has regions of swirling flow shaped like an eccentric ellipse.

It is hypothesized that the stabilizing effect of the shallowness on the growth of the mixing layer may be due to the non-linear interaction between the two flow instabilities. Van Prooijen & Uijttewaal (2002) argue that the different turbulent modes hardly influence each other in a shallow shear layer. However, it is well established that even in a deep shear layer (with no boundaries) the Kelvin-Helmholtz rolls experience secondary instability leading to the generation of streamwise vortices (Bernal & Roshko, 1986). It is argued that the three-dimensional effects in a shallow shear layer can only be amplified by the bottom boundary layer velocity profile and the Tollmien-Schlichting vortical structures. Thus, one could expect to see streamwise vorticity in the shear layer between the embayment and the main flow, and these streamwise vortices may be responsible for the variation of the exchange between the embayment and the main channel flow with depth.

2.3 Görtler instability

A boundary layer develops along the side walls of the embayment. It starts at the downstream wall of the cavity, grows along the far wall and ends at the tip of the upstream wall adjacent to the channel. This curving boundary layer, similar to a concave side of a river bend, is subject to three-dimensional flow instability governed by the ratio between centrifugal and viscous forces. A sufficient condition for centrifugal instability is an outward decrease in the magnitude of the angular velocity in some region of the flow with closed streamlines (Drazin & Reid, 1981). When centrifugal instability occurs in a boundary layer that develops along a concave wall, it is generally referred to as Görtler instability (Görtler, 1940) and it is known to generate streamwise spiral vortices in the boundary layer. This kind of vortex is one of the three-dimensional flow structures that may be expected along the walls of shallow-embayment flow.

Görtler vortices were already observed in a similar but not identical flow configuration generally referred to in the literature as an open cavity flow. It is usually modelled with a flow over a groove at the channel bed that spans over its whole width and has a square or a rectangular profile. It is made as wide as possible to render the wall effects negligible. To compare the open cavity flow with the current set-up, one needs to imagine the embayment being infinitely deep and the flow in it not being affected by either the free surface or the channel bed. Three-dimensional instability was found in open-cavity flows. Faure *et al.* (2007) experimentally showed the existence of pairs of streamwise vortices at the walls of the square cavity. They suggested that these structures are the consequence of a centrifugal instability related to the cavity core vortex. Brès & Colonius (2008) discuss the properties, structure and nature of such an instability using direct numerical simulations. They show that it is a centrifugal instability associated with the closed streamlines inside the cavity and that the growth rate of the dominant mode is directly driven by the Reynolds number. Viscosity damps the instability, and there is a critical Reynolds number above which the flow becomes three-dimensionally unstable. Moreover, Faure *et al.* (2007) suggest that these structures are Görtler-like vortices, governed by the Görtler number, G, defined from the curvature radius of the boundary layer, r_c, the kinematic viscosity of the fluid, ν, and the velocity inside the cavity, U_c, outside of the boundary layer of momentum thickness δ_2:

$$G = \frac{U_c \delta_2}{\nu} \left(\frac{\delta_2}{r_c} \right)^{1/2}. \tag{2.2}$$

The wavelength of the Görtler vortices (measured as a distance between two pairs of counter-rotating structures) was found to be 0.44L in the experiments of Faure *et al.* (2007), where L is the width of the embayment (0.24 m in the present study). Citro *et al.* (2015) performed a linear stability analysis on open-cavity flow and obtained a wavelength of the unstable mode around 0.47L. Direct numerical simulation of Brès & Colonius (2008) produced a wavelength of Görtler vortices of 0.4L. In the present study the depth of the flow is about 0.12L, thus, one cannot expect streamwise vorticies of the same wavelength as in the open cavity. However, an approximate calculation of the Görtler number for the current flow results in values well above the critical number of 0.3. Using the momentum boundary-layer thickness which grows along the embayment walls from about 0.001 to 0.003 m (obtained from the measurements presented in the Results chapter), the radius of curvature of 0.12 m (half-width of the embayment), and the main-gyre velocity of 0.02 and 0.06 m/s (for the lowest and highest free-stream velocity cases), we obtain G between 2 and 10 for the lowest free-stream velocity, and between 7 and 30 for the highest one. It is important to note that in the experiments of Faure *et al.* (2007) G was equal to 3.8-4.2. This indicates that in the current flow the centrifugal instability is strong, and even though the space is confined (small flow depth), one can expect streamwise Görtler vortices to appear.

2.4 The secondary circulation within the gyre

The recirculating flow in an embayment can be modelled as a vortex with a vertical axis above a solid horizontal boundary. This type of vortex has been studied thoroughly by meteorologists or, more broadly by geophysical fluid dynamicists, as it is also relevant to atmospheric flows, i.e. cyclones, storms, tornadoes (Doswell & Burgess, 1993). In a rotating flow, the radial position of every fluid particle is determined by cyclostrophic balance, a balance between centrifugal force and pressure gradient:

$$\frac{dp}{dr} = \frac{\rho u^2}{r}, \tag{2.3}$$

where r is the radial distance from the axis of rotation, u is the radial velocity, and p is the pressure. When this kind of vortex touches the ground, a boundary layer develops. Deceleration of the flow near the ground results in an imbalance; the pressure gradient becomes stronger than the centrifugal force. The flow near the surface gets curved towards the centre of rotation and results in a radial inflow within the boundary layer (Ekman, 1905). This process gives rise to a secondary circulation within the vortex. By continuity, the flow drawn in at the ground level gets lifted at the centre. In the case of an open channel flow, as it has a top boundary, one expects the cycle to close via radial outflow along the surface, and a subsequent descent, depicted in Figure 2.4. One of the models that could be used to estimate the intensity of the secondary circulation is the Bödewadt vortex

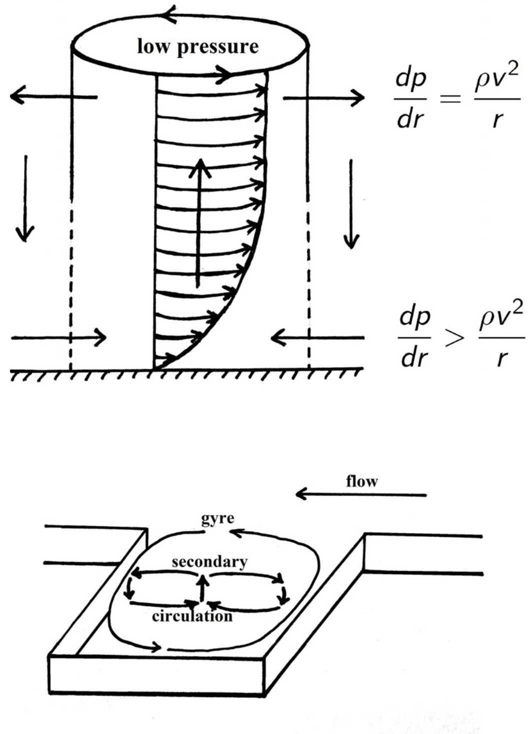

Figure 2.4: Secondary circulation within a rotating flow over a solid boundary. a) In a schematic vortex. b) In a shallow embayment.

(Bödewadt, 1940). This model assumes solid-body rotation above a horizontal boundary with the following boundary conditions: radial (u), tangential (v), and vertical (w) velocities are zero at the ground ($z = 0$), and $u = 0$, $v = 2\pi r\omega$ (where ω is the constant angular velocity of the solid-body rotation), as $z \rightarrow \infty$. With these boundary conditions an exact solution to the Navier-Stokes equations provides all three velocity components. It describes a spiral-like motion in terms of circulation and some dimensionless parameters (Figure 2.5). However, the Bödewadt model does not have a top boundary and therefore cannot predict the outward radial motion in the rotating flow, as this motion is solely a result of mass conservation in the presence of a "lid". Therefore, we cannot expect this model to predict accurate velocity profiles for the embayment flow, but it can nevertheless provide an approximation of the dependence of the secondary circulation, created by the embayment gyre, on the gyre rotation itself.

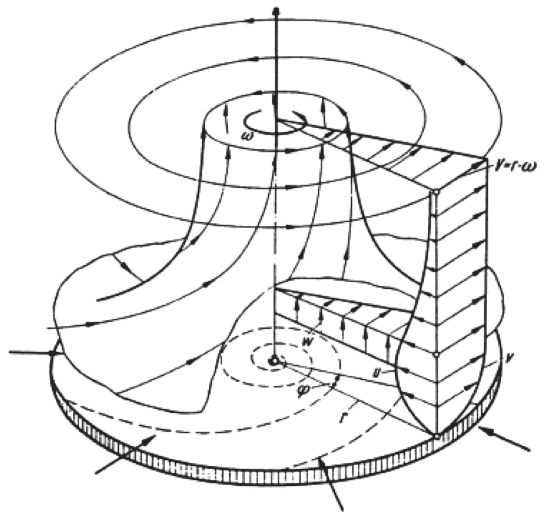

Figure 2.5: Rotation of flow near the ground. Velocity components: u radial; v tangential; w axial (Bödewadt, 1940). Picture taken from Schlichting (1968).

Indeed, the evidence of this circulation in a shallow embayment was provided by Jamieson & Gaskin (2007*b*). They referred to it as the "tea-cup" effect (when a cup of tea is stirred with a spoon, the tea leaves tend to accumulate in the centre of the cup's bottom due to the secondary circulation) and observed that near the bottom of the bay, instead of following the regular pattern of the main gyre, particles flow directly into the centre of the core region and settle. Tuna *et al.* (2013) also reported a deflection of streamlines towards the centre of the embayment near the bed. From the dye experiments of Jamieson & Gaskin (2007*a*) the general structure of the secondary flows was observed as a radially outward flow at the surface and a radially inward flow at the bed, with upwelling in the centre of the gyre and downwelling at the edges (shown in Figure 2). This average large-scale structure had contributions from intermittent events with their origins in the shear layer structures for example in which particles that had settled in the centre of the core were ejected upwards (Jamieson & Gaskin, 2007*b*). A two stage exchange process was suggested between the core and the gyre and between the gyre and the main flow (Jamieson & Gaskin, 2007*b*). However a detailed picture of this 3-D process and its quantitative effect on the main exchange is still not known.

2.5 Gravitational instability

Open-channel flows are subject to gravitational instability, governed by the Froude number (Fr); the ratio of inertial to gravitational forces. However, most studies pertaining to free-surface shallow mixing layers were performed assuming a rigid lid (flat water surface), implying Fr = 0 (Chu & Babarutsi, 1988*a*; Uijttewaal & Booij, 2000). Available experimental studies of shallow embayment flows (Booij, 1989; Altai & Chu, 1997; Uijttewaal *et al.*, 2001; Weitbrecht *et al.*, 2008) were also performed neglecting the effects of surface perturbations. Numerical studies of shallow embayment flows (Hinterberger *et al.*, 2007; McCoy *et al.*, 2008; Constantinescu *et al.*, 2009) have used the rigid-lid approximation as well. It is well justified. Ghidaoui & Kolyshkin (1999) performed a linear stability analysis in a shallow channel with a free surface and found that it worked well for low Fr. They proved that the critical bed-friction number calculated with and without the rigid-lid approximation changes no more than 10% for $Fr < 0.7$. This suggests that for $Fr < 0.7$ shear instability, which is generally thought of as the main mechanism of the exchange (Uijttewaal *et al.*, 2001), is barely dependent on Fr. However, Kimura & Hosoda (1997) and Tuna *et al.* (2013) showed that the effect of gravitational instability on the exchange process in a shallow embayment may be more significant than expected, and that the gravity waves cannot be ignored in certain limits. Kimura & Hosoda (1997) observed that in the street of shear-instability vortices there is a periodic amplification of a single vortex, and its frequency is in agreement with the gravity-wave dispersion relation. Tuna *et al.* (2013) showed that when surface gravity waves are strong, the position of the shear layer starts undulating horizontally with their frequency. In fact, Tuna *et al.* (2013) argue that it is the frequency of the "inherent" shear instability that causes gravity waves to amplify. They state that when the frequency of the shear instability matches the frequency of the surface gravity waves, they couple, causing a significant amplification of the gravity-wave amplitude. Tuna *et al.* (2013) also found that this coupling can lead to an increase in the Reynolds stresses, increased rms velocities, and time-averaged transverse velocities across the shear layer. All these lead to increased entrainment and consequently increased exchange coefficients between the embayment and the main channel. All this information appears controversial. On the one hand, gravitational instability was shown not to play a major role in shear flows for low Fr. On the other hand, it appears to have a significant effect on the exchange process. It is therefore evident that if in this work we are trying to investigate the effect of three-dimensional flow structures on the exchange process, gravitational instability cannot be left out of the picture. Also, an investigation is needed to establish whether there is a dependence of gravity-wave amplitudes on some parameter accessible to 2D models or not. That is, the exact mechanism of gravity-wave amplification is required as well as its effect on the exchange process.

All these 3D structures and the surface gravity waves will be examined in the experiments below to identify those that have the potential for affecting the exchange process, with the ultimate goal of parameterizing them and implementing in the 2D models.

2.6 3D particle tracking velocimetry

Particle tracking velocimetry (PTV) is a velocity measurement technique that is based on discrete visualization of a flow seeded with small, reflecting, neutrally-buoyant particles that play the role of flow tracers. The particles are recorded stereoscopically on image sequences from different viewing angles to determine 3D positions and hence trajectories. That is, 3D-PTV is a stereoscopic method based on the principle of triangulation. The location of a particle can be determined by measuring the angles to it from two known points. If one can assume that the object point, camera projective centre and image point lie on a straight line (collinearity condition), it is then possible to determine the 3D position of a particle by taking its pictures from two cameras, located at known positions. Taking successive images will provide particle displacements, and hence with interpolation, the velocity field.

This method has advantages compared to other widely-used measurement methods such as Laser Doppler Velocimetry (LDV), hot-wire anemometry and Particle Image Velocimetry (PIV) (Maas *et al.*, 1993). PTV is a non-intrusive method, i.e., the measurements do not affect the flow field, unlike hot-wire anemometry. It allows instantaneous velocities of the flow to be obtained in a relatively large volume with sufficient precision, whereas LDV gives only point measurements rather than field ones. Unlike PIV, PTV tracks individual particles over long times. Analysis of particle trajectories allows for a better quality of velocity measurements. PIV uses only 2 points to calculate the particle velocity, whereas having a particle trajectory allows one to perform a polynomial fit to the individual trajectory and to calculate the velocity by taking its derivative. It was also shown that PTV performs better than PIV in calculating all three components of velocity (Bown *et al.*, 2006), especially in near-wall regions (Kähler *et al.*, 2012). An even more obvious advantage of PTV over PIV measurements is that tracking particles in time, the Lagrangian approach, is more efficient than analysis of instantaneous velocity fields, the Eulerian approach, in the identification and analysis of vortical structures.

PTV is one of the oldest flow measurement techniques. It is merely intuitive to study fluid flow by observing trajectories of flow tracers. Nevertheless the collection of quantitative data at reasonable resolution became possible only in the last two to three decades. The first attempts to implement this technique date back to 1956 when Chiu & Rib (1956) used a stereoscopic arrangement using 2 cameras. To obtain 3D particle positions manual measurements of the images were required. Jacobi (1980) also tracked one particle at a time, but he reported a first application of photogrammetric modelling of the multimedia geometry (accounting for the refraction at the e.g. air/water interface). Chang *et al.* (1985) first digitized the film to derive particle image coordinates, and later Adamczyk & Rimai (1988) used a system based on electronic imaging, but it was limited to only 16 simultaneous trajectories. A considerable technical breakthrough was made by a group in Tokyo

(Nishino *et al.*, 1989) who developed a 3D-PTV system that could track up to 440 particles simultaneously. However, a complete mathematical model of photogrammetric 3D coordinate determination, taking into account the different refractive indices in the optical path was only developed in the early 90s by a research group in ETH Zurich (Papantoniou & Dracos, 1990; Maas *et al.*, 1993; Malik *et al.*, 1993). Maas *et al.* (1993) also proposed an epipolar line intersection technique in which the 3D particle positions are determined before construction of particle trajectories (another option is to track particles on each camera's 2D image space and then find the 3D spatial correspondance between these 2D trajectories). The epipolar line intersection technique is used in the current work and is described in more detail in Section 3.3.4. After this, in the history of 3D-PTV other adjustments to tracking algorithms were made to minimize errors and ambiguities. Willneff (2003) introduced a spatio-temporal matching algorithm in which characteristic velocity and Lagrangian acceleration of a particle from the previous frame are used to find the corresponding particle in the next frame. In this method the velocity of a particle is limited in all three components. This allows for the definition of a 3D search volume, whose size depends on the velocity at the previous time step and user-determined minimum and maximum velocity gradient in all three coordinate directions. Limiting the Lagrangian acceleration of a particle defines a conic search area. This method resulted in a considerable reduction of ambiguities and hence longer particle trajectories (Lüthi *et al.*, 2005). It is also taken advantage of below and is discussed further in Section 3.3.4.

CHAPTER 3
Experimental method

To investigate the flow structures of a shallow embayment the flow was physically modelled in a recirculating laboratory channel (flume). The experiments described in this work were conducted in the Environmental Hydraulics Laboratory in the department of Civil Engineering and Applied Mechanics at McGill University, Montréal. Fully three-dimensional measurements are desired to capture the full richness of all turbulent structures. This was achieved by the use of three-dimensional particle tracking velocimetry (3D-PTV). The details of the experimental apparatus, flow conditions, measurement method, and data processing are described in the following sections.

3.1 The channel flow facility

To recreate the patterns of recirculating flow, a laboratory channel (flume) with a square embayment on one side was used. The flume had a 2 m long and 0.4 m wide straight section with a 0.24 by 0.24 m^2 embayment at mid-channel and was run with the flow depth of 0.03 m (Figure 3.1). In order to provide a uniform inflow to the measurement section (the embayment), the flume has a transition curve at the inlet to the channel section and calming tanks at both ends to dissipate turbulence generated by the recirculation process. From the downstream reservoir the water is taken to the pump and returned back to the flume through the inlet at the bottom of the upstream tank. The inlet is made in the form of a “T” with holes distributed uniformly over the width of the reservoir to decelerate the flow and provide a uniform water supply over the width of the channel. Right after the diffuser the flow enters honeycomb forms to break up large flow structures as

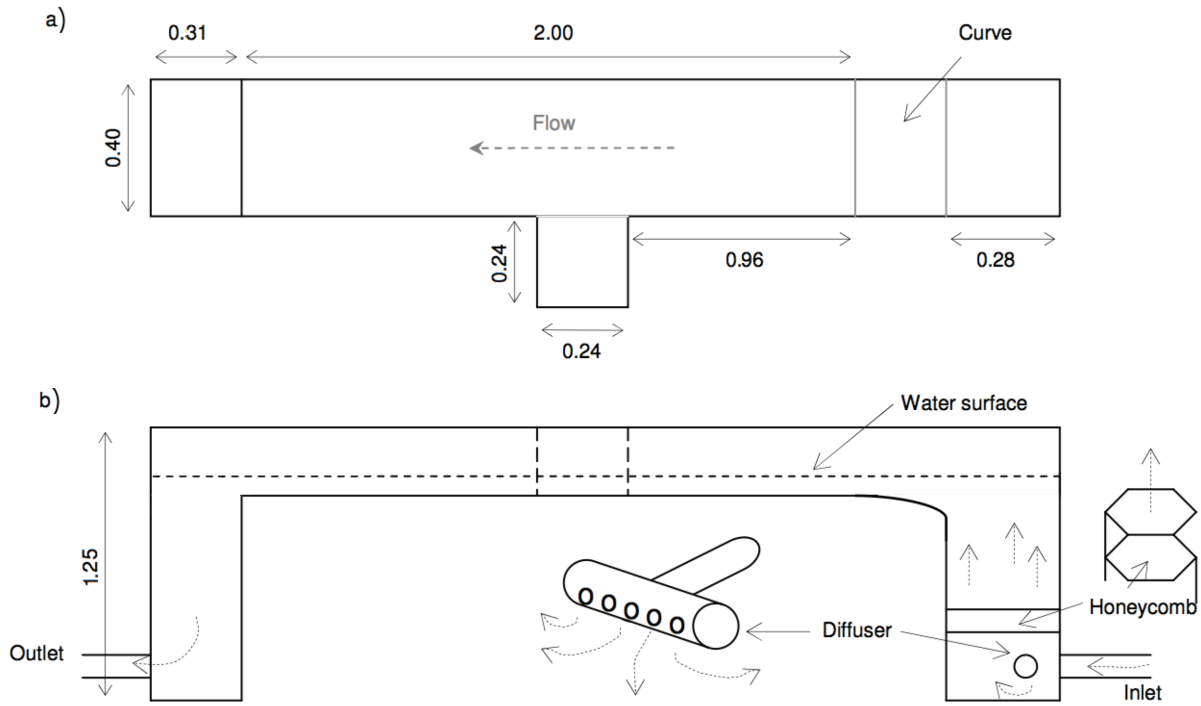

Figure 3.1: Schematic of the recirculating hydraulic channel (flume). a) Plan view. b) Side view. Dimensions are given in m. The schematic is adopted from Jamieson (2005).

it approaches the transition curve. A valve and flow meter located at the pump's outlet allow control of the discharge.

To reduce turbulent disturbances and ensure the smoothest flow, the flume was always run in a submerged state, i.e. the outlet tank had the same water level as the channel. This condition allows to avoid unnecessary air entrainment and turbulence generation that is common for flumes with an overflowing weir at the downstream end.

The hydraulic channel was made out of transparent plexiglas to provide visibility. However, plexiglas has a high thermal expansion coefficient. It was therefore necessary to control the temperature of the water to avoid leakage that occurred if cold water was put into the flume causing shrinkage. The flume was always filled with hot water and allowed to cool to room temperature. This also avoided the appearance of air bubbles in the flow since water has a lower solubility of gases at higher temperature, and when cooled down, gets further from saturation. In order to avoid the effect of water temperature on the geometry of the embayment flow, its walls were made out of glass.

3.2 Flow conditions

The flow conditions in the channel were chosen to match as closely as possible the dimensionless parameters, such as Reynolds number (Re), Froude number (Fr), and width-to-depth ratio of a small river. The Reynolds number is defined as the ratio between inertial and viscous forces:

$$Re = \frac{U_\infty H}{\nu}, \tag{3.1}$$

where U_∞ is the free-stream velocity, H is the water depth, and ν is the kinematic viscosity of water. The Froude number is the ratio of momentum forces to the gravitational force:

$$Fr = \frac{U_\infty}{\sqrt{gH}}, \tag{3.2}$$

where g is the acceleration of gravity. Re in a typical river is of the order of 10,000 to 1,000,000. The Fr in rivers (excluding mountainous creeks) is very small, of the order of 0.1-0.01. Both these dimensionless parameters are proportional to the characteristic velocity of the flow, so increasing the Re of the laboratory experiment inevitably leads to increasing Fr. Here, as in all experiments, we are facing the scaling problem, where it is not possible to match both these dimensionless parameters of the laboratory experiment to those of the prototype if the same fluid (water) is used. Usually, this issue is resolved by finding a range of conditions where, most importantly, the flow would be turbulent ($Re > 2,000$) and subcritical ($Fr < 1$). A third parameter that also has to be under consideration is the channel width-to-depth ratio. Rivers and channels are classified as shallow flows, as their depth is usually much smaller than their width. To replicate the shallow flow in the flume, the channel width-to-depth ratio had to be large. Its width is not variable, so only the depth could be adjusted. However, it could not be too small for the viscous effects not to become predominant (small Re).

In the current study it is intended not only to investigate the flow structures in an embayment flow but also to check for their qualitative dependence on surface gravity waves and different free-stream velocities. Thus, after considering all the limiting factors, three different flow conditions were chosen (Table 3.1). The flow depth was kept constant at 0.03 m, resulting in a width-to-depth ratio of 13 in the main channel and 8 in the embayment. The slope of the channel bed was zero, taking into account the very small slopes characteristic of rivers. Thus, the only parameter varied was the free-stream velocity. The smallest free-stream velocity case had a negligible gravity-wave amplitude. The highest one had a predominant gravity wave mode with the frequency of 0.36 Hz, and a peak amplitude of 0.9 mm (these data were obtained from the measurements described in the Results chapter, Section 5.3). The chosen flow conditions had Re and Fr numbers ranging between 3900 and 5400 and from 0.24 to 0.33, respectively. The corresponding slope of the water surface was about 0.18 to 0.38 ‰ (Table 3.1).

Table 3.1: Flow conditions

Discharge, m^3/s	Mean velocity in the channel, U_∞, m/s	Water depth, m	Re $U_\infty H/\nu$	Fr	Water surface slope, ‰
0.0016	0.13	0.03	3900	0.24	0.18
0.0019	0.17	0.03	4800	0.29	0.31
0.0021	0.19	0.03	5400	0.33	0.38

The Re number given in the Table 3.1 is a flow-depth Re calculated using the free-stream velocity (Equation 3.1). However, there are also other ways of assessing the Re that could be relevant. For the characteristic velocity scale one could use the rotation of the embayment gyre, let's call it Γ. For the characteristic length scale either the water depth, H, or the horizontal scale, the embayment width, L, could be chosen. Then $Re_{\Gamma,L} = 7,000 - 17,000$ for different free-stream velocities and $Re_{\Gamma,H} = 900 - 2,100$. This means that the horizontal scales are fully turbulent but in the vertical direction the viscous forces become relevant and there is a possibility of laminarisation inside the embayment gyre. Of course, the horizontal and vertical scales are coupled and it is not quite possible to be conclusive about where laminarisation will occur. It is obvious that in the centre of the embayment the velocities are extremely low resulting in a laminar flow; the Reynolds number ($Re_{U,H}$) goes down to about 50. However, even in a full-scale groyne field certain laminarisation can occur in the "dead zone" of the embayment centre. Evidently, in the scaled-down experimental setup the laminarisation will take place in a larger percentage of the space. This may result in the underestimation of the turbulent exchange, weaker small-scale structures and therefore more settling of particles in the gyre centre. However, the overall flow configuration and the general patterns are expected to be similar to those of a river embamyment.

Admittedly, the Re numbers of these experiments are very small compared to those of a river. However, even though the conditions in which these experiments were conducted were very limited, it is argued that the results of this work can still be of use in understanding the behaviour of a general problem of a shallow flow past an embayment, since the principal flow structures and their dependence or independence of surface gravity waves or on the dimensionless flow parameters will remain qualitatively similar. These experiments will not be able to provide a description of the flow in a real river. However, the advantage of having a laboratory setting is that one can measure the flow field with great resolution and precision, which is impossible in the field. Providing an insight into the flow structures that can be expected in a river embayment may also help field researchers narrow down the problem and focus their efforts, as they will have to check for only the dependences that were found in the laboratory.

3.3 3D particle tracking velocimetry (3D-PTV)

In the following sections the 3D-PTV experimental set-up, camera calibration, and data acquisition procedures will be described.

3.3.1 Experimental set-up

PTV is based on the measurement of the coordinates and tracking of individual particles seeded into the flow. This requires reliable identification, multi-image matching, coordinate determination, and matching in time of each individual particle (see Section 3.3 for details). With a large number of particles this process leads to ambiguities which cannot always be resolved. Therefore, a significant effort in performing 3D-PTV must be devoted to handling them by precise modelling of the air/water interface, the use of at least three synchronized cameras imaging the flow, and a careful calibration of the system (Maas *et al.*, 1993).

Three cameras were mounted above the hydraulic channel. Each captured the embayment in its field of view from a slightly different angle (see Figure 3.2). In this work, due to limited space below the channel, optical measurements were taken through the free surface of the flow. The optical error due to the unsteady interface is a minimum when the camera is pointed straight down and the light rays are nearly perpendicular to the interface (Snell's law). At the same time, if all the cameras are nearly parallel to each other, the error in the third (in this case vertical) coordinate becomes large. In order to find the optimum angle of the cameras a rough estimation of the errors due to the interface oscillation angle and amplitude was made (See Appendix A). Based on this analysis angles of approximately 6-8 degrees were chosen (Figure 3.2). A thorough assessment of the errors introduced by the surface oscillations is presented in Section 4.3.

Another important point is the size of the particles; particles which are too small cannot be seen by the camera or can also evoke a so-called "peak-locking"

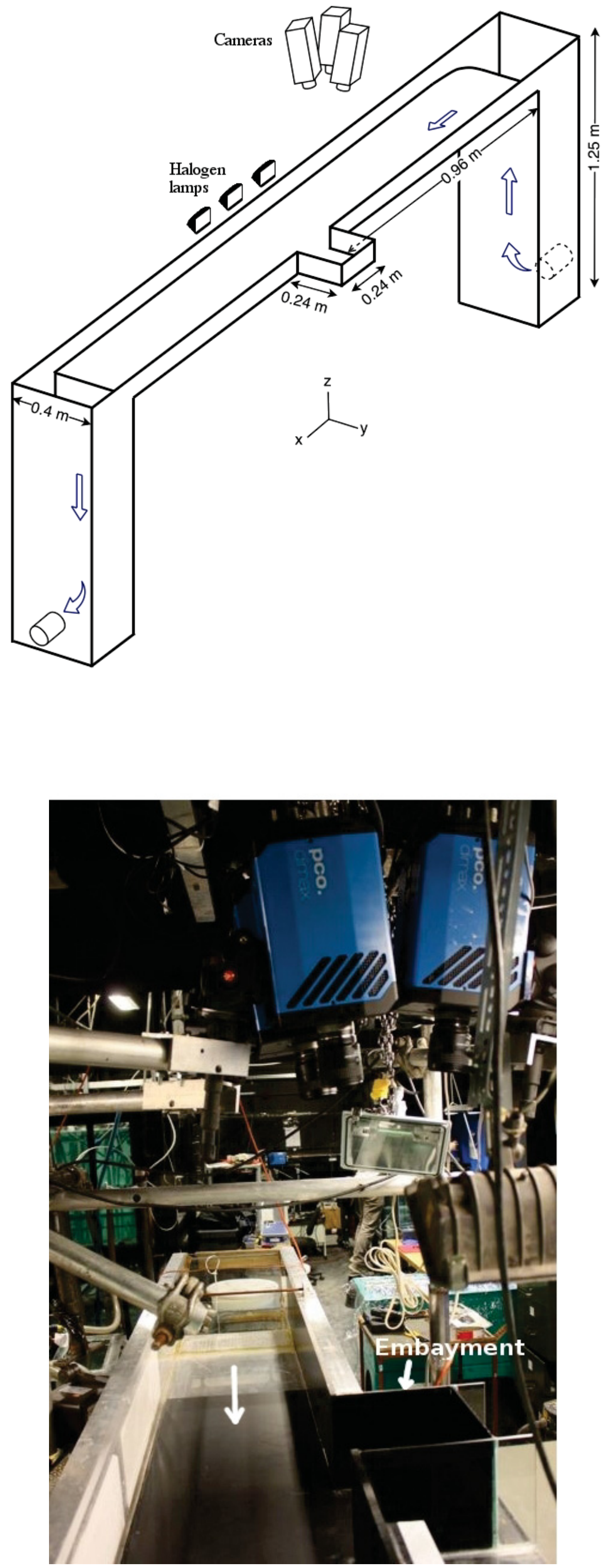

Figure 3.2: Three CCD cameras mounted above the flume to capture the flow field in the embayment. A schematic is shown above and a photograph from the downstream end of the flume is below.

effect, when the position of a particle “locks” onto a pixel and its displacement becomes proportional to the integer count of pixels (Weitbrecht *et al.*, 2002). To avoid this Raffel *et al.* (2013) suggest using particles with a diameter larger than 1.5 pixels. Particles which are too big can have the problem of not following the flow structures because of inertial forces. A compromise is given by particle dimensions between 2 to 5 pixels. In the present application high-resolution (2016x2016 pixels) CCD cameras were used to image a field of view of about 0.29x0.29 m^2 (Figure 3.3) which allowed to resolve particles of a relatively small diameter, about 0.23 mm. The particles were neutrally buoyant white polyethylene microspheres 212-250 μm in diameter (from Cospheric LLC). Every particle therefore occupied about 1.5-1.7 pixels in the image space.

In order to verify that the particles are indeed following the flow and they are not too large for the inertial effects to become predominant, we calculate the Stokes number, which is defined as a ratio between particles and fluid characteristic time scales:

$$St = \frac{\tau_p}{\tau_\eta}, \tag{3.3}$$

where τ_p is the particle's time scale that can be calculated as $\tau_p = \frac{\rho_p d^2}{18 \rho_f \nu}$ (ρ_p is particle density, d is particle diameter, ρ_f is fluid density, ν is kinematic viscosity) and τ_η is the fluid time scale or Kolmogorov time scale (see Section 3.4). For the lower and higher free-stream velocities the Stokes number is 0.03 and 0.07, respectively. Both values are well below 0.1, which indicates that the tracing accuracy errors are below 1% (Tropea *et al.*, 2007).

The seeding density of the particles must be chosen such that their average displacement in one frame interval is an order of magnitude less than the average particle spacing (Malik *et al.*, 1993). Thus the seeding density depends on the frame rate of the cameras. Using high-speed cameras allowed to record the flow at 600 Hz, resulting in an average particle displacement in one frame interval in the channel

Figure 3.3: High-speed camera PCO-DIMAX. The recordings were made at the frame rate of 600 Hz with image resolution of 2016x2016 pixels.

(the fastest part of the flow) of about 0.3 mm. Thus, the average distance between particles, r, had to be about 3 mm. The corresponding seeding density, n, can be found as:

$$n = \frac{1}{r^3}, \tag{3.4}$$

resulting in $n = 37$ particles/cm^3. In the current experiments particles tended to accumulate in the slow-moving gyre core in the centre of the embayment. Density of the particles was on average that of water and ideally, they would follow the fluid paths even in the region of weak flow. However, some particles were slightly denser than water and settled in the slow-moving gyre centre. In order to be able to resolve this region, the overall seeding density had to be considerably smaller. Approximately 15 g of particles were used in one experiment, resulting in an average particle density of about 6 particles/cm^3. In the rest of the domain the particle seeding density was quite uniform without additional efforts. It was provided naturally by turbulent mixing.

To view the white particles, black matt vinyl was glued onto the bottom of the channel and its walls. The studied area was illuminated by three halogen lamps. In order to avoid reflections off the water surface, illumination was performed through the plexiglas side of the channel instead of through the surface of the flow. The plexiglas wall above the water level was covered, so that light could only come through the plexiglas/water interface and that no light rays would be reflected off

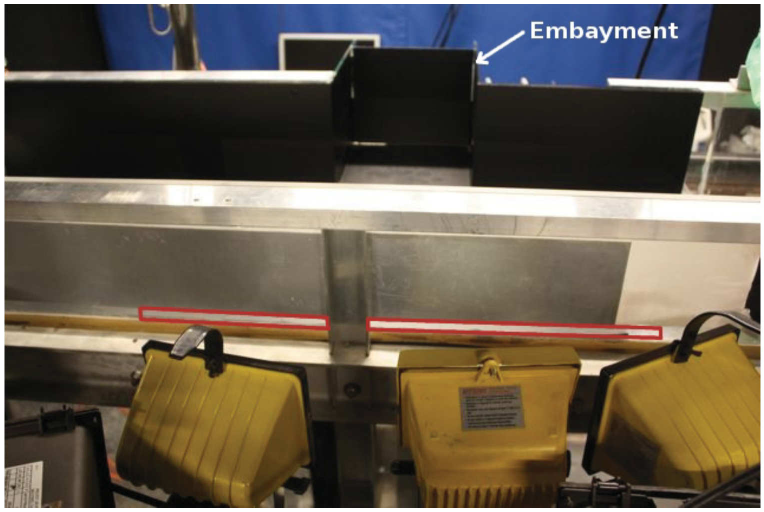

Figure 3.4: Three Halogen lamps illuminating the embayment. In order to avoid reflections off the water surface the light rays were only allowed to come through the thin regions below the water level indicated by the red rectangles.

the surface (Figure 3.4). Figure 3.5 shows a view of the bay from one of the cameras during an experiment. About 9,000 particles were identified on every frame.

3.3.2 Calibration of the cameras

As was mentioned before, the optical stereo-matching technique is based on the triangulation principle. A position of a particle in space can be determined by measuring the angles to it from two or more known points. Thus, the exact locations of the cameras' optical centres (pin-holes), their viewing angles with respect to the studied area along with refraction angles, lens distortion and some other parameters that are described below, have to be determined. To this end, the calibration of the cameras is performed. The calibration procedure consists of finding variable parameters in the algebraic relation between positions in the image space of the cameras and positions in real space. This relationship, proposed by Maas *et al.* (1993), is described with a mathematical model based on the collinearity condition, which states that the object point, camera projective centre and image point lie on a straight line. However, this mathematical relation has to be extended to describe the physical reality. It has to account for the light rays passing through two optical media; water and air, with different refractive indices, causing the light

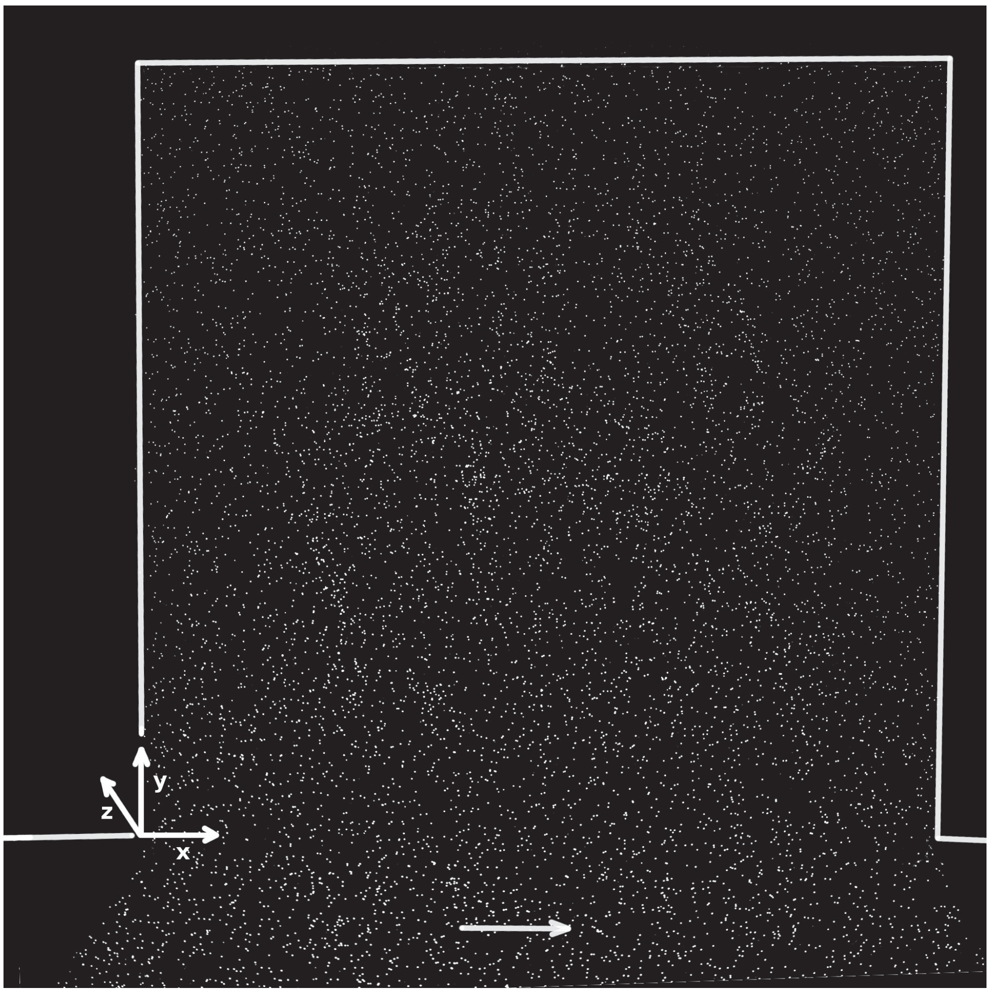

Figure 3.5: View of the embayment from one of the cameras; white dots are the polyethylene microshperes 212-250 μm in diameter.

rays to break. Lens distortion also has to be taken into account. Altogether, the model has 16 parameters describing the geometry of one camera:

- 6 parameters determine the camera's position and orientation (3 coordinates and 3 angles);
- 3 model the camera's interior orientation (the offset of the image principle point with respect to the projective centre);
- 5 describe the radial and tangential lens distortion (Brown, 1971);
- 2 parameters are introduced to compensate for electronic influences such as image digitization, storage, line jitter etc. (El-Hakim, 1986).

In the calibration procedure images of points with known positions are taken. Comparing their known coordinates with the measured ones, the 16 parameters are optimized using a least-squares method. One of the most common calibration techniques is to take a photo from each camera of a so-called calibration object placed in the area of interest. For accurate calibration this object has to span over the whole observation volume and contain many well-contrasted points with their positions known with high precision that will later be used to determine the measurement precision.

In this work, the calibration object was machined from black plastic, "Delrin" (machine drawings of the calibration object are provided in Appendix B). In order to cover the whole observation volume it was designed with many steps that would provide data at every depth (Figure 3.6). A pattern of 0.3 mm diameter holes was drilled with ± 0.05 mm tolerance. The holes were then filled with white silicone. To ensure that the surface of the silicone is flat (a concave shape results in uneven lighting and hence, identification errors), a razor blade was used to take off excess material. The calibration object was placed inside the embayment and photographed from three cameras through the still water surface that had the same depth as the experiments (0.03 m). An example of such a photograph from one of the cameras is given in Figure 3.6.

Placing the object in a known position, and given an initial guess of the camera positions, one can predict the expected positions of the white dots of the calibration object in each camera's image space. Comparing the guess with the real positions of the dots, the initial guess and all other parameters can be iteratively corrected until they converge. Once the calibration is complete, the parameters of the relation between the image space of the cameras and real space is determined. Thus, the correspondence between the particles viewed from the three cameras can be established using the epipolar-line intersection technique (see Section 3.3.4), resulting in their 3D coordinates.

3.3.3 Data acquisition

3D-PTV measurements require simultaneous imaging from all the cameras. To achieve synchronization between them a master-slave relationship was employed. One camera was chosen to trigger the other two through a consequent BNC (Bayonet NeillConcelman) connection. As was mentioned previously, the recordings were made at the frame rate of 600 per second. At this relatively high frame rate it is not possible to download the pictures from the cameras at the same rate as the recordings are made. Thus, the pictures were first saved in the cameras' RAM and then downloaded to the computers after the recording was finished. Because of the limited size RAM, it was possible to run one experiment for approximately 10 seconds at 600 fps before it was full. Hence, it was necessary to run several experiments to achieve data convergence. It took about 60 to 100 seconds of recordings to obtain converged statistics (see Section 4.2).

3.3.4 Post-processing of the data

High-resolution images from the cameras each took about 4 MB of memory. One hundred seconds of data for each of the 3 flow cases with 600 frames per second for three cameras resulted in 540,000 images and about 2 TB of memory. In order to process this data the images had to be transferred to a powerful computer with 24 GB RAM. The purpose of the post-processing is first, to extract the coordinates

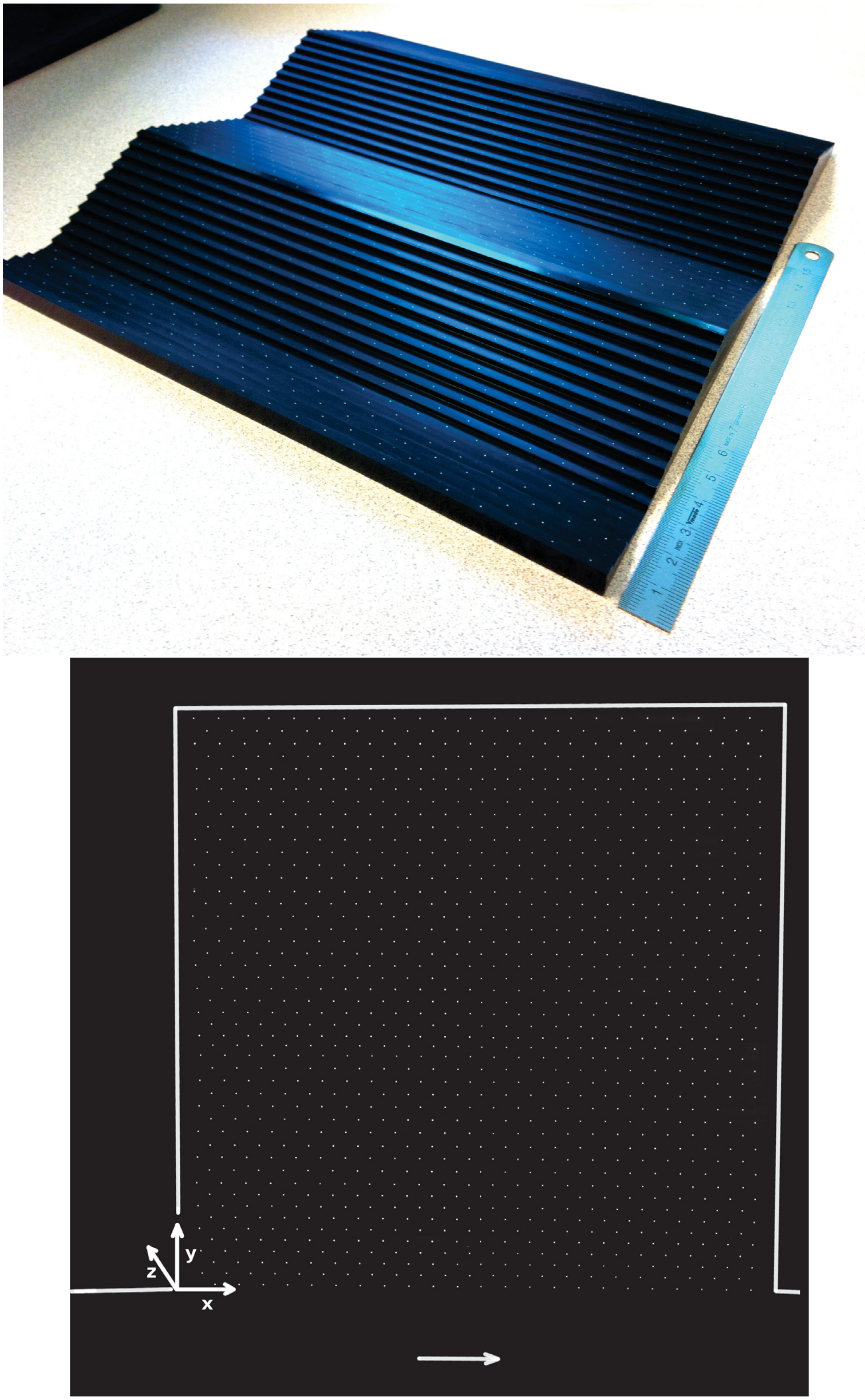

Figure 3.6: Calibration object: object of known geometry used to determine the position of the cameras relative to the region-of-interest

of the centres of the particles in the image space from every frame (particles recognition); second, establish the correspondences between particles viewed from different cameras and thus, obtain their 3D coordinates in real space; and lastly, track the particles in time. All these steps including the calibration of the cameras were performed using an open-source 3D-PTV software, that was initially developed at ETH Zurich (Willneff, 2003), and is supported today by many people around the world (OpenPTV, 2012). The parameters that were used in all the post-processing steps are given in the Appendix C.

Particle recognition is performed based on a grey value threshold and minimum particle size "recognized" by the code. Every recognized particle is attributed an ID number and the next step is to find the corresponding particles in each different camera view. Knowing the exact position of the cameras from the calibration procedure, we can use a so-called epipolar line intersection technique developed by Maas *et al.* (1993).

A particle on one camera has two coordinates in the image space (let's say, x and y). As we do not know the third coordinate (z), we can say that this particle is situated on a line of constant x and y. This line is perpendicular to the image plane of one camera, but it appears as an "epipolar" line on the image of another camera, that has a slightly different angle of view. By constructing this line on the second camera image, we can narrow down the search region of the corresponding particle to the area around this line. On the image from the third camera two epipolar lines can be drawn, and the particle that we are looking for has to be around the intersection of these lines. To improve the method, additional parameters are used. Particle size, brightness, characteristic velocity, acceleration, and their directions are employed in order to resolve the ambiguities in cases when there are several particles that happen to be on the same epipolar line.

Once the 3D-coordinates are obtained, a tracking procedure can be performed, where a particle is identified throughout subsequent images in time. This procedure is mainly based on the nearest neighbour principle. However, when there is an ambiguous situation (i.e. crossing trajectories), additional parameters are used. The method for solving ambiguities is based on prediction of the particle's position. The area in which the particle is expected to appear at the next frame is determined based on its past movement. Both the particle's coordinates and the predicted area are transferred to the image from another camera. The ambiguity is then eliminated by matching the "transferred" prediction and the one made on that particular image. This spatio-temporal matching technique was developed by J. Wilneff at the Swiss Federal Institute of Technology (ETH) (Willneff, 2003).

To obtain the 3D velocity and vorticity fields from the Lagrangian trajectories, the polynomial fit method of Lüthi *et al.* (2005) was employed. Determining velocities and accelerations through central differences has finite accuracy and therefore, sensitive to position errors. Thus, filtering is required. The method of Lüthi *et al.* (2005) consists of fitting a polynomial to a particle trajectory, $x_i(t)$, and calculating its velocity, $v_i(t)$, as the first derivative. The filtering is implemented as a moving cubic spline:

$$\hat{x}(i) = c_{i,0} + c_{i,1}t + c_{i,2}t^2 + c_{i,3}t^3, \tag{3.5}$$

where $i = 1, 2, 3$ for the three coordinate components. The coefficients $c_{i,j}$ are found by fitting the spline to 21 points of a trajectory. The filtered velocities are then defined as

$$\hat{u}(i) = c_{i,1} + 2c_{i,2}t + 3c_{i,3}t^2. \tag{3.6}$$

From the filtered velocities, spatial derivatives are interpolated for every particle trajectory point. Assuming that to a good approximation the velocity field in the proximity of x_0 is linear yields

$$\hat{u_i}(x_0) = c_{i,0} + c_{i,1}x_1 + c_{i,2}x_2 + c_{i,3}x_3, \tag{3.7}$$

where

$$c_{i,1} = \frac{\partial u_i}{\partial x_1}, \qquad c_{i,2} = \frac{\partial u_i}{\partial x_2}, \qquad c_{i,3} = \frac{\partial u_i}{\partial x_3}. \tag{3.8}$$

In principal four points are sufficient to solve (3.7) and (3.8) for c_i. However, more points are desirable to increase accuracy. The linear approximation is valid only over the length scale for which viscous effects are dominant. This separation value was determined empirically through the quality control built in the code of Lüthi *et al.* (2005). The interpolation sphere had a radius of about 7 mm. Solving Equation 3.7 for all the particles within this sphere allows the values of spatial derivatives for every trajectory point to be obtained. Hence, three vorticity components were then calculated.

The resulting velocity and vorticity components determined for the Lagrangian trajectories were interpolated onto a regular grid of 59x49x16 points with spatial increments of 5 mm in the horizontal and 2 mm in the vertical direction. Natural neighbour interpolation scheme was chosen for this calculation. However, it is important to note that the linear interpolation and the nearest neighbour schemes did not produce significantly different results. The velocity field was then averaged over time for the period of approximately 92 seconds, that is, 55,000 time steps.

3.4 Resolution and characteristic turbulent scales

In order to obtain accurate measurements of a turbulent flow it is necessary to assure the space and time resolutions are below the smallest turbulent length and time scales. It is thus important to verify that the current experimental procedure satisfies these criteria. The smallest scales in a turbulent flow are called Kolmogorov scales and are defined as functions of kinematic viscosity of the fluid (water), ν, and the turbulent kinetic energy dissipation rate, ϵ. The Kolmogorov length scale, η, is defined as follows:

$$\eta = \left(\frac{\nu^3}{\epsilon}\right)^{1/4}, \tag{3.9}$$

According to Taylor (1935), the energy dissipation can be approximated as:

$$\epsilon \approx \frac{u_{rms}^3}{L}, \tag{3.10}$$

where u_rms is the root mean square velocity of the flow fluctuations and L is the integral length scale of the flow. The average rms velocity of the flow varies between 0.015 to 0.028 m/s, being higher for the higher free-stream velocity (the values of the rms velocities used are calculated from the experimental results described in Chapter 5). The integral length scale can be estimated by the depth of the flow, 0.03 m. Substituting those values we obtain $\eta = 0.2 - 0.3$ mm, depending on the free-stream velocity (the lower Kolmogorov length scale corresponds to the higher free-stream velocity with a higher Re). The average particle displacement varies from about 0.06 mm inside the embayment to 0.3 mm in the channel flow. Thus, velocity values, calculated from particle positions are equal to, or even below, the Kolmogorov length scale. The corresponding time scale of the smallest structures in the flow (Kolmogorov time scale) is found as:

$$\tau_\eta = \left(\frac{\nu}{\epsilon}\right)^{1/2}, \tag{3.11}$$

resulting in the values of 0.04 to 0.09 s for the different free-stream velocities. The time resolution of the cameras with 600 Hz frame rate is 0.002 s, which is more than an order of magnitude smaller than the Kolmogorov time scales. (This may seem excessive, but as was mentioned in Section 3.3.1, it is related to the spatial resolution.) Therefore, both time and space resolutions are high enough to perform satisfactory measurements.

Since the seeding density of the particles in the flow is quite small, the average particle separation is about 6 mm, the quality of the calculation of the spatial derivative may be questioned. Indeed, a much larger spatial resolution is desired to resolve all the turbulence scales. To this end, an error estimation based on the calculation of the divergence (zero for incompressible flow) was performed. The results of this error analysis showed that, even though the spatial resolution is low, it is still possible to obtain accurate characteristics of the large-scale structures. The divergence calculation produced surprisingly good results which are presented at the end of the next chapter, Section 4.3.3.

CHAPTER 4
Flow validation and error analysis

This chapter presents the quality assessment of the experimental data obtained in this research. The first section discusses the free-stream conditions of the flow in the flume. The second section is a verification of the convergence of the time-averaged statistics. The last one presents the error analysis of velocity and the calculations of spatial velocity derivatives.

4.1 Free-stream flow conditions

Natural streams and channels are characterized by a fully-developed turbulent boundary layer that extends all the way to the surface. It is thus required that this condition be replicated in a laboratory flow. As the flow enters the flume, a boundary layer starts to develop along the channel bed. It grows until it reaches a steady state and its form stops changing with the downstream distance. Uijttewaal *et al.* (2001) state that $x/H = 50$ (H is the depth) is a sufficient downstream distance to reach a fully-developed turbulent flow in the main channel. In the current set-up the embayment extends from x/H=32 to 40, which is smaller than the required distance. It is thus necessary to verify that the boundary layer in the current experimental facility is fully developed. Time-averaged streamwise velocity profiles, $\overline{u}(z/H)$, are considered at 4 points at different downstream distances, x/H=33, 35, 37, and 39; their locations relative to the embayment are indicated in Figure 4.1. Figure 4.2 shows that the 4 profiles collapse to the same curve except for the point near the bed. The 4 points considered here were taken from the main experimental data. They were chosen to be as far from the embayment as possible, but some effects from the flow around it may still be present. Acceleration of the flow along the bed may either indicate that the boundary layer is still developing somewhat or it could be related to the presence of the embayment and its secondary currents. However, considering the fact that no clear trend with the downstream distance can be observed at all elevations $z/H > 0.1$, it is fair to conclude that the boundary layer is well developed.

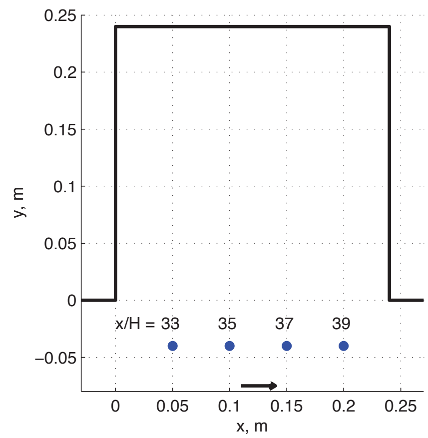

Figure 4.1: Position of the velocity profiles relative to the embayment.

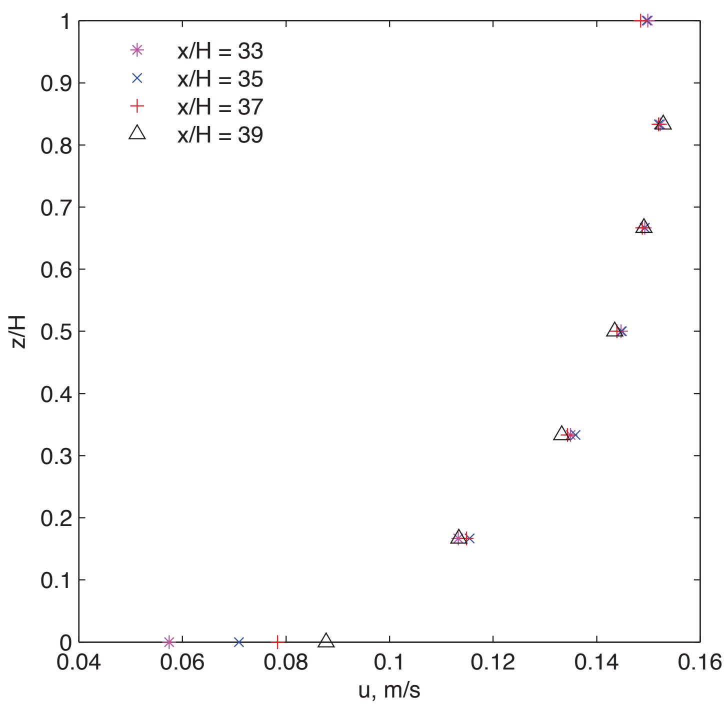

Figure 4.2: Free-stream velocity profiles as a function of elevation above the bed.

The general shape of the profile corresponds well with previous experimental and field studies. In quasi-uniform open-channel flow the mean streamwise velocity obeys the logarithmic law (Nezu & Onitsuka, 2002; Sukhodolov & Uijttewaal, 2010):

$$\frac{u}{u*} = \frac{1}{k} ln \frac{z}{z_0}, \tag{4.1}$$

where k is the von Kármán constant and z_0 is the hydrodynamic roughness parameter. It was also shown that closer to the surface, $z/H > 0.8$, the profile systematically deviates from the logarithmic law (Sukhodolov, 2014). This deviation of velocity is called the "velocity-dip" phenomenon, characterized by a deceleration of the streamwise velocity near the surface. This phenomenon is usually attributed to effects caused by the secondary circulation in an open channel flow (Nezu & Onitsuka, 2002). The deceleration can be clearly observed near the surface in Figure 4.2 for $z/H > 0.9$, whereas for $z/H < 0.9$ the profiles show the usual logarithmic shape (Figure 4.3).

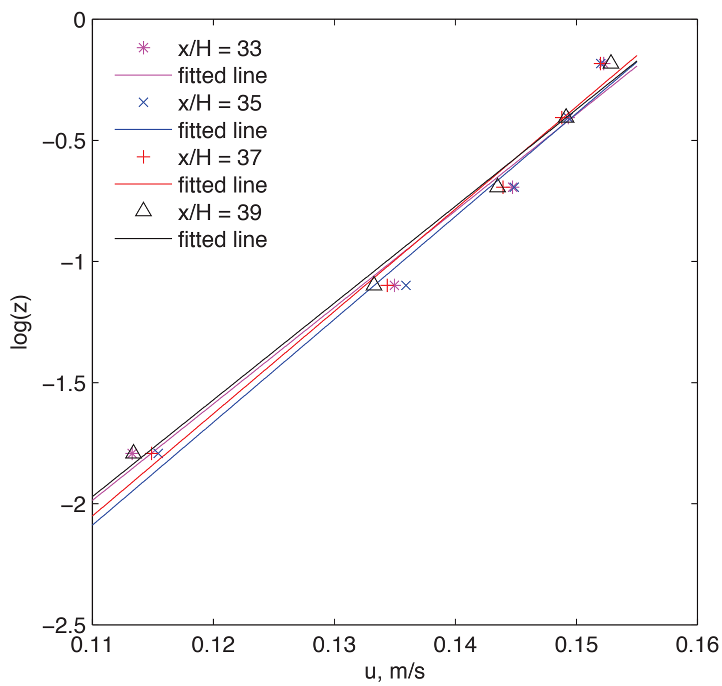

Figure 4.3: Free-stream velocity as a function of $\log z$.

4.2 Convergence of the data

In this work we are primarily focused on the time-averaged statistics of the flow. To check their convergence, cumulative averages of the 3 components of velocity, and the 3 components of vorticity were calculated for 36 positions in the embayment. Out of 216 plots about 80-90% show very quick convergence. For the lower free-stream velocity case (0.13 m/s), the velocity converges in 10 seconds and the vorticity in 20 seconds (images sampled at 600 Hz), see for example Figure 4.4. However, some points take longer to converge. At these points the cumulative average appears to have a slight periodic undulation which may be related to low-frequency flow structures or gravity waves, see for example the v velocity component in Figure 4.5. Also, when the magnitude of the mean velocity is close to zero the cumulative average is susceptible to slight drifts (e.g. u component in Figure 4.5). However, both the drift and the undulation only happen at about 10% of the locations and they appear to be small, less than 10% of the total variability. This will be further confirmed below by considering total velocity and vorticity fields averaged over different periods of time.

For the higher free-stream velocity (0.19 m/s) one could expect longer convergence times, as both turbulence and gravity waves are stronger. Indeed, the points that converged slowly in the slow flow take longer as the free-stream velocity is increased. For example, in Figure 4.6, the u-velocity requires about 90 s to approach its final value of about -2 mm/s and the vertical component (ω_z) continually exhibits small fluctuations until its mean value is achieved after about 80 s. More surprising is the fact that points which converged quickly for the slow flow converge even more quickly as the free-stream velocity is increased. See, for example, Figure 4.7, where all three vorticity components are fully converged within 10 seconds (instead of 20 s).

As already mentioned, 80-90% of the points converge very quickly. However, just to confirm that the other 10-20% that converged more slowly are indeed converged, we will consider two examples that represent the slowest convergence that could be found in the data: u and ω_z for the higher free-stream velocity in Figure 4.6.

Figure 4.8 shows the average horizontal speed at a depth of 0.026 m (corresponding to the location considered in Figure 4.6) for five averaging periods: 10.5, 31.5, 52.5, 73.5, and 94.5 seconds. The plots indicate approximate convergence of the horizontal speed by around 70 seconds. Even though the cumulative average of u showed a slight drift in Figure 4.6, it appears to be negligible compared to the variability this averaged field displays in space (Figure 4.8).

Figure 4.9 shows the contour plots of vertical vorticity, ω_z, in the bay at the same depth of $z = 0.026$ m. Although the cumulative point-wise averages exhibited some drift in time, all the major features of the spatial variation remain independent of averaging period at $t > 70$s, and it is clear that in this sense convergence was achieved. Lastly, we emphasize that these two examples were deliberately chosen to represent the slowest cases of data convergence for all positions, fields and free-stream velocities.

To conclude the discussion on the issue of convergence we plot the cumulative average of one of the key quantities that will be presented in the Results chapter. Figure 4.10 shows the contour plot of the horizontal vorticity, ω_y, for a vertical slice through the bay at $y = 0.11$ m. The graphs show the cumulative average of ω_y at the same five periods, 10.5, 31.5, 52.5, 73.5, and 94 seconds of data. As will be discussed in more detail, the flow herein is characterized by pairs of counter-rotating vortices situated on top of each other near the walls of the bay. The last two plots show that these flow features are converged, i.e. they do not change with the addition of new data, confirming the reliability of the results of this work.

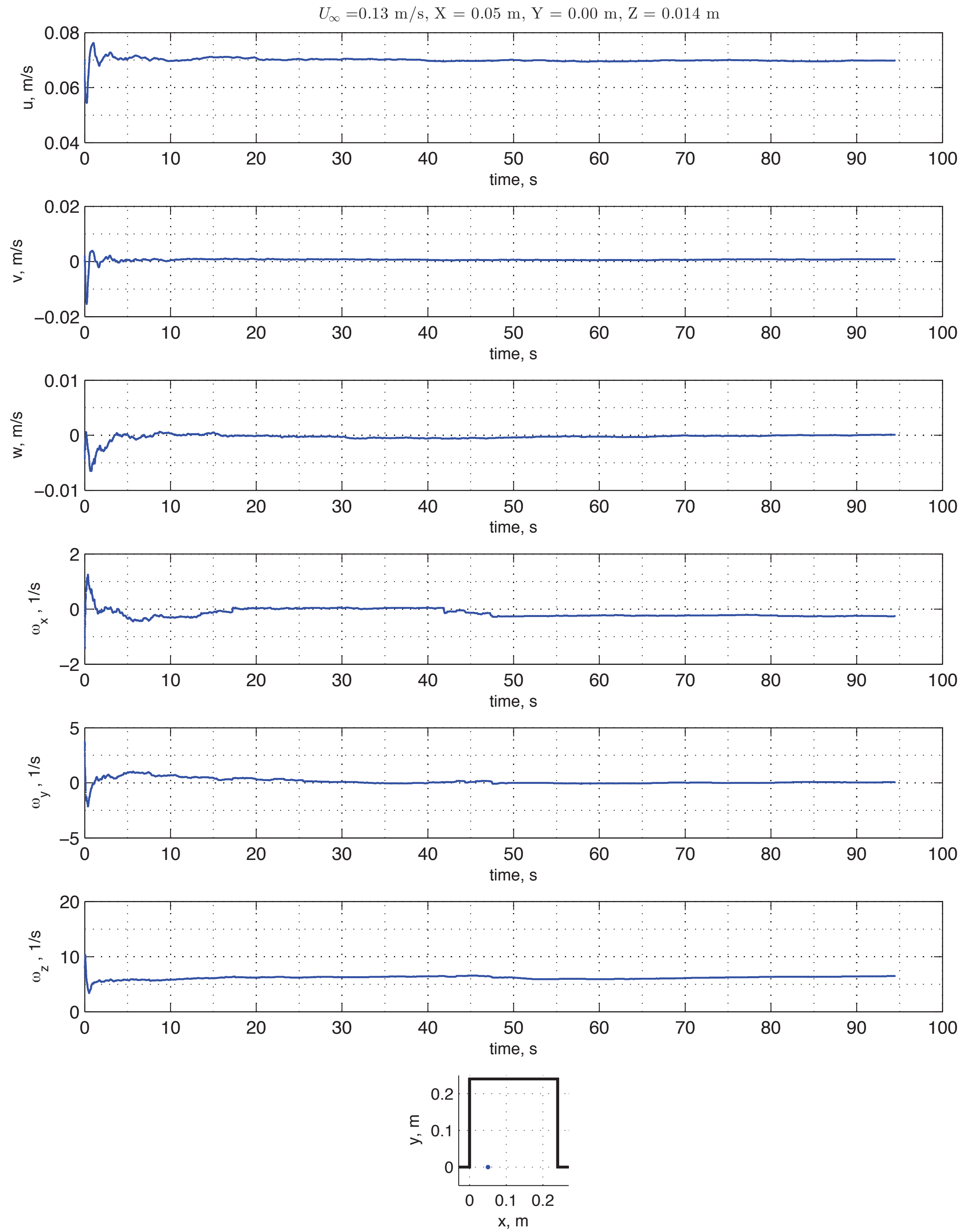

Figure 4.4: Data convergence: cumulative averages of three components of velocity (u, v, w), and three components of vorticity (ω_x, ω_y, ω_z) at one point in the embayment situated in the region of the mixing layer ($x = 0.05$ m, $y = 0$ m, and $z = 0.014$ m), for the lower free-stream velocity of 0.13 m/s.

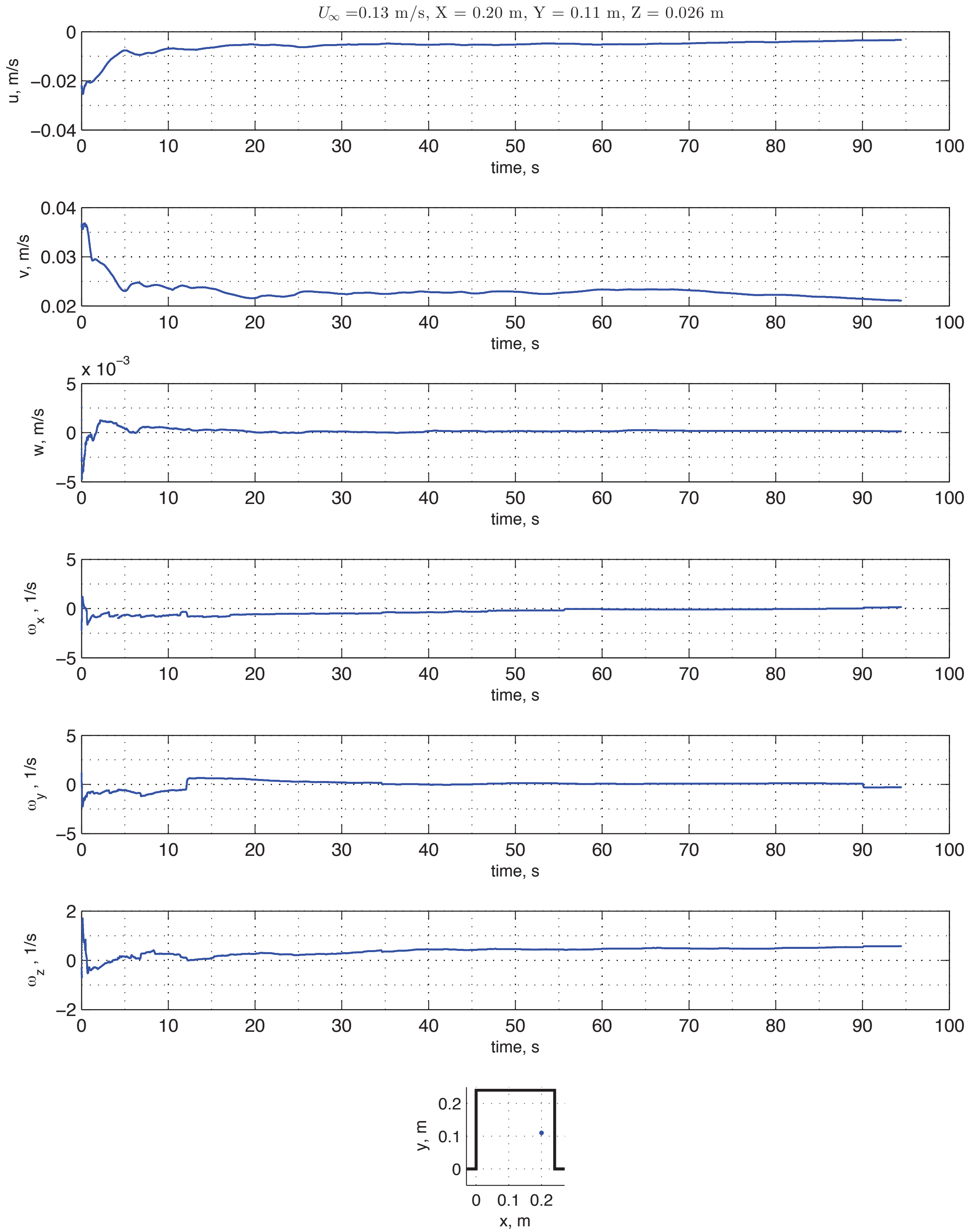

Figure 4.5: Data convergence: cumulative averages of three components of velocity (u, v, w), and three components of vorticity (ω_x, ω_y, ω_z) at one point in the embayment situated near the downstream wall of the embayment ($x = 0.2$ m, $y = 0.11$m, and $z = 0.026$ m), for the lower free-stream velocity of 0.13 m/s.

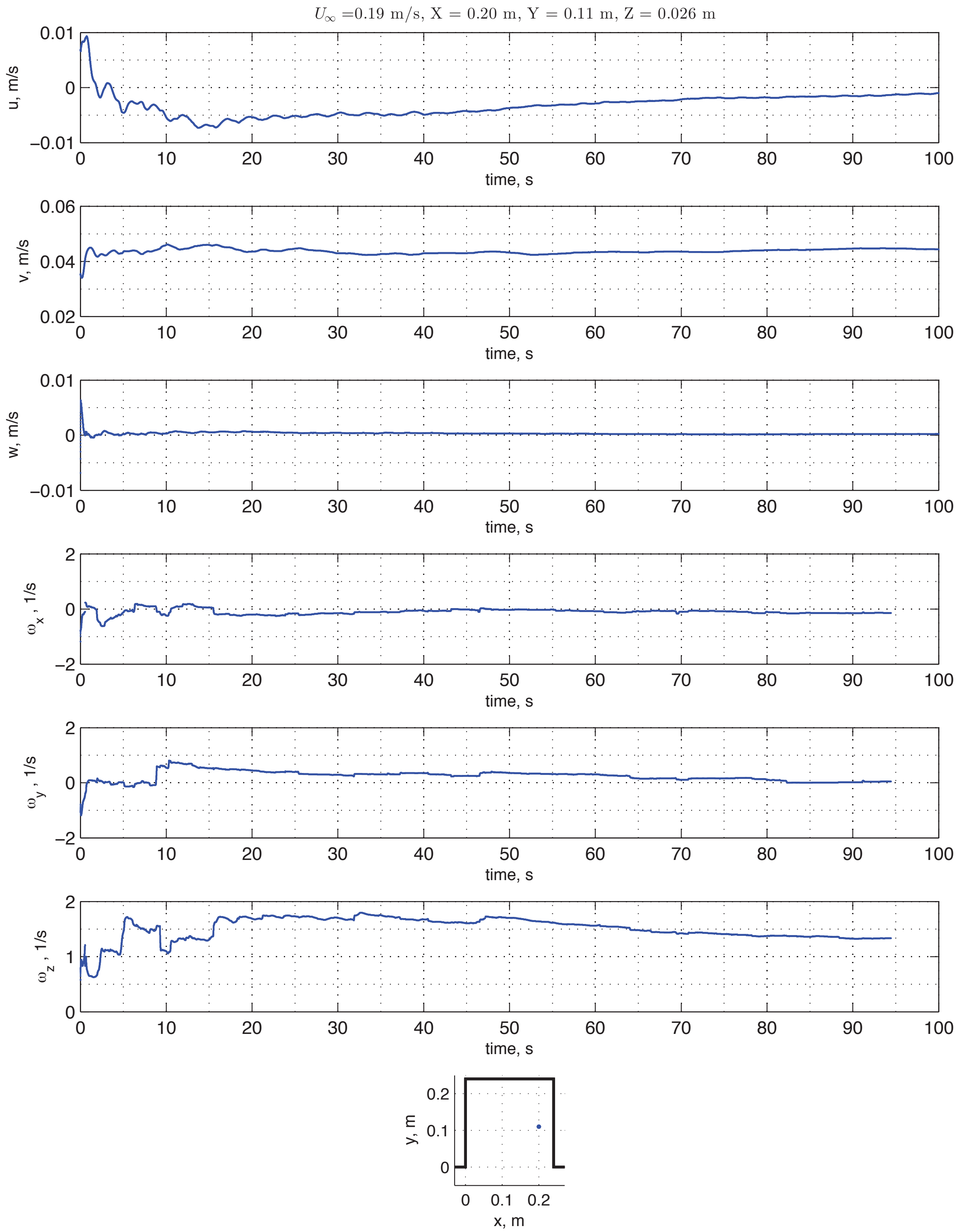

Figure 4.6: Data convergence: cumulative averages of three components of velocity (u, v, w), and three components of vorticity (ω_x, ω_y, ω_z) at one point in the embayment situated near the downstream wall of the embayment ($x = 0.2$ m, $y = 0.11$ m, and $z = 0.026$ m), for the higher free-stream velocity of 0.19 m/s.

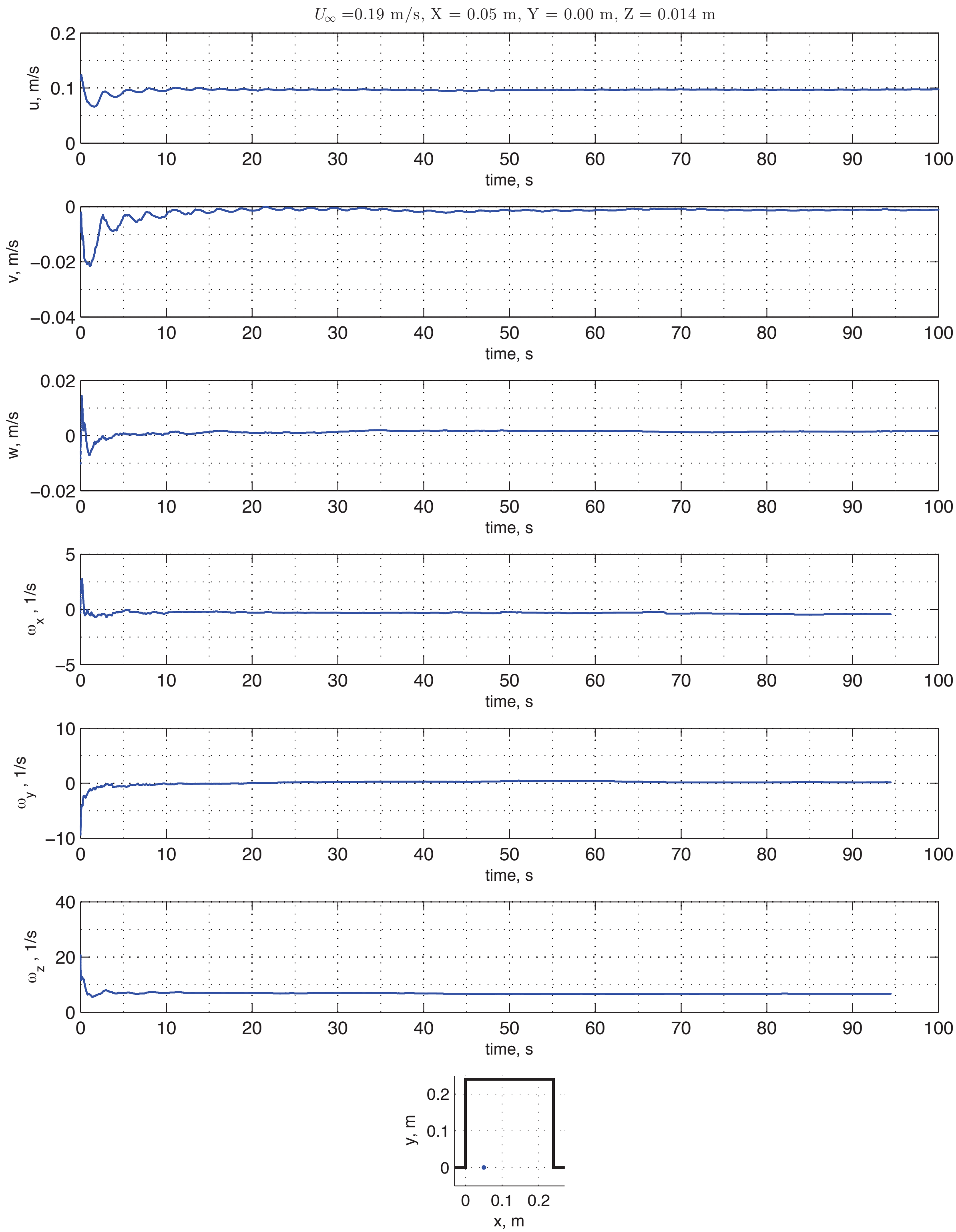

Figure 4.7: Data convergence: cumulative averages of three components of velocity (u, v, w), and three components of vorticity (ω_x, ω_y, ω_z) at one point in the embayment situated in the region of the mixing layer ($x = 0.05$ m, $y = 0$ m, and $z = 0.014$ m), for the higher free-stream velocity of 0.19 m/s.

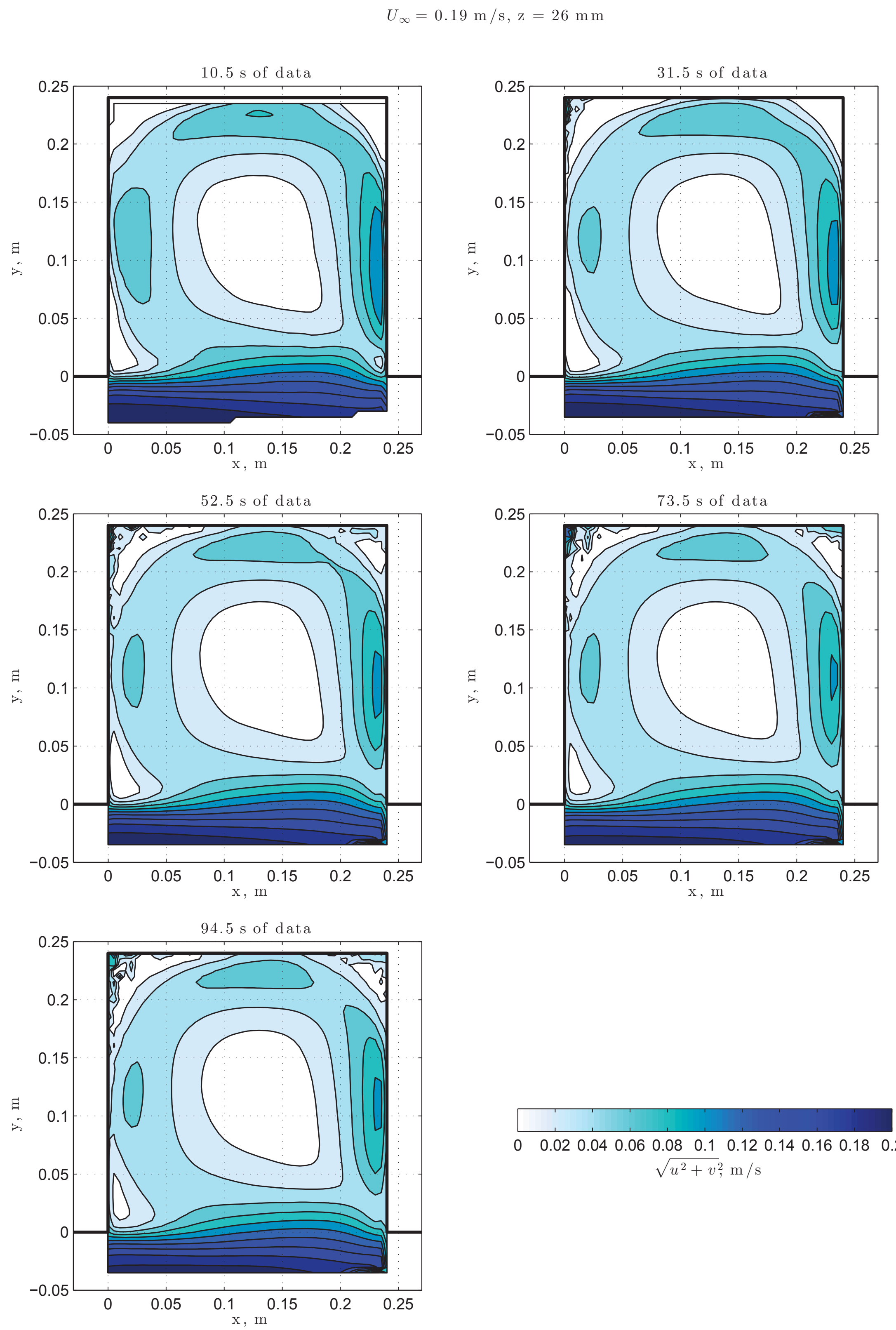

Figure 4.8: Data convergence: contour plots of the horizontal speed in the embayment at $z = 0.026$ m, averaged over different periods of time (10.5, 31.5, 52.5, 73.5, and 94.5 seconds respectively). $U_\infty = 0.19$ m/s.

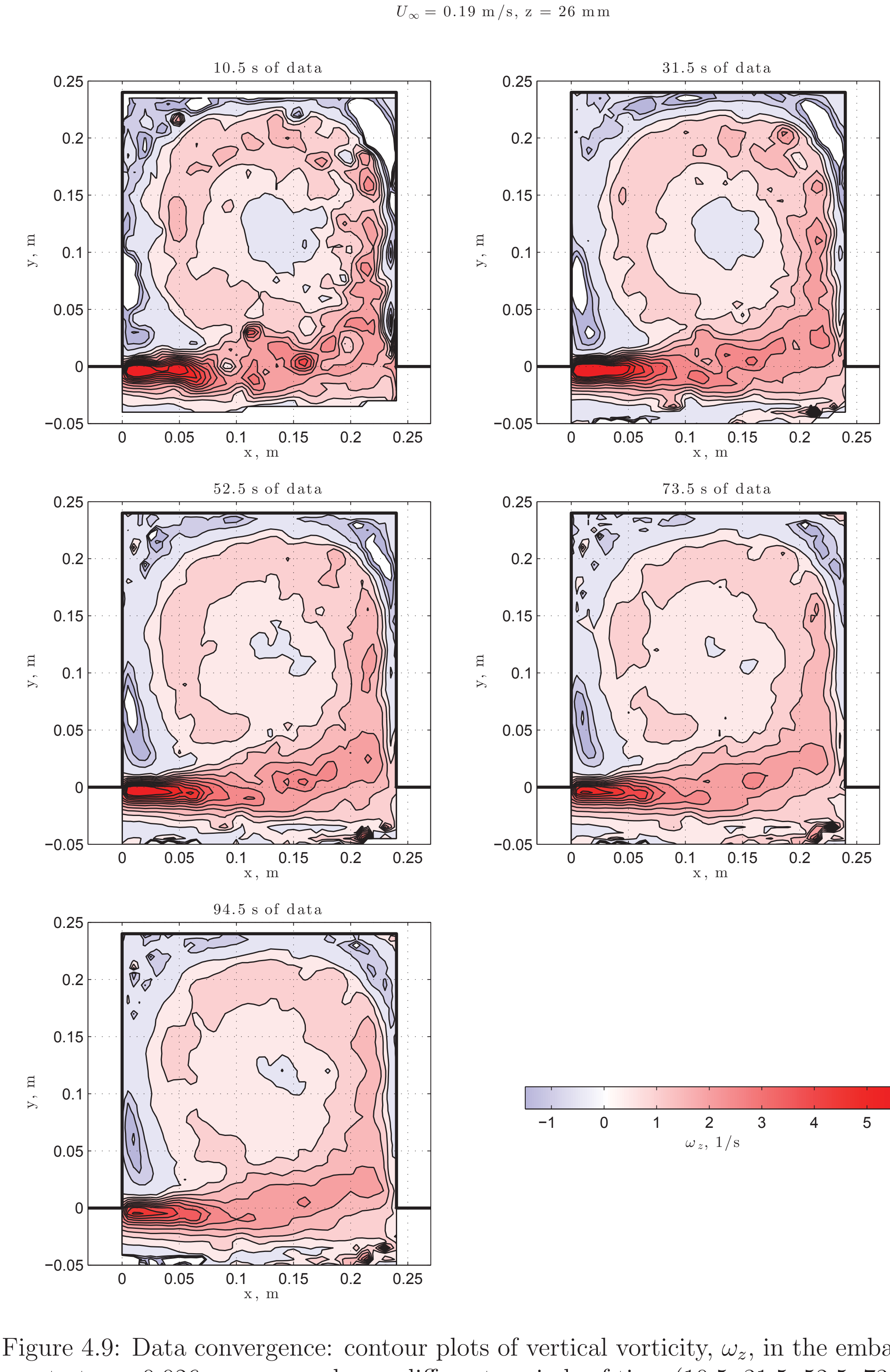

Figure 4.9: Data convergence: contour plots of vertical vorticity, ω_z, in the embayment at $z = 0.026$ m, averaged over different periods of time (10.5, 31.5, 52.5, 73.5, and 94.5 seconds, respectively). $U_\infty = 0.19$ m/s.

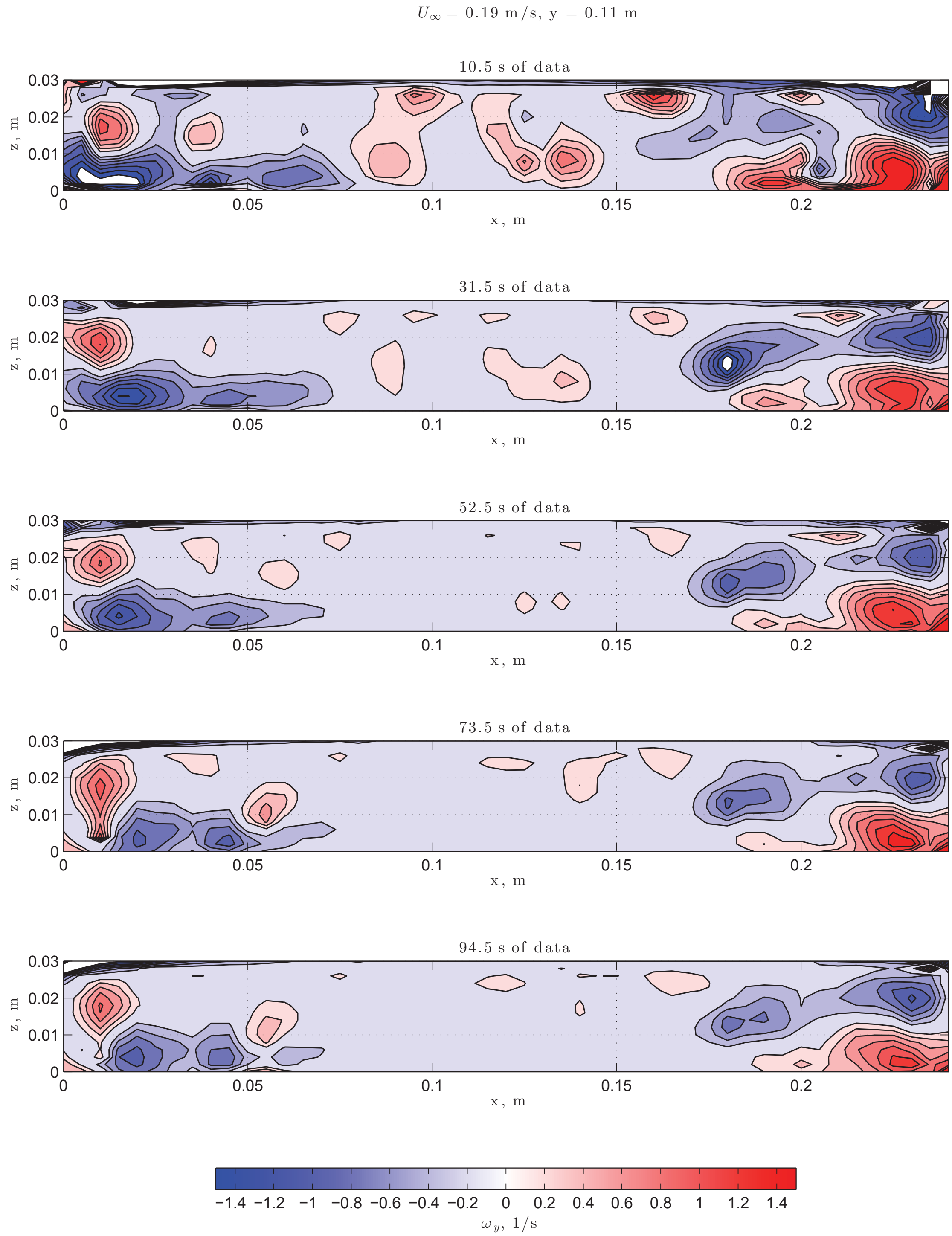

Figure 4.10: Data convergence: contour plots of horizontal vorticity, ω_y, at a vertical slice through the embayment at $y = 0.11$ m, averaged over different periods of time (10.5, 31.5, 52.5, 73.5, and 94.5 seconds, respectively)

4.3 Error analysis

This chapter examines the uncertainty of the statistics presented in the current research. All laboratory measurements have sources of uncertainty and they can generally be classified as due to either random or systematic errors. To eliminate the random component of the error in the time-averaged measurements, one must ensure convergence of the data (as discussed in Section 4.2). However, convergence does not guarantee quality, as some systematic errors may be introduced during the measurement procedure. Thus, an estimation of the systematic errors is crucial. Nevertheless, if instantaneous data is required, for example to study turbulence, then an analysis of the random component of the error is also necessary. This section will present estimations of both random and systematic components of the measurement error.

The sources of error in a multi-step procedure like 3D-PTV are numerous. Errors can be associated with each stage of the underlying data acquisition and analysis. The first stage is the determination of the particle position in the image space of each camera. Uneven lighting of the particles, imperfections in their geometry, digital noise in the cameras and connections, sensor noise, and discretization noise all lead to errors in the determination of the positions of the centre of mass of a particle. In the second stage, the determination of particle correspondences between cameras relies on the mathematical model describing the relation between their image space and real space, accounting for the position of the cameras, refraction of the light rays going through the water surface, lens distortion, etc. (see Section 3.3). This model is not perfect and introduces bias into the calculation. Moreover, it is built assuming a flat water-air interface. However, the present experiments are subject to a variation in surface elevation. There is a random component of the error produced by the gravity waves and small disturbances, and a systematic error due to a concave water curvature generated by the recirculating gyre in the embayment. This error source will be discussed in more detail later in this section.

In the third stage, particle trajectories are reconstructed from the 3D positions of the particles in real space at multiple times. Uncertainty in this stage occurs when particle trajectories cross or get too close to each other. However, the algorithm used to construct the trajectories is designed to resolve most of the uncertainties by applying additional criteria, based on the particle's characteristic velocity and acceleration from previous time steps. Malik *et al.* (1993) state that if the ratio of the average particle spacing to the mean particle displacement during one time step is much greater than unity, then tracking is relatively easy and unambiguous. In the present experiments this ratio is approximately 10 (the average distance between the particles is $\approx 3-4$ mm, and the average particle displacement in one frame in the main channel is about 0.3 mm). It is also important to note that the algorithm has user-defined discontinuity parameters that determine the maximum expected change in the velocity, acceleration, and direction of the particle in one time step. These parameters must be adjusted based on the particular set of data to minimize the errors. Velocities of the particles were calculated as first derivatives of a moving cubic spline fit to a particle trajectory, introducing a numerical error. Lastly, interpolation of the velocities onto a regular grid for time-averaging purposes is the final error source. From the above list of error sources, particular attention will be focused on those that appear to play a key role in the measurement bias and uncertainty, that is the quality of the camera calibration and the refraction errors produced by surface oscillations.

The first source of error to be examined is the calibration of the cameras. The calibration procedure consists of optimizing an algebraic relation between positions in the image space of the cameras and positions in real space using the data points provided by the calibration object of known geometry (see Section 3.3.2 for details). However, this mathematical model and the optimized parameters are not perfect and their inaccuracy introduces a systematic error. To quantify it the real positions of points on the calibration object were compared to calculated positions. The root

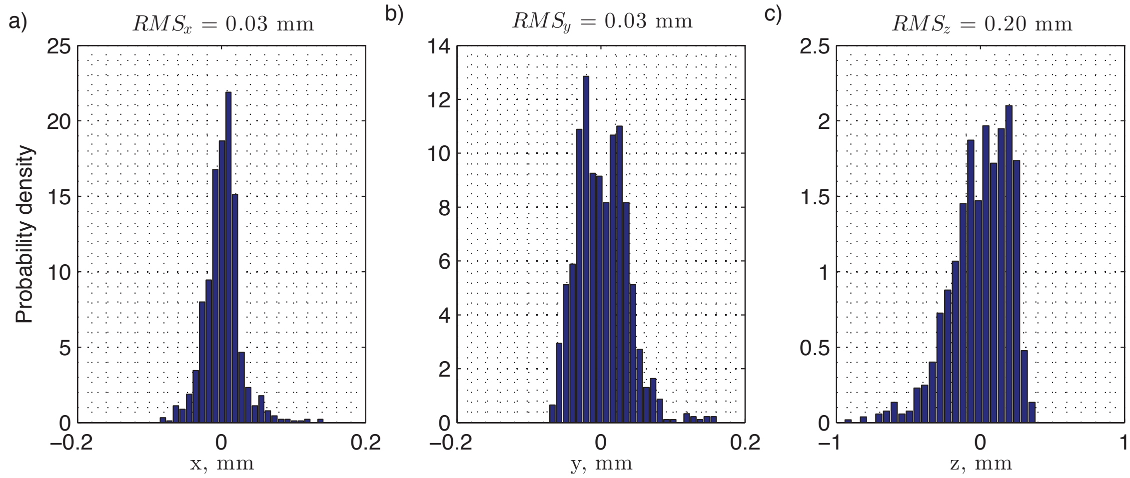

Figure 4.11: Discrete probability distributions of position-determination error in x, y, and z-directions (plots a, b, and c respectively). The error is measured in still water by comparing true and calculated positions of the dots on the calibration object.

mean square (rms) of this error is equal to 0.03 mm in the x-direction, 0.03 mm in the y-direction, and 0.20 mm in the z-direction (Figure 4.11). The vertical uncertainty is an order of magnitude higher than the horizontal uncertainty, as is expected as the cameras are arranged so that their axes are as close as possible to perpendicular to the water surface in order to minimize the effects of refraction (see Appendix A for details). It is important to note that the calibration procedure and the consequent error check were performed in still water. Thus, these position errors do not account for the effects of the flow, such as the curved air-water interface.

This brings us to the second major uncertainty in our measurements, which is due to the gravity waves and the stationary curvature of the water surface. Gravity waves appear in the channel when the natural frequency of the embayment couples with the frequency of a flow structure (see Section 2.5 for details; also, the genesis and the resonant mechanism of gravity waves will be discussed in the Results chapter). The maximum gravity-wave amplitude for the current experiments is about 1 mm, resulting in the surface inclination of about 0.2°. Also, the recirculating flow in the embayment induces a stationary concave water surface due to the centrifugal force. Assuming solid-body rotation and given the maximum rotation rate of the gyre for the current experiments, the angle of the surface concavity can reach about 0.1°. Shear-layer eddies at the interface between the channel and the embayment produce a concave water surface as well, but these disturbances are much smaller. Statistically stationary curvature of the surface could have been theoretically accounted for in the calibration procedure, but it is technically difficult to have a calibration object that would not disturb the water flow. Consequently, calibration was performed in still water and the error introduced by the curved water surface has to be estimated, as well as the component of the random error generated by gravity waves and shear-layer eddies.

Given the difficulty of estimating the contributions of every error source to the total accuracy of the data, in addition to estimating each error independently of the others, the calculation of the propagation of uncertainties remains extremely complex. To circumvent this problem, the approach used herein is to run test cases with known properties and statistics of the measured objects, which can result in estimations of the total, cumulative error.

Two test methods were developed to assess the measurement errors that were described above. The first method will calculate systematic and random components of the velocity error and will determine their spatial variation. However, this method while being very flexible does not account for the errors introduced at the last stages of PTV, such as calculation of the trajectories. Thus, a second method will be introduced to estimate the error more completely. However, it only allows to calculate the average velocity error within the domain. By using the two methods together, one can both estimate the overall error in a very robust way and get an estimation of its components and their variation in space. For the first method a pattern of known geometry was placed at the bottom of the embayment and photographed at the same frame rate, free-stream velocity, and all other characteristics as in the main experiments. Velocity errors were estimated by comparing the true positions of the dots in the pattern with the measured ones. The second test was performed using a "dumbbell-shaped" object. A particle was glued on each end of a thin, black rod. This so-called "dumbbell" was moved around the measurement volume while the water was running. The velocities of each particle were calculated independently. The component of the obtained velocity along the vector connecting the points should be zero, thus providing a way to measure velocity error in the experiments. These two methods and their results are described in the following two subsections. The last subsection is devoted to the calculation of the error in the spatial velocity derivative by applying the continuity equation to the measured data.

4.3.1 Velocity error test 1: stationary points in flowing water

In this test the difference between the measured and real positions of small white dots fixed within the domain of interest will be estimated at different channel free-stream velocities corresponding to those used in the main experiments. Velocity errors will be calculated from the position errors. Ideally, it is desired to have the dots equally distributed within the whole domain with their positions accurately fixed. However, it is technically difficult to have such an arrangement without disturbing the flow. To introduce the minimum disturbance a pattern of white dots was printed on an extra thin pane of glass that was placed at the bottom of the embayment. To ensure that this glass does not sag an extra rigid "Gorilla" glass was used. The details of the procedure are given as follows. A pattern of 512 equally spaced white dots, 0.3 mm in diameter, was printed on adhesive paper using a high quality laser printer. The paper was glued onto a 228x228 mm and 0.56 mm thick pane of "Gorilla" glass and coated with transparent flat finish (Figure 4.12). This glass pane with the pattern was placed on the bottom of the embayment and fixed with thin strips of tape at its edges while dry. The channel was then run at two free-stream velocities ($U_\infty = 0.13$ and 0.19 m/s), matching the lowest and the highest U_∞ chosen for the main experiments. The pattern did not fully occupy

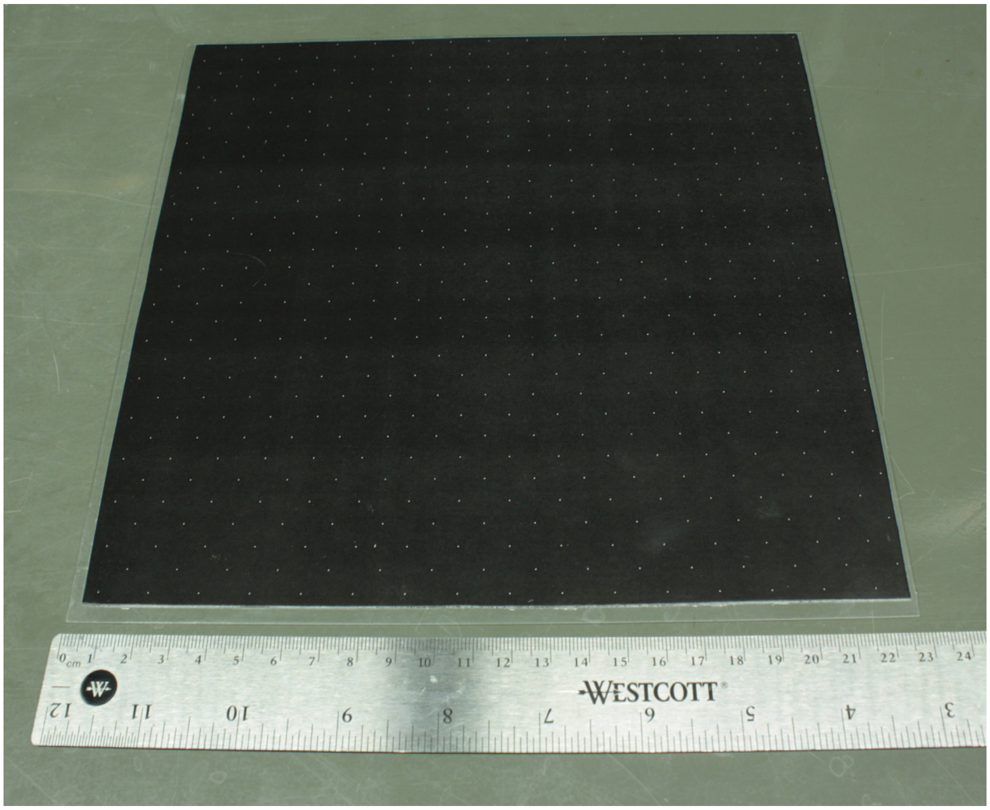

Figure 4.12: Test pattern of white dots printed on the adhesive paper using a high-quality laser printer. The paper was glued onto an extra thin (0.56 mm) pane of "Gorilla" glass and coated with transparent flat finish.

the whole view, so for one of the conditions ($U_\infty = 0.13$ m/s) several tests were performed with the pattern placed near the downstream end of the bay, near the upstream end of the bay, and in the region of the mixing layer. For the inside-the-bay positions, the test was run for 10 seconds, whereas it was run for 40 seconds in the mixing-layer region since the data converged more slowly there. From this test it was determined that the region of highest errors is located in the mixing layer. Thus, for the higher free-stream velocity (0.19 m/s), the test was run for only one position in the mixing layer for a period of 30 seconds. Figure 4.13 shows the view of the pattern from one of the cameras.

At every frame the measured positions of every dot in the pattern, $\mathbf{r_m}(x, y, t)$, were extracted and compared with their true position, $\mathbf{r_t}(x, y)$. As a result, a position error vector, $\Delta\mathbf{r}$, associated with every dot, for every frame in the test,

Figure 4.13: View of the error analysis pattern from one of the cameras. The pattern was printed on adhesive paper using high quality laser printer. The paper was then glued onto an extra thin (0.56 mm) pane of “Gorilla” glass and coated with transparent flat finish.

was obtained:

$$\Delta\mathbf{r}(x, y, t) = \mathbf{r_m}(x, y, t) - \mathbf{r_t}(x, y). \tag{4.2}$$

The total error can be divided into systematic and random components, later referred to as $\Delta\mathbf{R}$ and $\Delta\mathbf{r}'$. Taking the time average of $\Delta\mathbf{r}(x, y, t)$ yields the systematic error in position determination for every point at the bottom of the embayment, where the pattern dots are located:

$$\Delta\mathbf{R}(x, y) = \frac{1}{N}\sum_{i=1}^{N}\Delta\mathbf{r}(x, y, t_i), \tag{4.3}$$

where $T = N\Delta t$ is the duration of the data set. The standard deviation of $\Delta\mathbf{r}(x, y, t)$ quantifies the random component of the position-determination error for each point in the pattern:

$$\Delta\mathbf{r}'(x, y) = \sqrt{\overline{(\Delta\mathbf{r}(x, y, t) - \Delta\mathbf{R}(x, y))}^2}. \tag{4.4}$$

(Hereafter the overbar denotes time averaging and the angle brackets refer to space averaging.) Figure 4.14 and 4.15 show the contour plots of the systematic and random errors in position determination in x-, y-, and z-directions (plots a, b, and c, respectively). It is clear from the graphs that the systematic error is largest near the walls of the embayment, where the water surface curvature is largest. It is also possible that capillary action is increasing the surface curvature near the walls. The random component of the error is greatest in the region of the mixing layer, where shear instability produces larger surface disturbances. It is important to note that the systematic error calculation is generally less reliable as it can be affected by imperfections of the pattern print, of the glass pane, or local flow disturbances generated by the glass edges, whereas the random component is a fluctuation around the mean, and hence, unaffected by these factors. For example, in Figure 4.14c one can notice straight lines across the bay. That increase in the vertical systematic error is most likely associated with a flow disturbance that was generated by the glass pane (the lines correspond to the edges of the glass during different experiments). However the magnitude of these local increases in the position error are small (< 0.2 mm) compared to the errors consistently appearing near the walls of the embayment (up to 0.7 mm).

It is interesting to see that the random component of the error (0.01, 0.01, and 0.07 mm in x-, y-, and z-directions, respectively) is much smaller than the systematic error (0.11, 0.06, and 0.23 mm). Also, the systematic error calculated in still water from the calibration-object data was 0.03, 0.03, and 0.2 mm, being considerably larger than the random error component as well. One can therefore

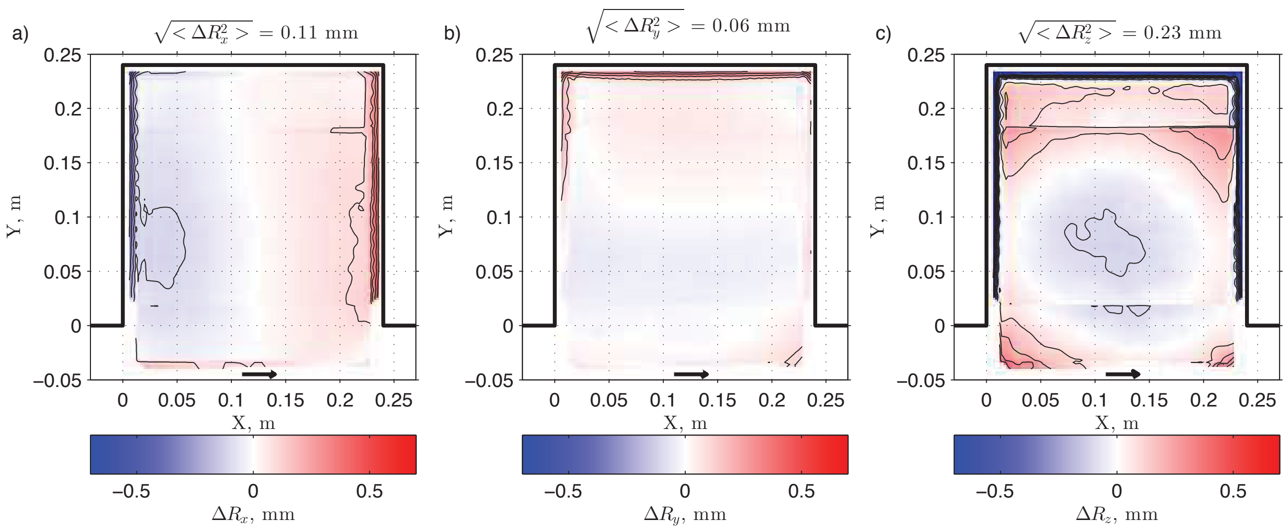

Figure 4.14: Systematic component of the position error, $\mathbf{\Delta R}$, in x, y, and z-directions (plots a, b, and c, respectively) for the lower free-stream velocity, $U_\infty = 0.13$ m/s.

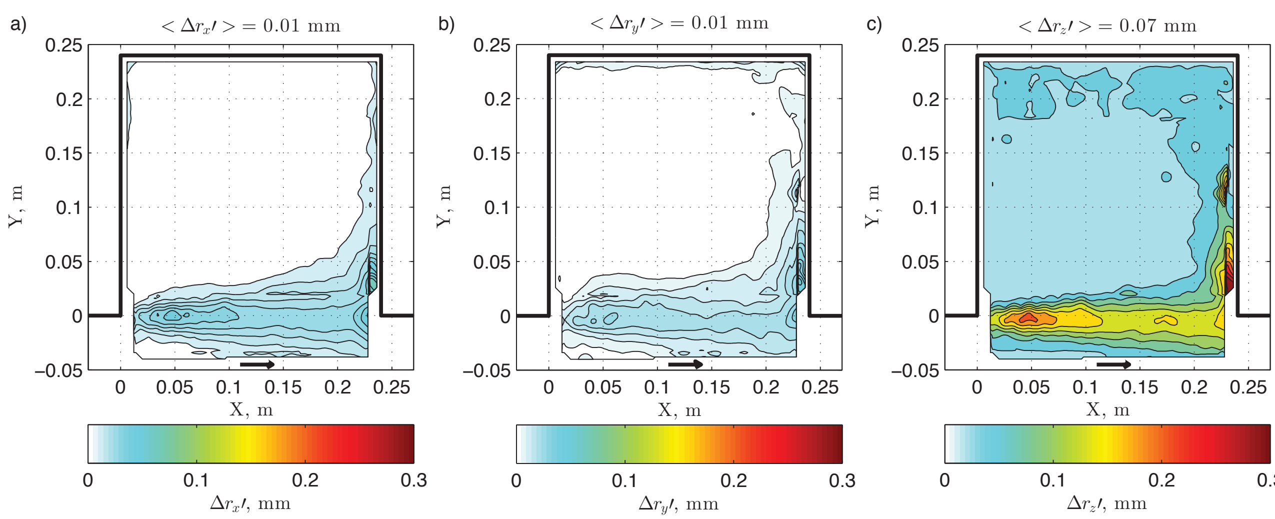

Figure 4.15: Random component of the position error, $\mathbf{\Delta r'}$, in x, y, and z-directions (plots a, b, and c, respectively) for the lower free-stream velocity, $U_\infty = 0.13$ m/s.

conclude that the effect of the water surface disturbance is significantly smaller than the effects of the calibration errors and the effects of statistically stationary water curvature. In other words, surface waves are not the most significant source of error in our arrangment. At the same time, this raises the question of possible systematic errors in the final measurements. It is thus necessary to estimate how these position-determination errors propagate into the velocity calculation of a moving particle. We will now proceed to the analysis of velocity errors.

The measured velocity of a particle, $\mathbf{u_m}$, is roughly determined by:

$$\mathbf{u_m} = \frac{\mathbf{r_2}(\mathbf{x_2})_\mathbf{m} - \mathbf{r_1}(\mathbf{x_1})_\mathbf{m}}{\Delta t}, \tag{4.5}$$

where $\mathbf{r_m}$ is the measured position vector, and Δt is the time between two frames. If a measured position vector is equal to the true position vector plus the position error:

$$\mathbf{r_m} = \mathbf{r} + \Delta\mathbf{r}, \tag{4.6}$$

then $\mathbf{u_m}$ can be written as:

$$\mathbf{u_m} = \frac{(\mathbf{r_2}(\mathbf{x_2}) + \Delta\mathbf{r}(\mathbf{x_2})) - (\mathbf{r_1}(\mathbf{x_1}) + \Delta\mathbf{r}(\mathbf{x_1}))}{\Delta t} = \mathbf{u} + \Delta\mathbf{u}, \tag{4.7}$$

where $\mathbf{u}$ is the true particle velocity, and the error in velocity, $\delta\mathbf{u}$, is therefore given by:

$$\delta\mathbf{u} = \frac{\Delta\mathbf{r}(\mathbf{x_2}) - \Delta\mathbf{r}(\mathbf{x_1})}{\Delta t}. \tag{4.8}$$

That is, the velocity error is determined by the difference in position error between the starting and end points of the particle's track between two successive frames. Indeed, if one imagines the position error to be the same everywhere, it is clear there will be no error produced in the velocity. Calculating the gradient in the position error for each particle at every time step is excessive, so an estimate will be performed using Taylor series:

$$\Delta \mathbf{r}(\mathbf{x_1}) = \Delta \mathbf{r}(\mathbf{x_2}) + \nabla(\Delta \mathbf{r}) \cdot (\mathbf{x_1} - \mathbf{x_2}) + ... \tag{4.9}$$

Substituting the Taylor series expansion (4.9) into the (4.8) one obtains:

$$\delta \mathbf{u} = \frac{\Delta \mathbf{r}(\mathbf{x_2}) - (\Delta \mathbf{r}(\mathbf{x_2}) + \nabla(\Delta \mathbf{r}(\mathbf{x_2})) \cdot (\mathbf{x_1} - \mathbf{x_2}))}{\Delta t} = \frac{\nabla(\Delta \mathbf{r}(\mathbf{x_2})) \cdot (\mathbf{x_1} - \mathbf{x_2}))}{\Delta t} \tag{4.10}$$

Expanding yields the following vector components:

$$\delta \mathbf{u} = \frac{1}{\Delta t} \begin{pmatrix} \frac{\partial}{\partial x}(\Delta r_x)(x_1 - x_2) + \frac{\partial}{\partial y}(\Delta r_x)(y_1 - y_2) + \frac{\partial}{\partial z}(\Delta r_x)(z_1 - z_2) \\ \frac{\partial}{\partial x}(\Delta r_y)(x_1 - x_2) + \frac{\partial}{\partial y}(\Delta r_y)(y_1 - y_2) + \frac{\partial}{\partial z}(\Delta r_y)(z_1 - z_2) \\ \frac{\partial}{\partial x}(\Delta r_z)(x_1 - x_2) + \frac{\partial}{\partial y}(\Delta r_z)(y_1 - y_2) + \frac{\partial}{\partial z}(\Delta r_z)(z_1 - z_2) \end{pmatrix}. \tag{4.11}$$

The error in velocity determination at a point is proportional to the gradient of the position error and the particle displacement, divided by the time step between the frames. The displacement of a particle per frame can be approximated by the time-averaged flow velocity, $\overline{\mathbf{u}}$, resulting in the following estimate of the velocity error:

$$\Delta \mathbf{u} = \begin{pmatrix} \frac{\partial}{\partial x}(\Delta r_x)\overline{u}_x + \frac{\partial}{\partial y}(\Delta r_x)\overline{u}_y + \frac{\partial}{\partial z}(\Delta r_x)\overline{u}_z \\ \frac{\partial}{\partial x}(\Delta r_y)\overline{u}_x + \frac{\partial}{\partial y}(\Delta r_y)\overline{u}_y + \frac{\partial}{\partial z}(\Delta r_y)\overline{u}_z \\ \frac{\partial}{\partial x}(\Delta r_z)\overline{u}_x + \frac{\partial}{\partial y}(\Delta r_z)\overline{u}_y + \frac{\partial}{\partial z}(\Delta r_z)\overline{u}_z \end{pmatrix}. \tag{4.12}$$

Given that the data obtained from the experiment with the glass pattern are two-dimensional (i.e. it is only possible to take horizontal derivatives of the position error field) the $\frac{\partial}{\partial z}(\Delta \mathbf{r})$ is unknown. This means that only the horizontal variability of the error can be accounted for in this test (a second error analysis test that will account for the vertical variability of the error will be performed, see Section 4.3.2). Thus, the final approximation for the velocity error is the following:

$$\begin{aligned} \Delta u_x &= \frac{\partial}{\partial x}(\Delta r_x)\overline{u}_x + \frac{\partial}{\partial y}(\Delta r_x)\overline{u}_y \\ \Delta u_y &= \frac{\partial}{\partial x}(\Delta r_y)\overline{u}_x + \frac{\partial}{\partial y}(\Delta r_y)\overline{u}_y \\ \Delta u_z &= \frac{\partial}{\partial x}(\Delta r_z)\overline{u}_x + \frac{\partial}{\partial y}(\Delta r_z)\overline{u}_y. \end{aligned} \tag{4.13}$$

Performing these operations on the systematic, $\Delta\mathbf{R}$, and random, $\Delta\mathbf{r}'$, components of the position error vectors from Figures 4.14 and 4.15, one obtains the systematic, $\Delta\mathbf{U}$, and random, $\Delta\mathbf{u}'$, components of the velocity error:

$$\begin{aligned}
\Delta U_x &= \tfrac{\partial}{\partial x}(\Delta R_x)\overline{u}_x + \tfrac{\partial}{\partial y}(\Delta R_x)\overline{u}_y \\
\Delta U_y &= \tfrac{\partial}{\partial x}(\Delta R_y)\overline{u}_x + \tfrac{\partial}{\partial y}(\Delta R_y)\overline{u}_y \\
\Delta U_z &= \tfrac{\partial}{\partial x}(\Delta R_z)\overline{u}_x + \tfrac{\partial}{\partial y}(\Delta R_z)\overline{u}_y
\end{aligned} \tag{4.14}$$

$$\begin{aligned}
\Delta u'_x &= \tfrac{\partial}{\partial x}(\Delta r'_x)\overline{u}_x + \tfrac{\partial}{\partial y}(\Delta r'_x)\overline{u}_y \\
\Delta u'_y &= \tfrac{\partial}{\partial x}(\Delta r'_y)\overline{u}_x + \tfrac{\partial}{\partial y}(\Delta r'_y)\overline{u}_y \\
\Delta u'_z &= \tfrac{\partial}{\partial x}(\Delta r'_z)\overline{u}_x + \tfrac{\partial}{\partial y}(\Delta r'_z)\overline{u}_y.
\end{aligned} \tag{4.15}$$

The spatial derivatives of $\Delta\mathbf{R}$ and $\Delta\mathbf{r}'$ were approximated by the central difference scheme. As mentioned above, this analysis was performed for two free-stream velocity cases, the lowest, and the highest ($U_\infty = 0.13$ and 0.19 m/s). To obtain velocity errors for these two cases the corresponding position error fields and time-averaged velocities were used. First, the lower free-stream velocity flow case will be discussed, then the higher one will follow.

Figure 4.16 shows the systematic velocity error in the embayment for the (lower) free-stream velocity of 0.13 m/s. The first graph is the total velocity error in absolute units of mm/s (denoted as norm $||\Delta\mathbf{U}|| = \sqrt{\Delta U_x^2 + \Delta U_y^2 + \Delta U_z^2}$), and the second graph is the velocity error as a percentage of the local average velocity. It is important to note that on this graph and every other one hereafter, where the error is expressed in terms of the percentage of the local average velocity, the velocity field was filtered to avoid division by zero/very small numbers. The filtering thresholds were chosen to be 0.4 mm/s for the lower free-stream velocity of 0.13 m/s, and 0.6 mm/s for the higher free-stream velocity of 0.19 m/s. These numbers were chosen based on the absolute values of the velocity errors that will be shown in this section. The fact that the velocity fields were filtered at these values means that in the actual data, signals below these values, have to be filtered out as noise

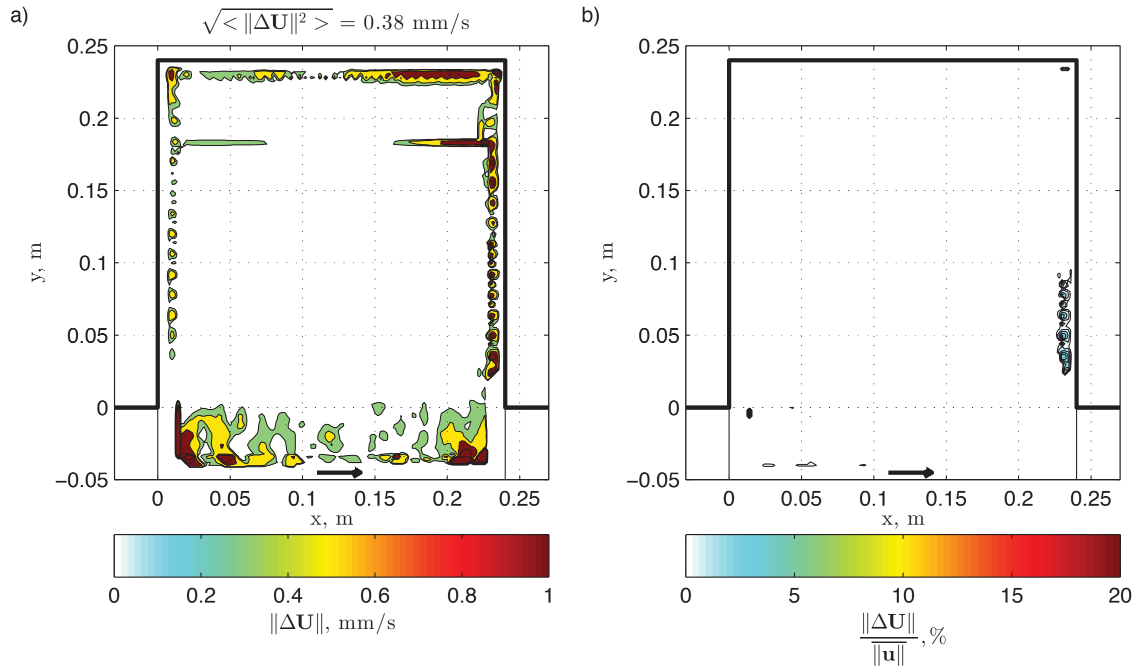

Figure 4.16: Contour plots of the norm of the systematic component of the velocity error vector, $||\Delta\mathbf{U}||$, for the (lower) free-stream velocity of $U_\infty = 0.13$ m/s. a) Absolute error. b) Error as a percentage of the local time-averaged velocity.

as well. From Figure 4.16, one observes that the regions of higher errors are the edges of the embayment, along the walls, and the mixing layer region, where the uncertainty varies from 0.3 mm/s to 2 mm/s. However, when divided by the local time-averaged velocity, these errors become small (no more than 4%). One may notice a stripe of larger error at about y = 0.18 m in Figure 4.16*a*. As was mentioned before, this line corresponds to the edge of the glass pane when it was placed to cover the mixing layer region. The presence of this error means that there was some disturbance generated by the glass. Thus, the overall error may be somewhat overestimated in our analysis.

As was already clear from Figure 4.14, the uncertainty in the vertical direction is much larger than that in the horizontal. Therefore, it is logical to expect the total velocity error is dominated by its vertical component, so that the uncertainty in the vertical direction must be further quantified. To this end, Figure 4.17, which plots the vertical component of the systematic velocity error, shows that the bias can

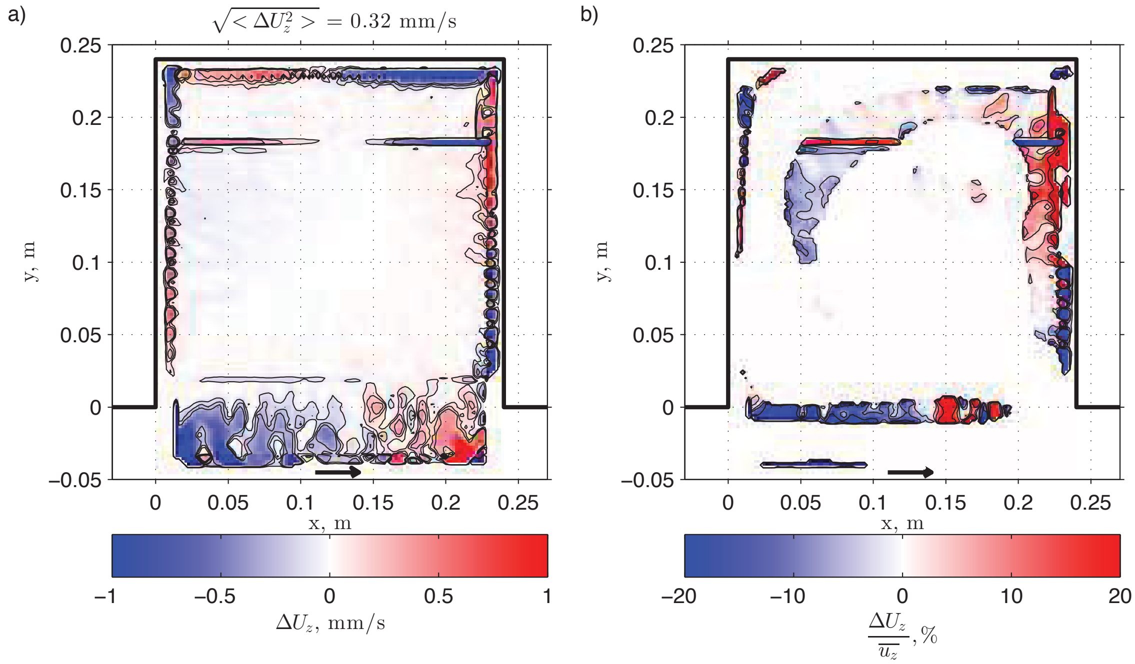

Figure 4.17: Contour plots of the vertical component of the systematic velocity error ,ΔU_z, for the (lower) free-stream velocity of $U_\infty = 0.13$ m/s. a) Absolute error. b) Error as a percentage of the local time-averaged velocity.

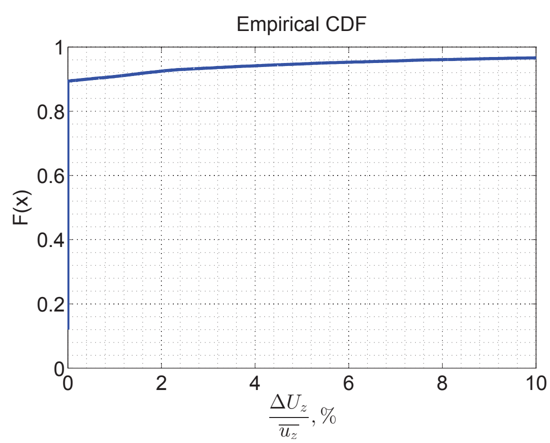

Figure 4.18: Empirical cumulative density function of the vertical component of the systematic velocity error, ΔU_z, as a percentage of the local time-averaged velocity, for the (lower) free-stream velocity of $U_\infty = 0.13$ m/s.

reach 1 mm/s or 20% of the local velocity in certain small regions. Those regions primarily correspond to zones of small vertical velocity. As was previously noted, the data on the systematic position error is less reliable than the data pertaining to the random component of the position error. (This is due to the imperfections of the glass pane, the printing of the pattern, and/or the disturbance of the flow at the edges of the glass pane.) Figure 4.18 shows the empirical cumulative density function of the vertical component of the systematic velocity error. Based on this graph, 98% of the data has a bias of less than 10% of the local vertical velocity, and 96% of the data have a bias less than 5%. Thus, even if we assume the systematic component of the error to be correct, it is clearly small enough to continue with our analysis.

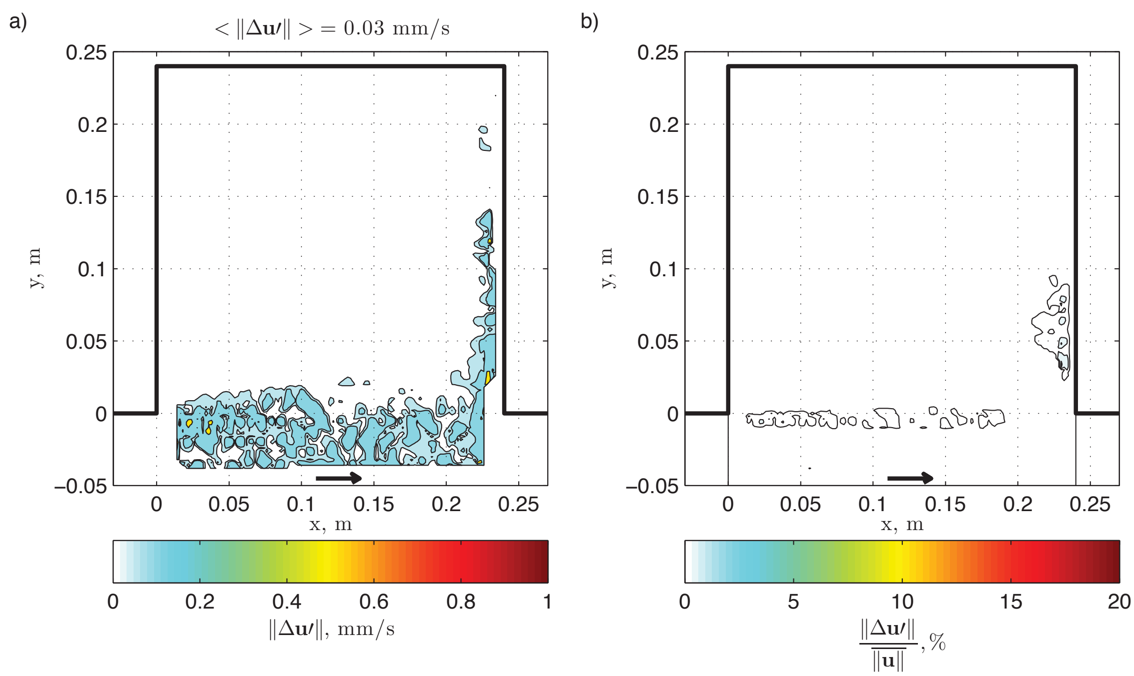

Figure 4.19: Contour plots of the norm of the random component of the velocity error vector, $||\Delta \mathbf{u}'||$, for the (lower) free-stream velocity of $U_\infty = 0.13$ m/s. a) Absolute error. b) Error as a percentage of the local time-average velocity.

The next step is the random velocity error that is primarily produced by the water surface disturbances. Figure 4.19 shows the total random component of the velocity error in absolute units of mm/s and as a percentage of the local average

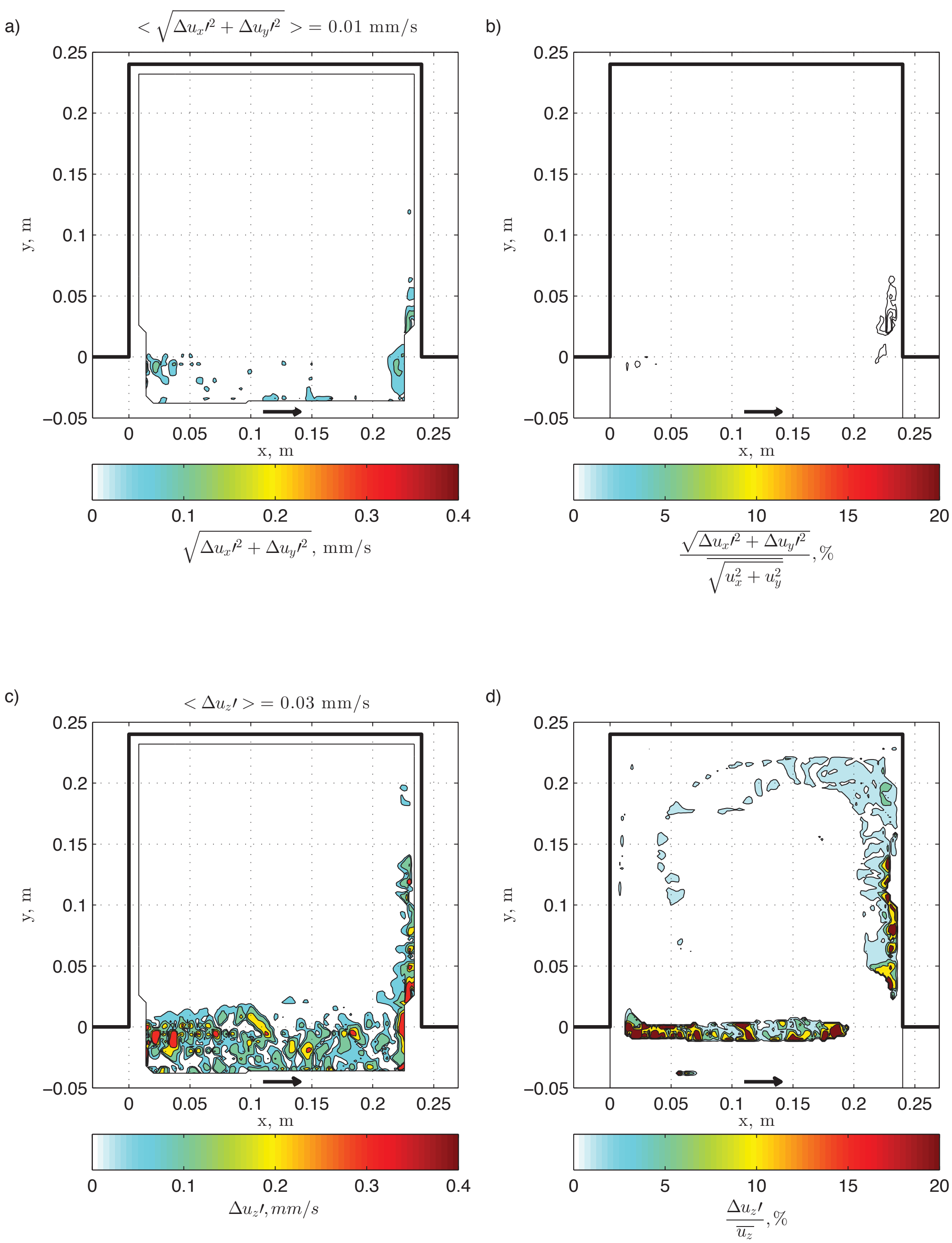

Figure 4.20: Contour plots of the random components of the error in horizontal (a, b) and vertical velocity (c, d), for the (lower) free-stream velocity $U_\infty = 0.13$ m/s. a), c) Absolute error. b), d) Error as a percentage of the local time-averaged velocity.

velocity calculated using (4.15). The error in Figure 4.19-b does not exceed 0.5% of the total velocity. Similarly to the systematic error, one can separate this error into horizontal and vertical components as there is a danger that the vertical component will be much larger in terms of the ratio to the local velocity. Indeed, Figure 4.20 shows that the horizontal component of the velocity error only goes up to 0.3%, whereas vertical error reaches 20% in some points. Even though some points have relatively large vertical velocity error, 96% of the data have an uncertainty of less than 1%, and 98% of the data have an uncertainty of less than 2% (Figure 4.21).

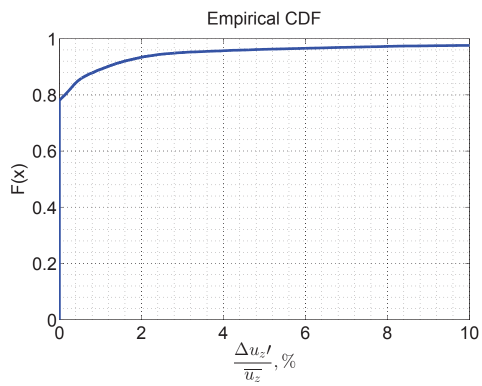

Figure 4.21: Empirical cumulative density function of the vertical component of the random velocity error, $\Delta u_z'$, as a percentage of the local time-averaged velocity, for the (lower) free-stream velocity of $U_\infty = 0.13$ m/s.

The previous analysis was performed for the lower free-stream velocity ($U_\infty = 0.13$ m/s). It is natural to expect the errors to be larger for the case of the higher free-stream velocity, as the water surface disturbances increase, and sloshing waves become more prominent. Indeed, we find that the absolute values of the errors are larger for $U_\infty = 0.19$ m/s. However the flow velocities are higher as well, hence, the relative error does not change as much as one could expect. In fact, the systematic velocity error did not increase at all with the increased free-stream velocity (Figure 4.22 and 4.23). The overall average of the total systematic error remained the same as for the lower free-stream velocity (Figure 4.22), whereas the vertical component of the systematic velocity error decreased from 0.32 to 0.17 mm/s (Figure 4.23). This may partially be attributed to the difference in the spatial

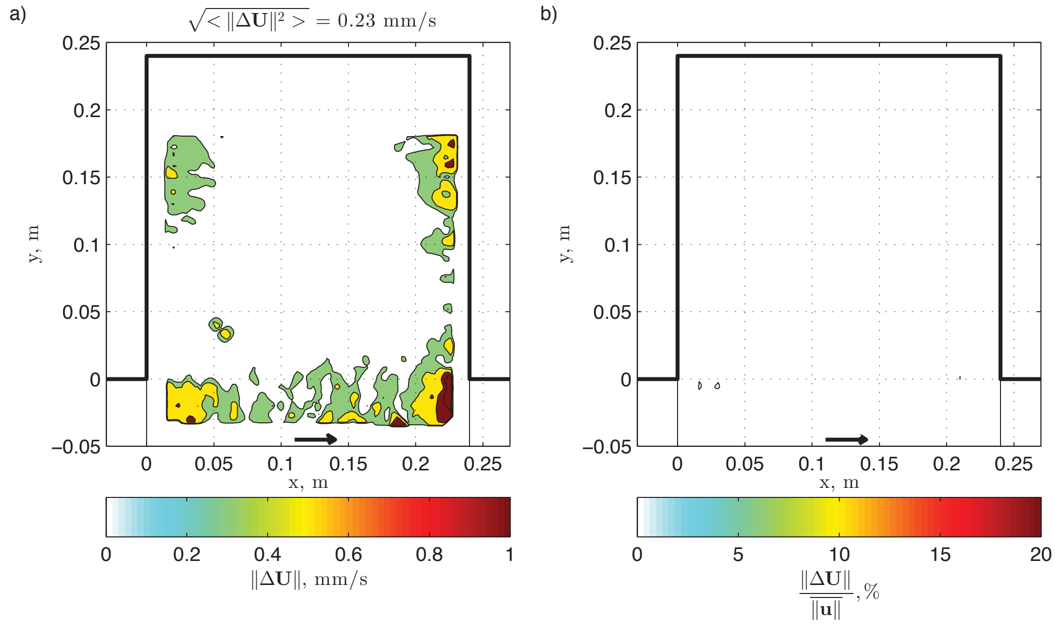

Figure 4.22: Contour plots of the norm of the systematic component of the velocty error vector, $||\Delta\mathbf{U}||$, for the (higher) free-stream velocity of $U_\infty = 0.19$ m/s. a) Absolute error. b) Error as a percentage of the local time-averaged velocity.

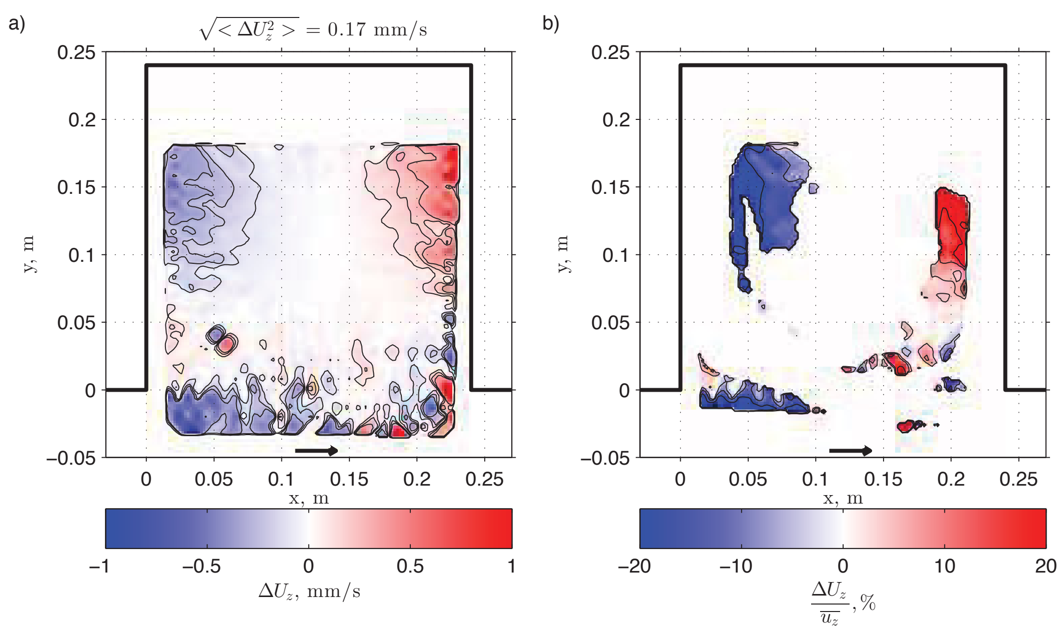

Figure 4.23: Contour plots of the vertical component of the systematic velocity error ,ΔU_z, for the (higher) free-stream velocity of $U_\infty = 0.19$ m/s. a) Absolute error. b) Error as a percentage of the local time-averaged velocity.

averaging area. For the lower U_∞ the data is available for the whole embayment including the regions of high error adjacent to the walls, whereas for the higher U_∞ only the data in the middle of the bay and in the shear layer are available. However, if one compares the absolute values of the systematic velocity error in the region that is available for both flow cases, one can see that they are very similar. This means the statistically-stationary curvature of the water surface did not change significantly with the increased free-stream velocity. On the other hand, the overall average of the total random velocity error increased from 0.03 mm/s to 0.09 mm/s (Figure 4.24). Its vertical component also increased from 0.03 mm/s to 0.08 mm/s (Figure 4.25). However, as mentioned before, the time-averaged flow velocity also increased, so in terms of the ratio to the local velocity, the percentage error did not increase as much, see Figures 4.24-*b* and 4.25-*b*.

Finally, to ensure that the measurement most sensitive to error - the vertical velocity - is still within tolerable uncertainty levels, even for the larger free-stream velocity, we present two empirical CDFs for the systematic and random components of the vertical velocity error. Figure 4.26 shows that 96% of the data has a systematic velocity error less than 4%. Figure 4.27 shows that 96% of the data have random velocity errors less than 2%.

This method of error analysis allowed the calculation of the spatial distributions of both systematic and random errors in velocity measurements. It is clear that the regions near the walls of the bay have much larger error than the rest of the flow. Based on this information, when presenting the results of the main experiments, the data within 5 mm of the wall will be excluded. It was also clear that the second most error-prone region is the shear layer. However, it was consistently shown that the errors are still within acceptable limits. The relative velocity error was calculated for the whole investigation domain by dividing the local absolute velocity error by the local average velocity obtained from the experiments. As expected, the relative error is high when the absolute velocities go to zero. A filtering

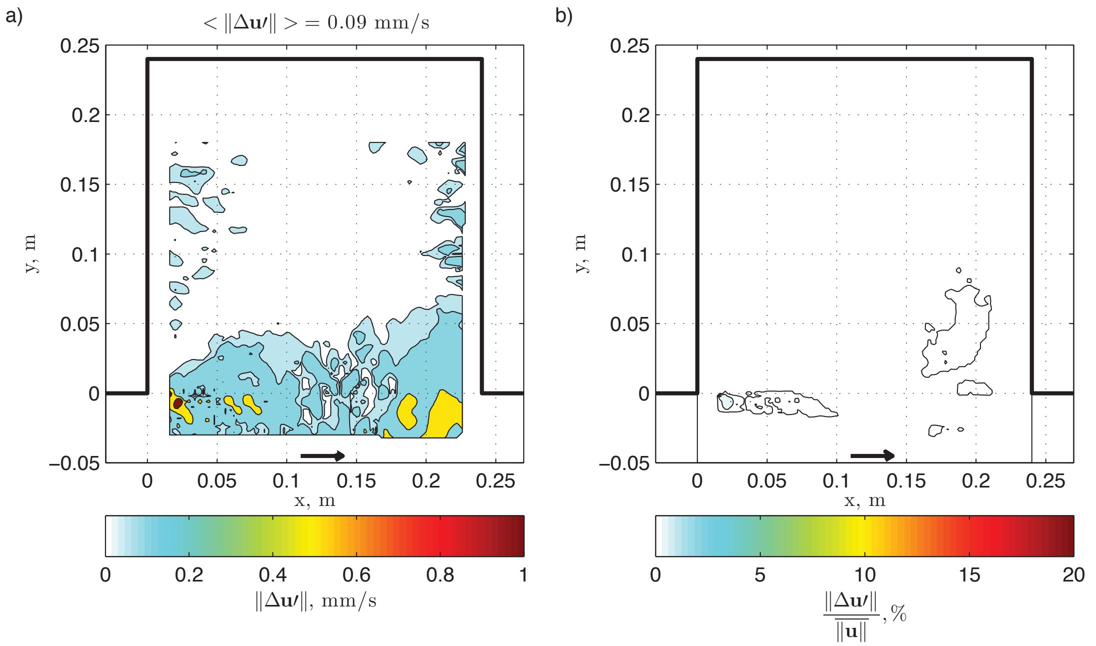

Figure 4.24: Contour plots of the norm of the random component of the velocty error vector, $||\Delta\mathbf{u}'||$, for the (higher) free-stream velocity of $U_\infty = 0.19$ m/s. a) Absolute error. b) Error as a percentage of the local time-average velocity.

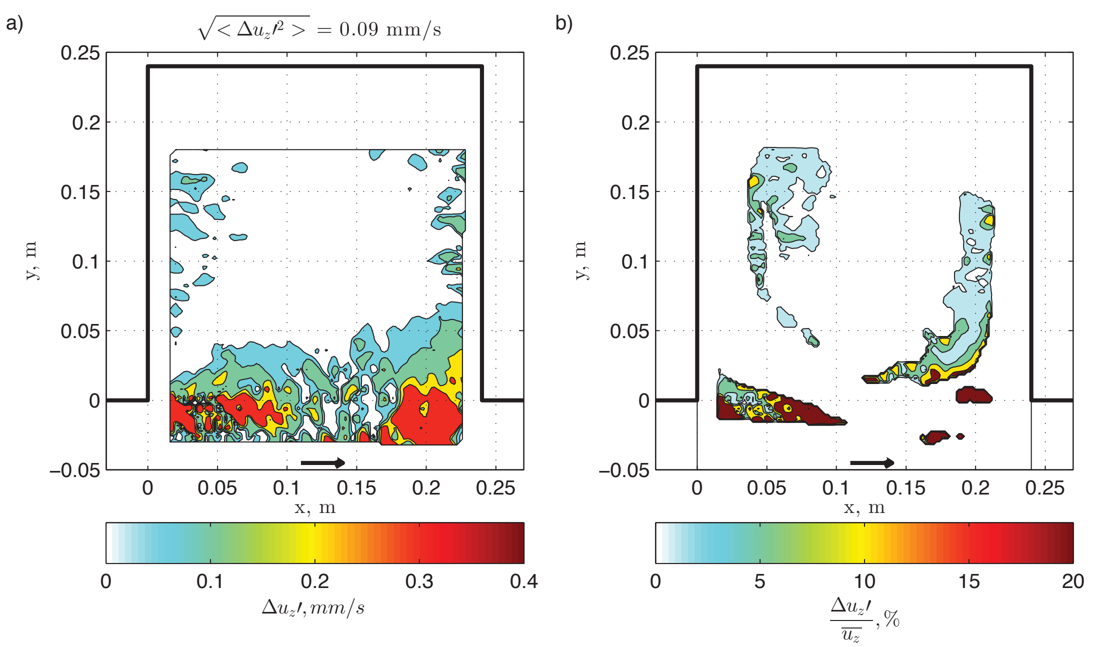

Figure 4.25: Contour plots of the vertical component of the random velocity error ,$\Delta u_z'$, for the (higher) free-stream velocity of $U_\infty = 0.19$ m/s. a) Absolute error. b) Error as a percentage of the local time-averaged velocity.

procedure was applied to these data with varying cutoff values for average local velocity until approximately 95% of the data had a velocity error below 5%. From this, one could conclude that velocities below 0.4 and 0.6 mm/s could be considered as substantially affected by errors for free-stream velocities of 0.13 and 0.19 m/s, respectively. Based on this the final data were filtered using these thresholds. Both systematic and random velocity errors are dominated by their vertical components. Nevertheless, normalizing (relatively large) vertical errors with (relatively low) vertical velocities showed that the measurements of the vertical velocity alone are reliable. It was also interesting to find that systematic errors are playing a more important role overall than random ones. This is somewhat surprising since non-stationary disturbances on the water surface, and sloshing waves were expected to pose a serious ambiguity to the measurements. It was found that calibration errors and statistically-stationary water curvature create a significantly larger error than the non-stationary surface disturbances. Also, the increase in the free-stream velocity did not have an effect on the systematic error. It did, however, result in higher random velocity errors. Most importantly, it was shown that for the most difficult case of a high free-stream velocity, where gravity waves have the largest amplitudes, it is nevertheless possible to obtain accurate PTV measurements through the free surface.

The above error analysis, of course, does not capture all the uncertainties that affect the quality of the data. Two main parameters that are not included are the variability of the position error in the vertical direction, $\frac{\partial}{\partial z}(\Delta\mathbf{r})$, and the errors that appear in the later stages of the PTV analysis, such as particle tracking and velocity calculations. To address these two issues a second method of error analysis was developed and implemented to capture the factors that were missing above.

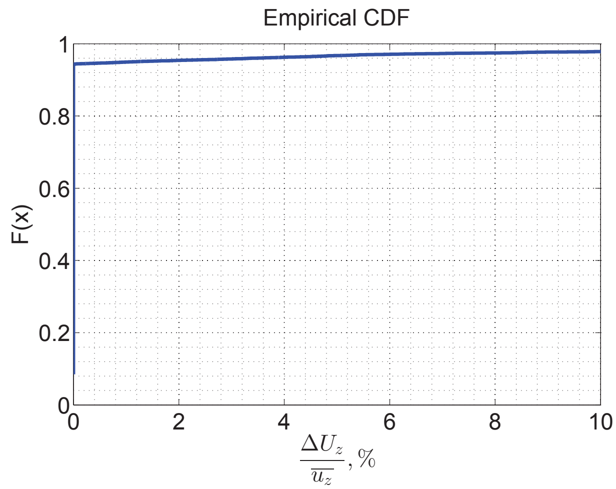

Figure 4.26: Empirical cumulative density function of the vertical component of the systematic velocity error, ΔU_z, as a percentage of the local time-averaged velocity, for the (higher) free-stream velocity of $U_\infty = 0.19$ m/s.

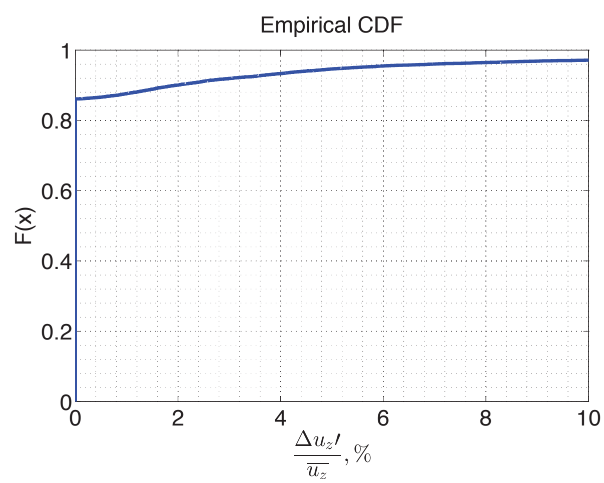

Figure 4.27: Empirical cumulative density function of the vertical component of the random velocity error, $\Delta u_z'$, as a percentage of the local time-averaged velocity, for the (higher) free-stream velocity of $U_\infty = 0.19$ m/s.

4.3.2 Velocity error test 2: moving points in flowing water

To calculate the velocity uncertainty of a PTV (or a PIV) system it is desirable to conduct a test in which the exact velocities of the tracking points are known. One of the common methods is to measure the velocities of points on a rotating disk (see, for example, Weitbrecht *et al.* (2002)). However, this method is not ideal for the current set-up primarily because of the imaging through the free surface. In a rotating-disk test the points always move on the same circular trajectories, whereas from the previous section we know that velocity error at a point depends on the direction in which the particle is moving. Also, the rotating disk is flat and will again be insensitive to the vertical derivative of the position error. A 3D complex object could have been constructed, but in that case it would have been impossible to rotate it inside the bay without creating significant disturbances to the flow in the embayment, including the water surface.

An alternative way of testing the quality of the velocity measurements that was more suitable to the experimental conditions had to be developed. There exists a well-known camera calibration technique for PTV systems called dynamic calibration or a dumbbell calibration (Gülan *et al.*, 2012). The idea is to move two points with a fixed distance between them within the domain of interest. Afterwards, the calibration parameters are optimized while maintaining the detected distance of the dumbbell points. In this study we expand on this idea, exploiting the principle that these two points, which have a constant separation, must also have zero relative velocity along the vector connecting them. To this end, two particles (polyethylene microspheres 212-250 μm in diameter), identical to those used for the experiments, were glued onto a black piece of plastic, and separated by a distance of 9.36 mm.

A thin handle was attached to the dumbbell to move the target inside the domain of investigation (Figure 4.28). Recordings of this dumbbell-shaped target moving around the field-of-interest were made for 3 runs (10 seconds each) for each of two free-stream velocities ($U_\infty = 0.13, 0.19$ m/s). After discarding the data that

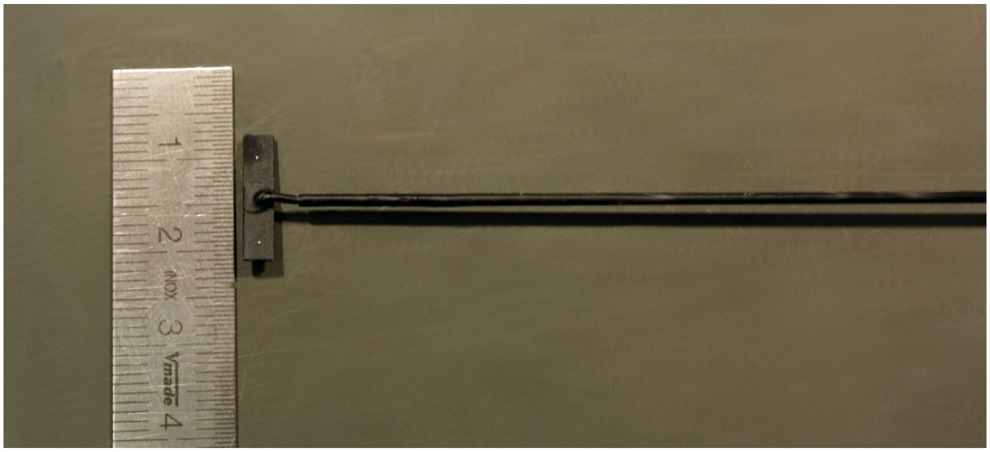

Figure 4.28: Dumbbell-shaped target with two polyethylene microspheres 212-250 μm in diameter glued onto it, with a distance 9.36 mm between them.

had obvious problems (for example when one of the points on the dumbbell was not visible because of the wrong angle of the plastic support) 23 seconds of data for $U_\infty = 0.13$ m/s, and 14 seconds for $U_\infty = 0.19$ m/s remained. It was attempted to move the target along the streamlines with approximately the same average velocity as the flow rotation in the embayment, to the extent possible, in order to obtain the same type of velocity errors that occur in the experiments. An example of a dumbbell target trajectory is given in Figure 4.29.

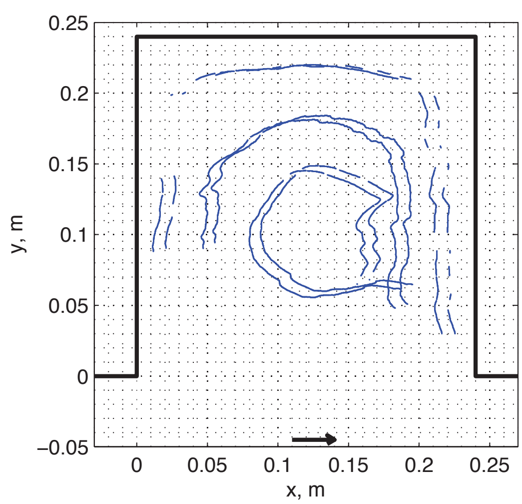

Figure 4.29: Example of the trajectories of the 2 particles on the dumbbell target, free-stream velocity of $U_\infty = 0.13$ m/s.

The recordings were post-processed using the same procedure as the actual experiments: particle positions were determined using Gaussian fits, particle correspondence obtained through the epipolar line intersection technique (both using OpenPTV (2012), and the calculation of particle velocities was performed using centred differences with low-pass filtering using a moving polynomial fitted to 21 trajectory points (Lüthi *et al.*, 2005). The distance between two particles, d, was

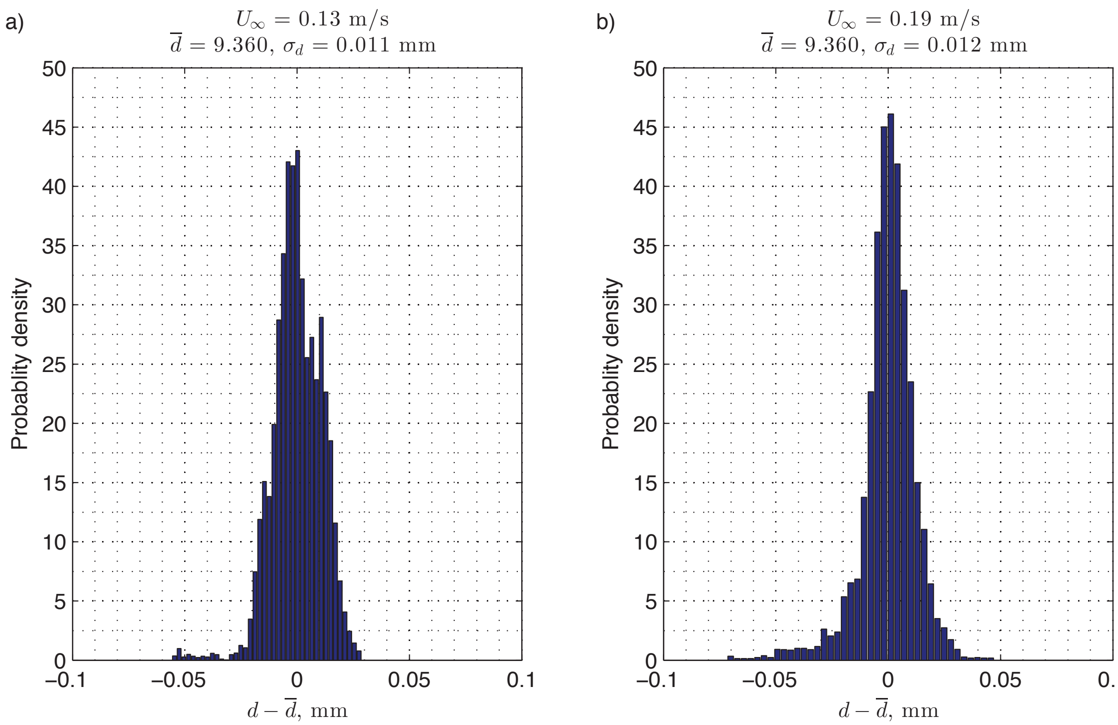

Figure 4.30: Empirical probability density functions of the time series of the distance between two particles on the dumbbell target, $d(t)$. a) $U_\infty = 0.13$. b) $U_\infty = 0.19$ m/s.

calculated as:

$$d = \sqrt{(x_2 - x_1)^2 + (y_2 - y_1)^2 + (z_2 - z_1)^2},$$

where x, y, and z are the coordinates of the particles. The distance between the points is constant, so the standard deviation of the $d(t)$ gives us an estimation of the position error of the system.

The velocity of the two dumbbell particles toward or away from each other was calculated as follows. If the velocity of the first particle is $\mathbf{u_1}$ and the velocity of the second particle is $\mathbf{u_2}$, then the velocity of particle one with respect to the other is equal to $\mathbf{u_1} - \mathbf{u_2}$. The scalar projection of the relative velocity $(\mathbf{u_1} - \mathbf{u_2})$ onto the vector connecting the two particles, $\mathbf{k}$, is

$$u_{1,2} = \frac{(\mathbf{u_1} - \mathbf{u_2}) \cdot \mathbf{k}}{|k|}.$$

Ideally, this value has to be equal to zero at all times, as the particles are attached to a solid body and are not moving toward or away from each other. The deviation of $u_{1,2}$ from zero can be used as a measure of velocity error in the experiment.

Thus, the time series of $d(t)$ and $u_{1,2}(t)$ were analysed. Figure 4.30 shows the probability density functions of $d(t)$ for two free-stream velocities (0.13 and 0.19 m/s). The standard deviations are equal to 0.011 and 0.012 mm respectively. In order to compare this result with the previous test (with the stationary pattern of known geometry), we need the total position error for the two free-stream velocities. From Figures 4.14 and 4.15 one can calculate the total position error as the square root of the sum of the squares of the components. After that, we sum the random and systematic parts to obtain the total position ambiguity of 0.32 mm for $U_\infty =$ 0.13 m/s. For $U_\infty = 0.19$ m/s (the data is not shown) the same operations result in a total position error of 0.38 mm. These values are more than an order of magnitude larger than those obtained with the dumbbell target test. This means, that the relative position error between points that are close together (for the dumbbell target it is about 10 mm) is more than an order of magnitude smaller than the absolute position error in some regions. This explains why it is possible to get quite accurate velocity measurements even with relatively large absolute position errors (0.32 mm and 0.38 mm).

Figure 4.31 shows the probability density functions of $u_{1,2}(t)$ for two free-stream velocities (0.13 and 0.19) with standard deviation values of 0.52 and 0.76 mm/s, respectively. These numbers are larger than the velocity errors obtained from the previous test with the stationary pattern, in which the total velocity error (random

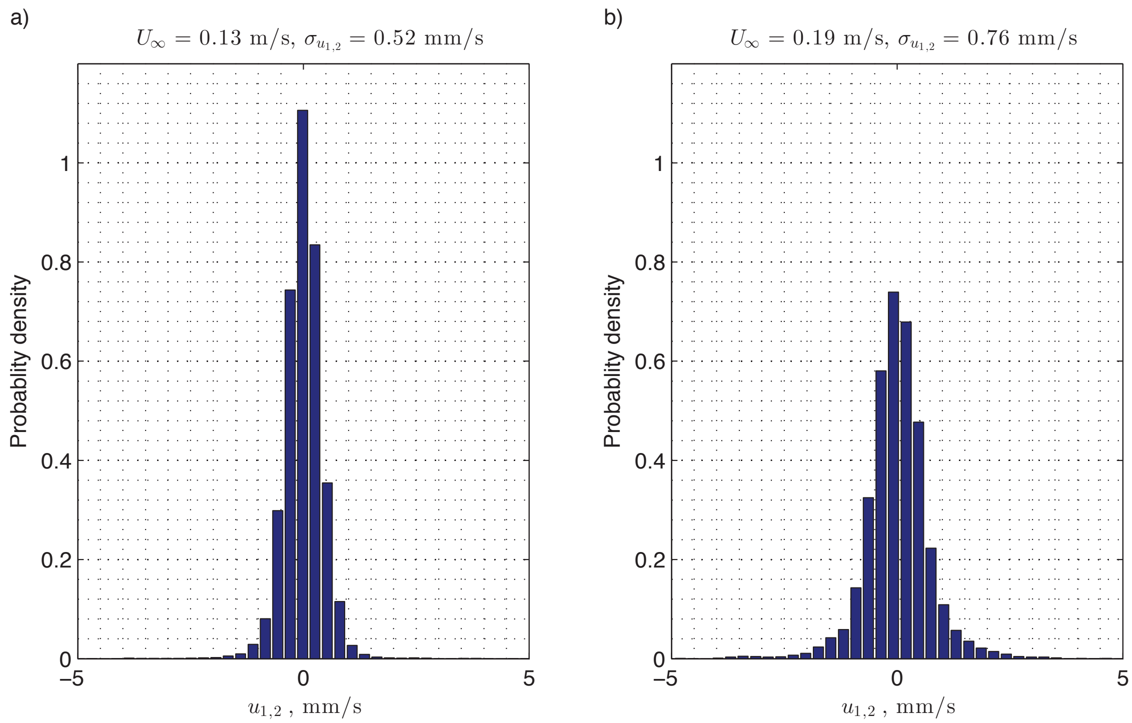

Figure 4.31: Empirical probability density functions of the time series of the projection of the relative velocity on the separation vector between the two points on the dumbbell target, $u_{1,2}$. a) $U_\infty = 0.13$. b) $U_\infty = 0.19$ m/s.

plus systematic) was 0.16 mm/s and 0.22 mm/s for the two free-stream velocities (0.13 and 0.19 m/s respectively). The fact that the position determination error is so small in the dumbbell target test and the velocity error is larger means that the error in the velocity measurements is mainly produced by the polynomial fit procedure that was not accounted for in the previous test. If that is true, the error will be largest at the ends of the trajectories where the quality of the fit is at its worst. Indeed, if one filters the data from the dumbbell target test by eliminating the first two and the last two points of each trajectory (trajectories are usually 199 points long), the rms values of the velocity errors are reduced to 0.39 and 0.68 mm/s for $U_\infty = 0.13$ and 0.19 m/s, respectively (Figure 4.32).

The dumbbell target was moved inside the bay by hand and the trajectories obtained were thus not especially smooth. Just a little shake of the hand could produce micro-movements that are not characteristic of the flow. Figure 4.33 shows

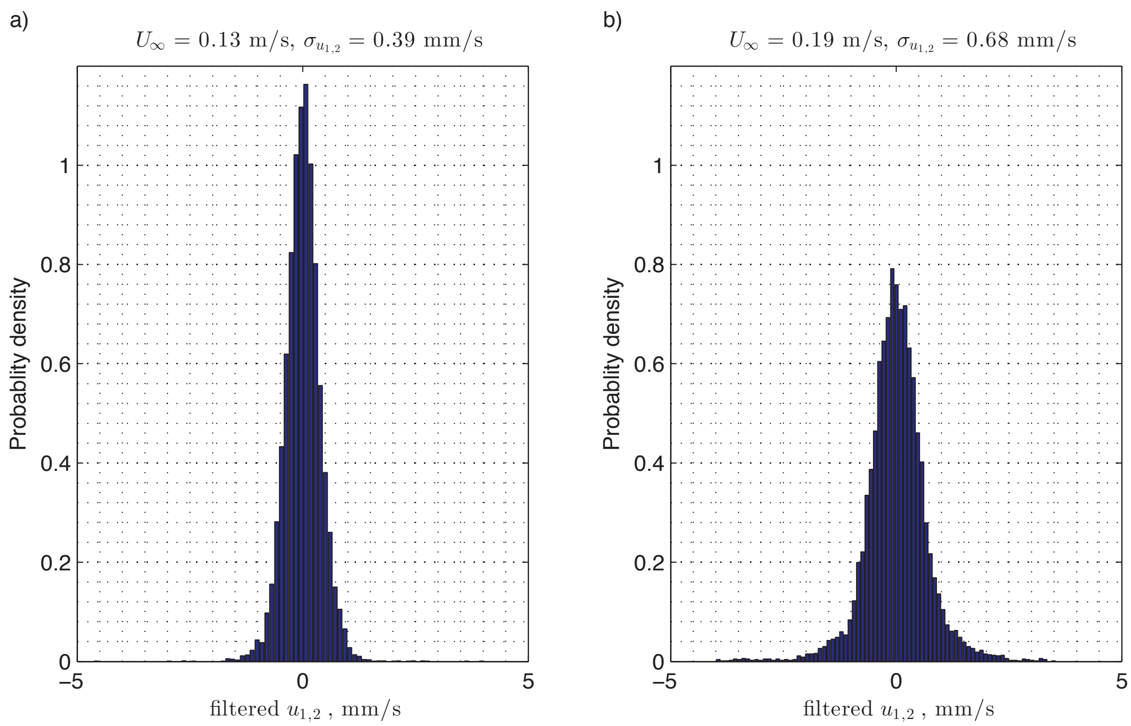

Figure 4.32: Empirical probability density functions of the time series of the projection of the relative velocity on the separation vector between the two points on the dumbbell target, $u_{1,2}$, filtered by eliminating the first two and the last two points in every trajectory. a) $U_\infty = 0.13$. b) $U_\infty = 0.19$ m/s.

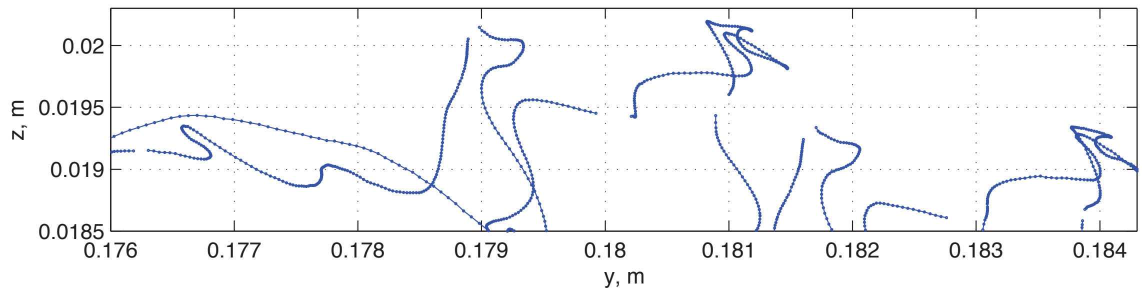

Figure 4.33: Side view of the trajectories of the particles on the dumbbell target, $U_\infty = 0.13$ m/s.

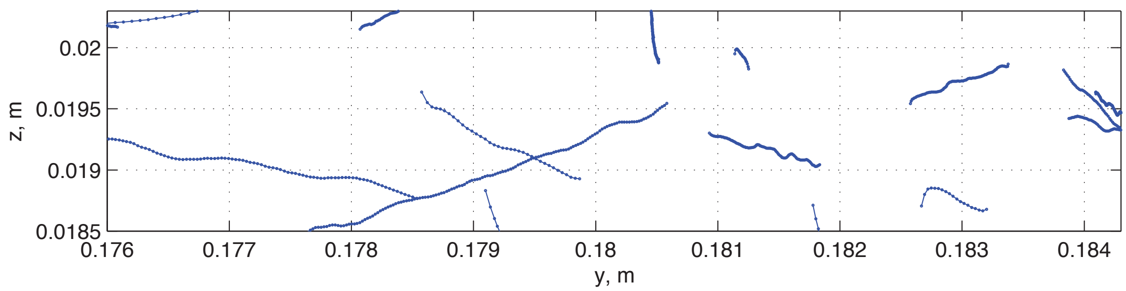

Figure 4.34: Side view of the trajectories of the particles, $U_\infty = 0.13$ m/s.

an example of such trajectories of the dumbbell target for the free-stream velocity of 0.13 m/s, and Figure 4.34 presents the particle trajectories from one of the actual experiments for comparison. The more complex the trajectory is, the more error is produced by the polynomial fit. It is hence argued that the values of velocity error of 0.52 and 0.76 mm/s are somewhat overestimated. It is also recommended that a better method for moving the dumbbell target around the investigation domain be used in the future. This, however, was not pursued in the present work given that the velocity errors were demonstrated to be small, less than 1 mm/s, even if they were overestimated.

The amount of data collected in tests with the dumbbell target does not allow one to draw conclusions about the spatial distribution of the velocity error. However, to check whether the tendencies generally correspond to the velocity error maps obtained in the previous chapter, a contour map of $(u_{1,2})_{rms}$ for the free-stream velocity of 0.13 m/s is presented in figure 4.35, where the rms values of $u_{1,2}$

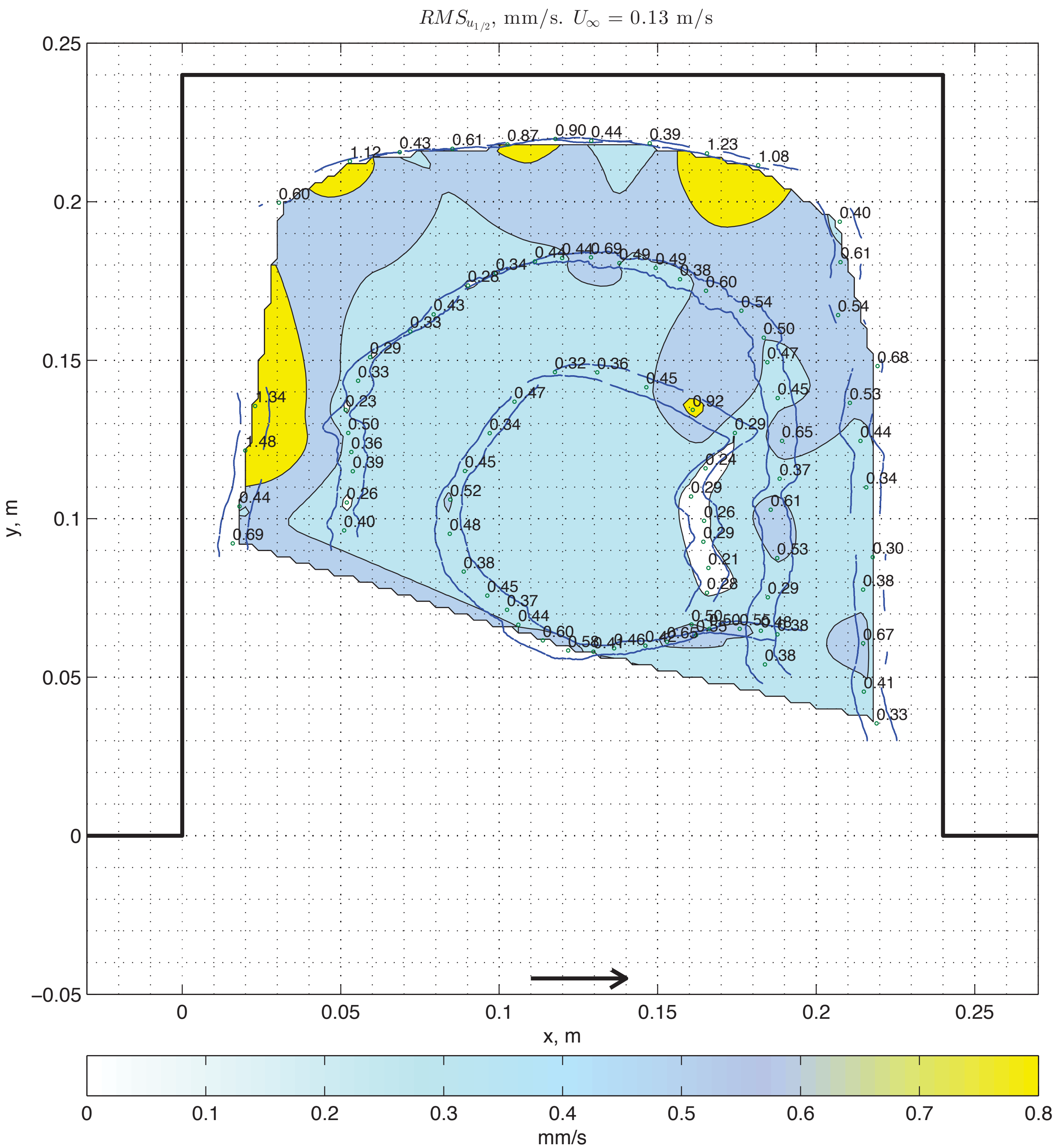

Figure 4.35: Top view of the trajectories of the particles on the dumbbell target, $U_\infty = 0.13$ m/s. The labels are the rms of the velocity of the dumbbell points towards or away from each other, $rms_{u_{1,2}}$. The statistic is calculated from trajectories segments approximately 30 to 199 time steps long.

are calculated for segments of trajectories from 30 to 199 time steps long. It is clear from this graph that the error is at its minimum in the centre of the embayment and grows towards the edges. The same tendency was observed in the previous test with the stationary pattern.

In conclusion, the two error analysis tests assessed velocity errors in two different ways. The test with the stationary flat pattern allowed one to construct velocity error contour maps and identify the most problematic regions. The areas within 5 mm of the walls, having the highest velocity errors, are eliminated from the final data. Also, thresholds were determined below which the velocities approached the noise level and therefore had to be filtered. The second test with the dumbbell-shaped target was designed to account for the vertical derivative of position error, $\frac{\partial}{\partial z}(\Delta \mathbf{r})$, the error produced by the velocity calculation using the centred-difference scheme, and the filtering procedure of the polynomial fit to the particle trajectories. The dumbbell target test gave velocity errors of 0.52 and 0.76 mm/s for the two free-stream velocities. These values are a little larger than the cutoff values of 0.4 and 0.6 mm/s obtained from the first test. However, it is argued that they are somewhat overestimated. It was shown that a significant part of the velocity error is produced by the polynomial fit filtering procedure at the ends of the trajectories. Eliminating only 2 points at the beginning and end of each trajectory (which are usually 199 points long) allows to reduce the errors to 0.39 and 0.68 mm/s, or by 10-25%, for $U_\infty = 0.13$ and 0.19 m/s, respectively. (This was not implemented in the present work.) Table 4.1 and 4.2 provide a summary of all the uncertainty values for all the position and velocity components. The absolute position determination error is about 1-1.2% of the total depth of the flow. However, the relative position error measured for the separation distance of 10 mm is 0.04%. This is why it was possible to obtain accurate velocity measurements even though absolute position error was not small. Thus, the error in total velocity determined from different tests and free-stream velocities varies from 0.2 to 0.4% of U_∞. It is hence fair to conclude as a result of this analysis that even for the most difficult case of a high free-stream velocity where gravity waves have the largest amplitudes, it is nevertheless possible to obtain accurate PTV measurements through the free surface.

Table 4.1: Summary of the position errors obtained from two uncertainty analysis experiments: i) the test with the stationary pattern of known geometry (Section 4.3.1), and ii) the test using a dumbbell-shaped target (Section 4.3.2).

Quantity	U_∞, m/s	**Position error, mm**			
		Stationary pattern test			Dumbbell target test
		Systematic	Random	Total	Total (relative pos. er.)
x	0.13	0.11	0.01	0.12	
	0.19	0.07	0.03	0.10	
y	0.13	0.06	0.01	0.07	
	0.19	0.09	0.03	0.12	
z	0.13	0.23	0.07	0.30	
	0.19	0.16	0.18	0.34	
$\lvert\vec{\mathbf{r}}\rvert$	0.13	0.26	0.07	**0.32** (1.1% of H)	**0.011** (0.04% of H)
	0.19	0.20	0.18	**0.38** (1.2% of H)	**0.012** (0.04% of H)

Table 4.2: Summary of the velocity errors obtained from two uncertainty analysis experiments: i) the test with the stationary pattern of known geometry (Section 4.3.1), and ii) the test using a dumbbell-shaped target (Section 4.3.2).

Quantity	U_∞, m/s	**Velocity error, mm/s**			
		Stationary pattern test			Dumbbell target test
		Systematic	Random	Total	Total
u	0.13	0.18	0.01	0.19	
	0.19	0.12	0.03	0.15	
v	0.13	0.10	0.005	0.10	
	0.19	0.08	0.02	0.10	
w	0.13	0.32	0.03	0.35	
	0.19	0.17	0.09	0.26	
$\lvert\vec{\mathbf{u}}\rvert$	0.13	0.38	0.03	**0.41** (0.3% of U_∞)	**0.52** (0.4% of U_∞)
	0.19	0.23	0.10	**0.33** (0.2% of U_∞)	**0.76** (0.4% of U_∞)

4.3.3 Velocity-derivative errors

In order to assess the quality of the derivative measurements by the 3D-PTV system the continuity principle is employed. The continuity equation for an incompressible fluid states that the total velocity divergence at every point in the flow is identically zero:

$$\nabla \cdot \mathbf{u} = \frac{\partial u}{\partial x} + \frac{\partial v}{\partial y} + \frac{\partial w}{\partial z} = 0 \tag{4.16}$$

Thus, velocity divergence was calculated for every point in the domain and its deviation from zero was used as a measure of the magnitude of the error. The relative error was assessed as the ratio between the total divergence and the vertical derivative point by point. Taking the rms values of the time series of this value results in the overall estimation of the error magnitude (Figure 4.36). The derivative uncertainty appears very localized; it is negligible almost everywhere except at a few points where it is as high as 10%. These "hot spots" may be either related to a random event of insufficient particle seeding density in a particular region of the flow or to a zero vertical velocity derivative at this point. However, the probability density distributions of the relative derivative error in the whole domain show very low rms values: 0.3, 0.7 and 1.7% for the three free-stream velocity cases $U_\infty = 0.13, 0.17$, and 0.19 m/s, respectively. The derivative error (as well as the velocity error described in the previous section) is higher for the higher free-stream velocities due to stronger surface perturbations produced by gravity waves, which are more pronounced at higher U_∞. Nevertheless, it is fair to conclude that the quality of the derivative measurement for all flow cases is good and the data obtained is reliable.

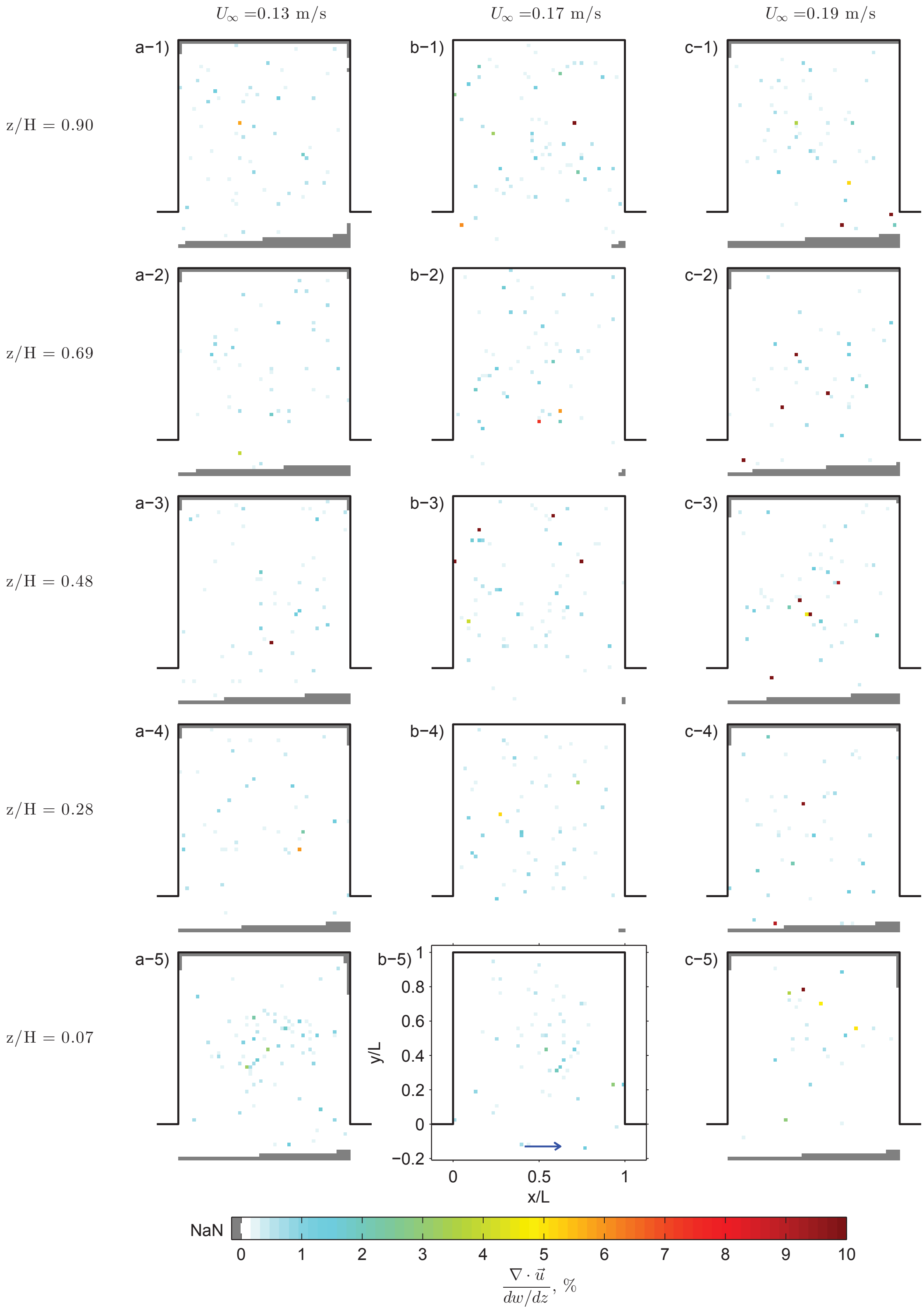

Figure 4.36: Colour plots of the rms values of the relative velocity derivative error, $\frac{\nabla \cdot \mathbf{u}}{\partial w/\partial z}$, at different elevations above the bed (z/H). The three columns correspond to cases of different free-stream velocities. a) $U_\infty = 0.13$. b) $U_\infty = 0.17$. c) $U_\infty = 0.19$ m/s.

CHAPTER 5
Results and discussion

This chapter presents the results of 3D-PTV measurements and their analysis. First, we introduce the general flow pattern by presenting some of its basic statistics (Section 5.1). The dependence on the free-stream velocity and some normalization issues are briefly discussed. Second, attention is focused on the three-dimensional features of the flow (Section 5.2). The geometry of the exchange through the interface between the embayment and the main flow is shown to be a function of depth. A "tea-cup" secondary circulation generated by the bottom boundary layer and the main gyre is described. Production of Görtler-like vortices at the boundary layer at the embayment side walls is also shown. Two- and three-dimensional characteristics of the flow are discussed based on spectral analysis. Gravitational instability of the embayment flow is addressed in Section 5.3 along with the resonant mechanism of gravity-wave amplification. The exchange coefficient between the main channel and the embayment is calculated and discussed in Section 5.4.

5.1 General flow pattern and free-stream velocity dependence

The general flow field observed in the current experiments corresponds well to previous research on shallow embayments (Babarutsi & Ganoulis, 1989; Altai & Chu, 1997; Kimura & Hosoda, 1997; Uijttewaal *et al.*, 2001; Weitbrecht *et al.*, 2008; Constantinescu *et al.*, 2009; Tuna *et al.*, 2013) as will be shown by examining the basic statistics of the flow. The time-averaged horizontal velocity and vorticity fields illustrate the geometry and intensity of the large-scale circulation in the embayment. Instantaneous vorticity fields show Kelvin-Helmholtz vortical structures in the shear zone. Dependence on the free-stream velocity will also be discussed.

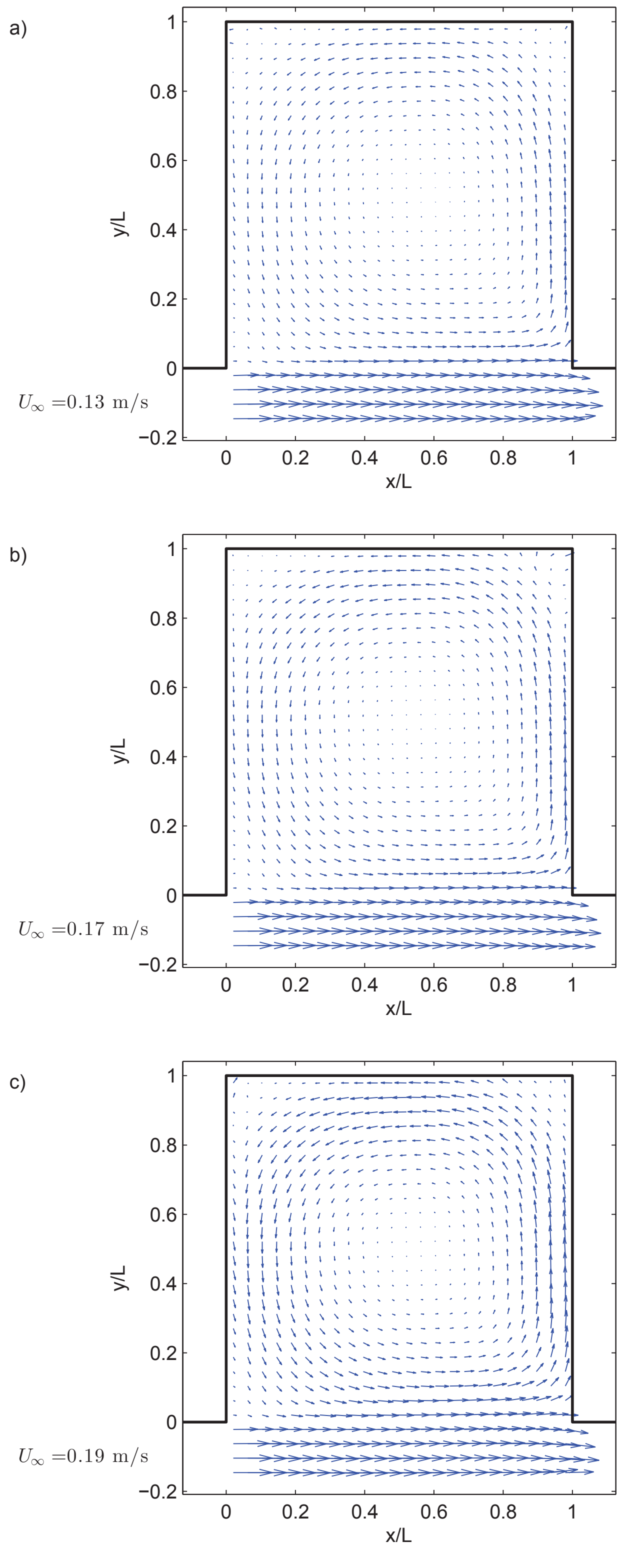

Figure 5.1: Top view of the time-averaged horizontal velocity vectors averaged in depth with their magnitude normalized by the free-stream velocity, $\frac{\sqrt{u^2+v^2}}{U_\infty}$. a) U_∞ = 0.13. b) U_∞ = 0.17. c) U_∞ = 0.19 m/s. Grid density is reduced by a factor of two for visualization purposes.

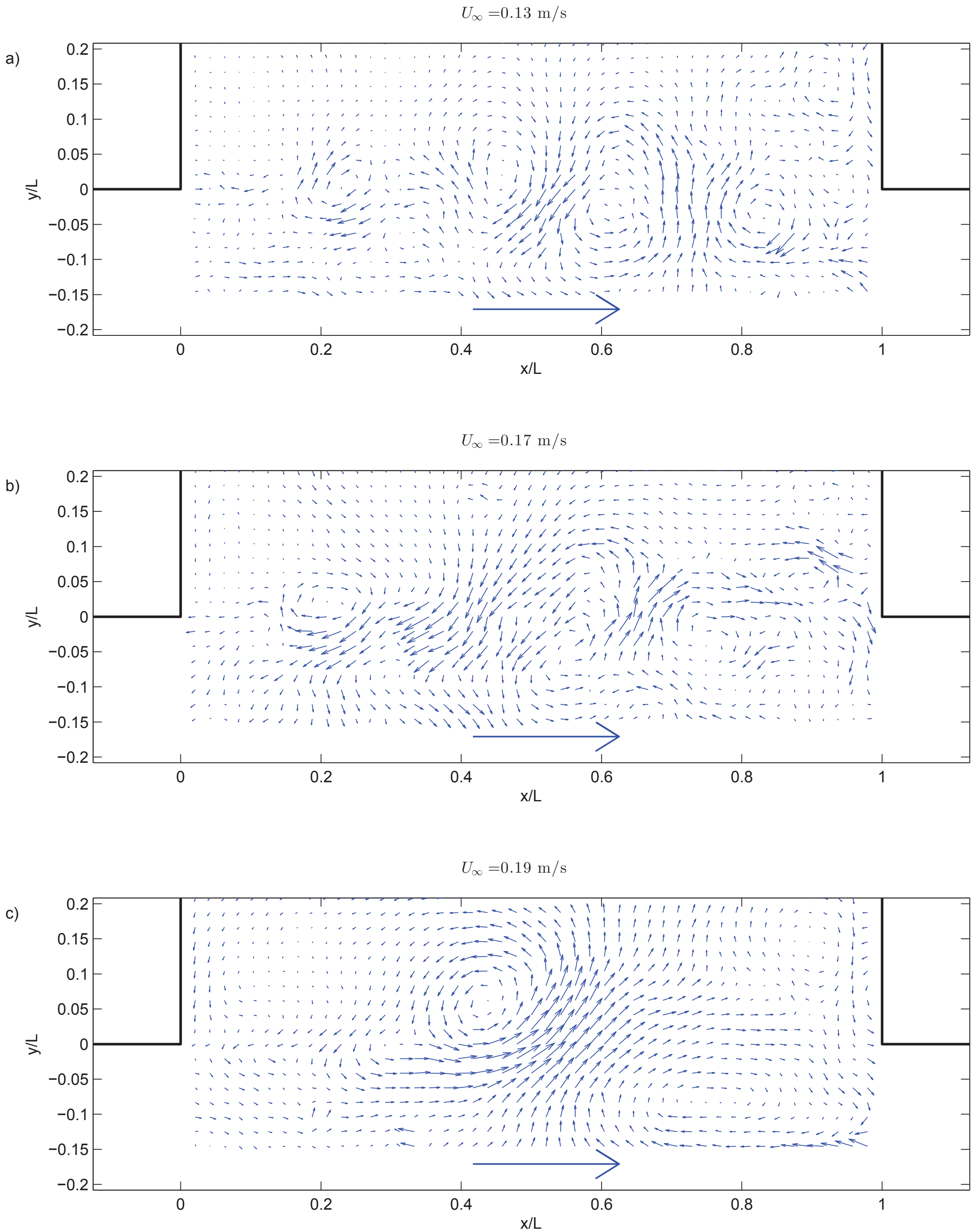

Figure 5.2: Top view of the depth-averaged instantaneous horizontal velocity fluctuation vectors in the embayment's shear zone, with their magnitude equal to $\sqrt{(u-\overline{u})^2+(v-\overline{v})^2}$. a) $U_\infty = 0.13$. b) $U_\infty = 0.17$. c) $U_\infty = 0.19$ m/s.

The general flow pattern in the embayment is a large gyre with a stagnation region or "dead zone" in its centre (see Section 2.1). This is shown in the series of normalized horizontal velocity vector plots in Figure 5.1. (Note that hereafter all figures with three panels present three cases of different free-stream velocities, U_∞ = 0.13, 0.17, 0.19 m/s.) The interface between the main flow and the embayment is occupied by the shear region with high transverse velocity gradients. In this region Kelvin-Helmholtz instability dominates the flow, resulting in the generation of vortical structures with a vertical axis of rotation that are shed from the upstream corner of the embayment, as seen in Figure 5.2, which presents the instantaneous depth-averaged velocity fluctuations in the mixing layer. In the corners of the cavity and at the leading (upstream) edge adjacent to the shear zone, there are also regions of low velocity, which can sometimes form smaller recirculating zones, as seen for example in Tuna *et al.* (2013).

Vertical vorticity plots (Figure 5.3) confirm the same flow structure as was presented in Figures 5.1 and 5.2: a high positive (counterclockwise) vorticity in the shear zone generated by Kelvin-Helmholtz instability and a less intense, but persistent, large-scale circulation in the embayment. In the corners of the bay and near the leading edge regions of negative vorticity indicate smaller recirculating zones of opposite sign. Surprisingly, the shear region appears to be more intense in the lower free-stream velocity flow. This is arguably the result of gravity waves that are very weak for $U_\infty = 0.13$ m/s and are quite pronounced for $U_\infty = 0.19$ m/s. Gravity waves tend to have a stabilizing effect on shear instability, resulting in reduced vorticity production (Balmforth, 1999; Kolyshkin & Ghidaoui, 2002).

It is common in the literature to consider the processes in the embayment as linearly dependent on the free-stream velocity (see chapter 1.1 for details). For example, Booij (1989) first suggested that the exchange process between a square harbour and the main channel is governed by a single time constant of a first-order system. Tuna *et al.* (2013) used a free-stream normalization in order to

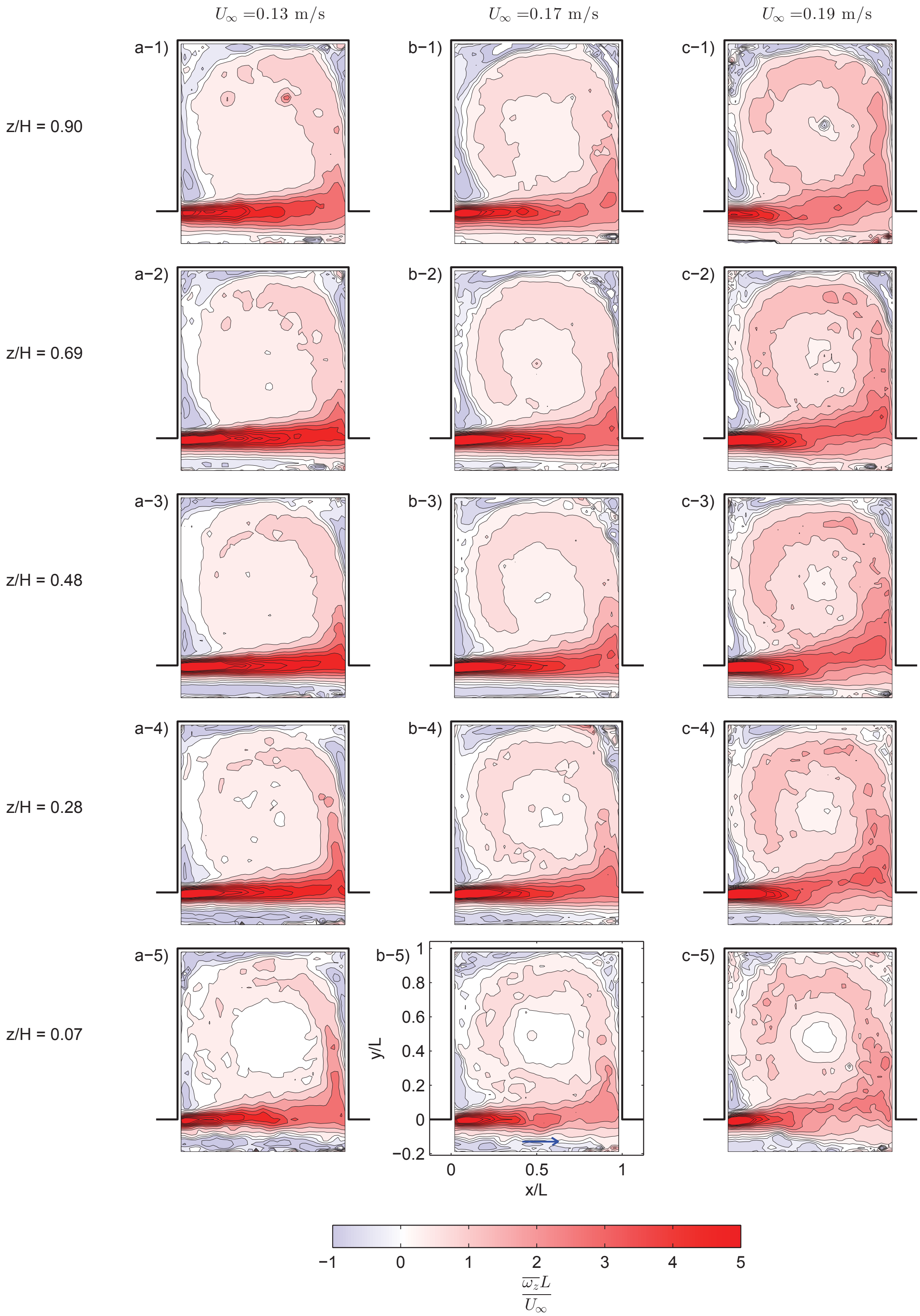

Figure 5.3: Contours of time-averaged vertical vorticity $\frac{\overline{\omega_z} L}{U_\infty}$ at different elevations above the bed (z/H). The three columns correspond to cases of different free-stream velocities. a) $U_\infty = 0.13$. b) $U_\infty = 0.17$. c) $U_\infty = 0.19$ m/s.

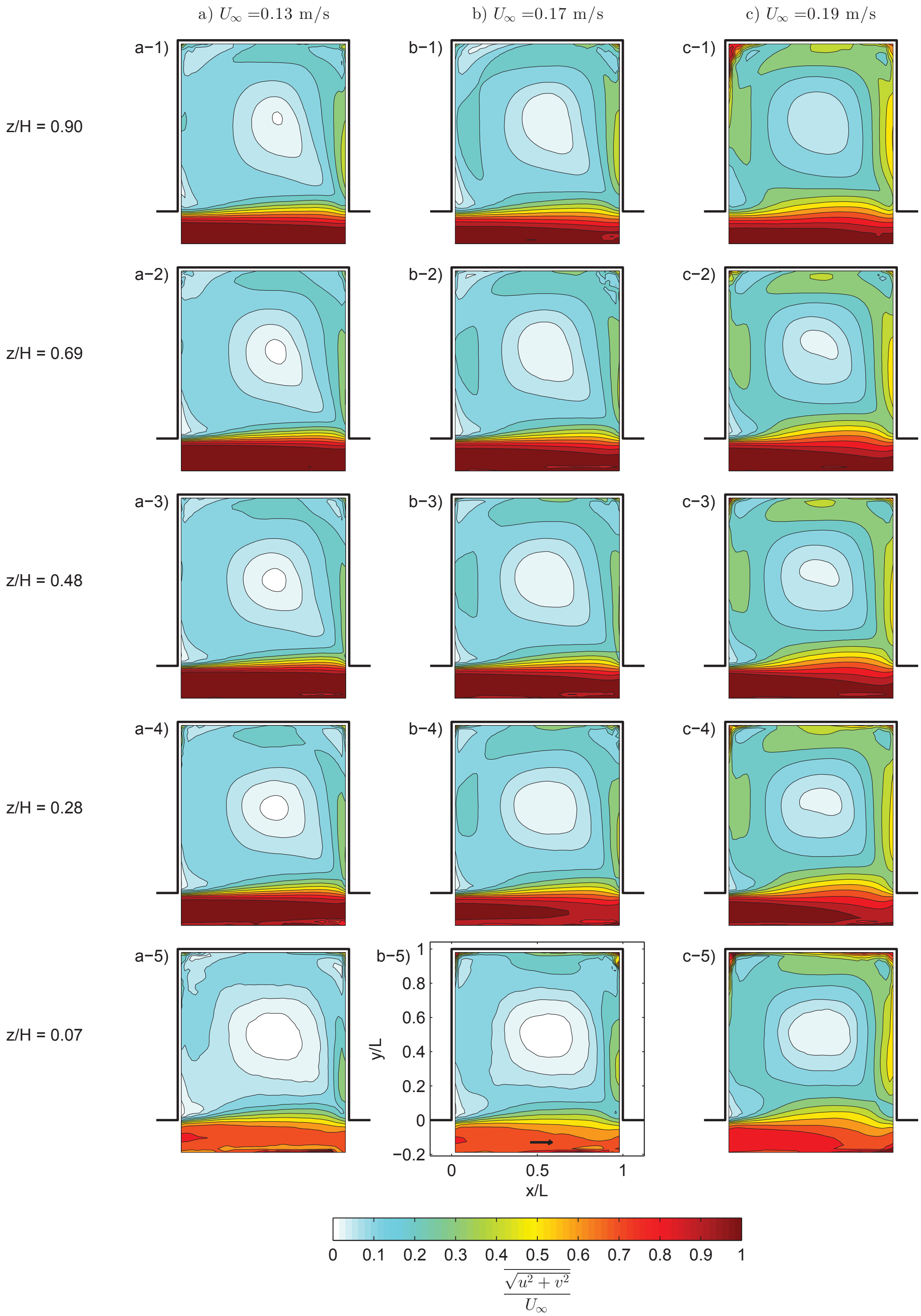

Figure 5.4: Contours of time-averaged horizontal speed $\frac{\overline{\sqrt{u^2+v^2}}}{U_\infty}$ at different elevations above the bed (z/H). The three columns correspond to cases of different free-stream velocities: a) $U_\infty = 0.13$; b) $U_\infty = 0.17$; c) $U_\infty = 0.19$ m/s.

remove the dependence of the transverse velocities and turbulence characteristics on the flow discharge. Indeed, the general flow pattern and its intensity is similar when normalized by U_∞ at all three increasing free-stream velocities (Figure 5.1). However, at higher free-stream velocities the high-momentum fluid, deflected by the end wall of the embayment, propagates further into the embayment as seen in the normalized velocity contour plots of Figure 5.4. This indicates that the strength of the gyre is not linearly dependent on the free-stream velocity. (Note that Figure 5.4 is another style of data representation that will be used throughout this chapter: 5 rows correspond to different elevations above the bed, z/H, and three columns a, b, and c correspond to three cases of different free-stream velocities.) Figure 5.3 is evidently showing the same characteristic. The (dark pink) contour line of higher vertical vorticity is penetrating further into the embayment for the higher free-stream velocity, even though the vorticity modulus presented on the plots is normalized by U_∞. This means, that normalization with free-stream velocity should be used with care, noting that not every flow characteristic is linearly dependent on it. It will be shown below (in Section 5.3) that even the exchange process shown to be a linear function of U_∞ by many researchers (Booij, 1989; Altai & Chu, 1997; Uijttewaal *et al.*, 2001) may drastically change in the presence of gravity waves and therefore is not always a linear function of U_∞.

5.2 Three-dimensional flow structures

One of the main objectives of this work is to investigate whether a two-dimensional model is a sufficient approximation of a shallow embayment flow, and if not, whether it can be corrected to account for the feedback of the 3D effects on the 2D fields (see Section 2.1 for details). To this end, this section is devoted to the analysis of the flow structures that deviate from the depth-averaged field.

5.2.1 The exchange velocity at the interface

As first observed by Gaskin *et al.* (2002) and Mizumura *et al.* (2003) particles tend to leave the embayment close to the surface and to enter it along the bed. Furthermore, McCoy *et al.* (2008) presented a detailed picture of the exchange flow for the case of a shallow embayment with a sudden increase in depth to the main channel. They showed that, on average, the fluid leaves the embayment via the top layer in the upstream half of the interface, and enters it mid-depth (almost over the whole length of the embayment). McCoy *et al.* (2008) attributed the 3D-effects in this flow to this geometry (a step at the channel bed), stating that in the regular configuration with a flat bottom, the flow is generally expected to have a shear zone dominated by large-scale quasi-two-dimensional coherent structures. In the present experiments there is no difference in the bed elevation between the main channel and the embayment and observations show a three-dimensional exchange flow through the shear layer similar to the one observed by McCoy *et al.* (2008).

As seen in the transverse velocity plots in Figure 5.5 the exchange flow between the embayment and the main channel is highly dependent on depth. The flow leaves the embayment (blue) at the surface and it enters it along the bottom (red). The flow leaving the embayment is confined in the vertical to be at $z/H < 0.28$, while the flow entering the embayment occurs between $z/H = 0.48$ and 0.9. The switch of the direction does not appear at the mid-depth. Instead, it happens around z/H=0.69. Another observation from figure 5.5 is that the inflow into the embayment is more localized in the x-direction than the outflow. For example, at

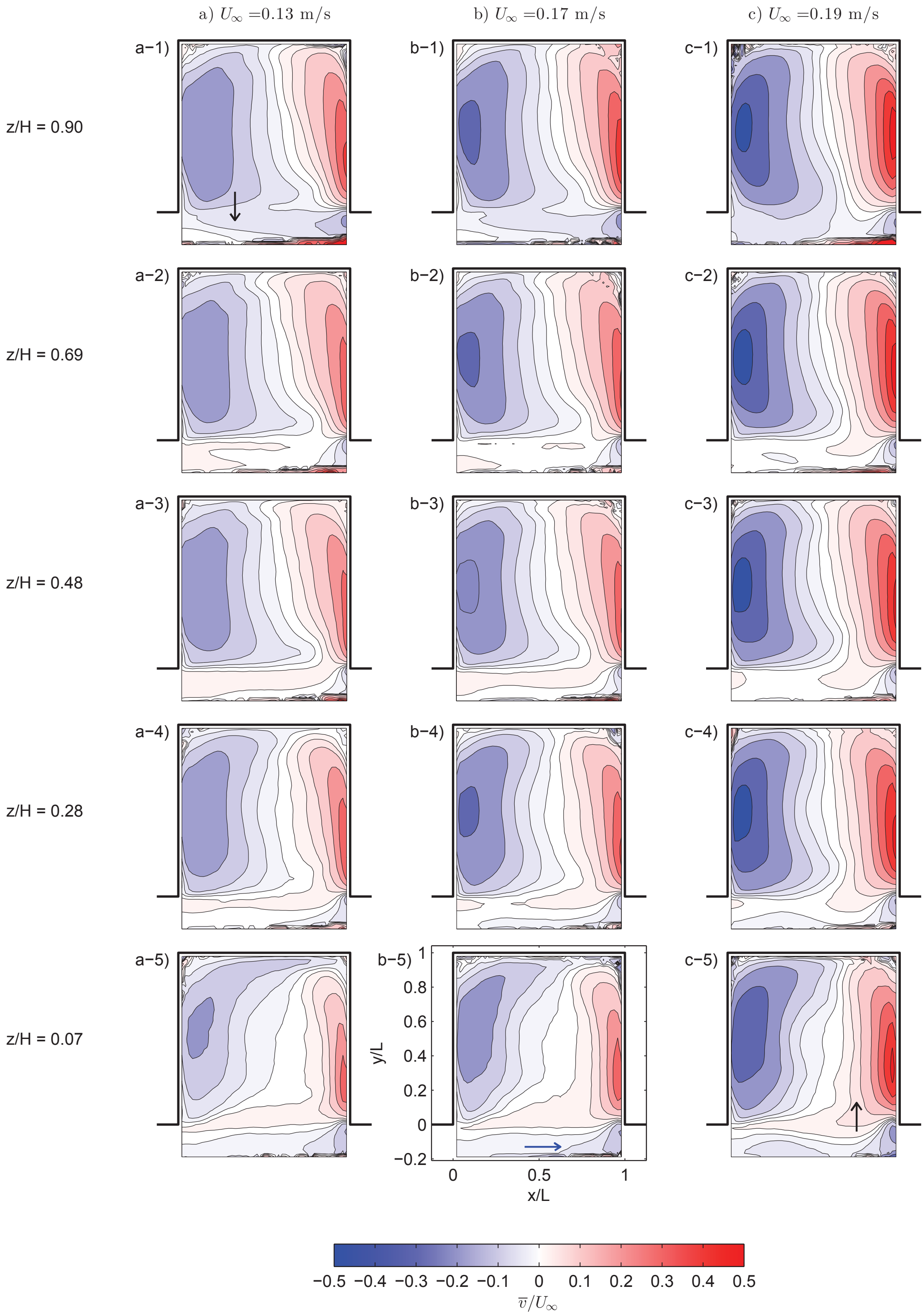

Figure 5.5: Contours of time-averaged transverse velocity $\frac{\overline{v}}{U_\infty}$ at different elevations above the bed (z/H). The three columns correspond to cases of different free-stream velocities. a) $U_\infty = 0.13$. b) $U_\infty = 0.17$. c) $U_\infty = 0.19$ m/s.

z/H=0.48 it enters the embayment through a very small opening at the downstream end of the interface and this opening appears smaller for a lower free-stream velocity $(a-3)$ and more extended in the x-direction for the higher free-stream velocity $(c-3)$. This difference may be attributed to either the effect of gravity waves (see Section 5.3), that are more prominent for higher free-stream velocities, or to a change in the streamwise flow structures that appear in the shear zone (see the left-hand side of the Figure 5.16).

The next three Figures 5.6, 5.7, 5.8 present vertical slices of transverse velocity at three positions y/L = 0.042, 0.021, and 0, respectively. At y/L = 0.042 or 10 mm into the embayment from the interface (Figure 5.6), one can observe that the direction of flow changes from the upstream end of the embayment to the downstream end, rather than with depth. However, the inflow along the bottom and outflow along the surface is still noticeable. As mentioned in the previous paragraph, the extent of the area through which the flow is entering the embayment appears thinner and more intense for the lower free-stream velocity than for the higher ones. Another interesting feature is the separation of the outflow velocity into two parts; the blue region has two peaks, one near the surface and another closer to the bottom. The bottom outflow eventually turns and continues to recirculate in the embayment, whereas the top one leaves the bay as seen in Figures 5.7 and 5.8. Closer to the interface at y/L = 0.021 or 5 mm into the embayment (Figure 5.7) the distribution of the transverse velocity magnitude becomes more elongated in the x-direction. At y/L = 0 (Figure 5.8) the outflow is mainly localized at the surface. One also can observe a strong outflow near the downstream wall of the embayment. However, it disappears at y/L=0.021 suggesting that it is not actually coming from inside the bay. From visual observation it appears that the mixing layer is deflected a little bit towards the embayment and at the downstream end its centreline ends at the the wall, not at the corner of the embayment. This creates a small region near the downstream corner where the flow first enters the embayment

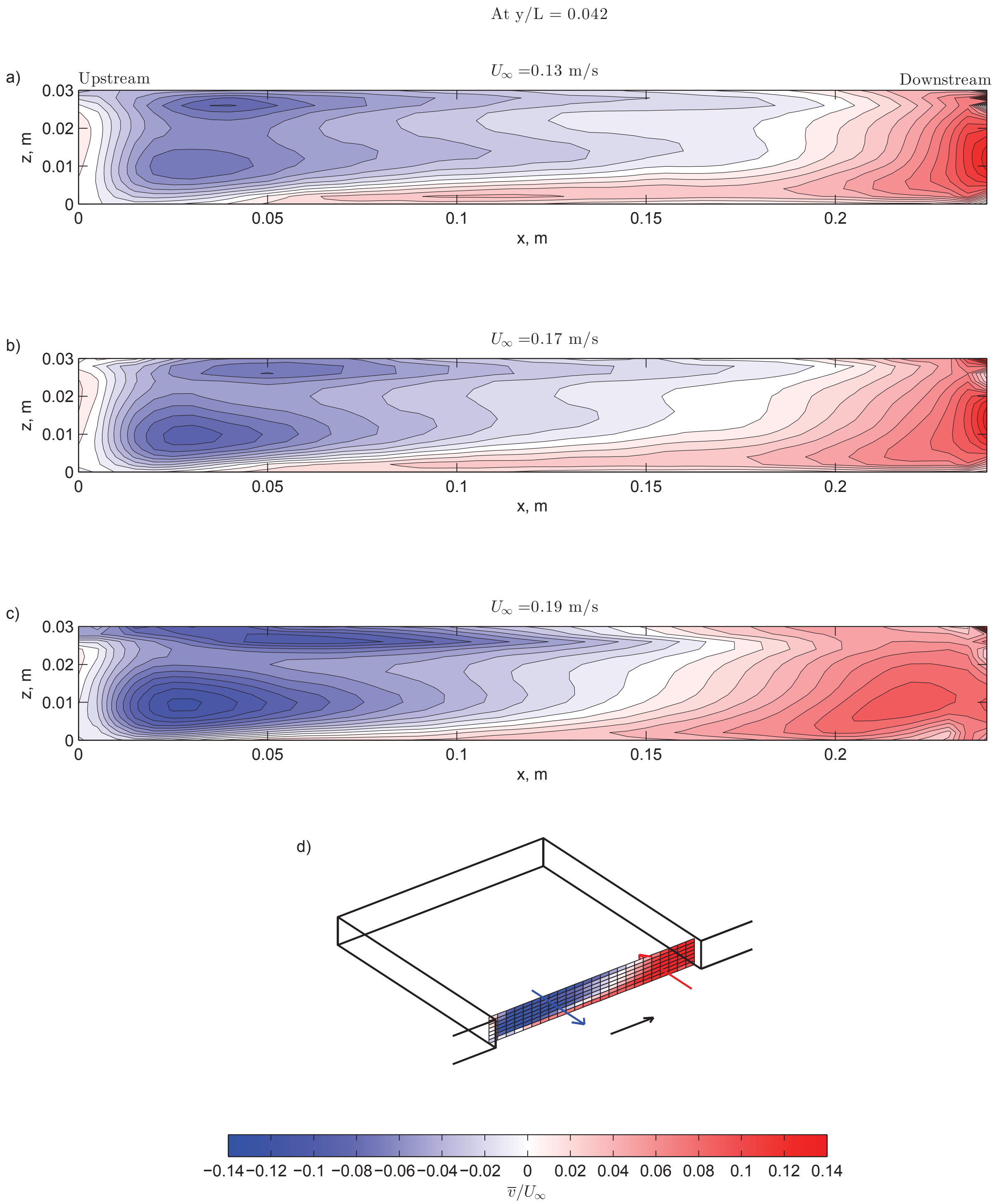

Figure 5.6: Contours of time-averaged transverse velocity $\frac{\overline{v}}{U_\infty}$ at a vertical plane at y/L=0.042 (or 10 mm into the embayment). a) U_∞ = 0.13; b) U_∞ = 0.17; c) U_∞ = 0.19 m/s. d) Location of the vertical plane.

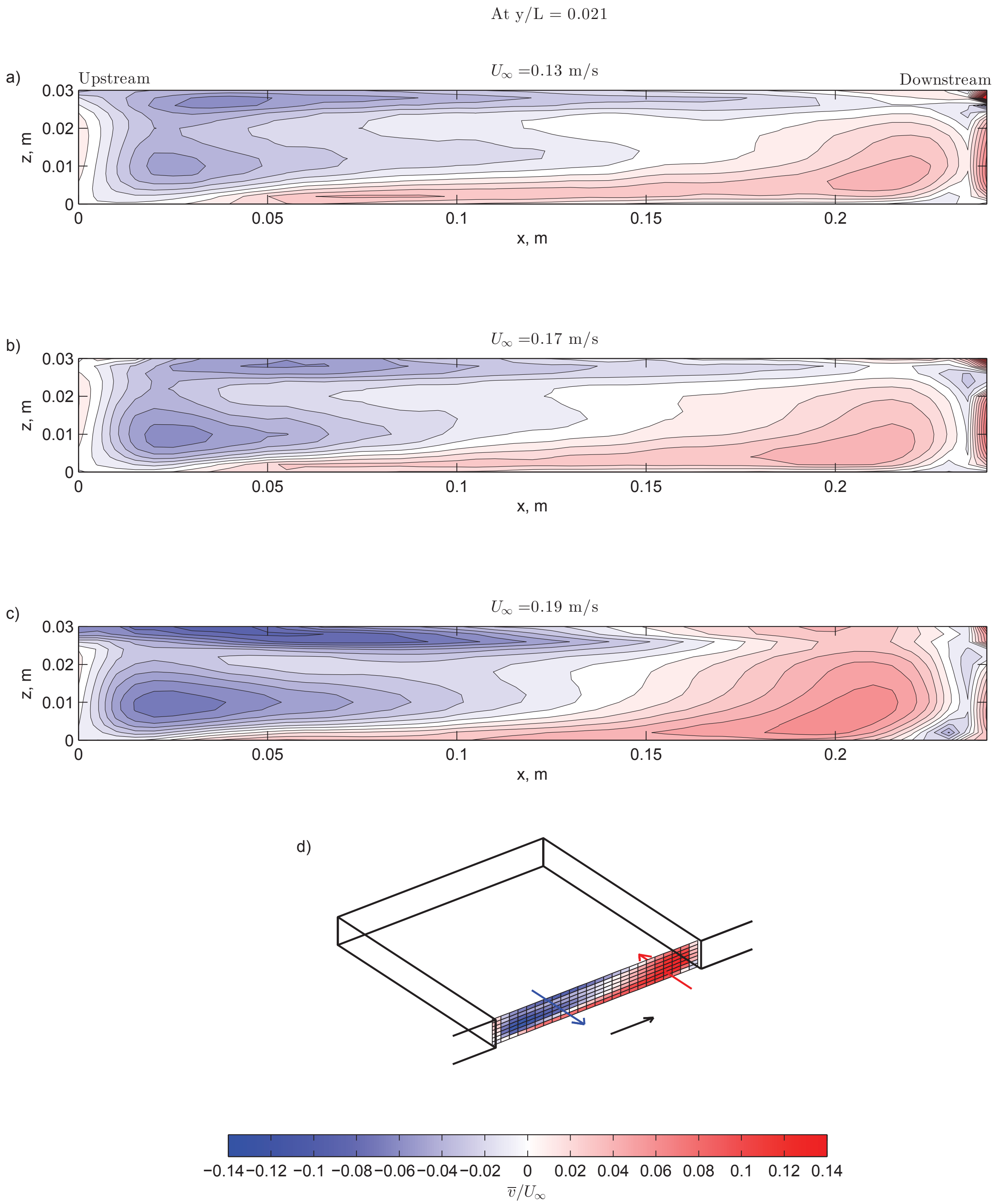

Figure 5.7: Contours of time-averaged transverse velocity $\frac{\overline{v}}{U_\infty}$ at a vertical plane at y/L=0.021 (or 5 mm into the embayment). a) U_∞ = 0.13; b) U_∞ = 0.17; c) U_∞ = 0.19 m/s. d) Location of the vertical plane.

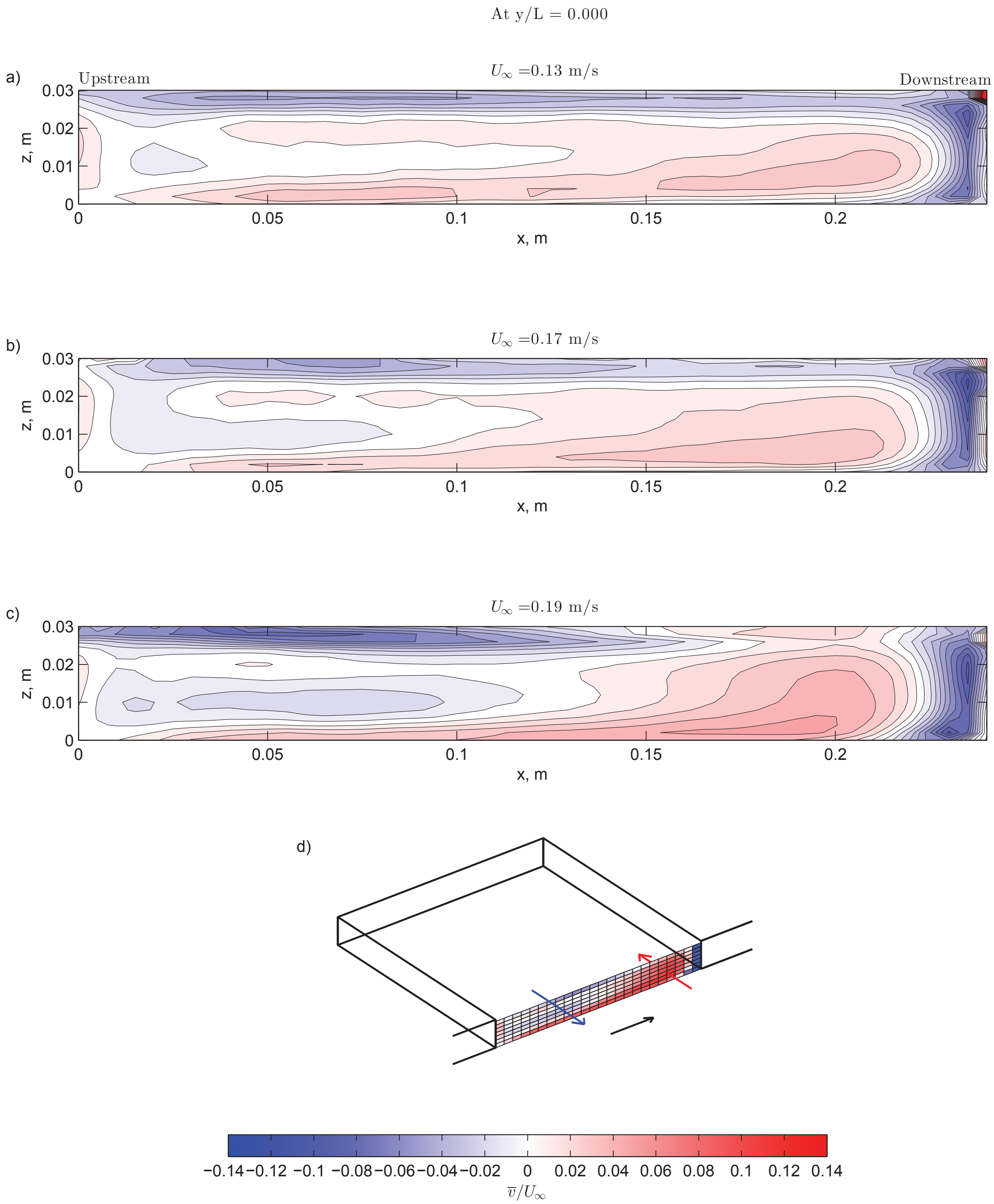

Figure 5.8: Contours of time-averaged transverse velocity $\frac{\overline{v}}{U_\infty}$ at a vertical plane at y/L=0.0 (at the interface between the main flow and the embayment). a) U_∞ = 0.13; b) U_∞ = 0.17; c) U_∞ = 0.19 m/s. d) Location of the vertical plane.

region and then gets ejected (Figure 5.9) creating an impression of an outflow from the embayment.

In summary, the observations show that the exchange between the embayment and the main channel is highly three-dimensional even in an embayment with a uniform bed. The flow is penetrates the bay along the bed closer to the downstream end of the interface. As it enters, it rapidly occupies the whole depth. It then circulates around in the large-scale gyre, rising closer to the surface. The flow then separates and the top layer leaves the embayment, whereas the rest continues to circulate. The area through which the water is leaving the embayment is confined to less than 20% of its depth. It leaves predominantly along the surface, whereas the inflow is mostly coming along the bed but is more concentrated near the downstream end of the interface.

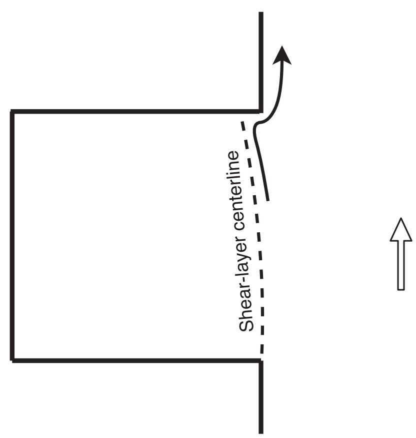

Figure 5.9: Schematic of the origin of the strong outflow region at the doswnstream wall of the embayment.

5.2.2 Secondary circulation in the main gyre

The first evidence of three-dimensional secondary circulation within the embayment was presented by Gaskin *et al.* (2002). As was described in Section 2.4, it originates in the deceleration of the main gyre by bottom friction, where the centrifugal force cannot balance the pressure gradient, resulting in radial inflow towards the centre of the embayment (Schlichting, 1968). It was observed that in a shallow embayment particles are sometimes drawn into the gyre core along the bottom and settle. They were also observed to be sporadically picked up from the bed (Jamieson & Gaskin, 2007*b*). However, if this process has a significant effect on time-averaged statistics is still unclear. Also, the exact shape and strength of this circulation is not well defined.

To learn more about this phenomenon streamlines were plotted from the time-averaged velocity field (Figure 5.10). They were calculated as lines tangent to the horizontal time-averaged velocity vectors starting at arbitrary points within the embayment organized in a regular grid (indicated by black dots). The three-dimensional secondary circulation can be clearly observed in these plots (Figure 5.10). Everywhere above $z/H = 0.48$ the streamlines spiral outwards. In other words, the flow rotates in a counterclockwise fashion with increasing radius of rotation. The radial inflow changes sign at its inflection point, which occurs between $z/H = 0.1$ and 0.4, where the streamlines are closed and the flow does not change radius of curvature (Figure 5.10 row 4). An intense counterclockwise inward spiralling can be seen at $z/H = 0.07$ (Figure 5.10 row 5), where the streamlines originating at the walls spiral into the core region after only two full turns around the embayment. In order to show the three-dimensional effect more clearly we will now subtract the depth average from the flow field. Figure 5.11 shows the streamlines of the flow that deviates from the depth average. The inflow near the bottom appears intense and uniform (Figure 5.11 bottom row). The outflow at $z/H > 0.48$ is less well defined. Sometimes the maximum divergence appears to be a point (for example,

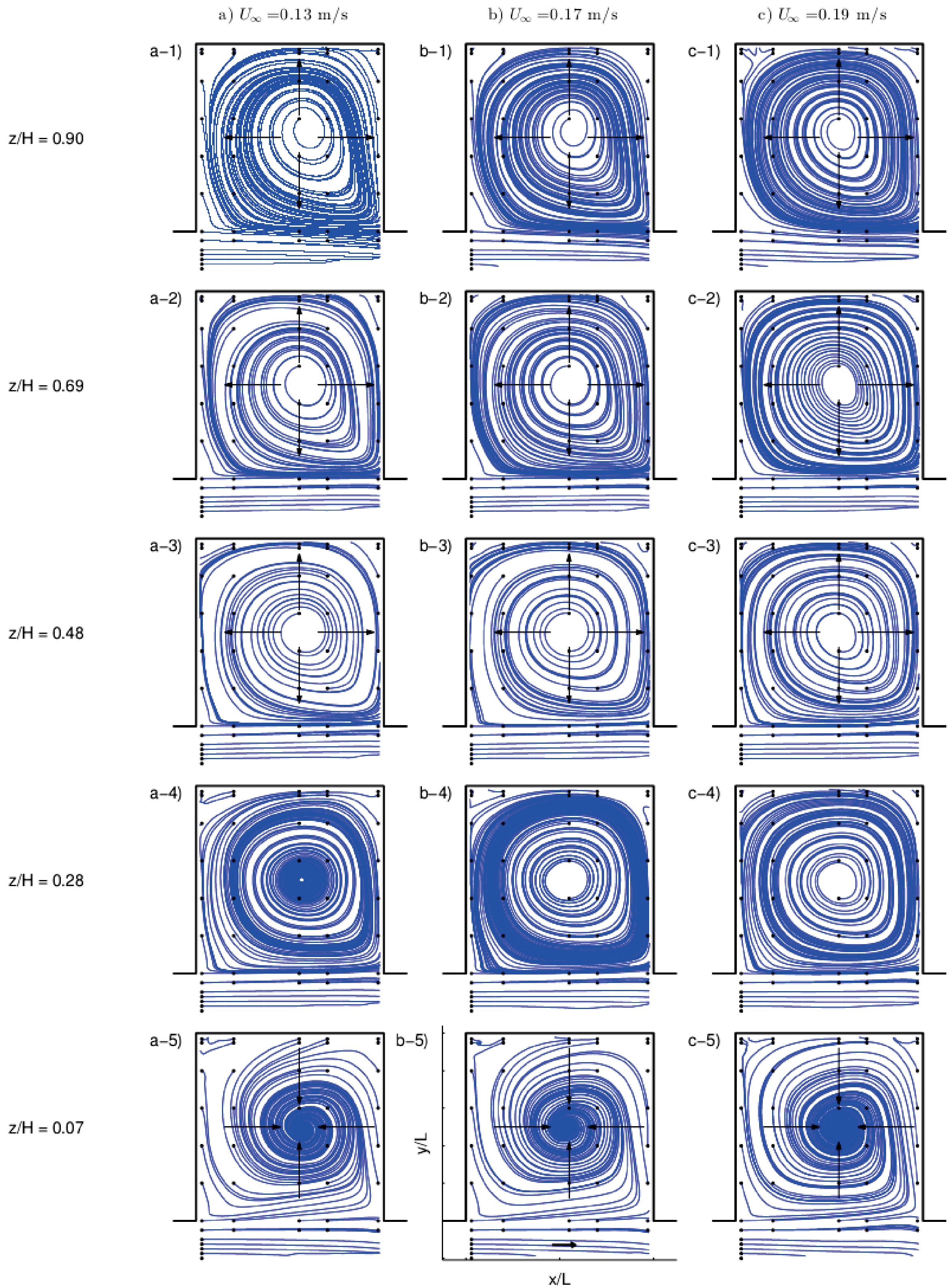

Figure 5.10: Streamlines of the time-averaged horizontal velocity field at different elevations above the bed (z/H). The starting locations of the streamlines are indicated with black dots. The three columns correspond to cases of different free-stream velocities. a) $U_\infty = 0.13$. b) $U_\infty = 0.17$. c) $U_\infty = 0.19$ m/s.

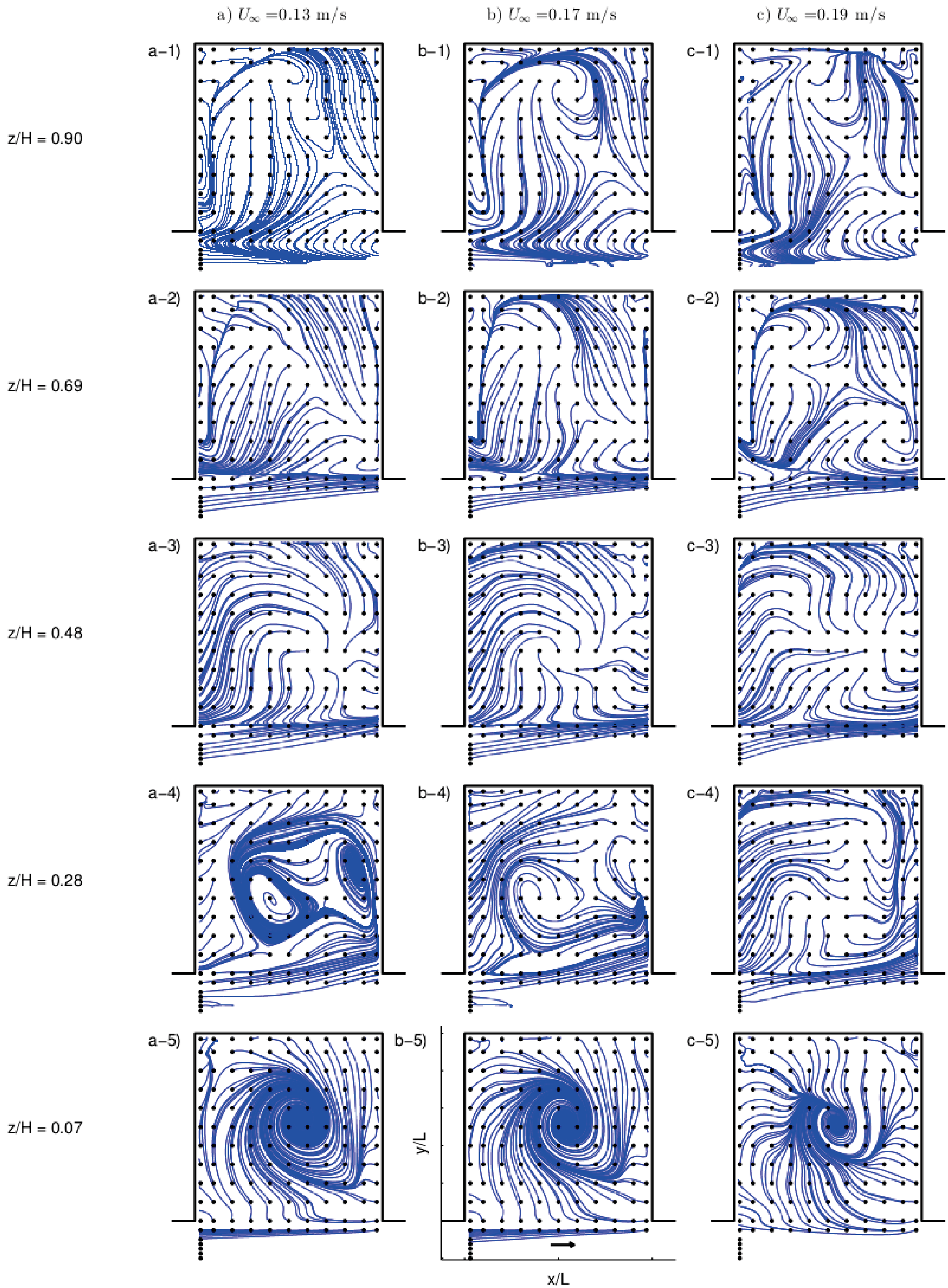

Figure 5.11: Time-averaged streamlines of the 3D mode of the velocity field (the depth-averaged component is subtracted from every point) at different elevations above the bed (z/H). The starting locations of the streamlines are indicated with black dots. The three columns correspond to cases of different free-stream velocities: a) $U_\infty = 0.13$; b) $U_\infty = 0.17$; c) $U_\infty = 0.19$ m/s.

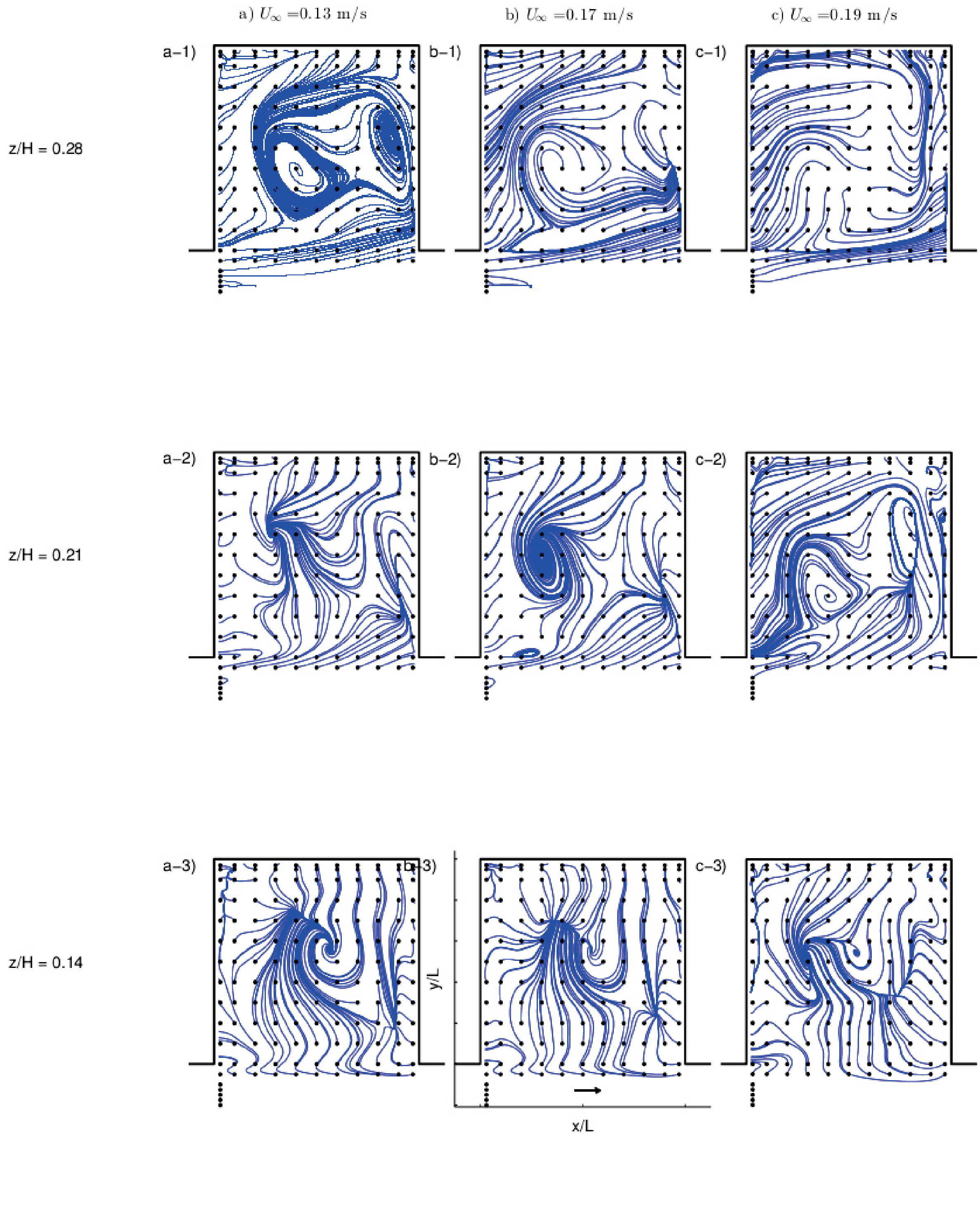

Figure 5.12: Time-averaged streamlines of the 3D mode of the velocity field (the depth-averaged component is subtracted from every point) at different elevations above the bed (z/H) around the inflection depth of the radial velocity. The starting locations of the streamlines are indicated with black dots. The three columns correspond to cases of different free-stream velocities: a) $U_\infty = 0.13$; b) $U_\infty = 0.17$; c) $U_\infty = 0.19$ m/s.

panel a-3), and sometimes it looks like a line (panel a-2 or c-1). At the depth of the inflection of the radial velocity, the streamlines of the secondary circulation are characterized by a dipole-like structure (Figure 5.11 a-4, b-4 or Figure 5.12 a-1, b-2, c-2 showing more plots around the inflection point). The origin of this structure still remains unclear.

The inflection point of the radial velocity appears around z/H = 0.21 to 0.28 (Figure 5.12). An interesting question is "what determines this depth?". Since the radial inflow is caused by the deceleration of the vortex near the bottom boundary, it is logical to assume that the inflection depth is associated with the bottom boundary-layer thickness. Figure 5.13 shows the vertical profiles of the intensity of the main gyre rotation at 3 positions indicated at panel d. Depending on the point, either $\pm u$ or $\pm v$ velocity was chosen to represent the tangential velocity of the gyre. From these plots it is clear there is a boundary layer developing along the bed of the embayment. It's thickness varies for U_∞=0.13, 0.17, and 0.19 from z/H = 0.27 to 0.22, and 0.17, respectively. Lower free-stream velocities have thicker boundary layer (Blasius, 1913). The inflection point for the lower free-stream also appears higher than for the higher free-stream velocities (Figure 5.12). From the summary in Table 5.1 it is clear the inflection point of the radial velocity indeed appears approximately at the depth of the boundary layer thickness.

Table 5.1: Approximate values of the depth of the inflection point of the radial velocity compared to the bottom boundary-layer thickness.

U_∞, m/s	Boundary-layer thickness	Inflection depth
0.13	0.27 H	0.28 H
0.17	0.22 H	0.21-0.26 H
0.19	0.17 H	0.21 H

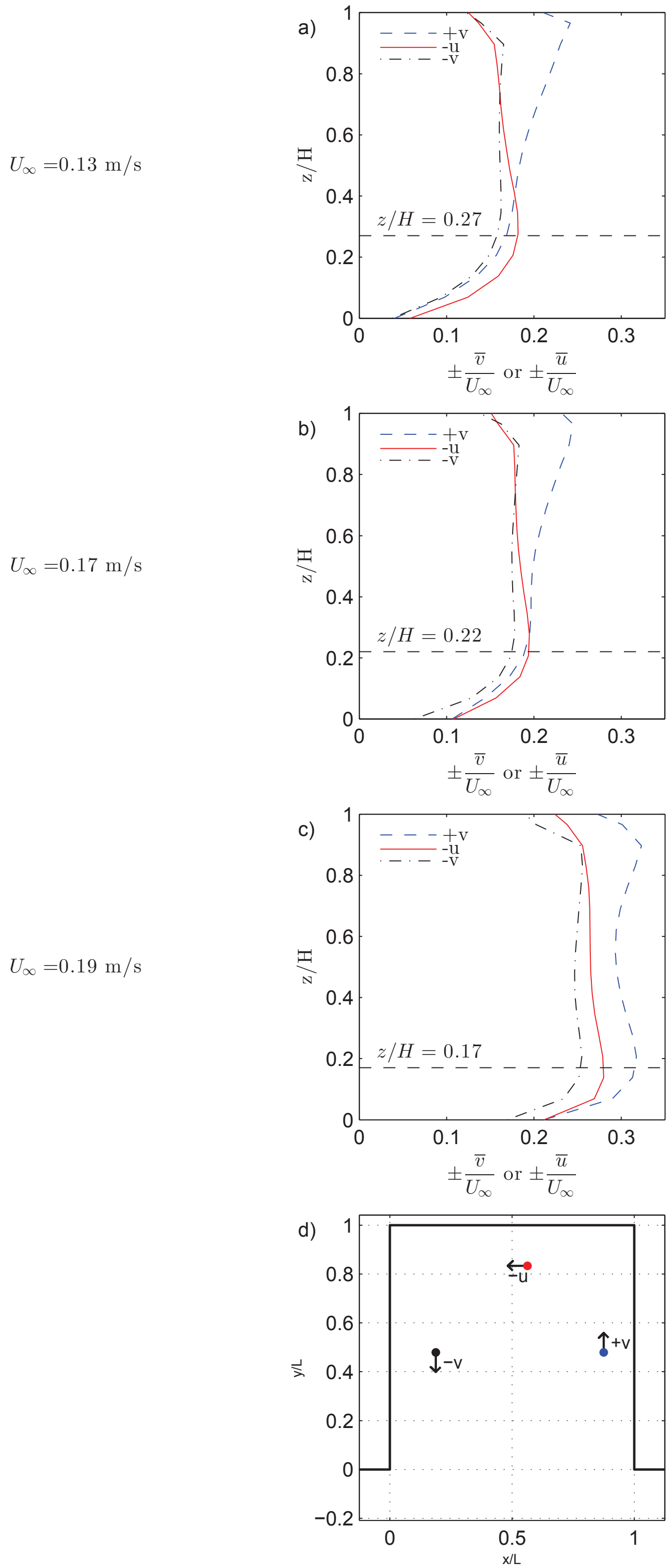

Figure 5.13: Vertical profiles of time-averaged main gyre circulation velocity. a) $U_\infty = 0.13$. b) $U_\infty = 0.17$; c) $U_\infty = 0.19$ m/s. d) Position of the vertical profiles.

According to the Bödewadt (1940) model (see Section 2.4), the secondary circulation is directly proportional to the angular velocity of the gyre rotation. Indeed, in Figure 5.10 it can be observed that the intensity of spiral motion is weaker on *a*-5 than on *c*-5. It takes the particles about one full turn around the embayment to reach the centre for the lower free-stream velocity (*a*-5) and for the higher one they go directly into the core (*c*-5).

By continuity, flow towards the centre along the bed and outward closer to the surface will result in upwelling in the centre of the embayment. Figure 5.14 shows a colour plot of the time-averaged vertical velocity. Red represents upwelling, and blue downwelling. It is evident that at every depth in the centre region of the bay there is an upward motion, whereas near the walls, there are regions of downwelling. One can also notice the presence of more localized elongated structures along the walls. These structures will be addressed in the next section.

To conclude this discussion, the "tea-cup"-like secondary circulation is present in the time-averaged flow field in the shallow embayment. The flow spirals inwards near the bed, rises in the centre and spirals outwards closer to the surface. The inward spiralling is a relatively intense flow that occupies the bottom 20-30% of the flow depth, corresponding to the thickness of the bottom boundary layer. The outward motion is less well defined spatially. The repelling point, from which streamlines originate, appears to change its position with depth and the mean-stream velocity. It also changes form, sometimes appearing as a line. It is possible that the position of the maximum divergence wanders around the embayment with time and if it converges at all, only slowly. Using the Bödewadt model or a similar one it may be possible in the future to determine the relationship between the angular velocity of the gyre and the secondary circulation. Knowing the intensity of the radial inflow at the bottom of the embayment allows for the calculation of the shear stresses and therefore the critical size of the sediments which will either settle or be picked up and re-entrained into the circulation.

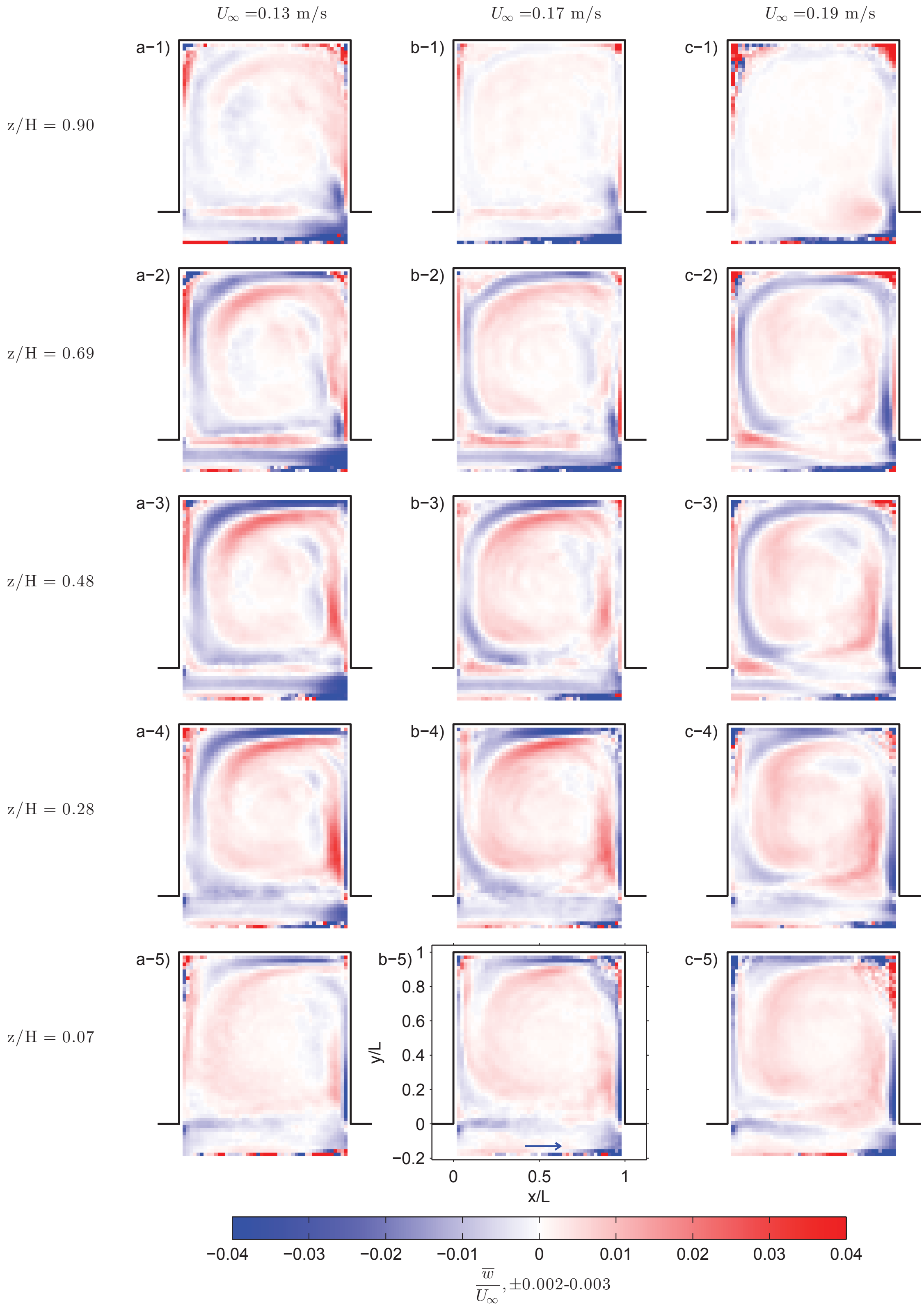

Figure 5.14: Contours of time-averaged vertical velocity, $\overline{w}/U_\infty$, at different elevations above the bed (z/H). The three columns correspond to cases of different free-stream velocities. a) $U_\infty = 0.13$. b) $U_\infty = 0.17$. c) $U_\infty = 0.19$ m/s.

5.2.3 Görtler vortices

In the previous section the effect of the bottom boundary layer on the flow was discussed. This section is devoted to the effects of the boundary layer at the side walls of the embayment. It will be shown that there are Görtler-like streamwise vortices that appear there.

One can notice in Figure 5.14 that there is a strong vertical flow with alternating direction all around the walls of the embayment. Streaks of upwelling and downwelling are situated side by side suggesting a non-zero horizontal vorticity at the edges of the gyre. For the lower free-stream velocity the direction of the vertical flow does not change with depth. For example, at the upstream end of the bay (left-hand side of graphs) one can see an upwelling region (red) near the wall and a downwelling region beside it (blue) at all elevations (a-1 to a-5) with a maximum at mid-depth. For the highest free-stream velocity, near the surface there is also an upwelling region near the upstream wall and a downwelling region beside it (c-2). However, on panel c-5 one can see that the direction of the vertical motion has switched; near the upstream wall there is a downwelling region (blue) and an upwelling region beside it (red). $z/H = 0.28$ appears to be transitional; the upwelling and downwelling streaks at the upstream wall appear discontinuous at this elevation (panels b-4 and c-4).

Streamwise vortices located near the walls of the embayment are shown in Figures 5.15 and 5.16. Figure 5.15 presents contour plots of time-averaged transverse vorticity at a vertical plane $y = 0.11$ m (or $y/L = 0.46$) for three free-stream velocities. For the highest U_∞ (panel c) both near the upstream and downstream walls, there is a pair of counter-rotating vortices located one above the other, explaining the alternation of upwelling and downwelling regions with depth in Figure 5.14-c. On panel b the downstream end has a pair of vortices, but at the upstream end they are not as pronounced. For the lowest U_∞ (Figure 5.15-a) at the downstream wall

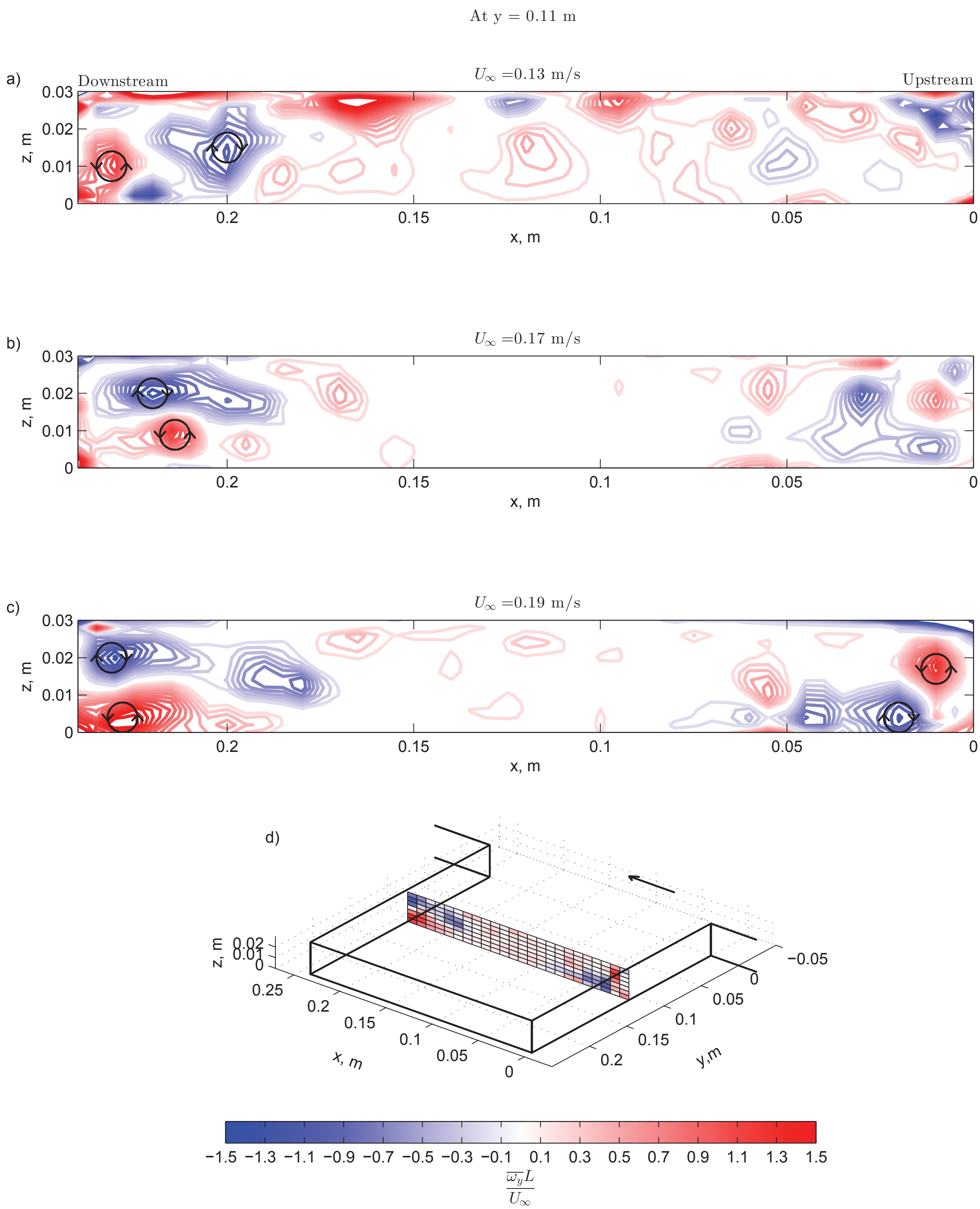

Figure 5.15: Contour plots of time-averaged transverse vorticity, $\overline{\omega_y}$, at a vertical plane $y = 0.11$ m. a) $U_\infty = 0.13$ m/s. b) $U_\infty = 0.17$ m/s. c) $U_\infty = 0.19$ m/s. d) Location of the vertical plane.

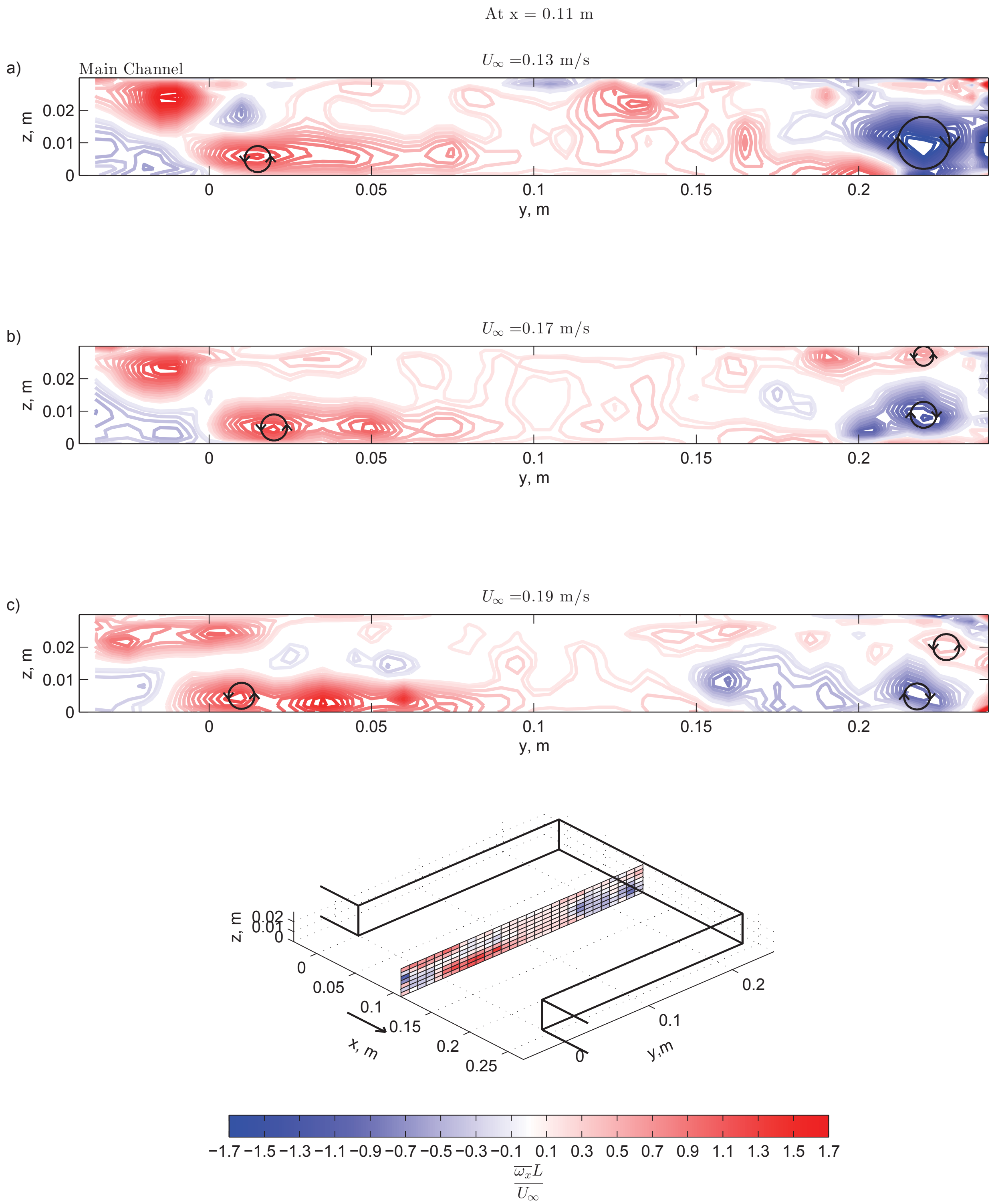

Figure 5.16: Contour plots of time-averaged streamwise vorticity, $\overline{\omega_x}$, at a vertical plane $x = 0.11$ m. a) $U_\infty = 0.13$ m/s. b) $U_\infty = 0.17$ m/s. c) $U_\infty = 0.19$ m/s. d) Location of the vertical plane.

there is only one streamwise vortex occupying the whole depth. Its counterpart appears to be beside it instead of underneath.

Figure 5.16 presents contour plots of streamwise vorticity at another vertical plane, which now is perpendicular to the channel flow, $x = 0.11$ m (or $x/L = 0.46$). The distribution of the vorticity with depth near the far wall of the embayment is similar to the previous figure. For the higher free-stream velocity (panels b and c) there is a pair of counter-rotating vortices on top of each other. For the lower U_∞ one vortex is occupying the whole depth of the flow. This principle difference in the flow structure for different free-stream velocities can be very important for prediction of the exchange between the main flow and the embayment or the scouring process near the walls. It is thus crucial that conditions determining the shape of these vortices be identified.

Judging from figure 5.14 (vertical velocity) the streamwise vortices are present along the whole circumference of the embayment along the walls. To see if this is indeed the case, one would need to plot the vorticity component perpendicular to the plotting plane at every angle through the centre of the recirculating gyre, which is both technically difficult and ambiguous since the gyre is not completely axisymmetric. However, another way to reveal the existence of a streamwise component of vorticity is through calculation of helicity. Helicity, h, is defined as the scalar product of velocity and vorticity vectors. If the two vectors are parallel, helicity is large. If the vorticity vector is perpendicular to the velocity, helicity is zero. Figure 5.17 presents the colour plot of relative helicity, H (h normalized by the magnitudes of velocity and vorticity point by point:

$$H = \frac{\mathbf{u} \cdot \boldsymbol{\omega}}{|u||\omega|}. \tag{5.1}$$

Hence, H varies from -1 to +1 indicating the relative importance of streamwise vorticity at that location. From Figure 5.17 it is clear that everywhere around the walls of the embayment streamwise spiral vortices are more important than the main

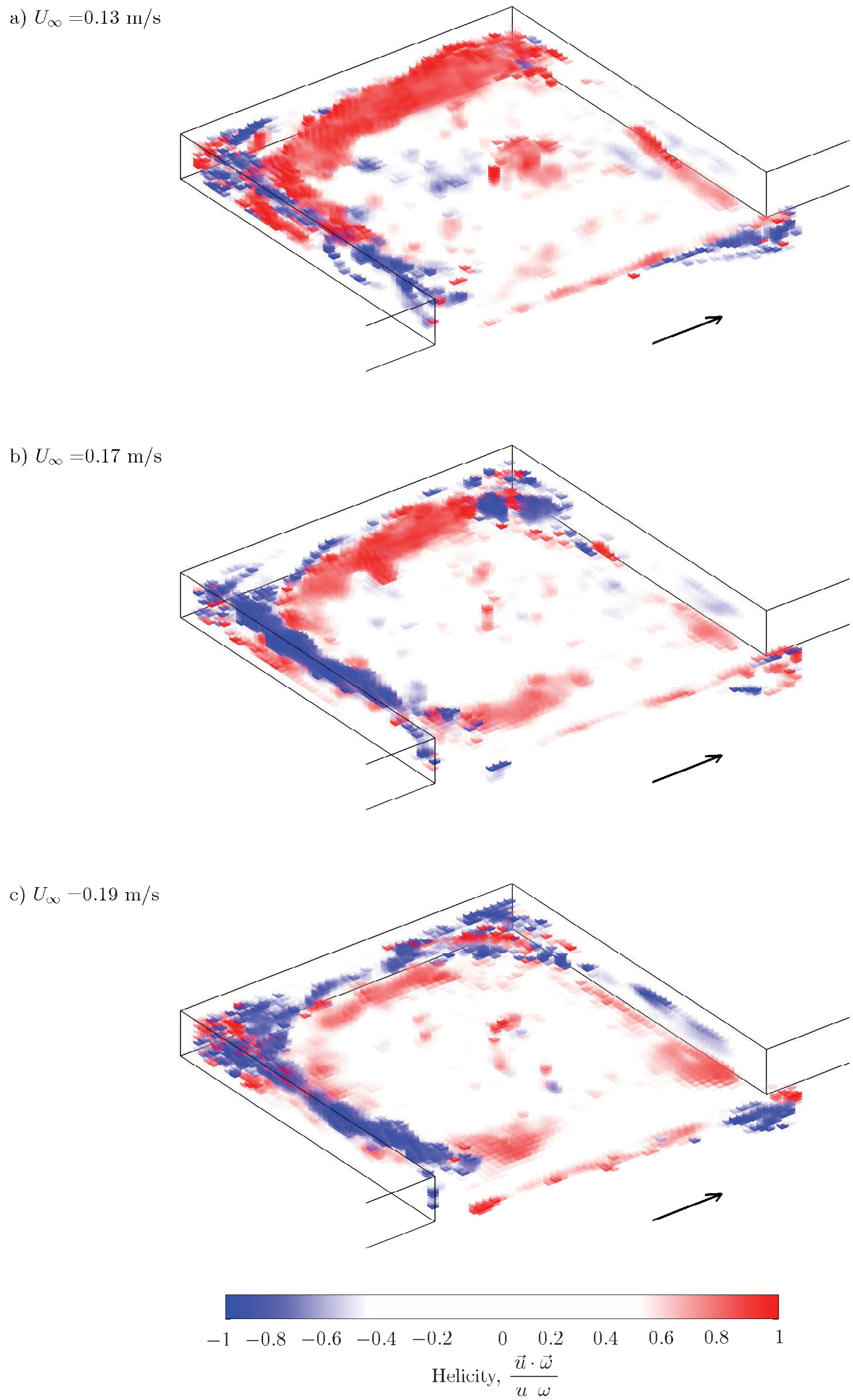

Figure 5.17: Colour plots of time-averaged relative helicity, $\mathbf{u}\cdot\boldsymbol{\omega}$, normalized point-wise by the magnitudes of velocity, u, and vorticity, ω. a) $U_\infty = 0.13$ m/s. b) $U_\infty = 0.17$ m/s. c) $U_\infty = 0.19$ m/s.

gyre circulation that has a vorticity component perpendicular to the flow. One can also see that there are regions of positive and negative helicity situated on top of each other for the highest U_∞ (panel *c*). Red regions are located near the bottom. They indicate that vectors of vorticity and velocity are pointing in the same direction. Hence, the vortex is producing inflow towards the centre of the embayment along the bottom, which is consistent with the vorticity plots (Figures 5.15 and 5.16). Near the surface, the direction of rotation changes (blue). These vortices produce surface inflow towards the centre of the bay. For the intermediate main-stream velocity (Figure 5.17-*b*), one can notice that near the far wall, a counterclockwise vortex (red) occupies most of the depth. However, near the upstream wall it divides into two counter-rotating structures. For the lowest free-stream velocity (Figure 5.17-*a*), all walls are dominated by a counterclockwise longitudinal vortex with a trace of its counterpart near the upstream wall. This suggests that for the higher free-stream velocity, 3D instability is more likely to appear, and that the flow tends to be more heterogeneous with respect to flow depth for the higher free-stream velocity.

As discussed in Section 2.3, similar streamwise vortex pairs were observed before in a different flow configuration called an open-cavity flow, which can be described as the embayment herein but infinitely deep such that the effect of the bottom or top boundary (free surface) is rendered negligible. Open-cavity flow is generally considered two-dimensional, but recent studies discovered 2D flow to be unstable (Citro *et al.*, 2015). Faure *et al.* (2007) showed experimentally the existence of pairs of streamwise Görtler-like vortices at the walls of a square open cavity. However, it is now an open question whether the vortices observed in the current experiments are indeed these Görtler-like vortices. According to Görtler (1940), longitudinal vortices appear in the boundary layer of a concave wall, which means that the location of the observed streamwise structures should correspond to the thickness of the boundary layer at the side walls of the embayment. The side boundary-layer in the embayment grows from about 1.5 to 2.5 cm for $U_\infty = 0.13$

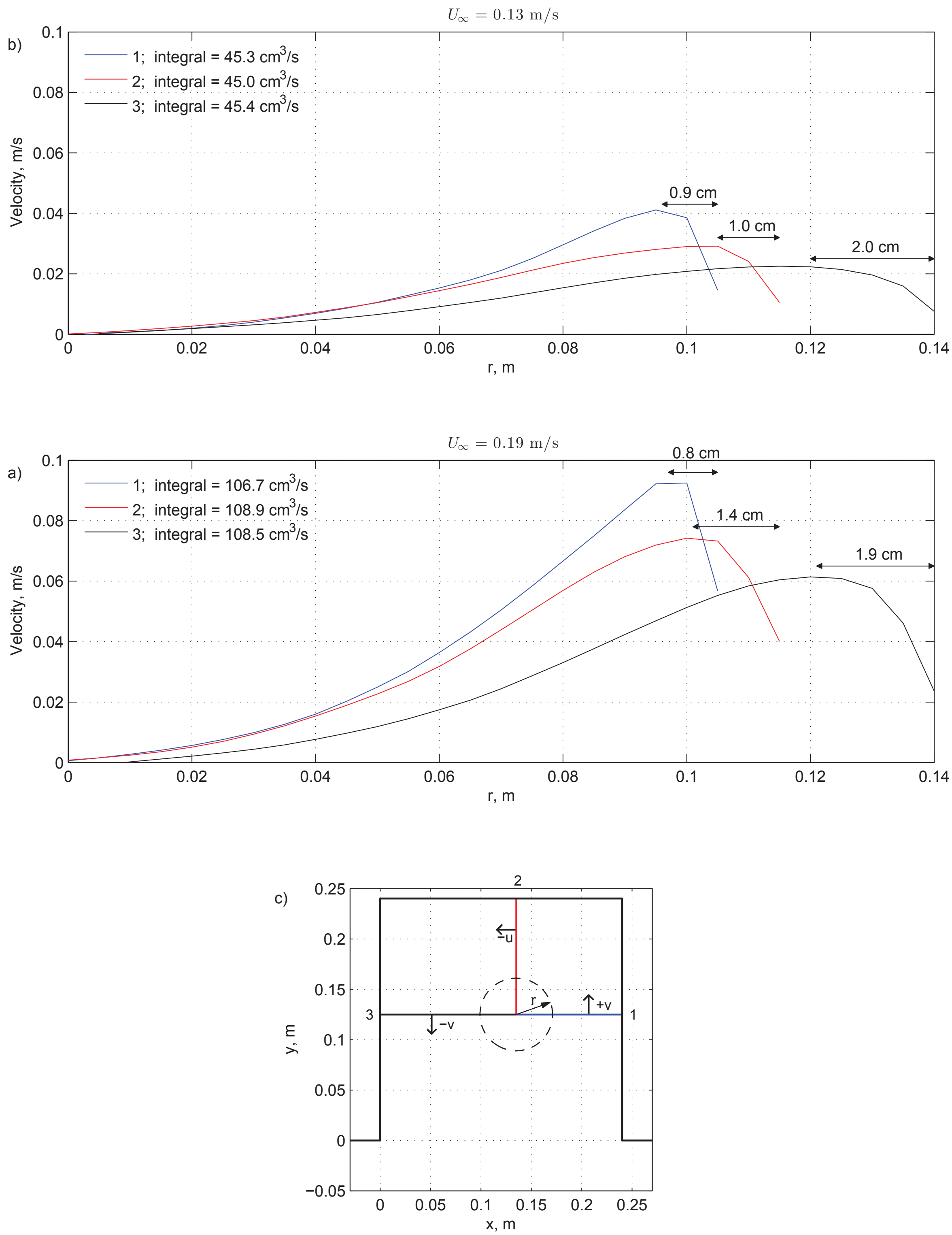

Figure 5.18: Transverse depth- and time-averaged velocity profiles of the main-gyre circulation. $r = 0$ corresponds to the centre of the gyre core. The centre of the core is not located at the geometric centre of the embayment. Hence the distance from the centre to the different embayment walls varies. a) $U_\infty = 0.13$ m/s. b) $U_\infty = 0.19$ m/s. c) Location of the 3 profiles.

m/s and from 1 to 2 cm for $U_\infty = 0.19$ m/s as can be seen in Figure 5.18 showing the depth- and time-averaged profiles of velocity from the centre of the gyre to the three walls of the embayment. (The boundary-layer thickness was determined as the distance to the peak in the velocity profile.) According to Figure 5.15 the cores of the longitudinal vortices are located at about 1 to 3 cm from the walls, indicating that their location indeed corresponds to the side boundary layer in the embayment, and therefore the origin of these vortices can be explained by the Görtler instability.

The wavelength of the Görtler vortices in open-cavity flow, measured as a distance between two pairs of counter-rotating structures, is about $0.4L$, where L is the width of the embayment (0.24 m in the present study) (Faure *et al.*, 2007; Citro *et al.*, 2015; Brès & Colonius, 2008). This wavelength is considerably larger than observed in the present experiments. Here, the wavelength of the pair of vortices for the shallow embayment is basically the flow depth, as the pair of longitudinal vortices occupies the entire height. The depth of the flow is $0.12L$, thus, the wavelength of the Görtler vortices is 3-4 times smaller than that observed in open-cavity flow. This difference is likely to be the result of the limited space formed by the two boundaries; channel bed and free-surface, that are confining the structures. The Görtler number, G, calculated in Section 2.3 grows with boundary-layer thickness as the flow passes the three embayment walls. For the lower free-stream velocity it grows from 2 to 10, and for the higher one from 7 to 30, whereas the critical G is equal to 0.3. In the experiments of Faure *et al.* (2007) $G \approx 4$. This means the three-dimensional instability in the shallow embayment is much stronger in the current experiments than in those of open-cavity flow, and even the confined space and friction forces from both boundaries are not strong enough to stabilize the 2D flow in the shallow embayment.

5.2.4 Turbulence spectra and dimensionality of the flow

In this section the question of the sufficiency of a two-dimensional model to describe a shallow-embayment flow will be addressed. One of the ways to distinguish between a fully three-dimensional and a quasi-two-dimensional turbulent flow is spectral analysis. It will be shown in this section that in the region of the shear layer u, v, and w components of velocity exhibit fully 3D behaviour, whereas inside the embayment the spectra of u and v velocity fluctuations may indicate quasi-two-dimensional flow dynamics.

According to Kolmogorov's theory, based on the idea of local isotropy of turbulence statistics for large enough Re and negligible viscosity, there exists an inertial range of scales where a universal law of downscale energy cascade can be applied. In this range the turbulence energy spectrum depends solely on the dissipation rate of turbulent kinetic energy and has a logarithmic slope of -5/3 (Kolmogorov, 1941; Monin & Yaglom, 1971). However, two-dimensional flow dynamics exhibit very different properties. 2D flows are characterized by an inverse energy cascade, and a downscale enstrophy cascade in which turbulent structures tend to merge and grow in size, forming a turbulence spectra that has a subrange with -3 logarithmic slope (Kraichnan, 1971). It was also shown that a -3 slope appears in quasi-two-dimensional flows where the large scales have strong 2D properties and a -3 slope, and the small scales exhibit a -5/3 slope. For example, Uijttewaal & Booij (2000) show inertial subranges (with a -3 and -5/3 slopes) for a shallow shear layer dominated by quasi-two-dimensional large-scale structures.

Engelhardt *et al.* (2004) measured the spectra of the fluctuations of the three velocity components in two groynes on the Elbe river. They found that the velocity spectra for 5 points within the embayment collapse on each other and that the u and w components have a -5/3 slope, and the transverse velocity component, v, exhibits a -3 subrange. Also, the energy spectrum was measured by McCoy *et al.*

(2008) in an embayment with a sudden increase in the flow depth at the embayment-channel interface. They found that the transverse velocity-fluctuation spectra in the mixing layer has a -5/3 slope, whereas in the embayment it is -3. It is logical to expect a -3 subrange within the shear zone, similar to Uijttewaal & Booij (2000), as the shear layer is dominated by quasi-two-dimensional Kelvin-Helmholtz vortical structures. Thus, McCoy *et al.* (2008) attribute the -5/3 spectra in the shear layer to the non-uniform depth in their experimental set-up (a step at the entrance to the bay), which exhibits three-dimensional effects. In the present experiments there is a uniform bottom in the channel and in the embayment. In order to identify regions dominated by fully 3D turbulence and regions possessing 2D flow characteristics in the current geometry, frequency spectra of velocity fluctuations at different points in the embayment are employed.

Let us define $\hat{u}_i$ as the Fourier transform of velocity fluctuations u_i, where $u_i = [u, v, w]$. The discrete Fourier transform is then

$$\hat{u}_i(f_k) = \frac{1}{N} \sum_{j=0}^{N-1} u_i(t_j) e^{-2\pi i f_k t_j}, \tag{5.2}$$

where $k = -N/2, ..., -1, 0, 1, ...N/2$, $f_k = \frac{k}{T}$, $t_j = j\Delta t = j\frac{T}{N}$, N is the number of points in the data set (6298) and T is the length of the data series in seconds (10.2 s). The energy spectrum is then defined as $\frac{1}{2}\hat{u}\hat{u}^*$, where $\hat{u}^*$ is a complex conjugate of $\hat{u}$. The energy spectrum was averaged over 9 experimental runs each one of which is 10.2 s long.

Spectral densities in the region of the mixing layer for the streamwise velocity component, u (Figure 5.19), indicate Kolmogorov's -5/3 inertial range associated with energy cascade from large- to small-scale turbulent structures (Kolmogorov, 1941). Spectral densities inside the embayment display a steeper slope, close to -3, indicating a possibility of 2D flow dynamics (Kraichnan, 1971). (Note that the peaks at 0.37 and 0.81 Hz is the response to the gravity waves that will be discussed in the

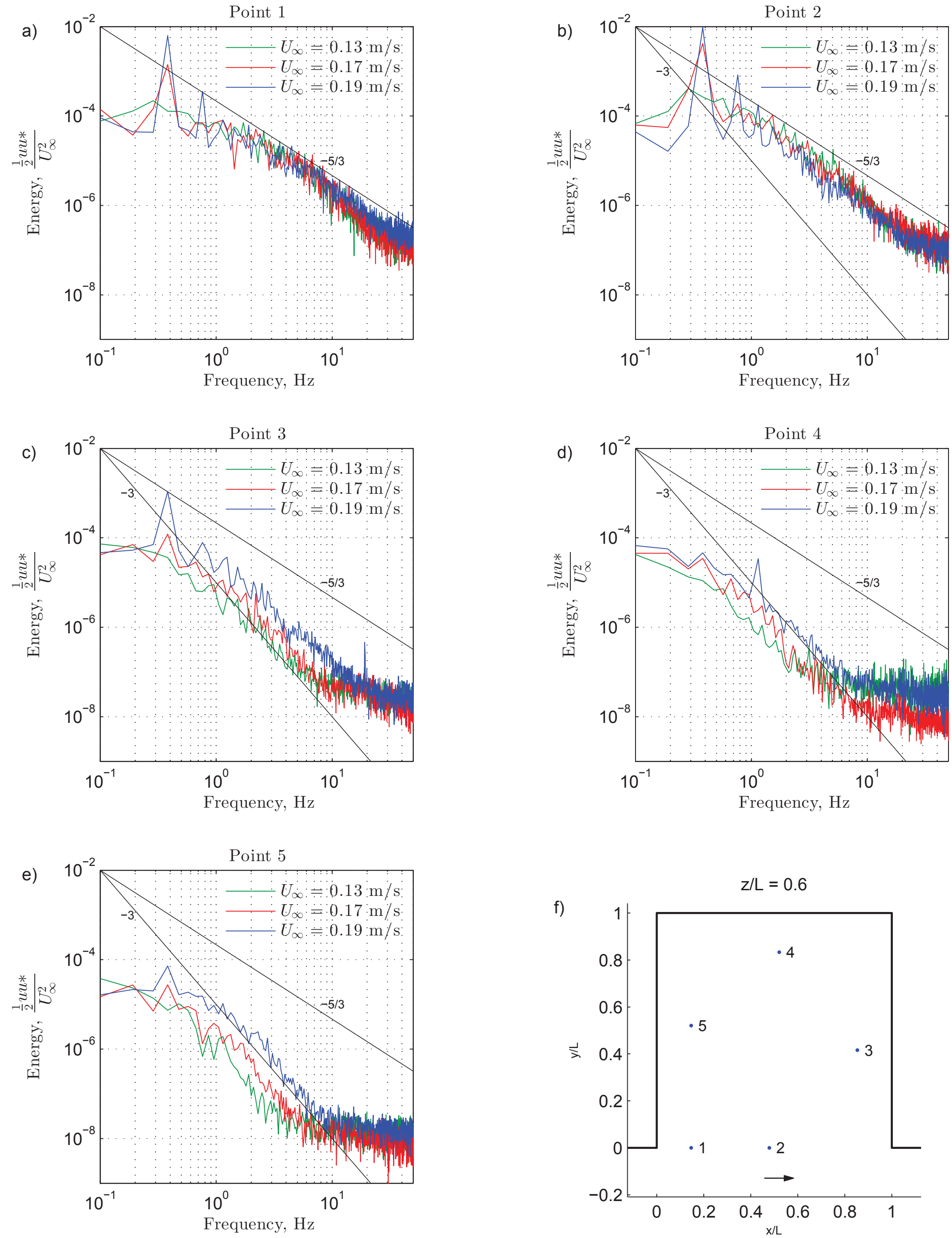

Figure 5.19: Energy spectra of streamwise velocity fluctuations measured at 5 positions within the embayment (indicated on panel f) at z/L=0.6. The three colours represent the three different free-stream velocities.

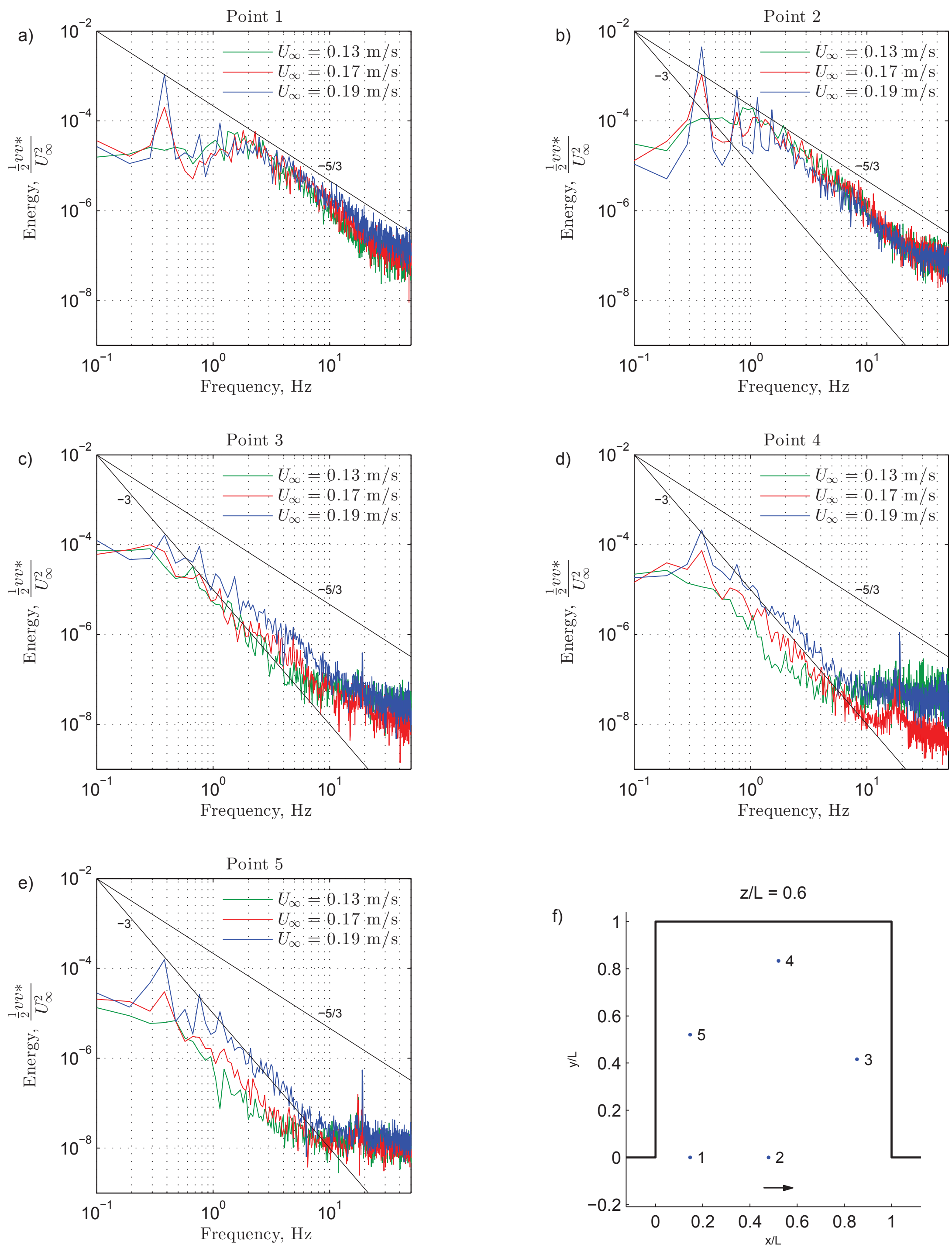

Figure 5.20: Energy spectra of transverse velocity fluctuations measured at 5 positions within the embayment (indicated on panel f) at z/L=0.6. The three colours represent the three different free-stream velocities.

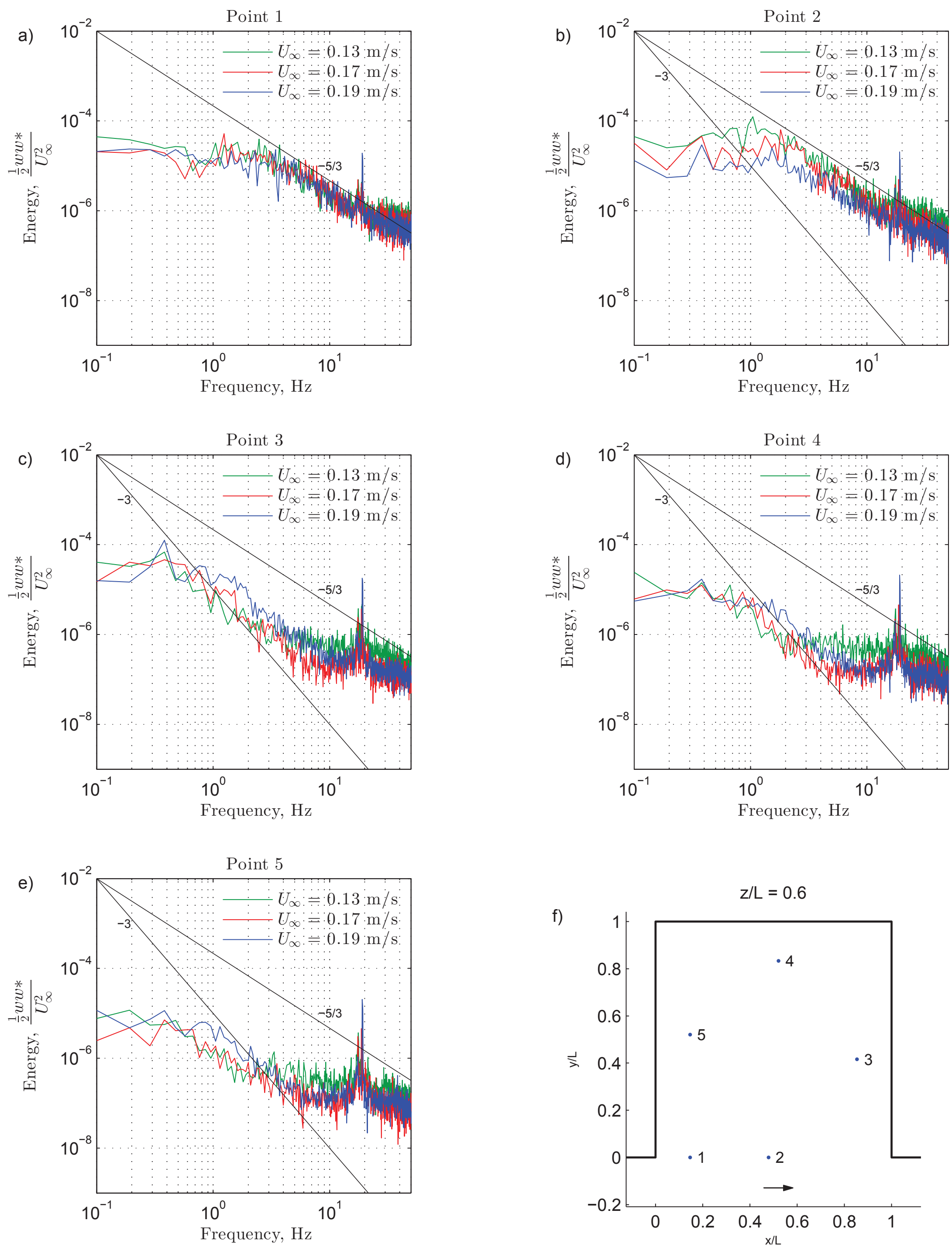

Figure 5.21: Energy spectra of vertical velocity fluctuations measured at 5 positions within the embayment (indicated on panel f) at z/L=0.6. The three colours represent the three different free-stream velocities.

Section 5.3.) The transverse velocity component, v, indicates a similar tendency (Figure 5.20), where the shear zone has a -5/3 spectral slope, and a steeper spectra inside the embayment. The vertical component of the velocity fluctuations, w, however, show a different behaviour (Figure 5.21), having an approximately -5/3 slope everywhere. (A peak in the spectra at about 20 Hz is a response to external vibrations in the laboratory.) One can also notice that the vertical energy spectra have lower energy at large scales than the horizontal ones. This is expected as the vertical fluctuations are confined by the water depth and therefore cannot contain energy in modes slower than approximately H/W, where H is the water depth, and W is the characteristic vertical velocity.

It is thus fair to conclude that in spite of the fact that one could expect a quasi-two-dimensional behaviour in the shear zone that is dominated by large-scale Kelvin-Helmholtz structure, a -5/3 slope appearing in the spectra of all three velocity components, shows fully three-dimensional dynamics. Inside the embayment, the slopes of the spectra are steeper. Engelhardt *et al.* (2004) showed that only the transverse component had a -3 sub-range, whereas in the current experiments both, u and v components indicate a possible quasi-two-dimensional behaviour. In Section 5.2.1 it was shown that the exchange process between the embayment and the main channel is highly dependent on depth. The -5/3 spectral slope in the shear zone supports this conclusion, showing that the flow in this region is fully three-dimensional. The - 3 spectral slope inside the embayment indicates that this flow may be treated with a quasi-two-dimensional approximation. However, we would like to note that the interpretation of frequency spectra in low-Reynolds number flows must be done with care. All theoretical results of Kolmogorov and Kraichnan pertaining to the spectral slopes were obtained for the two-point correlation wave number spectra. In laboratory experiments it is difficult to obtain data that would allow one to calculate a two-point correlation function. It is hence common to use

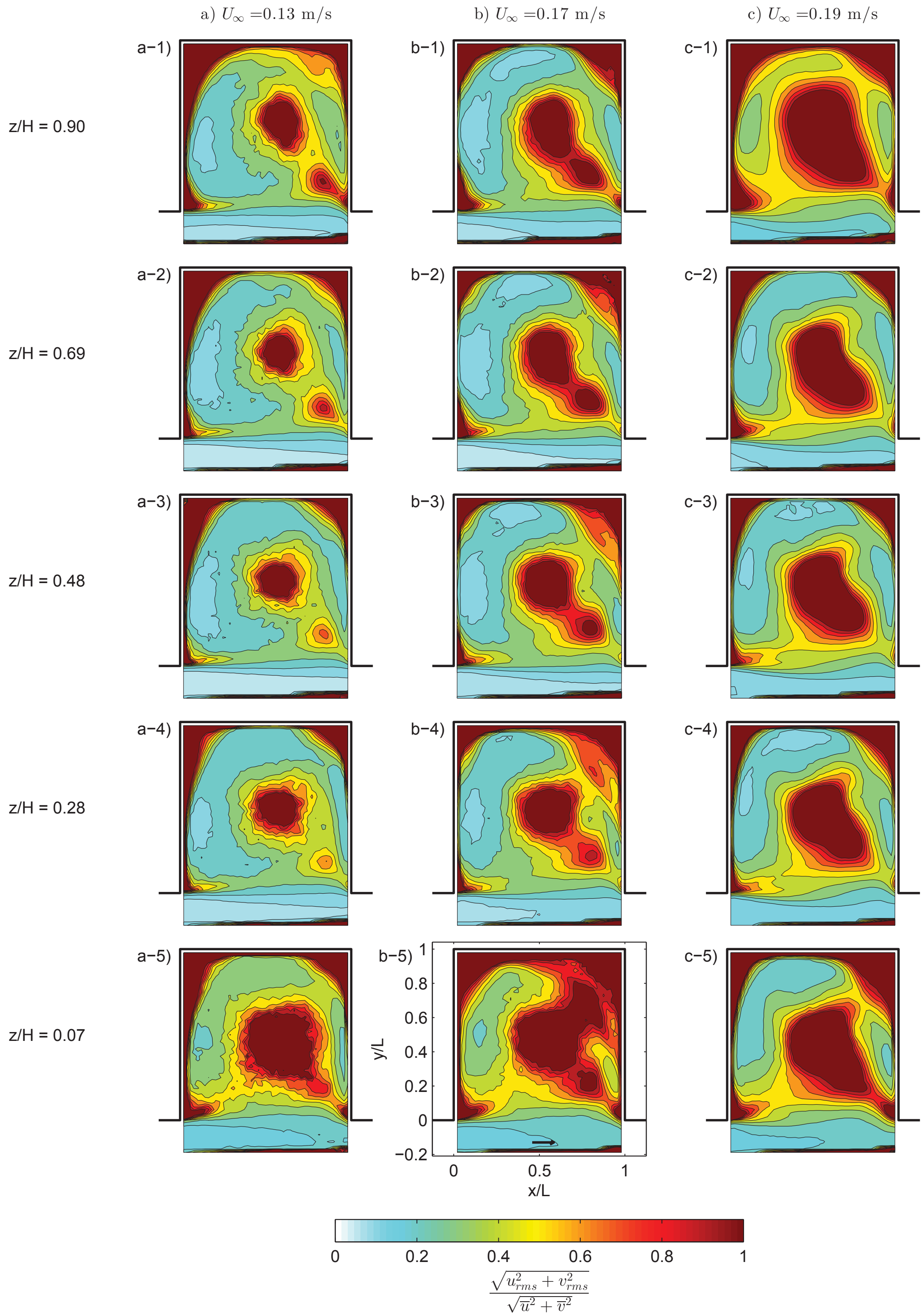

Figure 5.22: Colour plots of the ratio between horizontal time-averaged velocity and its rms at different elevations above the bed (z/H). The three columns correspond to cases of different free-stream velocities: a) $U_\infty = 0.13$; b) $U_\infty = 0.17$; c) $U_\infty = 0.19$ m/s.

an analogy between the wave number spectrum and the Eulerian frequency spectrum. However, this analogy holds only when there is a sufficiently strong mean flow or large-scale structures advect the small-scales past the probe. In the limit where the mean flow is infinitely fast, Eulerian measurements can mimic two-point correlation measurements. This analogy is called Taylor's hypothesis or the "Frozen turbulence" approximation, which was shown to hold for $u_{rms} \ll \overline{u}$ in grid turbulence, but was also shown to introduce a bias in free-shear flows (Lumley, 1965; Tong & Warhaft, 1995). It is thus important to use this analogy with care and at least verify that the advection time-scale is much larger than the rms velocity at the point of interest. Figure 5.22 shows the ratio between the mean flow and the rms velocities at every point in the embayment. It is evident that in the channel outside of the bay the mean velocity is much larger than the fluctuations for all water depths and free-stream velocities. The spectra in this region show a -5/3 slope. However, in most regions within the embayment Taylors approximation is not valid as the mean flow is of the same order as the rms velocities, especially near the walls and in the core of the gyre. This is particularly evident at higher free-stream velocities, where the intensity of the turbulent fluctuations increase faster with Re than the mean flow. It is thus an open question as to whether a steeper slope within the embayment, for this work and for the work of Engelhardt *et al.* (2004) and McCoy *et al.* (2008), is indeed an indication of 2D flow dynamics, or is purely an effect of insufficient advection velocity. Two-point correlation spectra are needed to resolve this issue. Obtaining this statistic from the current data is arguably possible but not straightforward, mainly because the interpretation of the spatial correlation function in a non-homogeneous flow is a challenge.

5.3 Gravity waves

Open-channel flows are subject to surface gravity waves. Most of the previous research neglected their potential effect on the flow in a shallow embayment. However, the recent study of Tuna *et al.* (2013) showed that gravity waves can have a significant effect on the exchange process between the embayment and the main flow. They also argue that gravity waves are amplified when the natural frequency of the embayment "couples" with an "inherent" frequency of the shear layer (see Section2.5 for details). It is therefore clear that in order to have a complete understanding of the exchange process, it is also necessary to consider the effect of gravity waves. They will be quantified in the current experiments in terms of their amplitude and frequency. It will be shown that the three cases of different free-stream velocities have significant differences in terms of the surface perturbation. The lower free-stream velocity case has negligible gravitational instability, whereas the highest free-stream velocity flow is subject to high-amplitude surface waves. The reasons pertaining to this difference are discussed. It will be shown that the possible source of the resonant response to the gravitational instability is coupling with the most energetic mode within the main gyre circulation. The effect of gravity waves on the exchange will be addressed in the next section.

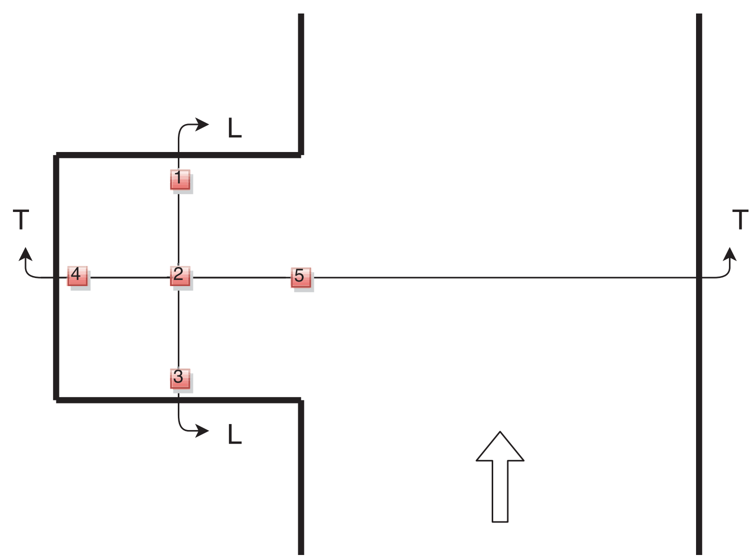

Figure 5.23: Five locations at which free-surface elevation was measured. For each 2x2 cm water column, for each time step, z-positions of the highest particle within the column represents the position of the free surface.

In order to measure free-surface oscillations, the maximum particle elevations were extracted from the main experimental data. Five vertical water columns, 2 by 2 cm each, were chosen inside the measurement volume (Figure 5.23). The elevation of the top particle at every time step was obtained from each column. On the longer time scale this position is argued to be representative of the free-surface elevation. This method of measuring the surface level produces a lot of noise, as the top particle in the column may happen to be quite far from the free surface for a particular time step. Therefore, these data cannot be used for analysis of small-scale perturbations. However, the slower modes of the gravity waves appear well-defined in the time series. Panels a, b, and c in Figure 5.24 show the time series of the surface elevation and their amplitude spectra for location 1, situated near the downstream wall of the embayment (Figure 5.23), for three free-stream velocities $U_\infty = 0.13$, 0.17, 0.19 m/s, respectively. The amplitude spectrum was plotted (i.e. the square root of the usual power spectrum, $\sqrt{zz*}$) in order to display the amplitudes of the waves. It is evident from the spectra on this figure that for the lower free-stream velocity (U_∞=0.13 m/s) the gravity waves are very weak; the amplitude does not exceed 0.2 mm. The amplitude of the peak increases to 0.3 mm for the U_∞=0.16 m/s, but for the highest free-stream velocity, the amplitude increases to 0.9 mm at a frequency of 0.36 Hz. The peaks at the same frequency of 0.36 Hz are pronounced at the lower free-stream velocity cases as well, but they are not as energetic (the labelled peaks will be discussed later in this section).

In the works of Tuna *et al.* (2013) and Kimura & Hosoda (1997) one kind of gravity wave was observed in the shallow embayment flow. It takes a form of longitudinal sloshing. Its first mode produces high-amplitude surface oscillations up against the upstream and downstream walls of the embayment and has a node in the centre of the bay. Kimura & Hosoda (1997) showed that this gravity wave in a shallow embayment is of the seiche kind or in other words, a non-dispersive shallow-water wave. Thus, its frequency is given by:

$$f(n) = \frac{n\sqrt{gH}}{2L}, \tag{5.3}$$

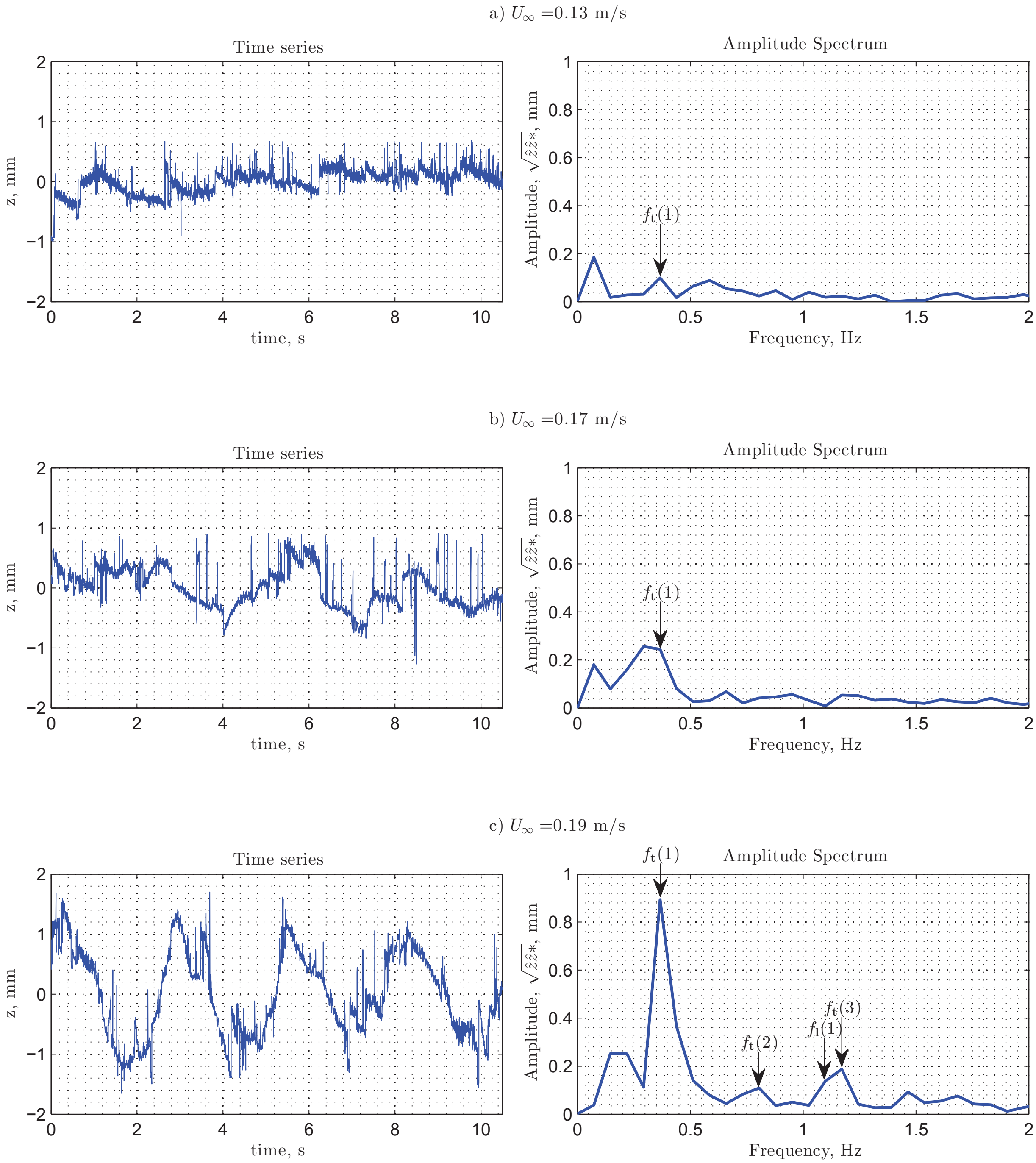

Figure 5.24: Time series of the free-surface oscillations and their amplitude spectra at the downstream end of the embayment (location 1 at the schematic in Figure 5.23). a) $U_\infty = 0.13$ m/s. b) $U_\infty = 0.17$ m/s. c) $U_\infty = 0.19$ m/s.

where $f(n)$ is the frequency of the gravity wave, n is the mode of oscillation ($n = 1, 2, 3...$), g the acceleration of gravity, H the depth of the flow, and L is the cavity width (Méhauté, 1976).

If this type of wave produces the high-amplitude spectral peak at $U_\infty = 0.19$ m/s, then one should see a phase shift of half the period of the oscillation between two locations; the upstream and downstream ends of the embayment. Figure 5.25 presents the time series and amplitude spectra for the free-stream velocity $U_\infty = 0.19$ m/s at four locations (downstream end, upstream end, centre of the embayment, and the shear zone - a, b, c, and d plots, respectively). From these it appears that at all four strongest oscillations (period of about 2.7 s) are almost perfectly in phase with each other, with a slight shift for the shear-layer zone. This indicates that it is not longitudinal sloshing inside the bay that is dominating the flow, but a transverse wave that goes across the channel.

The longitudinal wave does appear in the spectrum, though. Based on equation (5.3), the frequency of the first mode of the longitudinal seiche is equal to $f_l(n = 1) = 1.11$ Hz. In the Figures 5.25 a and c (downstream and upstream ends of the embayment, where one expects to see high-amplitude sloshing) there are peaks of about 0.2 mm at frequency of 1.1 Hz. At that same frequency there are no peaks present in the centre of the embayment (Figure 5.25 b) or in the shear zone (Figure 5.25 d).

One could also notice peaks at even lower frequency of about 0.08 Hz for the lower free-stream velocities and 0.15-0.2 Hz for the higher one (Figure 5.24). These peaks are most likely associated with the first and second harmonics of a gravity wave travelling over the whole flume length (for the length of 2.9 m equation (5.3) gives $f(1)$=0.09 Hz and $f(2)$=0.18 Hz).

It is, however, clear that the transverse wave has the highest amplitude and therefore is likely to be playing the most important role in the flow. Judging from the data, it is logical to assume that the transverse gravity wave is bounded by the

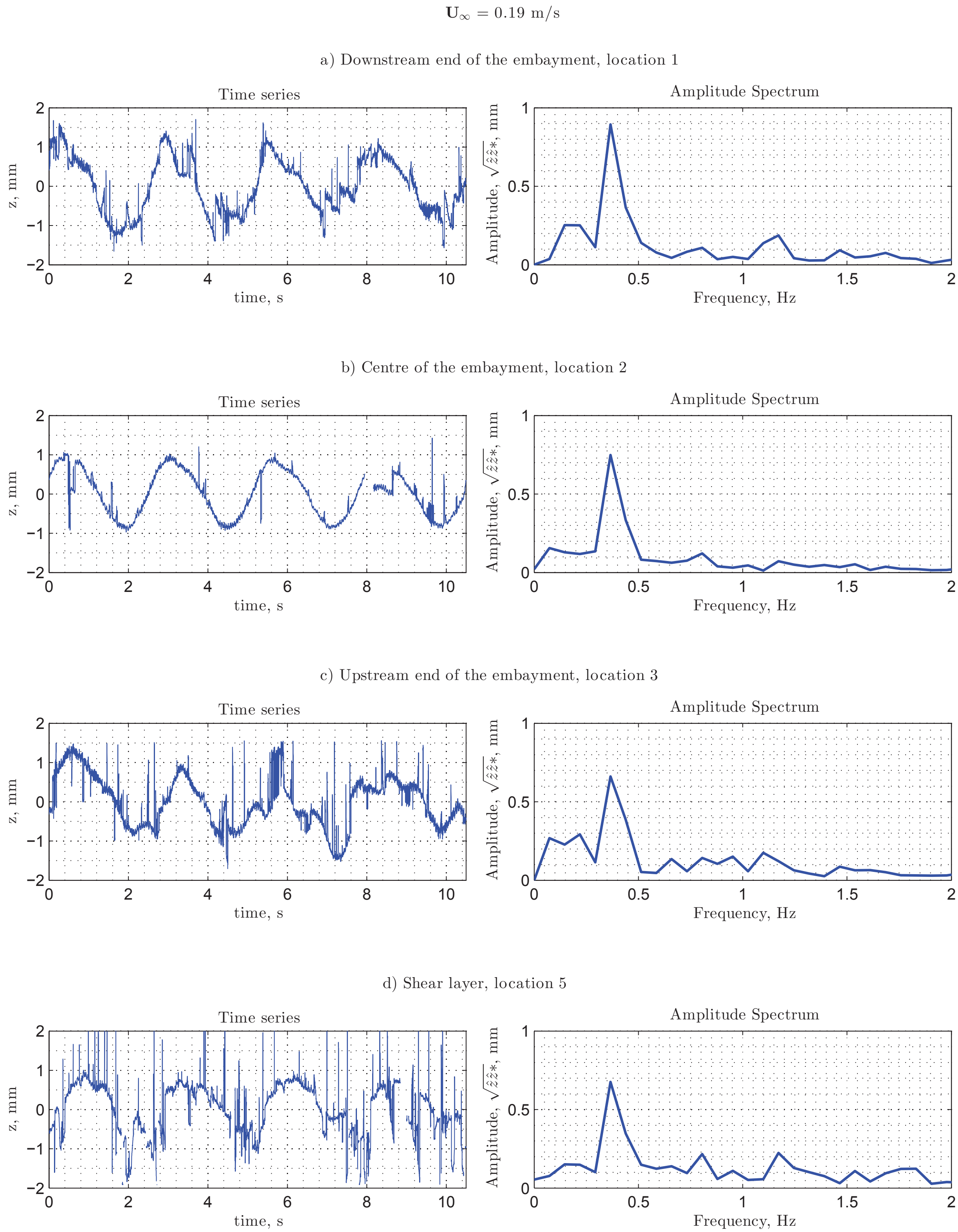

Figure 5.25: Time series of the free-surface oscillations and their amplitude spectra at four locations indicated on the schematic in Figure 5.23. a) Location 1, downstream end of the embayment. b) Location 2, centre of the embayment. c) Location 3, upstream end of the embayment. d) Location 5, shear layer.

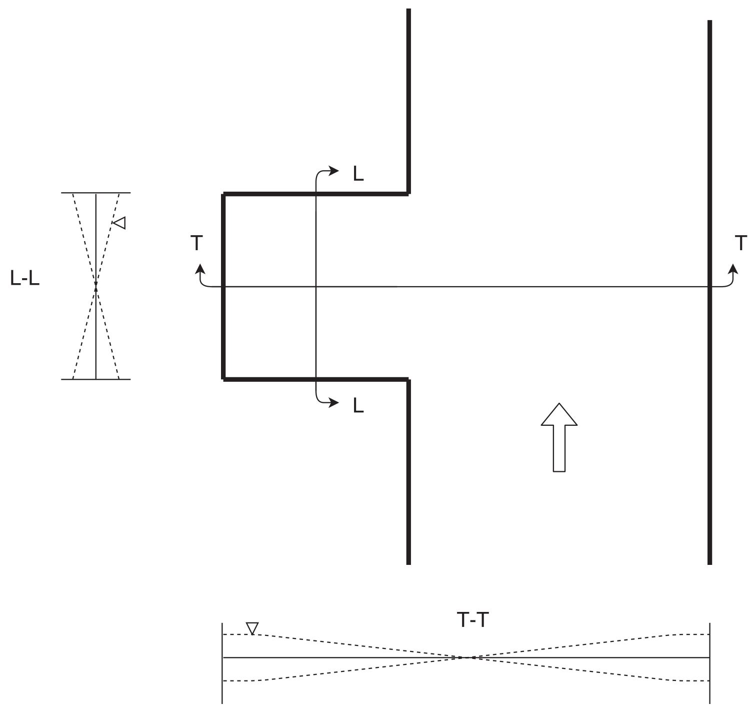

Figure 5.26: Transverse (T-T) and longitudinal (L-L) profiles of the water levels in the channel, showing the first modes of longitudinal and transverse gravity waves.

Table 5.2: Measured and calculated frequencies of transverse and longitudinal gravity waves.

Mode	Transverse gravity-wave frequency, Hz		Longitudinal gravity-wave frequency, Hz	
	Calculated	Measured	Calculated	Measured
1	0.42	0.37	1.11	1.10
2	0.83	0.81	2.22	2.34
3	1.25	1.17		

channel wall on one side and the far embayment wall on the other, such that its first mode has a length of twice the width of the channel plus the width of the bay, 2(0.24 m +0.40 m) = 1.28 m (see the scheme on Figure 5.26). If we assume this oscillation is also of a seiche kind (as did Nezu & Onitsuka (2002)), then the frequencies of the first, second and third modes are 0.42, 0.83, and 1.25 Hz, correspondingly. The assumption of this wave being a non-dispersive shallow-water wave is reasonable, as the degree of "shallowness", measured in the width-to-depth ratio, is even larger for this region across the channel than for the embayment itself. In Figure 5.24 c-2 the measured frequencies of the peaks for the high free-stream velocity are indicated as $f_t(1)$, $f_t(2)$, and $f_t(3)$, which are equal to 0.37, 0.81, and 1.17 Hz, corresponding to the first three modes of transverse gravity waves. Table 5.2 presents a summary of measured and calculated gravity-wave frequencies.

The transverse gravity wave in a shallow channel with a pair of consecutive embayments was observed and described in Tuna & Rockwell (2014). To calculate the frequency of the transverse gravity wave, the authors used the following equation:

$$f(n) = \frac{n\sqrt{gH}}{4W}, \tag{5.4}$$

where W is the width of the cavity. It is assumed that the wave-length of the transverse gravity wave is equal to 4 times the cavity width. If this formulation is adopted for the current set-up, the wave-length of the first mode of the transverse gravity wave would be equal to 4×0.24 m = 0.96 m. Hence the frequency of the first mode instead of 0.42 Hz, as before, would become 0.56 Hz. The measured frequency of the peak in the spectrum is 0.36 Hz, and at a frequency of 0.56 Hz, there is a low-amplitude region for all locations inside the embayment (Figure 5.25).

It is interesting to observe how fast the amplitude of the gravity wave grows when the free-stream velocity in the channel is gradually increased. The peak amplitude goes from 0.2 to 0.3, and then to 0.9 mm with the free-stream velocity changing from 0.13 to 0.17, and then to 0.19 m/s (Figure 5.24). Tuna *et al.* (2013)

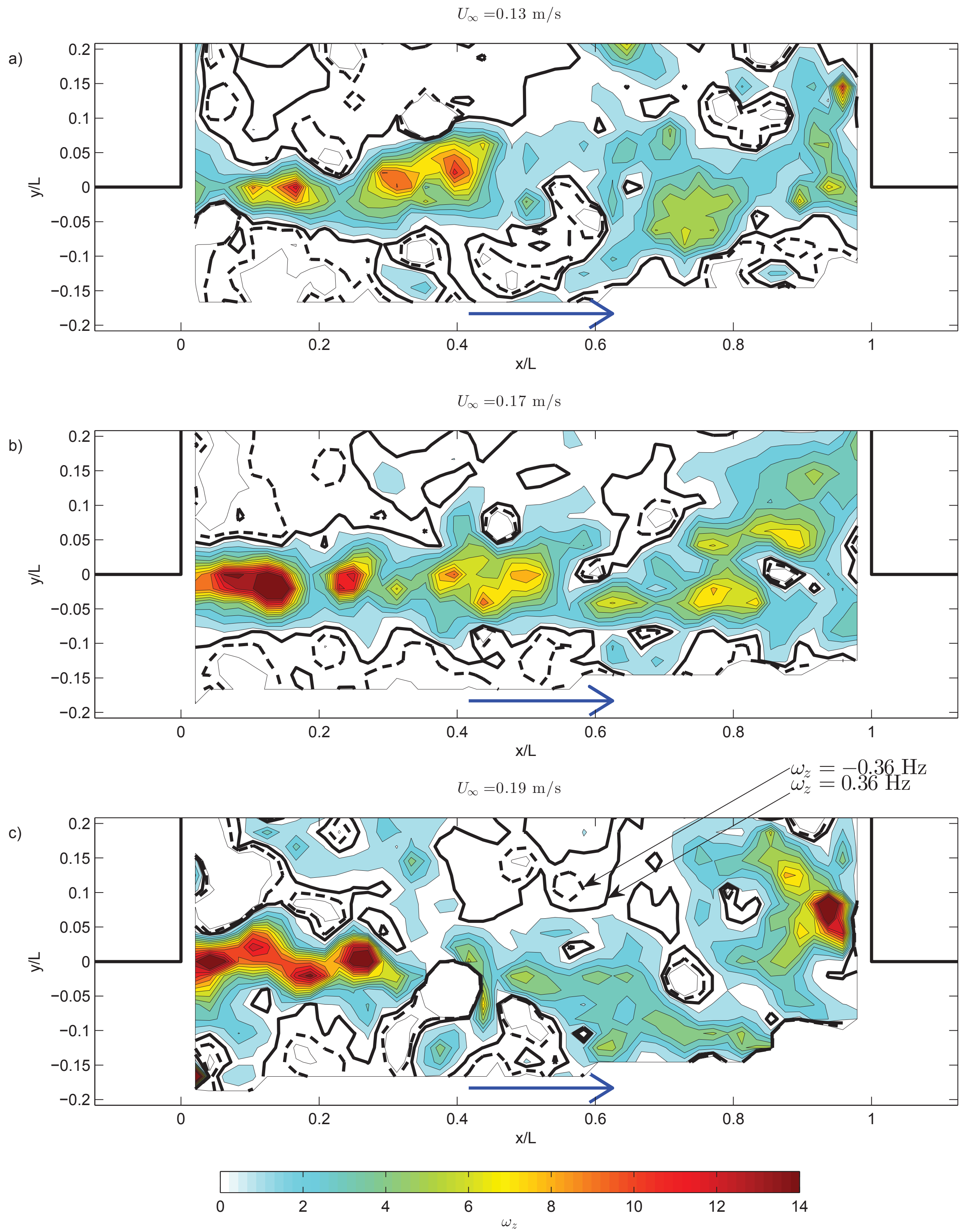

Figure 5.27: Contour plots of the instantaneous vertical vorticity, ω_z, in the shear zone of the embayment at the elevation of z/H=0.62. a) $U_\infty = 0.13$ m/s. b) $U_\infty = 0.17$ m/s. c) $U_\infty = 0.19$ m/s. Contours of $\omega_z = \pm 0.36$ Hz are indicated with black solid and dashed lines.

and Wolfinger *et al.* (2012) argue that the rapid growth of the gravity wave amplitude is caused by the coupling between the gravity wave and the shear instability. However, it is not quite clear what the frequency of the shear layer is and how to determine it. Thus, it is fair to assume from the rapid growth of the peak amplitude, that some sort of resonance occurs. As to what causes it, it is argued to still be an open question. In the present study it was attempted to find the frequency that resonates with the gravity-wave frequency, generating an enhanced response, and its source.

The frequency of the gravity wave at which the response is amplified in the current experiments is the first mode of the transverse gravity wave, $f_t(1) = 0.36$ Hz (Figure 5.25). It will now be attempted to find another process with a matching frequency of 0.36 Hz. Figure 5.27 shows a contour plot of the instantaneous vertical vorticity, ω_z, for the three free-stream velocities (panels a,b, and c correspond to $U_\infty = 0.13$, 0.17, and 0.19 m/s, respectively) at z/H=0.62. From this figure it is evident that the frequency of the rolls in the shear zone is about 6-14 Hz, which is an order of magnitude faster than the gravity wave frequency (0.36 Hz). On figure 5.27 contours of vertical vorticity equal to $f_t(1)$, $\omega_z = \pm 0.36$, are indicated with thick solid and dashed lines. The signal at this frequency is weak and spatially disorganized, leading to the conclusion that ω_z in the shear zone is not the source of the resonance. The frequency of the vortex generation at the upstream corner of the embayment also appears to be much faster than the resonant frequency. The spacing between the vortices in figure 5.27 is 1.8-2.4 cm, and approximate velocity in the shear zone is 0.04-0.11 m/s, resulting in a vortex generation frequency of 3-4 Hz, which is again an order of magnitude larger than $f_t(1) = 0.36$ Hz. This is also consistent with the numerical results of Kimura & Hosoda (1997), which showed the period of vortex generation caused by shear-layer instability is shorter than the period of the seiche.

Tuna *et al.* (2013) presented the evidence that when the gravity waves are strong, the shear layer in an embayment starts undulating with the frequency of the gravity wave. Indeed, if the phase average of the vertical vorticity is calculated, the undulation of the shear layer with the gravity-wave frequency is evident. Figure 5.28 presents the vertical vorticity averaged for each of the 9 phases $\Phi = 0$ to $360°$ with a $45°$ step. The averaging was performed over 1 run of 10.2 seconds. Hence, with the period of the gravity wave being 2.7 s (1/0.36 Hz), every graph in Figure 5.28 is an average of 3 to 4 frames. From the graph it can be seen that the shear layer exhibits undulations with exactly the frequency of the gravity wave. For comparison, on figure 5.29 the same quantity (phase averaged ω_z) is presented for the lower free-stream velocity of $U_\infty = 0.13$ m/s, where the gravity waves are weak. No undulations in the shear layer can be observed in this figure.

The frequency of the shear-layer oscillation is the same as the frequency of the first mode of the transverse gravity wave that produces high-amplitude surface elevations. This supports the idea of Tuna *et al.* (2013) that the frequency of the shear instability couples with the gravity-wave frequency. However, it is still not clear what is the cause and what is the effect; whether the undulation is a result of the strong gravity wave that came into resonance with some other frequency, or actually the undulation appeared first and triggered the resonant response of the gravity wave. This question is difficult to answer. Especially because in a physical system it is frequently a non-linear two-way relationship that is present.

Nevertheless, since the question is still open, the search for the resonant frequency was continued. All frequencies in the shear zone appeared to be too large to match that of the gravity wave. Slower modes focus attention on the embayment itself. What is the frequency of the main-gyre rotation and can it resonate with the gravity wave? At every radial distance the embayment gyre has a different rotation period, hence it is not obvious how to determine its overall frequency. However, not all frequencies are of interest, but it is the most energetic one that would drive

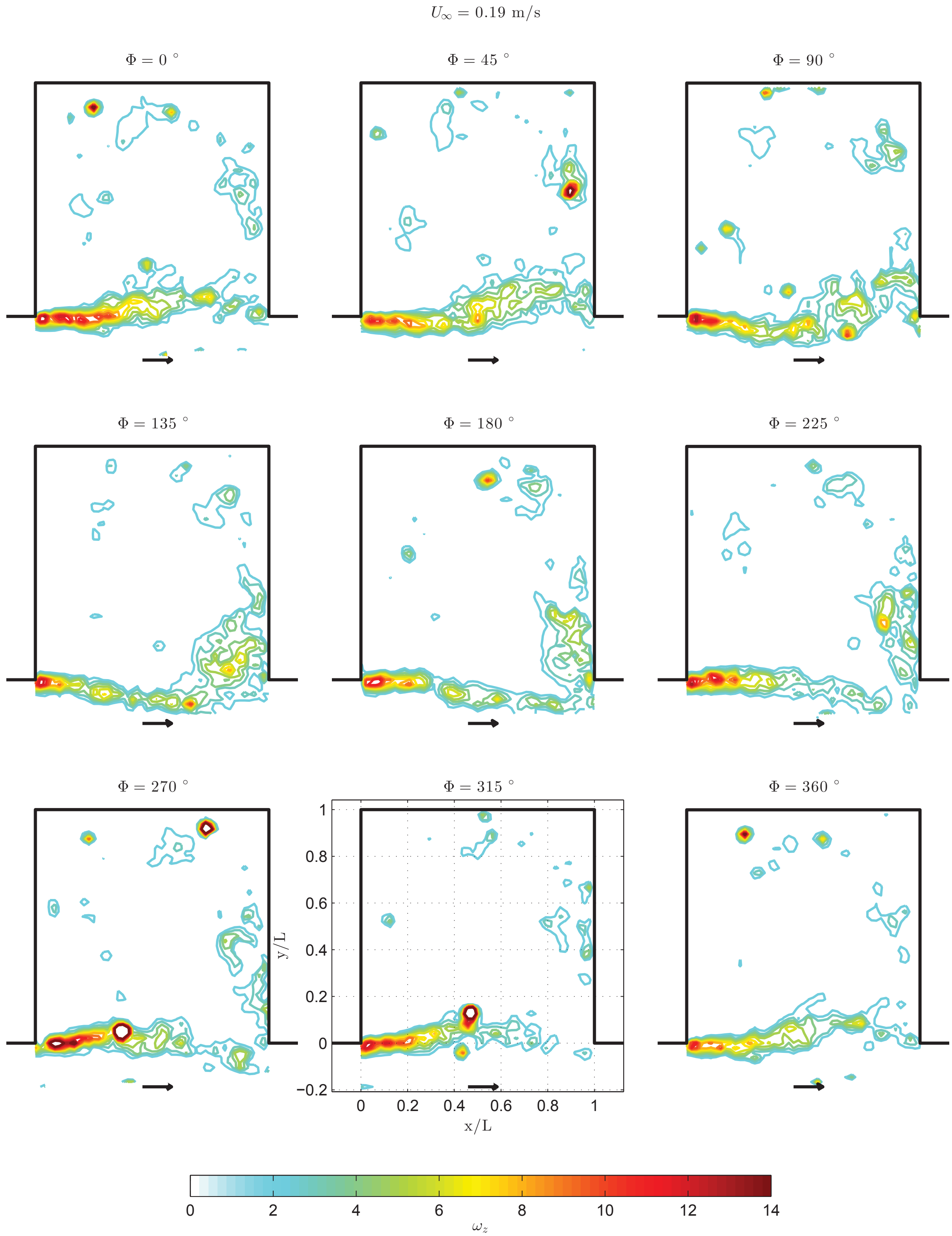

Figure 5.28: Contour plots of the phase averaged vertical vorticity, ω_z, at z/L = 0.62 for $U_\infty = 0.19$ m/s. Φ is the phase of the first mode of the transverse gravity wave, which has a period of 2.7 s (or a frequency of 0.36 Hz. Φ changes from 0° to 360° with a step of 45°, corresponding to 9 panels.

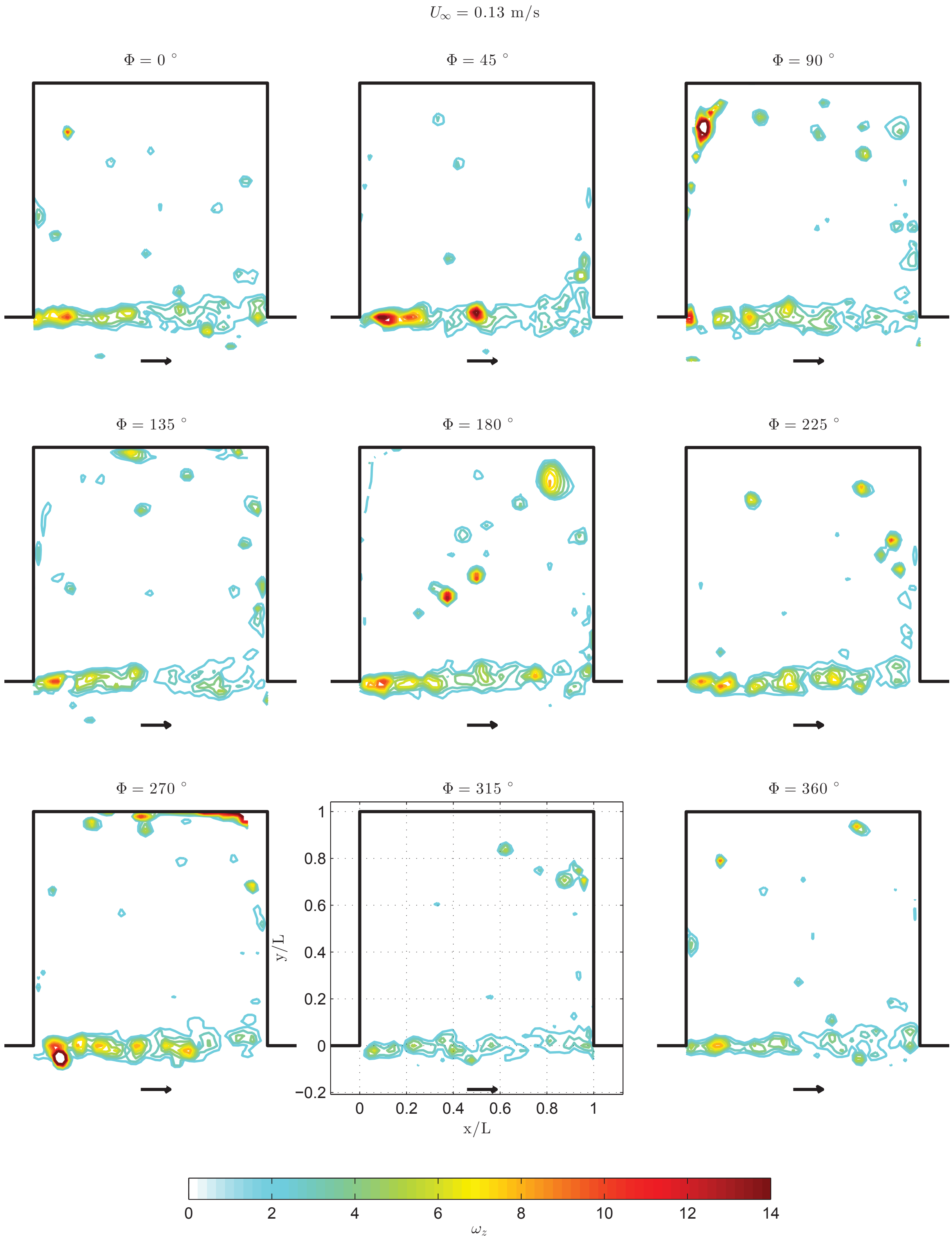

Figure 5.29: Contour plots of the phase averaged vertical vorticity, ω_z, at z/L = 0.62 for $U_\infty = 0.13$ m/s. Φ is the phase of the first mode of the transverse gravity wave, which has a period of 2.7 s (or a frequency of 0.36 Hz. Φ changes from 0° to 360° with a step of 45°, corresponding to 9 panels.

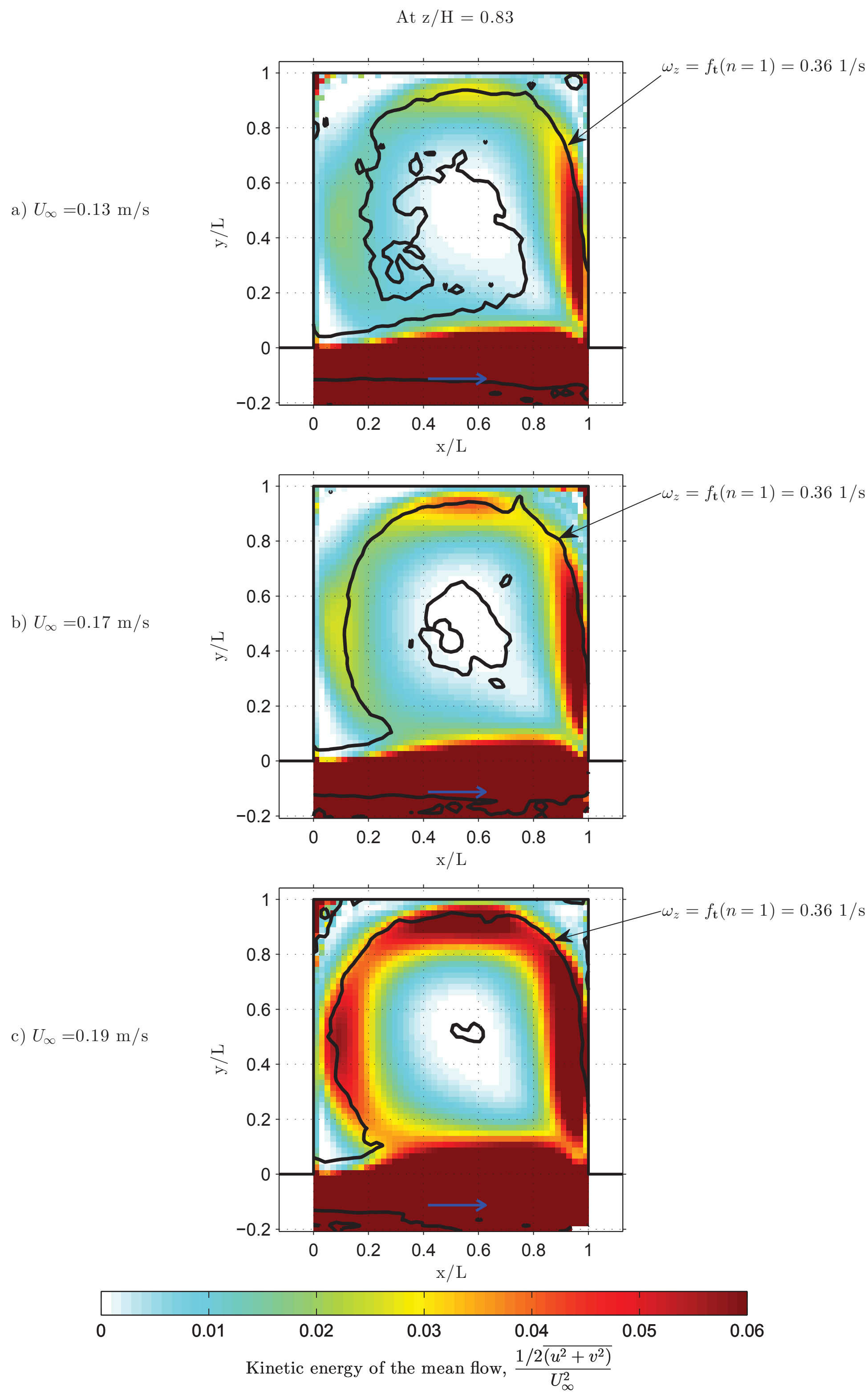

Figure 5.30: Colour plots of the mean kinetic energy of the horizontal flow at the elevation of z/H=0.83. Black thick contour indicates the position of the vertical vorticity, ω_z, equal to the frequency of the first mode of the transverse gravity wave (0.36 Hz). a) $U_\infty = 0.13$ m/s. b) $U_\infty = 0.17$ m/s. c) $U_\infty = 0.19$ m/s.

the flow. In Figure 5.30 colour plots of horizontal kinetic energy (KE) in the embayment are shown. On top of the KE plots there is a contour of vertical vorticity, ω_z, equal to the gravity wave frequency, $f_t(1) = 0.36$ Hz. For the case of the lower free-stream velocity (panel a) the ω_z contour does not follow the flow pattern. The line is not smooth and it crosses the stream lines. For the higher free stream velocity (panel b), the vorticity line follows the high kinetic energy region, but near the upstream wall of the embayment it is deflected inwards leaving the high KE zone. The highest free-stream velocity case (panel c) has the strongest correspondence between the the line of largest KE and the vertical vorticity contour of 0.36 Hz. This observation means the amplification of the gravity-wave amplitude in the embayment flow is possibly caused by resonant coupling with the most energetic mode in the recirculation gyre. The intensified gravity wave is forcing the shear layer to undulate with the same frequency, enhancing exchange between the main channel and the cavity.

5.4 The exchange between the main flow and the cavity

Recent papers by Rockwell and his research group (Wolfinger *et al.*, 2012; Tuna *et al.*, 2013; Tuna & Rockwell, 2014) show the amplified gravity waves in a shallow embayment lead to an increase in the Reynolds stresses, the rms velocities, and time-averaged transverse velocities across the shear layer. All these lead to increased exchange coefficients between the embayment and the main channel. In this section it will be confirmed that gravity waves are increasing the entrainment. The exchange coefficients will be also quantified.

Following the papers of the Rockwell group, in order to compare the turbulent exchange between the cases with weak and strong gravity waves, the horizontal Reynolds stress (Figure 5.31) and transverse rms velocity (Figure 5.32) are considered. From both figures it is evident that the case of $U_\infty = 0.19$ m/s, where gravity waves are intensified, has considerably larger Reynolds stresses and transverse velocity fluctuations. However, from Figure 5.32 it is also clear that there is a significant difference between the two cases of lower free-stream velocities. The amplitude of the gravity wave between $U_\infty = 0.13$ and $U_\infty = 0.17$ m/s is only 0.1 mm different, but the transverse fluctuations are significantly larger for $U_\infty = 0.17$ m/s. This may be attributed either to the gravity wave, that even with a slight increase in the amplitude can significantly change the flow, or, as mentioned before, to the fact that normalization by the free-stream velocity is not an effective way to remove the effect of changing discharge.

To quantify the mixing between the main channel and the embayment, the exchange coefficient will be calculated as proposed by Weitbrecht *et al.* (2008). The instantaneous exchange velocity, $E(t)$, spatially averaged over the main stream-cavity interface, is defined as:

$$E(t) = \frac{1}{L} \int_0^L |v(t)| dx, \tag{5.5}$$

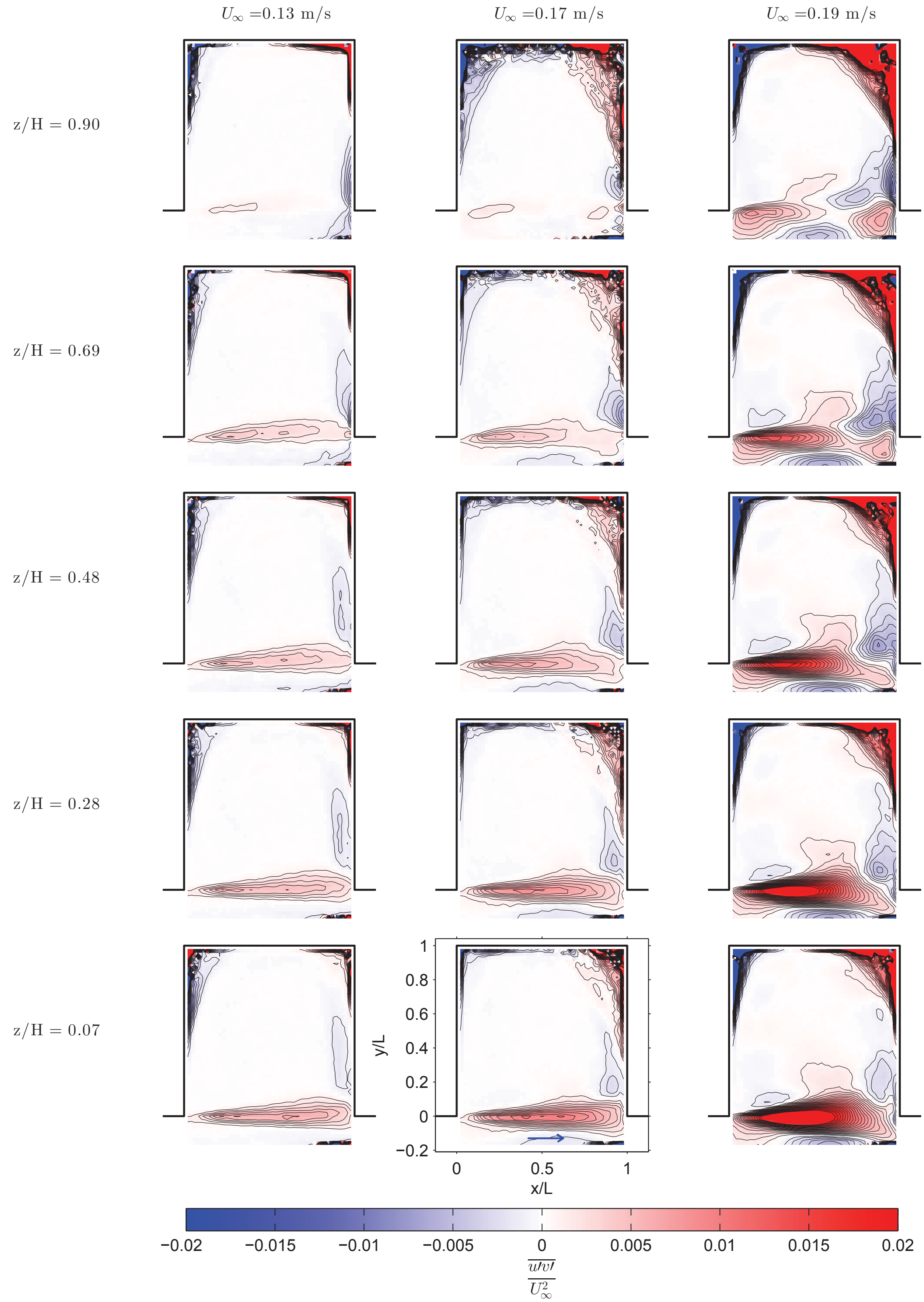

Figure 5.31: Contour plots of the horizontal Reynolds stress, $\frac{\overline{u\prime v\prime}}{U_\infty}$, at different elevations above the bed, z/H. a) $U_\infty = 0.13$ m/s. b) $U_\infty = 0.17$ m/s. c) $U_\infty = 0.19$ m/s.

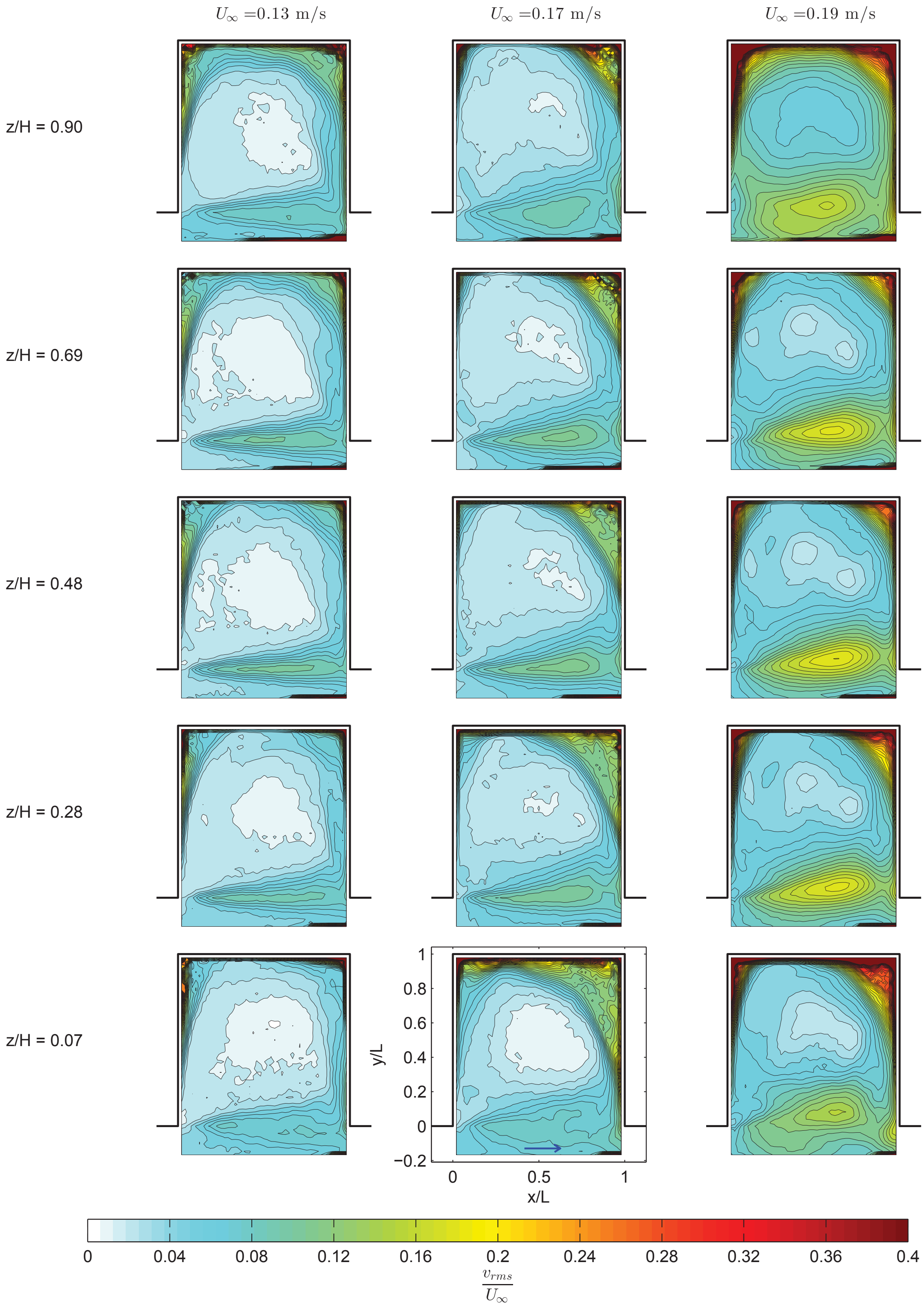

Figure 5.32: Contour plots of the transverse rms velocity, $\frac{v_{rms}}{U_\infty}$, at different elevations above the bed, z/H. a) $U_\infty = 0.13$ m/s. b) $U_\infty = 0.17$ m/s. c) $U_\infty = 0.19$ m/s.

where $v(t)$ is the transverse component of velocity at the main stream-cavity interface, L is the width of the embayment. The mass exchange coefficient, k, is then defined as

$$k = \frac{\overline{E(t)}}{2U_\infty}, \tag{5.6}$$

where $\overline{E(t)}$ is the time-average of the exchange velocity (Weitbrecht *et al.*, 2008; Tuna *et al.*, 2013).

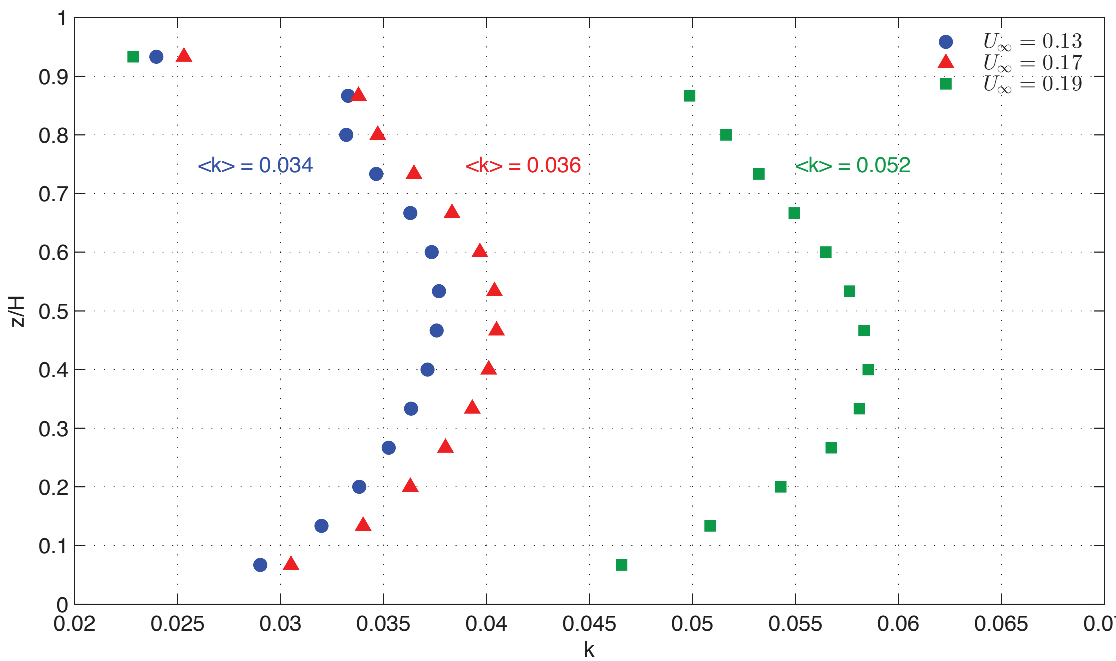

Figure 5.33: Vertical profiles of the exchange coefficient, k, between the main channel and the embayment for the three free-stream velocities, U_∞.

The exchange coefficient between a cavity and an embayment has been considered to be a constant value is around 0.01-0.03 (Altai & Chu, 1997; Valentine & Wood, 1977). Uijttewaal *et al.* (2001) obtained a constant value of k=0.024, irrespective of the river flow velocity and the cavity shape. However, Uijttewaal *et al.* (2001) also note that when the exchange coefficient was measured by floating particles, it yielded a k that was twice as large. Tuna *et al.* (2013) obtained k=0.03 for the case of negligible gravity waves and 0.04 for the case with gravity waves.

Figure 5.33 presents the vertical profiles of the exchange coefficient for the three free-stream velocities. For the two cases of weak gravity waves (U_∞ = 0.13

and 0.19 m/s) the exchange coefficient is similar and equals about 0.034 and 0.036, respectively. In the case with a strong gravity wave, $k = 0.052$. This value is considerably larger than the exchange coefficient obtained by Tuna *et al.* (2013) for the case of intense gravity waves, even though the amplitude of the wave in their work is 0.08 of the flow depth, and in the present work it is only 0.03. Hence, one could expect a stronger influence of gravity waves on the flow and hence a larger k in their work. The reason the exchange coefficient is so much larger in the current experiments may be that the dominant gravity wave in this study is a transverse gravity wave, whereas in Tuna *et al.* (2013) it is longitudinal one. In a recent paper Tuna & Rockwell (2014) present results of two sets of experiments with transverse and longitudinal gravity waves dominating the flow. Judging from Figure 12 of their paper (transverse velocity magnitude across the interface) it appears plausible that transverse gravity waves enhances mixing more efficiently than longitudinal ones.

In Figure 5.33 the exchange is stronger at middle depth than at the surface which appears to contradict the findings of Uijttewaal *et al.* (2001) where the floating particles measurements resulted in the higher exchange. The reason for this contradiction is not completely clear. However, this may be associated with the fact that in the current calculation of the exchange we account for the region at the downstream end where the exchange appears to be strong, but in reality the flow enters the embayment to leave it immediately (see Figure 5.9). Another reason may be associated with the experimental errors of the measurement techniques used in Uijttewaal *et al.* (2001), where the floating particles overestimate the local exchange or the integration of the dye concentration over the depth results in the lower exchange values.

To conclude the discussion of gravity waves, it is fair to state that they can considerably affect the flow in a shallow embayment. The exchange coefficient was observed to increase by nearly a factor of two for the case where gravity waves were present. It is important to note that considering gravitational instability initially was not with the scope of the present investigation. Thus, when choosing the flow conditions, it was attempted to minimize gravity waves appearing in the channel, but it was found that even relatively small gravity waves can change the flow considerably. It is hence important to recognize the resonant conditions under which gravity waves rapidly increase in amplitude. It was shown in the present work that a resonance may be occurring between the first mode of transverse gravity waves and the most energetic mode of the main gyre circulation.

It was fairly noted by the external reviewer of this thesis, Dr. Uijttewaal, that the method used here to calculate the exchange rate does not eliminate the direct effect of the surface gravity waves. Averaged over the wave period, the net exchange may remain unchanged, but the exchange velocity can be overestimated. The authors agree with this statement and wish to thank Dr. Uijttewaal for pointing it out. Indeed, one way to recalculate the exchange would be to set a region through which the flow has to go through before being counted as "entered" or "left" the embayment instead of the current method where an arbitrary surface was set as the limit that has to be crossed. Setting a region that has to be transpassed would allow to eliminate wave-induced oscillations that do not contribute to the net exchange as long as this region is wider than the amplitude of the oscillation. The authors believe that this recalculation will result in better accuracy. However, the overall conclusions on the gravity waves increasing the exchange rate will likely remain unchanged. It is quite clearly seen from visual observations or, for example, Figure 5.28 that the induced oscillations not only produce the flow to ondulate but also result in stronger mixing.

CHAPTER 6
Conclusions

The following chapter presents the conclusions pertaining to the present work and is divided into four sections. The first reviews two topics related to experimental aspects of this work: the possibility of optical measurements through a free interface and its limitations, and two error-analysis techniques that were developed in the course of this study. The results of their application to the current experiments are also discussed. Section 6.2 summarizes the contributions of this work to the understanding of shallow embayment flows. A short summary of these original contributions is given in Section 6.3. Finally, suggestions for future work are made in Section 6.4.

6.1 Experimental aspects

6.1.1 Free-surface 3D-PTV

To the author's knowledge, prior to this work 3D particle tracking velocimetry (3D-PTV) through a free water surface had never been performed. The reason being that one would expect large errors to be produced by the varying refraction angles of the unsteady curved surface through which particle positions are tracked. In this work it was shown that even when gravity waves are present, producing surface slopes of up to $0.2°$, and changes in surface elevation of up to 3% of the water depth, the uncertainty in velocity measurements was less than 0.4% of the free-stream velocity. This result may be surprising as the overall absolute position errors produced are not at all small. They were as large as 1.2% of the water depth, H. However, variation of the error field in space is very gradual. The gravity waves are slow and have a large wavelength. The errors produced by the calibration procedure are also slowly varying. As a result, the relative position error is very small. The relative position error measured for two points with 10 mm ($H/3$) separation is less than $0.04\%H$. It is thus clear that when the characteristic length and period of surface perturbations are much larger than the characteristic displacement of a particle per frame and the data sampling period, it is relatively straightforward to obtain accurate velocity measurements. It is also possible to obtain accurate measurements of the spatial derivatives of the velocity field through an open surface if the particle seeding density is such that the average distance between particles is much smaller than the wavelength of surface perturbations. These results are not only applicable to open-channel measurements, but could also be useful for experimentalists dealing with any kind of fluid interface. For example, optical measurements in a stratified medium can be performed through an interface that exhibits some perturbations on its surface, as long as the waves are relatively long.

6.1.2 Error analysis techniques

Two novel techniques were developed to assess the uncertainty in open-surface 3D-PTV measurements. Moreover these techniques can be applied to any optical flow measurements that employ flow tracers. "Regular" 2D- or 3D-PTV, without any open surface, can use these techniques to quantify the error in the velocimetry. They can also be adapted to PIV experiments.

The first technique evaluates the positions of dots arranged in a regular pattern on the bottom of the flow. The difference between the real and measured positions of each dot results in a map of the error distribution within the domain of interest. This method is especially useful for studies in complicated geometries as it allows distinct estimates of the errors in different regions. It permits analysis of random and systematic components of the errors separately, which is important if one wishes to consider not only time-averaged statistics, but also instantaneous velocity or vorticity fields. However, the dot pattern that was used is flat and was positioned at the bottom of the channel. This means that only the horizontal variability of the error is accounted for. In the present flow, this is beneficial as gravity waves are moving in the horizontal direction and the vertical error is largest at the bottom of the channel (Snell's law), as that is the furthest from the cameras. It should also be noted that this method neglects all the error sources that are introduced into the data after the determination of the particle positions. For example, finite differencing and interpolation errors associated with the velocity calculation. This brings us to the second error analysis technique that was developed to account for the error sources that were neglected in the first one.

The second technique of error analysis is based on the principle that two points on a solid body have constant distance between each other. A dumbbell-shaped object (a thin black rod with the particle glued onto it at each end, see Figure 4.28) was moved around the domain of interest. The recordings of the tracks of the two particles were then processed. This method estimated the velocity error of the 3D-PTV method by calculating the velocity of the two particles along the vector connecting them, which should be zero. Thus, the rms of the deviation of this value from zero results in the magnitude of the velocity error. The advantage of this method is that it accounts for all the sources of error in all the multiple steps of the PTV procedure, including construction of particle tracks, calculation of velocity with the centred difference scheme, and the filtering procedure that performs a polynomial fit between successive particle positions. It also accounts for the variation of position error with depth, which was neglected in the previous technique. The disadvantage of this method compared to the previous one is that it does not readily lend itself to an estimate of the spatial distribution of the velocity error. Thus, if some local disturbances are present in the flow they are more likely to be captured by the stationary dot pattern method.

These two error analysis techniques were successfully applied to the open-surface 3D-PTV system that was used for the current experiments. The stationary pattern test resulted in a velocity error of 0.3% and 0.2% (of U_∞) for the free-stream velocity cases of 0.13 and 0.19 m/s (the lowest and highest in the experiments). The dumbbell target test gave a velocity error of 0.4% of U_∞ for the same two free-stream velocities. The higher error value in the dumbbell target test is associated with a more complete account of error sources.

The stationary pattern test also allowed a detailed analysis of the error sources and their behaviour. It was found that the vertical position and velocity errors are 2-3 times larger than the horizontal ones. This was expected, as all three cameras are mounted above the channel, and the angle between them was chosen to be relatively small (Appendix A). Since the vertical velocity is also generally the smallest in a shallow flow, the resulting relative error in the vertical direction was the most significant one. Areas of high vertical velocity errors were identified, and the regions within 5 mm of the embayment walls were found not to provide reliable PTV measurements, as the systematic error there can locally reach 20% of the vertical velocity. It was also found that the systematic component of the velocity error was considerably larger than the random component, sometimes by an order of magnitude. For example, for the lowest free-stream velocity, the systematic error is about 0.3% of U_∞, and the random error is 0.03%. This means that errors produced by the non-stationary waves on the water surface are much smaller than those produced by the stationary water curvature or by the measurement procedure itself. The weakest point of the measurement procedure was the calibration of the cameras. A test was performed to determine the position errors in still water. This quantified the errors associated with the algorithm and the calibration method, resulting in vertical position errors of 0.2 mm (with its maximum at the edges of the domain, near the embayment walls), whereas the vertical position error in the stationary-pattern test with running water gave an error of 0.30 and 0.34 mm for the two flow cases (U_∞ =0.13 and 0.19 m/s). It is thus fair to conclude that the imperfections of the calibration procedure are responsible for more than half of the error produced in the experiments. At the same time, waves on the surface did not have a significant effect on data quality. This again confirms that optical data acquisition here through a non-stationary interface is not only possible but also relatively straightforward for the flow conditions studied herein.

6.2 Shallow embayment flow

3D-PTV measurements were performed in a shallow embayment flow, which was modelled in a laboratory flume with a square embayment 0.24 by 0.24 m^2 at mid-channel. The bed was flat and the water depth was about 0.03 m. Experiments were performed for three different free-stream velocities, U_∞, equal to 0.13, 0.17, and 0.19 m/s, resulting in water-depth Reynolds numbers (Re) in the channel of 3900, 4800, and 5400, respectively. The Froude numbers varied accordingly from 0.24 to 0.33.

Instantaneous and time-averaged 3D velocity and vorticity fields were obtained for the entire embayment and the shear zone for each of the flow cases. Given that one of the important questions pertaining to shallow flows and shallow embayments is whether two-dimensional models are an appropriate approximation for the flow therein, three-dimensional PTV experiments were undertaken to quantify the three-dimensional features of the flow, with the ultimate goal of their parametrization, or at least the definition of the parameter regime in which two-dimensional models are appropriate. The results of the 3D-PTV measurements discussed in this thesis are summarized below.

The exchange process between the embayment and the main channel was shown to be fully three-dimensional. The flow enters the embayment along the bed closer to the downstream end of the interface. As it enters, it rapidly occupies the whole depth and then circulates in the large gyre. When it returns near the interface with the main channel flow, it separates, and the top layer leaves the embayment, whereas the rest continues to circulate inside the embayment. The area through which the water is leaving the embayment is confined to the top 20% of the water depth. The inflow is mostly coming along the bed, but it is more concentrated at the downstream end.

A secondary circulation inside the main gyre in the embayment was shown to exist in the time-averaged flow field. The flow spirals inwards near the bed, rises in the centre and spirals outward closer to the surface. The "tea-cup" like mechanism was proposed by Gaskin *et al.* (2002) for this secondary circulation. Its mechanism is based on a balance between the pressure-gradient and centrifugal forces within the main gyre. Near the bottom the flow is decelerated by bed friction, and the centrifugal force cannot balance the pressure gradient. Consequently, the flow is drawn into the core of the gyre. It was shown that the radial inflow occupies only the bottom 20-30% of the flow depth, which corresponds to the thickness of the bottom boundary layer, confirming that this inflow is generated by the deceleration of the flow near the bed. The inward spiralling is a relatively intense confined flow, whereas the outward motion is spatially less defined and more difficult to capture. The streamlines of the radial outflow have a complicated shape. The point from which streamlines originate appears to change its position with depth and mean-stream velocity. It also changes form, sometimes appearing as a line. It is possible that the position of the maximum divergence wanders around the embayment with time and converges slowly, if at all.

Görtler-like vortices were discovered in the boundary layer developing along the side walls of the shallow embayment. For the highest free-stream velocity there is a pair of counter-rotating streamwise vortices situated on top of each other. This vortex pair exists along all three side walls of the embayment. They bend, following the main gyre curvature. The vortex near the bed has positive helicity (vorticity and velocity vectors are aligned) and produces a radial inflow near the bed, reinforcing the "tea-cup" secondary circulation. The second vortex has negative helicity (vorticity and velocity vectors have opposite directions), and it produces the radial inflow near the surface, weakening the secondary circulation. In the case of the lowest free-stream velocity, there is only one streamwise Görtler-like vortex instead of a pair, although some traces of its counterpart appear. It has positive helicity and occupies almost the whole flow depth, producing radial inflow near the bottom and radial outflow near the surface, both reinforcing the secondary circulation. The case of the intermediate free-stream velocity appears to be transitional with one streamwise vortex at the far wall of the embayment and a counter-rotating pair at the upstream wall. This was found to be analogous to results in open-cavity flows in which Görtler vortices were also observed. To compare with the present ones, one could imagine the embayment being infinitely deep, and the flow in it not being affected by either free-surface or the channel bed. In that flow (unbounded open cavity) the wavelength of the Görtler vortices (measured as a distance between two pairs of the counter-rotating structures) was found to be about $0.4L$ (Faure *et al.*, 2007; Citro *et al.*, 2015; Brès & Colonius, 2008), where L is the width of the embayment. In the shallow embayment, the corresponding wavelength of the Görtler vortices is $0.12L$-$0.24L$ depending on the free-stream velocity. The wavelength, being considerably smaller than that in the open-cavity flow, is likely to be a result of the confined space formed by the two boundaries, channel bed and free-surface. These streamwise Görtler-like vortices are likely to play an important role in the exchange between the embayment and the main flow and in the scouring and sedimentation process. It is thus important to recognize the conditions in which they may appear. This can be accomplished with a linear stability analysis and more experimental data with varying free-stream velocity.

The frequency spectra of the velocity fluctuations at different points within the domain showed that the shear zone exhibits a -5/3 spectral slope and the points within the embayment exhibit steeper slopes, close to -3, suggesting that the large-scale structures within the embayment may possess two-dimensional characteristics, whereas the shear zone is dominated by fully three-dimensional turbulent structures. It is also noted that the frequency spectra inside the embayment should be interpreted with care. The theoretical results of Kolmogorov (1941) and Kraichnan (1971) concerning slopes of turbulence spectra were obtained using two-point correlation functions. The analogy between the two-point correlation spectrum and the frequency spectrum can be made only when the Taylor "Frozen turbulence" approximation is valid. This requires a strong mean flow or a high enough Re, which assures large separation of scales and therefore small scales being advected past the probe by the large scales. In the main channel, the mean flow is an order of magnitude stronger than the rms velocities. However, inside the embayment this is not always true. Hence, the steeper slopes of the spectra inside the embayment may be associated with the breakdown of the Taylor approximation due to insufficient advection velocity.

Free-surface oscillations were inferred from the time series of the vertical position of the particle closest to the water surface in 2x2 cm columns. Two types of gravity waves were observed: a longitudinal wave with a wavelength of twice the size of the embayment, and transverse one with a wavelength of twice the channel width plus the embayment width. In the case of the lowest free-stream velocity, the gravity waves have negligible amplitudes. For the intermediate free-stream velocity, the first mode of the transverse gravity wave starts to be more pronounced. The highest free-stream velocity exhibits a 1 mm peak of the amplitude of the first mode of the transverse gravity wave (or $0.03H$, where H is the water depth). The increase in the gravity-wave amplitude with the free-stream velocity is attributed to a resonant response. The sources of the resonant frequency were investigated. The coupling of gravity waves with the frequency of the inherent shear instability suggested by Tuna *et al.* (2013) was not confirmed. It is instead suggested that the first mode of the transverse gravity wave resonates with the most energetic mode of the large-scale gyre within the embayment.

Consistent with the results of Tuna *et al.* (2013) it was confirmed that gravity waves in a shallow embayment significantly increase the transverse rms velocities and the Reynolds stress at the interface between the embayment and the main flow. Consequently the exchange between the embayment and the channel flow intensified. The exchange coefficient, k, calculated for the low free-stream velocity case with negligible gravity-wave amplitude was found to be about 0.034. This value of k is in agreement with those measured by Altai & Chu (1997); Valentine & Wood (1977); Uijttewaal *et al.* (2001). These authors suggest k is a constant between 0.01 to 0.03 independent of the free-stream velocity. However, the higher free-stream velocity flow with high-amplitude gravity waves produced an exchange coefficient of 0.052. It is thus fair to conclude that the exchange coefficient, k, may not be constant for shallow flows where gravity waves are significant. Another interesting observation is that Tuna *et al.* (2013) found an exchange coefficient of 0.04 for the case with high-amplitude gravity waves, which is somewhat smaller than the one obtained in the present experiments (0.052), even though the amplitude of their gravity waves was much larger ($0.08H$ as opposed to our $0.03H$). This difference is attributed to the different gravity-wave modes that are dominant in these two experiments. For the present case it is the transverse gravity wave, whereas in Tuna *et al.* (2013) it was the longitudinal one. This suggests that the transverse gravity wave has a stronger effect on the exchange process than the longitudinal one.

6.3 Original contribution of this study

In this work contributions were made both to the measurement techniques, and to the physical understanding of a shallow embayment flow. It was first shown that it is possible to obtain accurate particle velocities and their spatial derivatives through an open water surface. When the average displacement of the particles per frame is much smaller than the wavelength of the surface waves, the errors in velocity measurements produced by the surface oscillations are small. Two error analysis techniques were developed to assess the systematic and random components of the errors, their spatial distribution, and their possible sources. The two methods were applied to the current experimental set-up and it was found that the contribution of the unsteady surface oscillations to the velocity error are smaller than those of the 3D-PTV method itself in still water.

The second major contribution of this work is the analysis of the flow field in a shallow embayment. The exchange process between the embayment and the main flow was shown to be fully three-dimensional with significant variations in depth. A secondary circulation inside the main gyre in the embayment was shown to exist in the time-averaged flow field and associated with the bottom boundary layer. Görtler-like vortices were discovered in the boundary layer that curves along the sides of the embayment. Frequency spectra of the velocity fluctuations exhibited a -5/3 slope inside the shear layer and a -3 slope inside the embayment, suggesting that the large-scale structures within the embayment may possess two-dimensional characteristics, but not within the shear layer. Gravity waves were confirmed to significantly increase the exchange between the embayment and the main flow. A frequency of a closed streamline inside the recirculation gyre was proposed to be a source of gravity-wave amplification. It is suggested the gravity wave mode couples with the most energetic mode of the gyre resulting in a resonant response in the form of high-amplitude gravity waves.

6.4 Future work

The exchange coefficient, k, is the most important parameter for shallow embayment flows from the practical point of view. It is the parameter that is required by current operational numerical models, predicting pollution dispersion in rivers with groyne fields and bays. Many researchers have attempted to calculate k, and it is argued in the literature that k is a constant independent of free-stream velocity or geometry of the embayment. Yet we observed it to be non-constant and it was suggested, and confirmed in this thesis, that this could be attributed to the presence of gravity waves. Thus, it is necessary to identify the conditions under which gravity waves are amplified. It was suggested in this work that the they resonate with the most energetic mode in the main gyre circulation. It is thus necessary to establish a relation between the free-stream velocity and the gyre intensity. If such a relation is established it will be possible to predict the resonant state of gravity waves and consequently, the variation in the exchange coefficient. If gyre circulation can be predicted, several other problems will also be solved. The occurrence of Görtler vortices depends on the ratio between the boundary-layer curvature and its velocity. Knowing the main gyre intensity will allow for stability analysis and determination of the parameter regime in which streamwise vortices appear on the side boundaries. The "tea-cup" secondary circulation is also dependant on the ratio between viscous forces in the boundary-layer and the intensity of the gyre circulation. Knowing the gyre circulation will allow prediction of the intensity of the secondary circulation. This goal of determining the dependence of the gyre circulation on free-stream velocity is a relatively simple but labour-intensive task. It will involve a large number of laboratory experiments with varying discharges. However, it is believed that it would be very beneficial.

Appendices

APPENDIX A
Choosing the angle of the cameras

There are two major factors that have to be taken into account when choosing the viewing angles of the cameras. Assume the air/water interface through which the images are taken is horizontal, and the camera angle is measured from vertical (cameras perpendicular to the interface have viewing angle zero). Then, one can say that

- The larger the angle of the camera is the larger the errors produced by the unsteady surface oscillations become.
- However, when the cameras angle is too small, the relative vertical error of a PTV system becomes much larger than the horizontal one.

Thus, to choose the cameras angle properly, it is necessary to assess both factors and find the right balance between them.

In the PTV model, we assume that the imaging interface is flat and has a given elevation. Thus, the error produced by the surface perturbations consists of two components, the error due to the changing slope of the interface and the error due to its changing elevation. First, let's consider the effect of the slope of the water surface. Using Snell's law we can relate the angle of incidence, θ_1, and the angle of refraction, θ_2, of the light rays travelling from a particle to one of the cameras (Figure A.1):

$$\frac{\sin\theta_1}{\sin\theta_2} = \frac{n_{air}}{n_{water}} = c \tag{A.1}$$

$$\theta_1 = \sin^{-1}(c\sin\theta_2), \tag{A.2}$$

where n is the refractive index of the respective medium. However, if the water surface is tilted by an angle β, there will be an error in predicted θ_1 (Figure A.1).

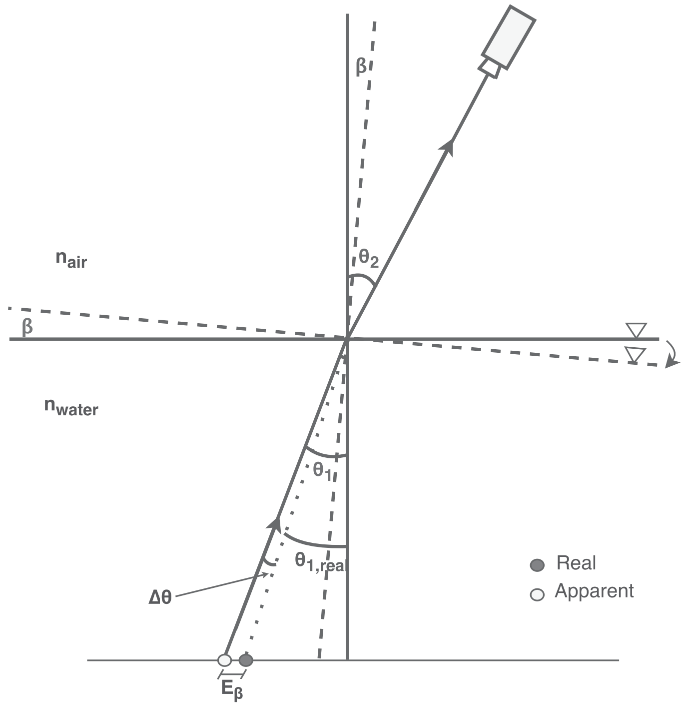

Figure A.1: Schematic of the horizontal position error produced by the tilted water surface.

The real angle will be equal to:

$$\theta_{1,real} = \sin^{-1}[c\sin(\theta_2 - \beta)] + \beta, \tag{A.3}$$

and the angular error produced by the surface tilt, $\Delta\theta$, can be written as following:

$$\Delta\theta = \theta_1 - \theta_{1,real} = \sin^{-1}(c\sin\theta_2) - \sin^{-1}[c\sin(\theta_2 - \beta)] + \beta \tag{A.4}$$

The error in position determination resulting from the angular error is proportional to the distance of a particle from the interface. The maximum error will occur for the particles at the bottom of the embayment. Thus, to calculate the maximum position error,E_β, we will use the distance H, the flow depth:

$$E_\beta = H(\tan\theta_1 - \tan\theta_{1,real}), \tag{A.5}$$

Figure A.2 shows the dependence of the error from the surface slope and the cameras viewing angle, in degrees (a) and in mm (b). It is evident that at relatively

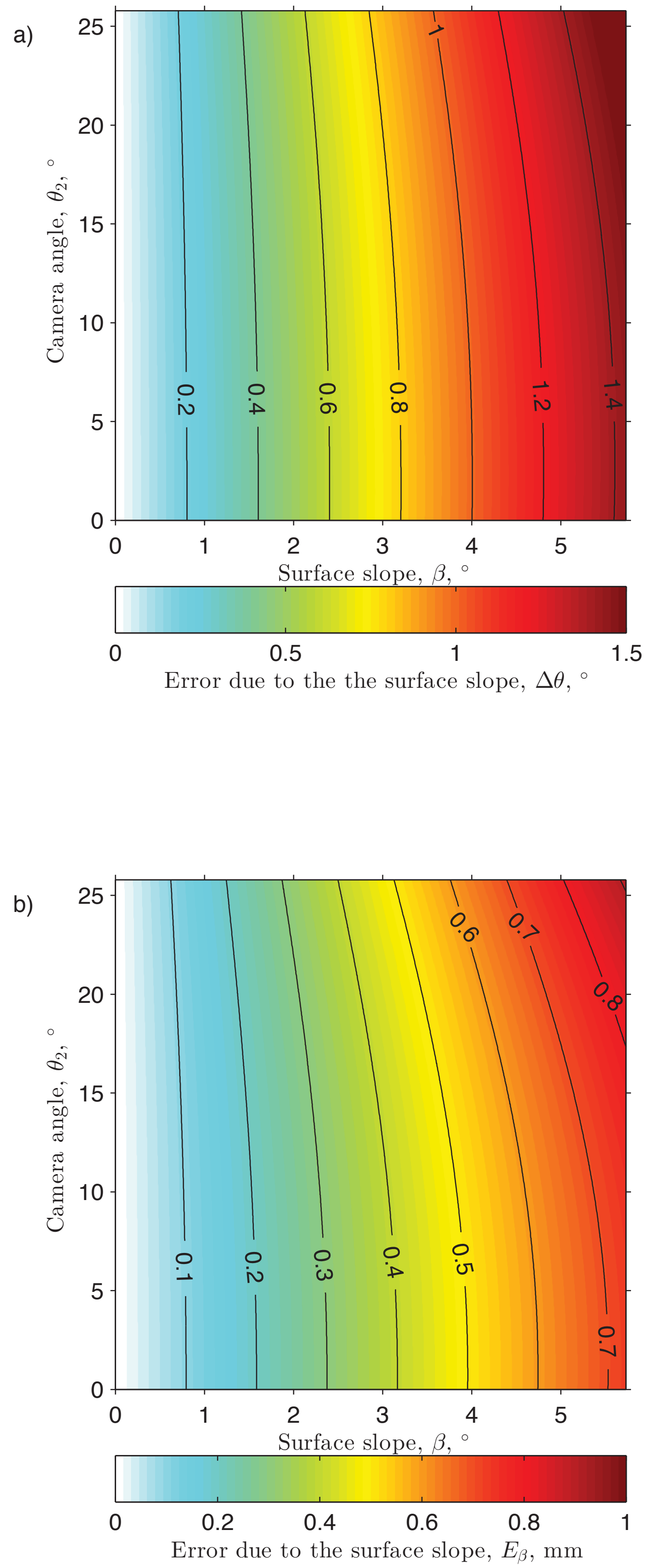

Figure A.2: Error due to the slope of the water surface. a) in degrees. b) in mm calculated for the flow depth $H = 0.03$.

small camera angles ($\theta_2 < 20°$) the error is almost independent of θ_2 and grows linearly with β.

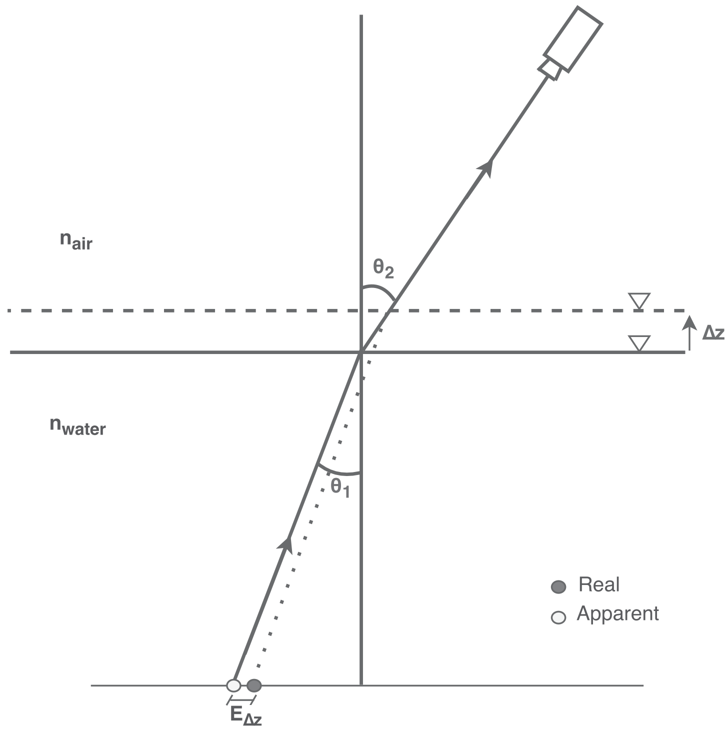

Figure A.3: Schematic of the horizontal position error, $E_{\Delta z}$, produced by elevated water surface.

Next, let's consider the changing elevation of the surface. Figure A.3 shows a schematic of the light rays going through the interface elevated by distance Δz. Simple trigonometry leads to the following expression for the resulting position error, $E_{\Delta z}$:

$$E_{\Delta z} = \Delta z[\tan\theta_2 - \tan\theta_1]. \tag{A.6}$$

Unlike E_β, the error $E_{\Delta z}$ grows both with the camera viewing angle and with the elevation of the surface (Figure A.4). The total error, E, produced by the surface perturbations

$$E = \sqrt{E_\beta^2 + E_{\Delta z}^2} \tag{A.7}$$

grows with the camera viewing angle. Hence, to minimize the error one would want to make the camera angles as small as possible. However, as was mentioned before,

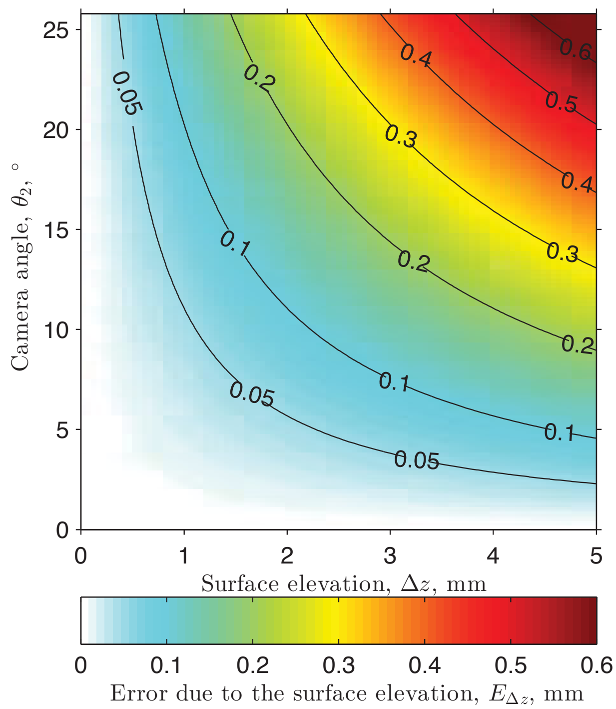

Figure A.4: Horizontal position determination error due to the surface elevation.

if the angle of the cameras is too small the vertical error becomes large. The relation between the vertical and horizontal errors can be estimated as $\frac{E}{\tan\theta_2}$ (Figure A.5).

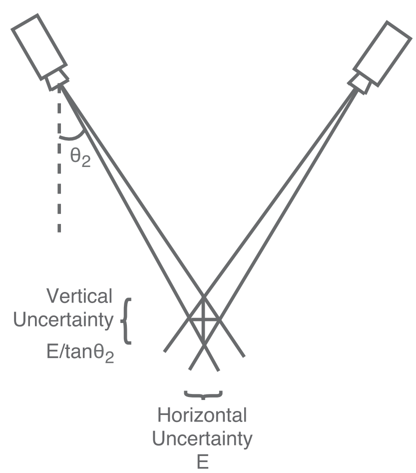

Figure A.5: Schematic of the relation between the vertical and horizontal uncertainties.

All these relations can be used in the future to find the appropriate camera angles for the surface perturbations characteristic of a particular flow. For the present work the maximum elevation of the surface produced by the gravity waves is about 1 mm and the resulting surface angle is approximately 0.2°. FigureA.6 presents the horizontal (a) and vertical (b) errors as functions of the camera angle for the particular case of these surface disturbances. The vertical error grows rapidly with decreasing camera angle, θ_2, for $\theta_2 < 5^\circ$. However, increasing the angle beyond 10° does not improve the vertical accuracy. The horizontal error increases with θ_2, slowly before 5° and faster after. Thus, to choose the appropriate camera angle one should consider making it as small as possible to minimize the horizontal error but not go below $6-7^\circ$ to keep the vertical error small as well. In the experimental setup herein the precision with which the camera angles could be adjusted was limited. The resulting angles measured from the calibration procedure ranged between 6° and 8° for the three cameras. The corresponding position errors for these angles are about 0.04 mm in the horizontal direction and 0.3 mm in vertical, which corresponds well with the position errors obtained in the Error Analysis Section (see Table 4.1), 0.1 and 0.3 mm, respectively. It is relevant to note that this result corresponds well with the recent work of Elsinga & Orlicz (2015) who assessed the errors in the particle-based velocimetry techniques produced by a density jump in a shock wave. They also found that the best way to treat these errors is to put a camera as perpendicular to the flow as possible. Five degrees was found to be optimal.

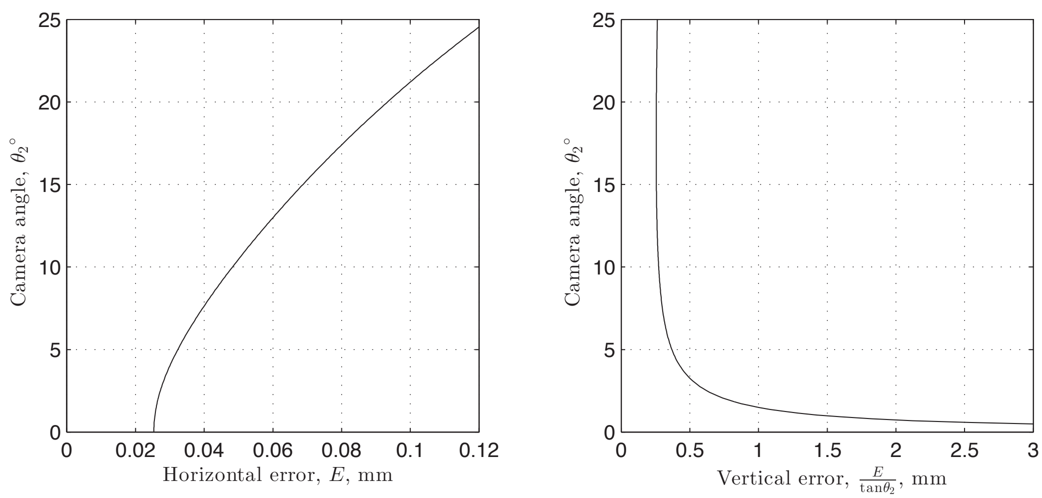

Figure A.6: Total error produced by the surface oscillations in the present study, for the water depth $H = 0.03$ m, the maximum surface elevation $\Delta z = 0.9$ mm, and surface slope $\beta = 0.2°$.

APPENDIX B
Drawings of the calibration object

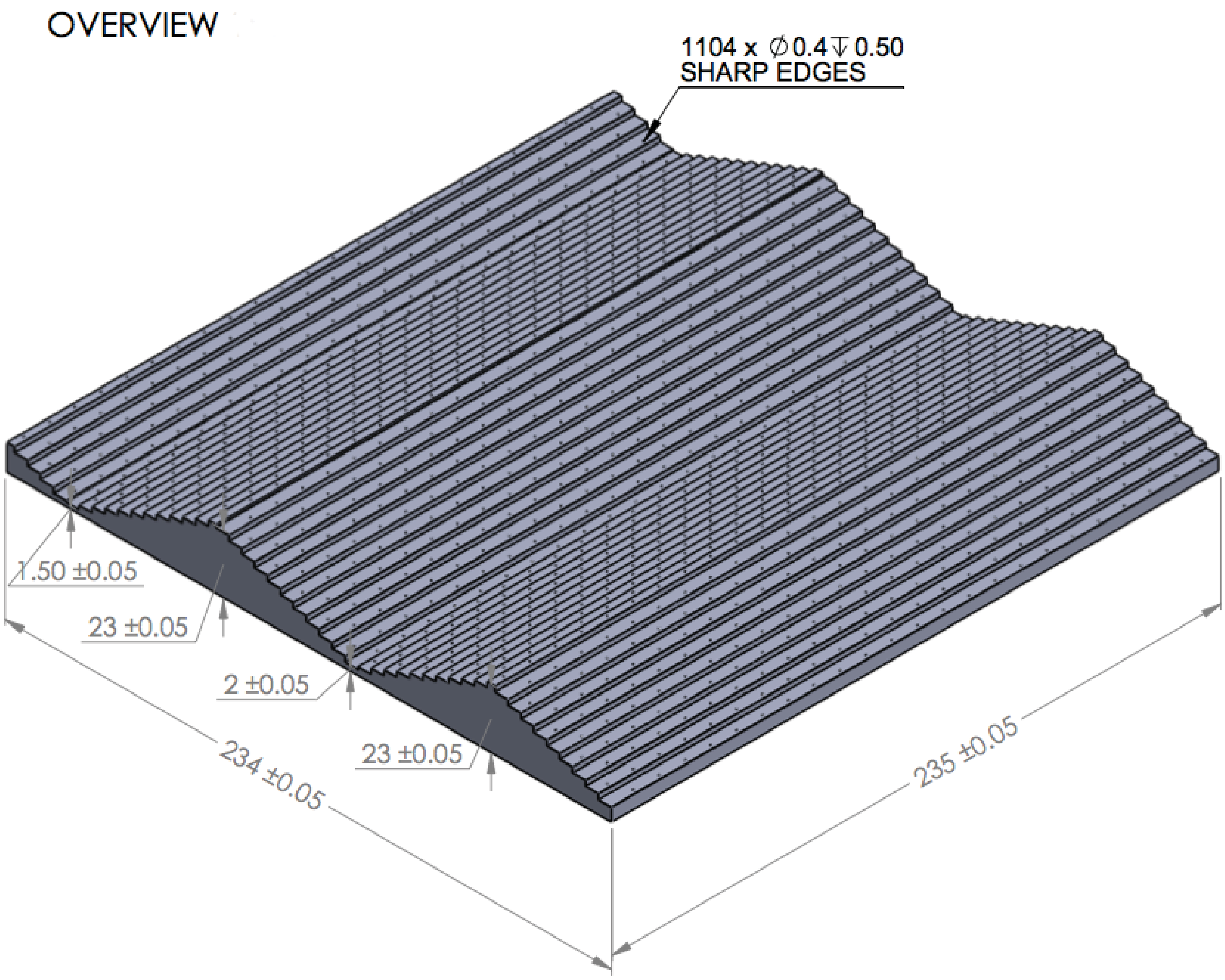

TOP VIEW

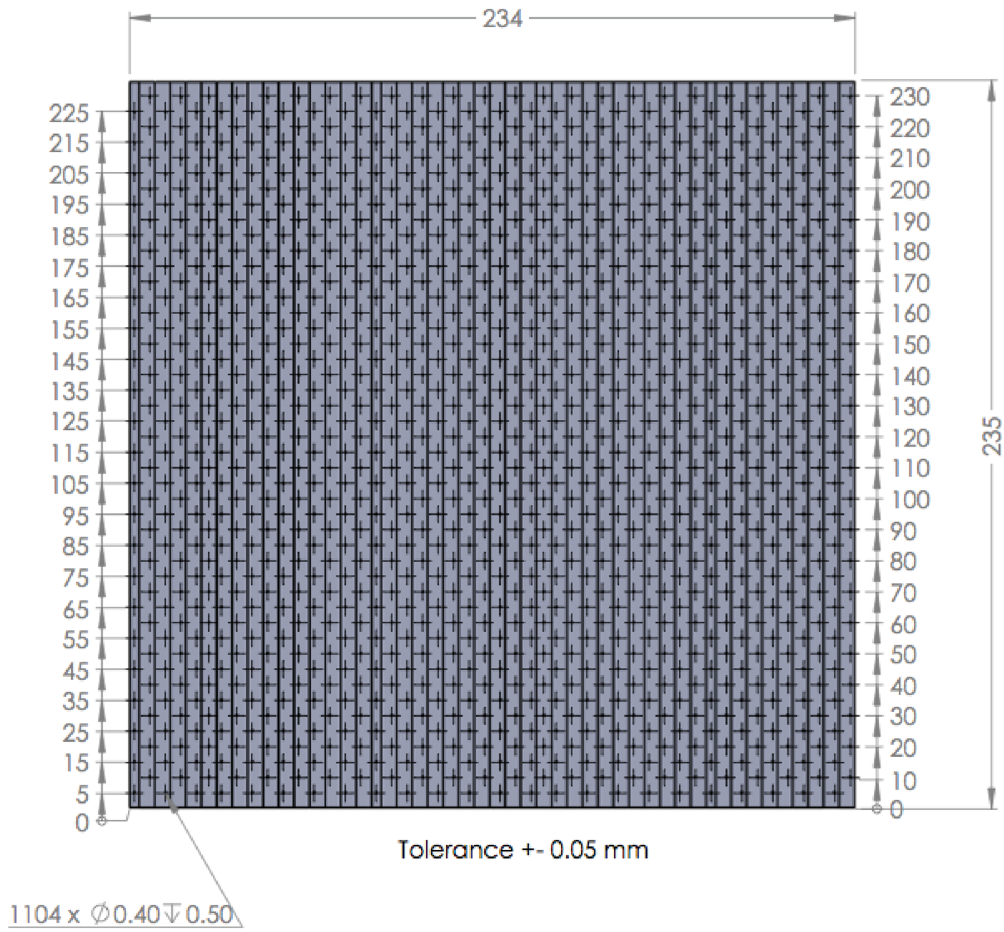

SIDE VIEW

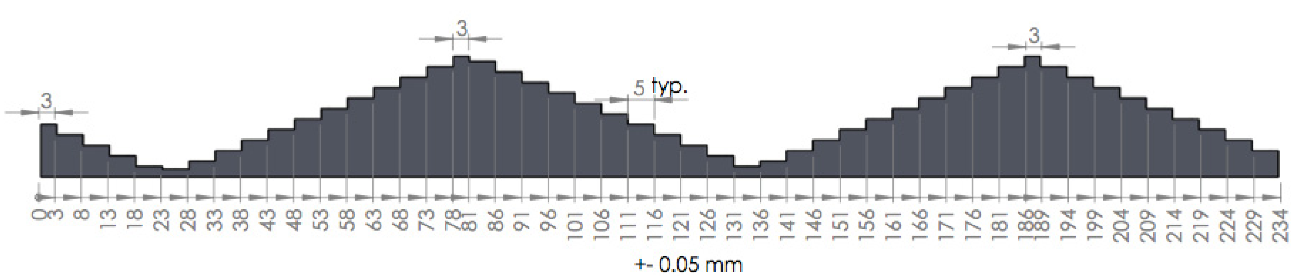

COMMENTS:

Typical **width** of the steps is **5 mm** except for 3 top ones

All the distances should be **measured from the edge** of the object to avoid accumulation of the tolerance

Tolerance of all the distances is **+-0.05 mm**

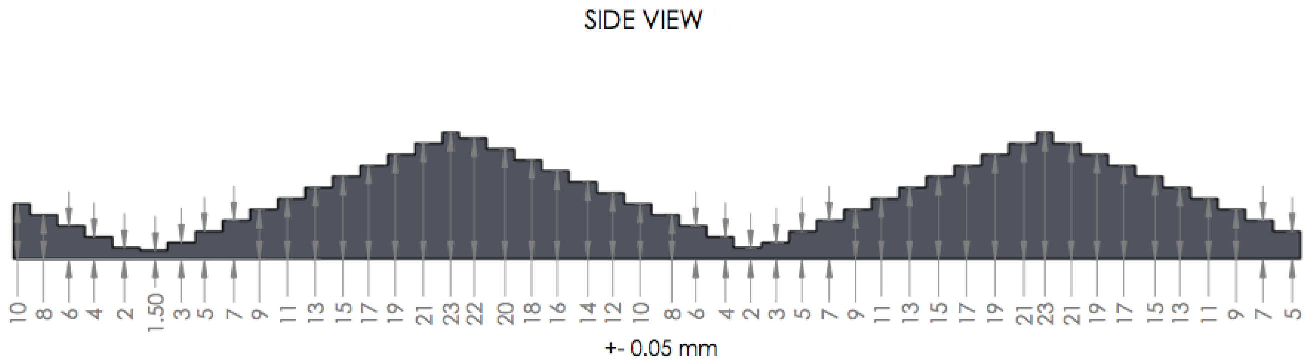

COMMENTS:

Typical height of the steps is **2mm** except for two lowest ones (1 mm and 0.5 mm) and one top one (1 mm)

All the distances should be **measured from the bottom edge** of the object to avoid accumulation of the tolerances

Tolerance of all the distances is **+-0.05 mm**

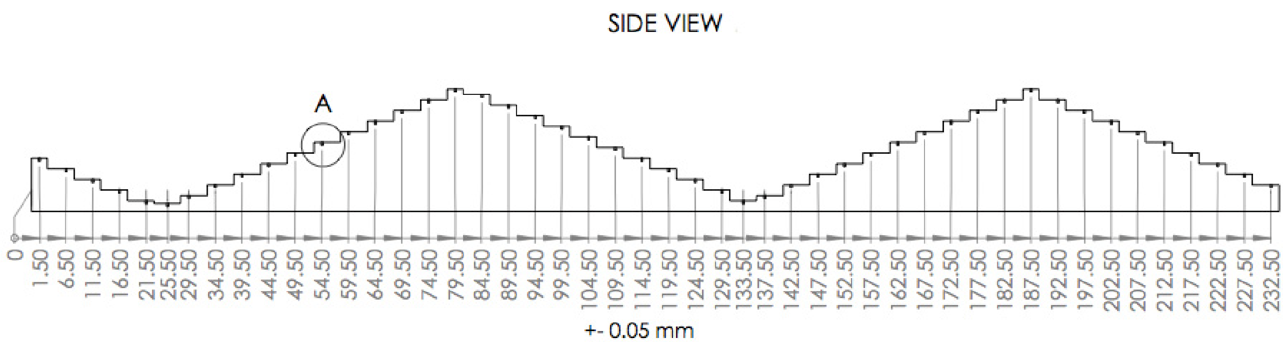

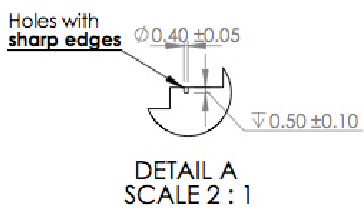

COMMENTS:

Typically, the centers of the holes are **1.5 mm from the edge of the step** except for two bottom steps, where the holes are at the center, 2.5 mm from both sides

All the distances should be **measured from the edge** of the object to avoid accumulation of the tolerances

APPENDIX C
Parameters in the PTV post-processing

There are three groups of parameters in the PTV software (OpenPTV, 2012): main, calibration, and tracking parameters. In the main parameters the general information about the data files and the experimental set-up should be provided:

- the number of cameras and the path to the image files;
- the refractive indices of the media through which the images are taken;
- the grey value thresholds for particle recognition;
- the size of the domain; and
- the parameters for correpondance between the particles seen from different cameras.

In the calibration parameters window one has to specify:

- the path to the calibration images;
- the grey value thresholds for the recognition of the calibration object dots;
- the points for manual pre-orientation of the cameras (preferably should be at the four corners of the domain);
- whether to use additional parameters for the calibration procedure (in this work the use of additional parameters such as lens distortion and affin transformation did not result in a better quality of the calibration);
- dumbbell calibration parameters (used when instead of the calibration object a dumbbell-shaped object is employed for calibration, this was not implemented herein);
- the shaking parameters (to avoid local minima during the calibration optimization procedure).

Tracking parameters should be chosen based on the characteristic velocities and acceleration of the flow. After making an initial guess based on the flow characteristics it is recommended to "play" with them to optimize the result. The goal is to have as many long trajectories as possible, which is usually achieved by increasing the maximum velocities and acceleration allowing for a wider search area. However, if the search area is too big, the code will start to connect different particles into trajectories having big jumps in the paths. Thus, it is important to choose these parameters carefully such that the total number of established trajectories is maximized while still being below the limit beyond which the connections established are spurious. To performs the parameter search one proceeds as follows: i) change the tracking parameters, ii) specify a 20-30 frame period in "Parameters for sequence processing", iii) run the code, iv) use "tracking tab" → "show trajectories" to see whether the connections within trajectories are reasonable, v) note the number of tracks that were lost (displayed in the terminal), vi) repeat the procedure.

All parameters used in the post-processing in this work are presented below. The last image shows the parameters in the code of Lüthi *et al.* (2005) which calculates velocities and velocity derivatives of particles based on their tracks obtained through the OpenPTV software. More information on the usage of the OpenPTV and of the subsequent post-processing codes can be found at

- http://alexlib.github.io/docs/intro.html
- http://3dptv.github.io/.

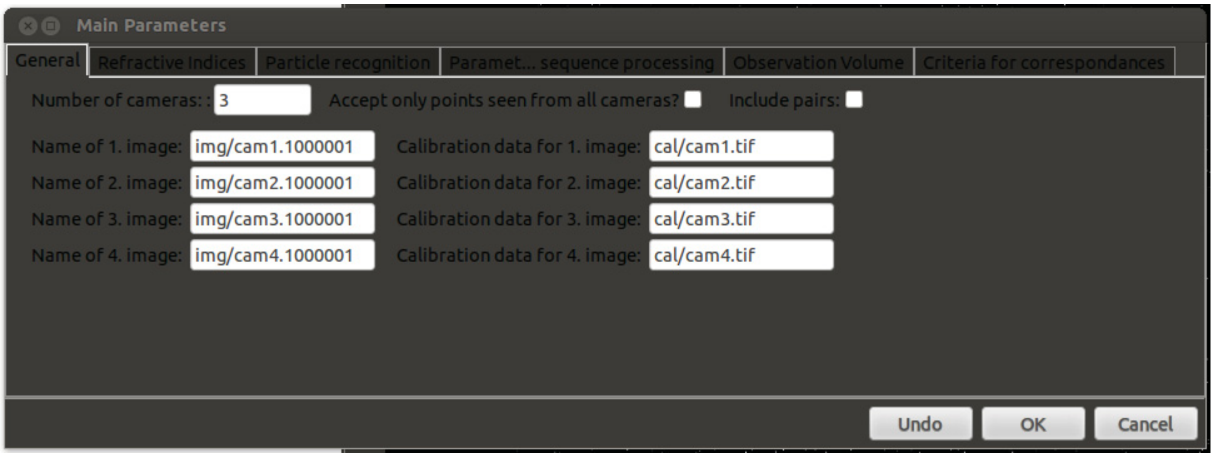
Main Parameters
General
Refractive Indices
Particle recognition
Paramet... sequence processing
Observation Volume
Criteria for correspondances
Number of cameras: : 3
Accept only points seen from all cameras?
Include pairs:
Name of 1. image: img/cam1.1000001
Calibration data for 1. image: cal/cam1.tif
Name of 2. image: img/cam2.1000001
Calibration data for 2. image: cal/cam2.tif
Name of 3. image: img/cam3.1000001
Calibration data for 3. image: cal/cam3.tif
Name of 4. image: img/cam4.1000001
Calibration data for 4. image: cal/cam4.tif
Undo
OK
Cancel

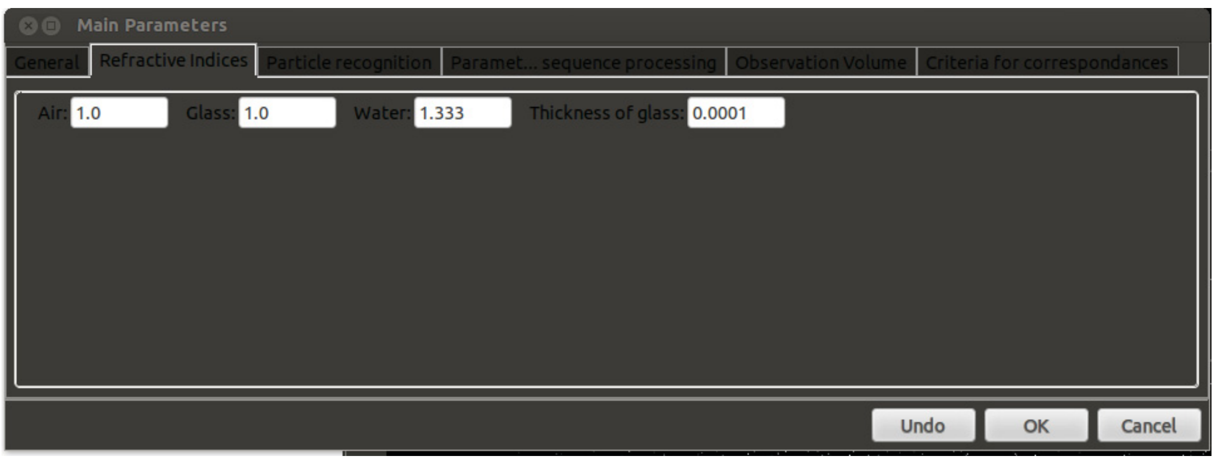
Main Parameters
General
Refractive Indices
Particle recognition
Paramet... sequence processing
Observation Volume
Criteria for correspondances
Air: 1.0
Glass: 1.0
Water: 1.333
Thickness of glass: 0.0001
Undo
OK
Cancel


Main Parameters
General
Refractive Indices
Particle recognition
Paramet... sequence processing
Observation Volume
Criteria for correspondances
Gray value treshold:
1st image: 14
2nd image: 10
3rd image: 8
4th image: 5
min npix: 2
min npix x: 1
min npix y: 1
max npix: 500
max npix x: 40
max npix y: 40
Sum of grey value: 8
Tolerable discontinuity: 2
Size of crosses: 4
Subtract mask:
Base name for the mask:
Use existing_target files?
Undo
OK
Cancel

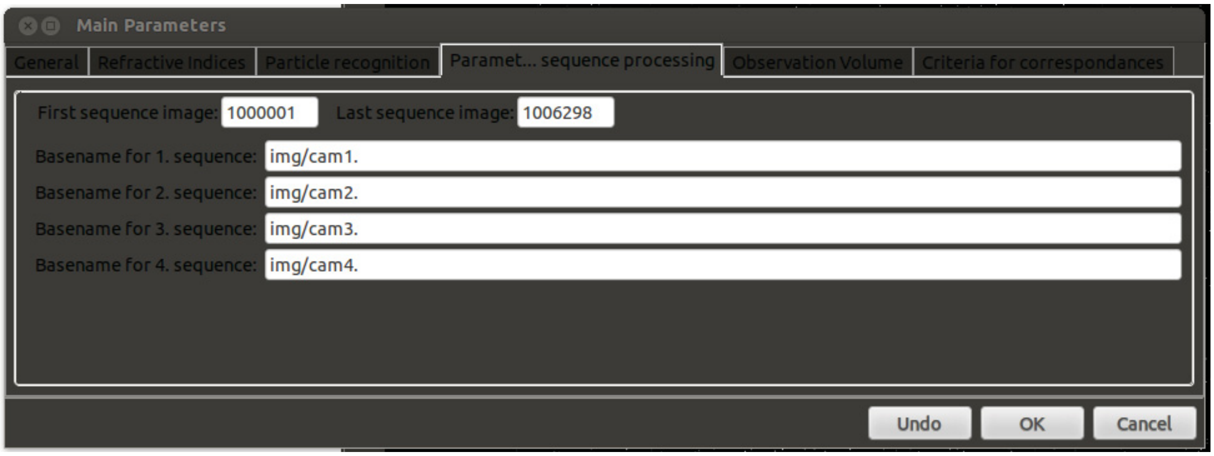
Main Parameters
General
Refractive Indices
Particle recognition
Paramet... sequence processing
Observation Volume
Criteria for correspondances
First sequence image: 1000001
Last sequence image: 1006298
Basename for 1. sequence: img/cam1.
Basename for 2. sequence: img/cam2.
Basename for 3. sequence: img/cam3.
Basename for 4. sequence: img/cam4.
Undo
OK
Cancel

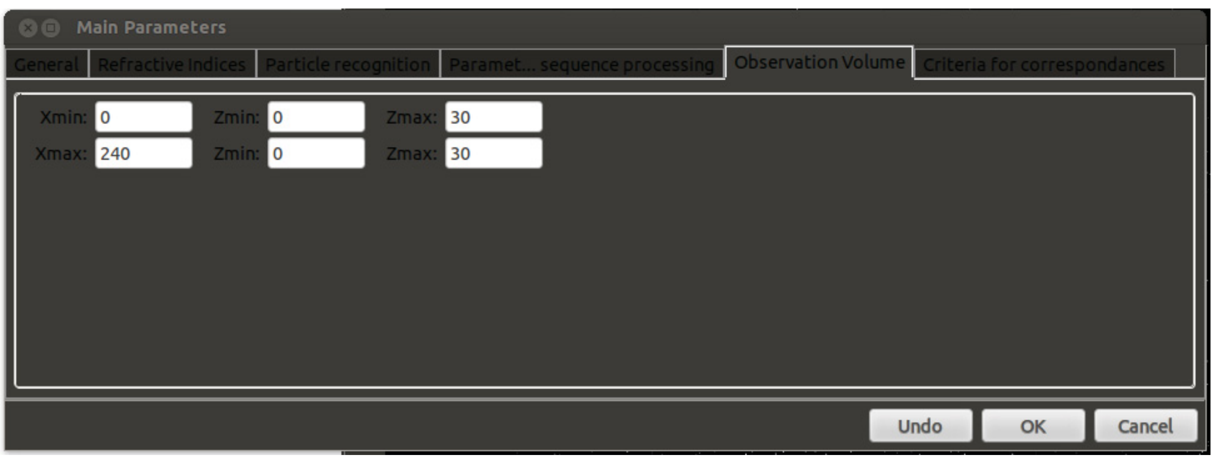
Main Parameters
General
Refractive Indices
Particle recognition
Paramet... sequence processing
Observation Volume
Criteria for correspondances
Xmin: 0
Zmin: 0
Zmax: 30
Xmax: 240
Zmin: 0
Zmax: 30
Undo
OK
Cancel


Main Parameters
General
Refractive Indices
Particle recognition
Paramet... sequence processing
Observation Volume
Criteria for correspondances
min corr for ratio nx: 0.02
min corr for ratio ny: 0.02
min corr for ratio npix: 0.02
sum of gv: 0.02
min for weighted correlation: 33.0
Tol band: 1.0
Undo
OK
Cancel

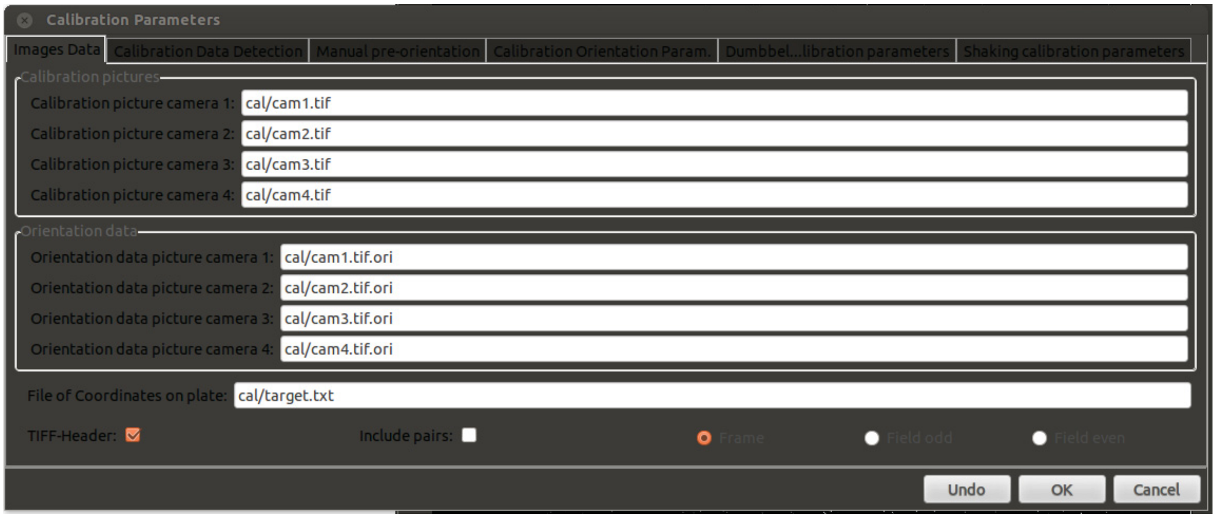
Calibration Parameters
Images Data
Calibration Data Detection
Manual pre-orientation
Calibration Orientation Param.
Dumbbel...libration parameters
Shaking calibration parameters
Calibration pictures
Calibration picture camera 1: cal/cam1.tif
Calibration picture camera 2: cal/cam2.tif
Calibration picture camera 3: cal/cam3.tif
Calibration picture camera 4: cal/cam4.tif
Orientation data
Orientation data picture camera 1: cal/cam1.tif.ori
Orientation data picture camera 2: cal/cam2.tif.ori
Orientation data picture camera 3: cal/cam3.tif.ori
Orientation data picture camera 4: cal/cam4.tif.ori
File of Coordinates on plate: cal/target.txt
TIFF-Header:
Include pairs:
Frame
Field odd
Field even
Undo
OK
Cancel

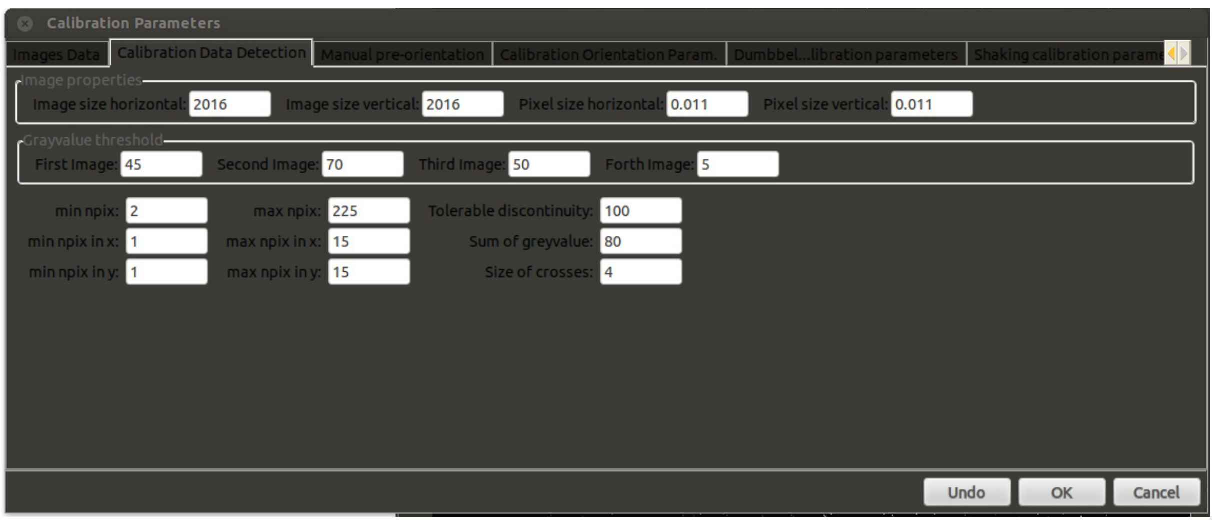
Calibration Parameters
Images Data
Calibration Data Detection
Manual pre-orientation
Calibration Orientation Param.
Dumbbel...libration parameters
Shaking calibration parame
Image properties
Image size horizontal: 2016
Image size vertical: 2016
Pixel size horizontal: 0.011
Pixel size vertical: 0.011
Grayvalue threshold
First Image: 45
Second Image: 70
Third Image: 50
Forth Image: 5
min npix: 2
max npix: 225
Tolerable discontinuity: 100
min npix in x: 1
max npix in x: 15
Sum of greyvalue: 80
min npix in y: 1
max npix in y: 15
Size of crosses: 4
Undo
OK
Cancel


Calibration Parameters
Images Data
Calibration Data Detection
Manual pre-orientation
Calibration Orientation Param.
Dumbbel...libration parameters
Shaking calibration parame
Image 1
P1: 1
P2: 23
P3: 967
P4: 989
Image 2
P1: 1
P2: 23
P3: 967
P4: 989
Image 3
P1: 1
P2: 23
P3: 967
P4: 989
Image 4
P1: 1
P2: 23
P3: 967
P4: 989
Undo
OK
Cancel

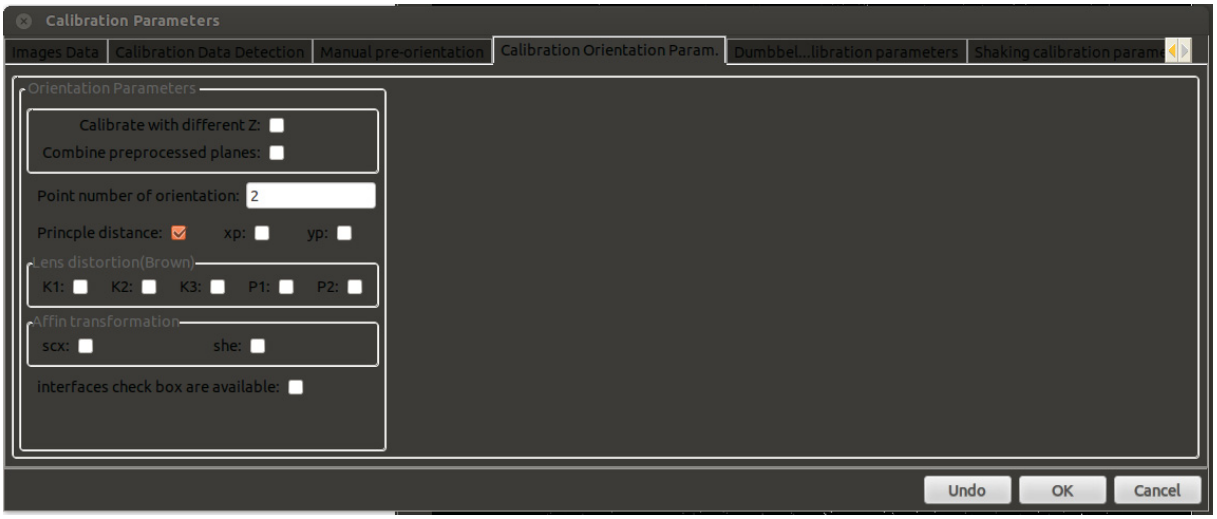
Calibration Parameters
Images Data
Calibration Data Detection
Manual pre-orientation
Calibration Orientation Param.
Dumbbel...libration parameters
Shaking calibration parame
Orientation Parameters
Calibrate with different Z:
Combine preprocessed planes:
Point number of orientation:
2
Princple distance:
xp:
yp:
Lens distortion(Brown)
K1:
K2:
K3:
P1:
P2:
Affin transformation
scx:
she:
interfaces check box are available:
Undo
OK
Cancel


Calibration Parameters
Images Data
Calibration Data Detection
Manual pre-orientation
Calibration Orientation Param.
Dumbbel...libration parameters
Shaking calibration parame
dumbbell epsilon:
3.0
dumbbell scale:
25.0
dumbbell gradient descent factor:
0.05
weight for dumbbell penalty:
1.0
step size through sequence:
1
number of iterations per click:
500
Undo
OK
Cancel


Calibration Parameters
Images Data
Calibration Data Detection
Manual pre-orientation
Calibration Orientation Param.
Dumbbel...libration parameters
Shaking calibration parame
shaking first frame:
10001
shaking last frame:
10001
shaking max num points:
10
shaking max num frames:
5
Undo
OK
Cancel

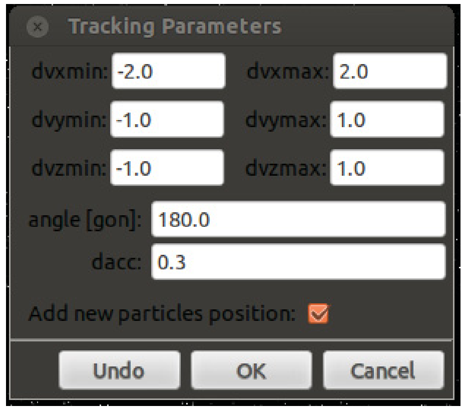
Tracking Parameters
dvxmin: -2.0
dvxmax: 2.0
dvymin: -1.0
dvymax: 1.0
dvzmin: -1.0
dvzmax: 1.0
angle [gon]: 180.0
dacc: 0.3
Add new particles position:
Undo
OK
Cancel

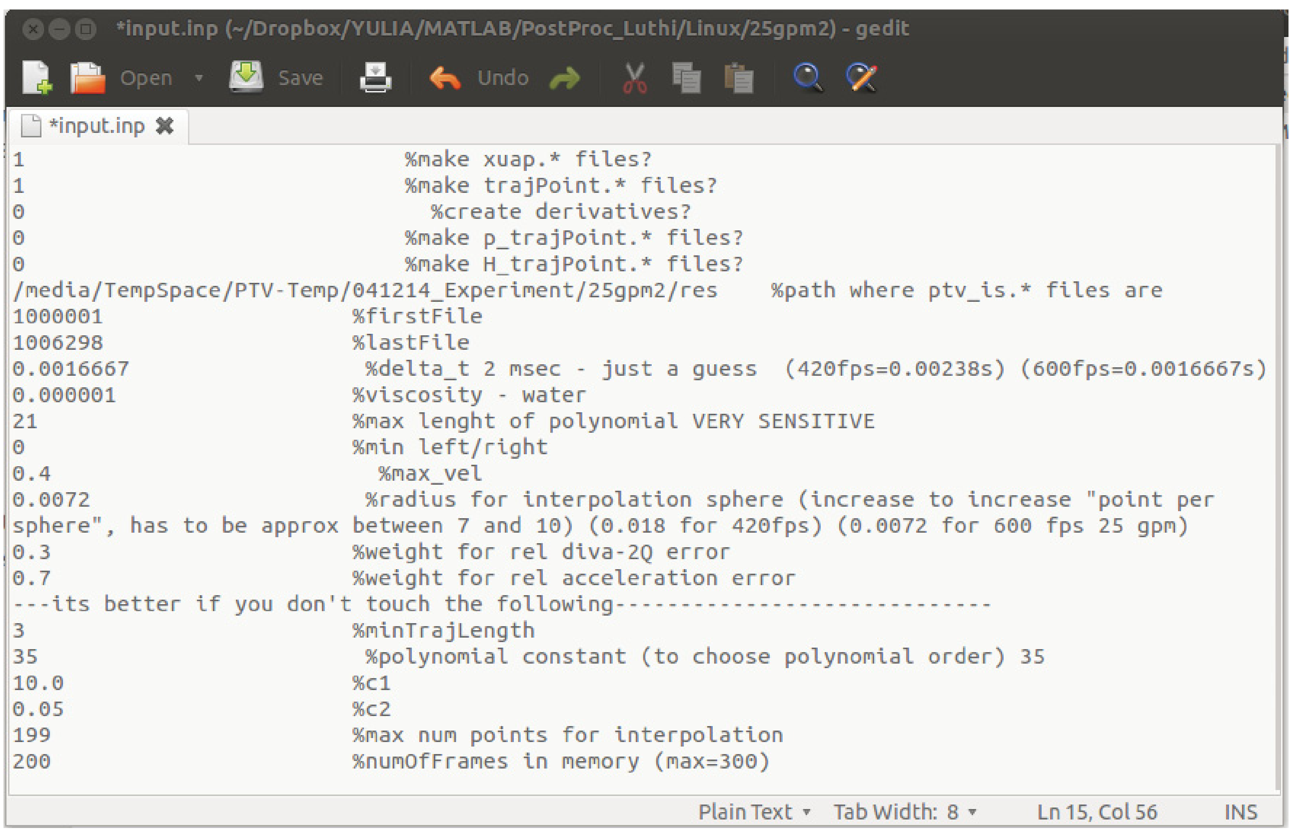
*input.inp (~/Dropbox/YULIA/MATLAB/PostProc_Luthi/Linux/25gpm2) - gedit
Open
Save
Undo
*input.inp
1 %make xuap.* files?
1 %make trajPoint.* files?
0 %create derivatives?
0 %make p_trajPoint.* files?
0 %make H_trajPoint.* files?
/media/TempSpace/PTV-Temp/041214_Experiment/25gpm2/res %path where ptv_is.* files are
1000001 %firstFile
1006298 %lastFile
0.0016667 %delta_t 2 msec - just a guess (420fps=0.00238s) (600fps=0.0016667s)
0.000001 %viscosity - water
21 %max lenght of polynomial VERY SENSITIVE
0 %min left/right
0.4 %max_vel
0.0072 %radius for interpolation sphere (increase to increase "point per
sphere", has to be approx between 7 and 10) (0.018 for 420fps) (0.0072 for 600 fps 25 gpm)
0.3 %weight for rel diva-2Q error
0.7 %weight for rel acceleration error
---its better if you don't touch the following----------------------------
3 %minTrajLength
35 %polynomial constant (to choose polynomial order) 35
10.0 %c1
0.05 %c2
199 %max num points for interpolation
200 %numOfFrames in memory (max=300)
Plain Text
Tab Width: 8
Ln 15, Col 56
INS

APPENDIX D
Convergence of turbulent fluctuations

In this work the primary focus was on the time-averaged statistics of the flow. Their convergence was shown in Section 4.2. However, as some turbulence statistics were used in the course of this research (for example, the Reynolds stresses in Figure 5.31), it is necessary to check their convergence. Root mean square (rms) values of turbulent velocity fluctuations were calculated based on different time periods (with one time step increments) for 36 positions in the embayment. At most of the points the rms values converge in 10 seconds, as in Figure D.1. However, some of the others take longer; up to 70 seconds, as in Figure D.2. It is therefore evident that the 90 seconds of data used in this study is sufficient to obtain not only converged mean values but also rms velocity statistics. It is also important to note that the magnitude of the velocity fluctuations is on average an order of magnitude larger than the that of the velocity us calculated in Section 4.3. The rms velocities vary between 2-4% of the free-stream velocity in the shear zone and up to 30% of U_∞ near the walls, whereas the magnitude of the velocity error is 0.2-0.4% of U_∞, indicating that the rms values obtained are the true velocity fluctuations of the flow.

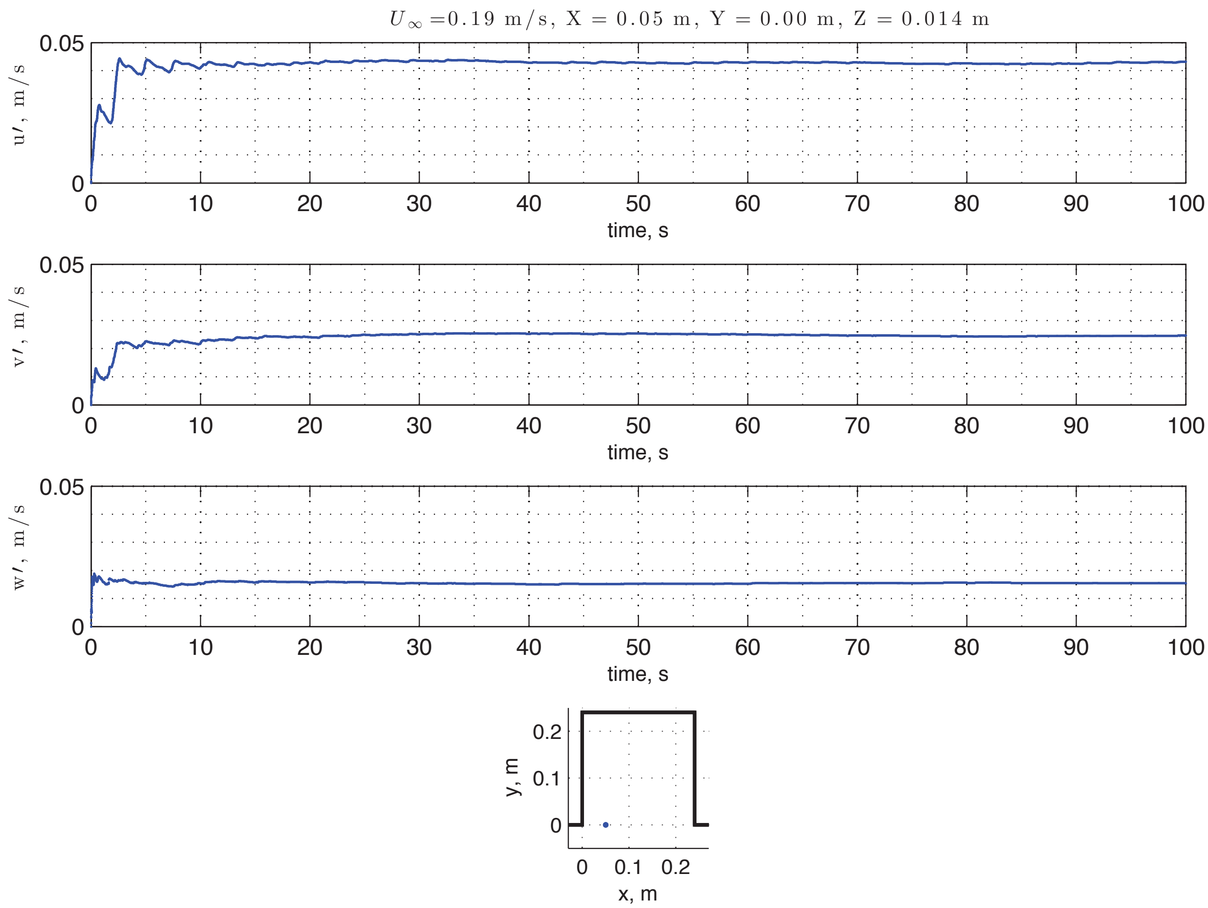

Figure D.1: Cumulative root mean square values of three components of velocity fluctuations ($u\prime$, $v\prime$, $w\prime$) at one point in the embayment $x = 0.05$ m, $y = 0$ m, and $z = 0.014$ m for the higher free-stream velocity of 0.19 m/s.

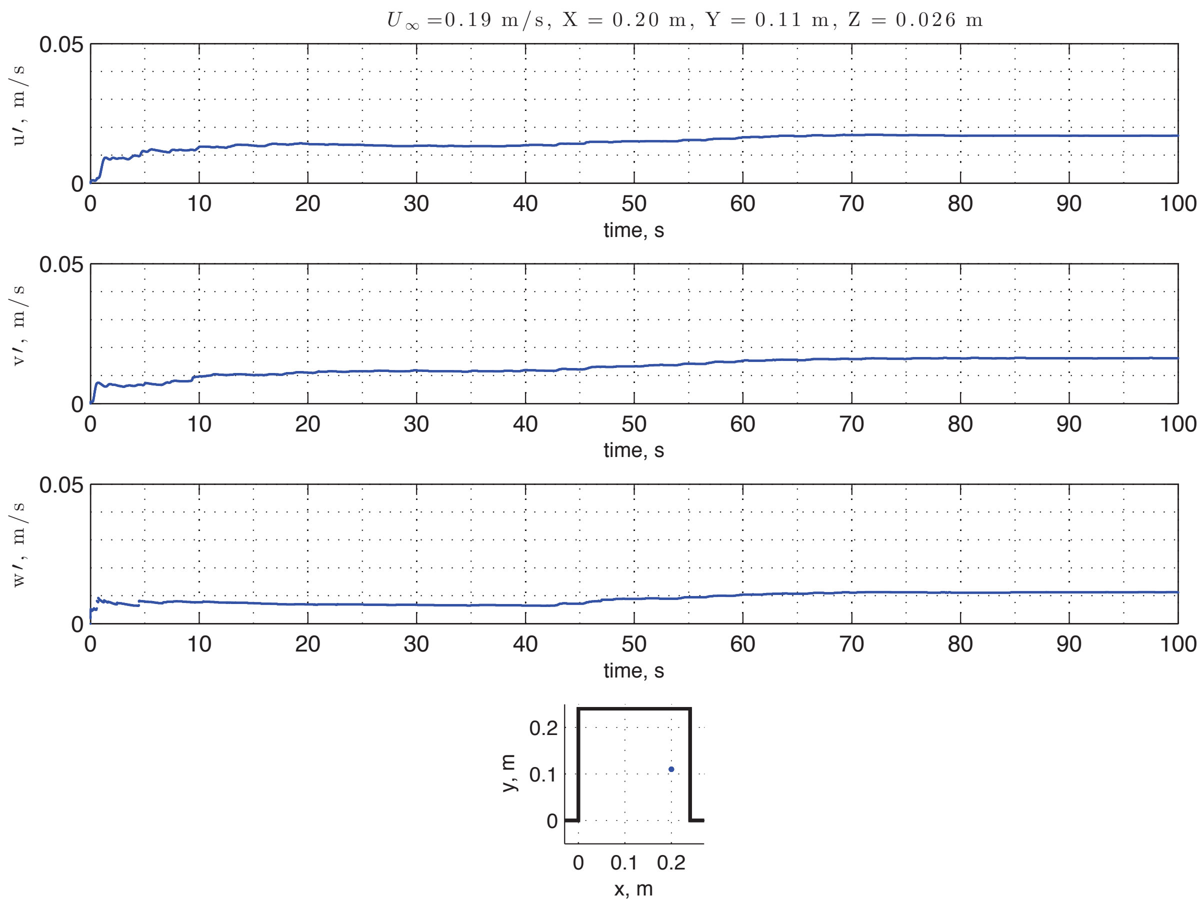

Figure D.2: Cumulative root mean square values of three components of velocity fluctuations ($u\prime$, $v\prime$, $w\prime$) at one point in the embayment $x = 0.2$ m, $y = 0.11$ m, and $z = 0.026$ m for the higher free-stream velocity of 0.19 m/s.

REFERENCES

ABBOT, MB 1979 Computational hydraulics: Elements of the theory of free surface flows. *Pitman, London* .

ADAMCZYK, AA & RIMAI, L 1988 Reconstruction of a 3-dimensional flow field from orthogonal views of seed track video images. *Experiments in Fluids* **6** (6), 380–386.

ALTAI, W & CHU, VH 1997 Retention time in recirculating flow. In *Environmental and Coastal Hydraulics@ sProtecting the Aquatic Habitat*, pp. 9–14. ASCE.

BABARUTSI, S. & GANOULIS, J. 1989 Experimental investigation of shallow recirculating flows. *Journal of Hydraulic Engineering* **115**, 906.

BALMFORTH, NJ 1999 Shear instability in shallow water. *Journal of Fluid Mechanics* **387**, 97–127.

BATCHELOR, G 1967 *An Introduction to Fluid Mechanics (Cambridge*. Press, Cambridge UK.

BERNAL, LP & ROSHKO, A 1986 Streamwise vortex structure in plane mixing layers. *Journal of Fluid Mechanics* **170**, 499–525.

BLASIUS, H. 1913 Das aehnlichkeitsgesetz bei reibungsvorgngen in flssigkeiten. *Mitteilungen ber Forschungsarbeiten auf dem Gebiete des Ingenieurwesens* **131**, 1–41.

BÖDEWADT, UT 1940 Die drehströmung über festem grunde. *ZAMM-Journal of Applied Mathematics and Mechanics/Zeitschrift für Angewandte Mathematik und Mechanik* **20** (5), 241–253.

BOOIJ, R 1989 Exchange of mass in harbours. In *Proceedings of 23rd IAHR Congress*.

Bown, MR, MacInnes, JM, Allen, RWK & Zimmerman, WBJ 2006 Three-dimensional, three-component velocity measurements using stereoscopic micro-piv and ptv. *Measurement Science and Technology* **17** (8), 2175.

Brès, Guillaume A & Colonius, Tim 2008 Three-dimensional instabilities in compressible flow over open cavities. *Journal of Fluid Mechanics* **599**, 309–339.

Brown, D. 1971 Close-range camera calibration. *Photogram. Eng. Remote Sens* **37**, 855–866.

Chang, TPK, Watson, AT & Tatterson, GB 1985 Image processing of tracer particle motions as applied to mixing and turbulent flowi. the technique. *Chemical engineering science* **40** (2), 269–275.

Chen, Daoyi & Jirka, Gerhard H 1997 Absolute and convective instabilities of plane turbulent wakes in a shallow water layer. *Journal of Fluid Mechanics* **338**, 157–172.

Chiu, Wan-Cheng & Rib, Louis N 1956 The rate of dissipation of energy and the energy spectrum in a low-speed turbulent jet. *Eos, Transactions American Geophysical Union* **37** (1), 13–26.

Chu, VH, Wu, JH & Khayat, RE 1983 Stability of turbulent shear flows in shallow channel. In *Proc. XX IAHR Congress, Moscow*, , vol. 3, pp. 128–133.

Chu, Vincent H & Babarutsi, Sofia 1988*a* Confinement and bed-friction effects in shallow turbulent mixing layers. *Journal of hydraulic engineering* **114** (10), 1257–1274.

Chu, Vincent H. & Babarutsi, Sofia 1988*b* Confinement and bed-friction effects in shallow turbulent mixing layers. *Journal of Hydraulic Engineering* **114** (10), 1257–1274, cited By (since 1996): 44 Export Date: 6 March 2011 Source: Scopus.

Citro, Vincenzo, Giannetti, Flavio, Brandt, Luca & Luchini, Paolo 2015 Linear three-dimensional global and asymptotic stability analysis of incompressible open cavity flow. *Journal of Fluid Mechanics* **768**, 113–140.

Constantinescu, G., Sukhodolov, A. & McCoy, A. 2009 Mass exchange in a shallow channel flow with a series of groynes: Les study and comparison with laboratory and field experiments. *Environmental fluid mechanics* **9** (6), 587–615.

Doswell, Charles A & Burgess, Donald W 1993 Tornadoes and tornadic storms: A review of conceptual models. *GEOPHYSICAL MONOGRAPH-AMERICAN GEOPHYSICAL UNION* **79**, 161–161.

Drazin, PG & Reid, WH 1981 *Hydrodynamic stability. Cambridge monographs on mechanics and applied mathematics*. Cambridge University Press, New York.

Ekman, V Walfrid 1905 On the influence of the earth's rotation on ocean currents. *Arkiv for matematik* **2** (1).

El-Hakim, SF 1986 Real-time image metrology with ccd cameras. *Photogrammetric Engineering and Remote Sensing* **52** (11), 1757–1766.

Elsinga, GE & Orlicz, GC 2015 Particle imaging through planar shock waves and associated velocimetry errors. *Experiments in Fluids* **56** (6), 1–12.

Engelhardt, Christof, Krüger, Angela, Sukhodolov, Alexander & Nicklisch, Andreas 2004 A study of phytoplankton spatial distributions, flow structure and characteristics of mixing in a river reach with groynes. *Journal of plankton research* **26** (11), 1351–1366.

Faure, Thierry M, Adrianos, Panayotis, Lusseyran, François & Pastur, Luc 2007 Visualizations of the flow inside an open cavity at medium range reynolds numbers. *Experiments in Fluids* **42** (2), 169–184.

Gaskin, S, Kemp, L & Nicell, J 2002 Lagrangian tracking of specified flow parcels in an shallow embayment using phosphorescent particles. In *Hydraulic Measurements and Experimental Methods Conference, CD-Rom, Session C6, EWRI and IAHR, Estes Park, Colorado, USA, July 28-Aug 1*, pp. 1–9.

Ghidaoui, MS & Kolyshkin, AA 1999 Linear stability analysis of lateral motions in compound open channels. *Journal of Hydraulic Engineering* **125** (8), 871–880.

Görtler, H 1940 Uber eine dreidimensionale instabilitat laminarer grenzschichten an konkaven wanden. *Ges. d. Wiss. Gottingen, Nachr. ad Math* **2** (1).

Gülan, Utku, Lüthi, Beat, Holzner, Markus, Liberzon, Alex, Tsinober, Arkady & Kinzelbach, Wolfgang 2012 Experimental study of aortic flow in the ascending aorta via particle tracking velocimetry. *Experiments in fluids* **53** (5), 1469–1485.

Hinterberger, C, Fröhlich, J & Rodi, W 2007 Three-dimensional and depth-averaged large-eddy simulations of some shallow water flows. *Journal of Hydraulic Engineering* **133** (8), 857–872.

Jacobi, Ole 1980 Photogrammetric tracking of a moving particle in running water. *International Archives of Photogrammetry* **23**, 369–374.

Jamieson, E 2005 Experimental investigation of recirculating flow in an open channel embayment using three-dimensional particle tracking. Master's thesis, Civil Engineering, McGill University, Canada.

Jamieson, E & Gaskin, SJ 2007*a* Experimental investigation of recirculating flow in an open channel embayment using three-dimensional. In *Hydraulic measurements and experimental Methods, EWRI and IAHR, Lake Placid, New York, Sept 10-12*, pp. 1–6.

Jamieson, E & Gaskin, SJ 2007*b* Laboratory study of 3-dimensional characteristics of recirculating flow in a river embayment. In *32nd Congress of IAHR, July 1-6, Venice, Italy*, pp. pp. 1–9.

Kähler, Christian J, Scharnowski, Sven & Cierpka, Christian 2012 On the uncertainty of digital piv and ptv near walls. *Experiments in fluids* **52** (6), 1641–1656.

Kimura, Ichiro & Hosoda, Takashi 1997 Fundamental properties of flows in open channels with dead zone. *Journal of Hydraulic Engineering* **123** (2), 98–107.

Klebanoff, PS, Tidstrom, KD & Sargent, LM 1962 The three-dimensional nature of boundary-layer instability. *Journal of Fluid Mechanics* **12** (01), 1–34.

Kolmogorov, Andrey Nikolaevich 1941 Dissipation of energy in locally isotropic turbulence. In *Dokl. Akad. Nauk SSSR*, , vol. 32, pp. 16–18.

Kolyshkin, AA & Ghidaoui, MS 2002 Gravitational and shear instabilities in compound and composite channels. *Journal of Hydraulic Engineering* **128** (12), 1076–1086.

Kraichnan, Robert H 1971 Inertial-range transfer in two-and three-dimensional turbulence. *Journal of Fluid Mechanics* **47** (03), 525–535.

Lumley, JL 1965 Interpretation of time spectra measured in high-intensity shear flows. *Physics of Fluids (1958-1988)* **8** (6), 1056–1062.

Lüthi, Beat, Tsinober, Arkady & Kinzelbach, Wolfgang 2005 Lagrangian measurement of vorticity dynamics in turbulent flow. *Journal of Fluid mechanics* **528**, 87–118.

Maas, HG, Gruen, A & Papantoniou, D 1993 Particle tracking velocimetry in three-dimensional flows. *Experiments in Fluids* **15** (2), 133–146.

Malik, NA, Dracos, Th & Papantoniou, DA 1993 Particle tracking velocimetry in three-dimensional flows. *Experiments in Fluids* **15** (4-5), 279–294.

McCoy, Andrew, Constantinescu, George & Weber, Larry J 2008 Numerical investigation of flow hydrodynamics in a channel with a series of groynes. *Journal of Hydraulic Engineering* **134** (2), 157–172.

Méhauté, Bernard 1976 *An introduction to hydrodynamics and water waves*. Springer.

Mizumura, K., Yamasaka, M. & Adachi, J. 2003 Side outflow from supercritical channel flow. *Journal of Hydraulic Engineering* **129**, 769.

Monin, AS & Yaglom, AM 1971 Statistical fluid dynamics. *Vols. I and IIMIT Press, Cambridge (1971, 1975)* .

Nezu, I & Onitsuka, K 2002 Piv measurements of side-cavity open-channel flows wando model in rivers. *Journal of visualization* **5** (1), 77–84.

Nishino, Koichi, Kasagi, Nobuhide & Hirata, Masaru 1989 Three-dimensional particle tracking velocimetry based on automated digital image processing. *Journal of fluids engineering* **111** (4), 384–391.

OpenPTV 2012 Openptv documentation. Http://alexlib.github.io/docs/intro.html.

Papantoniou, D & Dracos, Th 1990 Lagrangian statistics in open channel flow by 3-d particle tracking velocimetry. *Eng. Turb. Model. Expt. Elsevier* .

van Prooijen, Bram C & Uijttewaal, Wim SJ 2002 A linear approach for the evolution of coherent structures in shallow mixing layers. *Physics of Fluids (1994-present)* **14** (12), 4105–4114.

Raffel, Markus, Willert, Christian E, Kompenhans, Jürgen *et al.* 2013 *Particle image velocimetry: a practical guide*. Springer.

Schlichting, H 1968 *Boundary-layer theory*. McGraw-Hill New York.

Sukhodolov, Alexander N 2014 Hydrodynamics of groyne fields in a straight river reach: insight from field experiments. *Journal of Hydraulic Research* **52** (1), 105–120.

Sukhodolov, Alexander N & Uijttewaal, Wim SJ 2010 Assessment of a river reach for environmental fluid dynamics studies. *Journal of Hydraulic Engineering* .

Tong, Chenning & Warhaft, Z 1995 Passive scalar dispersion and mixing in a turbulent jet. *Journal of Fluid Mechanics* **292**, 1–38.

Tropea, Cameron, Yarin, Alexander L & Foss, John F 2007 *Springer handbook of experimental fluid mechanics*, , vol. 1. Springer Science & Business Media.

Tuna, BA & Rockwell, D 2014 Self-sustained oscillations of shallow flow past sequential cavities. *Journal of Fluid Mechanics* **758**, 655–685.

Tuna, BA, Tinar, E & Rockwell, D 2013 Shallow flow past a cavity: globally coupled oscillations as a function of depth. *Experiments in fluids* **54** (8), 1–20.

Uijttewaal, WSJ & Booij, R 2000 Effects of shallowness on the development of free-surface mixing layers. *Physics of Fluids (1994-present)* **12** (2), 392–402.

Uijttewaal, WSJ, Lehmann, D. & Van Mazijk, A. 2001 Exchange processes between a river and its groyne fields: Model experiments. *Journal of Hydraulic Engineering* **127**, 928.

Valentine, Eric M & Wood, Ian R 1977 Longitudinal dispersion with dead zones. *Journal of the Hydraulics Division* **103** (9), 975–990.

Weitbrecht, V, Kühn, G & Jirka, GH 2002 Large scale piv-measurements at the surface of shallow water flows. *Flow Measurement and Instrumentation* **13** (5), 237–245.

Weitbrecht, V., Socolofsky, S.A. & Jirka, G.H. 2008 Experiments on mass exchange between groin fields and main stream in rivers. *Journal of Hydraulic Engineering* **134**, 173.

Willneff, J 2003 A spatio-temporal matching algorithm for 3d particle tracking velocimetry. PhD thesis, Institute of Technology, Germany.

Wolfinger, M, Ozen, CA & Rockwell, D 2012 Shallow flow past a cavity: coupling with a standing gravity wave. *Physics of Fluids (1994-present)* **24** (10), 104103.